The *GridGEM module*: a new GEM based readout module for a large TPC

and

A new algorithm for the measurement of the kinematic edges positions in SUSY decays

Dissertation

zur Erlangung des Doktorgrades
des Department Physik
der Universität Hamburg

vorgelegt von

Sabato Stefano Caiazza

aus Potenza, Italien

Hamburg
2018

Tag der Disputation: **28.03.2018**

Folgende Gutachter empfehlen die Annahme der Dissertation:

1. Gutachterin: Prof. Dr. Erika Garutti
2. Gutachterin: Dr. Jenny List

Abstract

The ILC is a planned linear collider, designed to provide polarized electrons and positrons at energies higher than 250 GeV, possibly up to 1 TeV, never before reached at a lepton collider. At the interaction point there will be two detectors, which will perform high precision measurement at those energies. To achieve those performances, many of the components have to be developed beyond the current state of the art. Moreover a preliminary simulation and analysis work is required to understand what type of measurements will those experiments be able to perform and which precision can they achieve.

In this thesis we will be mostly concerned with the ILD experiment, which features a large volume TPC used as its main tracker. The first part of this thesis focusses on the design, development and test of the first prototype of a new GEM-based readout module for that TPC, built around an innovative ceramic support system which will allow a reduction of the dead space in the sensitive area of a factor of 3, as compared to traditional solutions.

In the second part of this work we will focus on the development of a computational technique to measure the position of edge-like kinematic end-points in physical distributions. Therefore this work will focus in particular on the characterisation of the algorithm to define a procedure to reliably evaluate the statistical and systematic errors associated with the measurement. At the ILD such a technique would be particularly useful to measure the end-point in the kinematic distributions of the decay products of new physical states like those hypothesized by Supersymmetry. To evaluate the performance of the algorithm and of the experiment in that scenario we applied that new technique to the process $e^-e^+ \to \tilde{e}_R\bar{\tilde{e}}_R \to e^\pm e^\mp \tilde{\chi}^0_1\tilde{\chi}^0_1$ and measured the position of the kinematic edge in the momentum distribution of the final state leptons obtaining a factor of 2 improvement on the accuracy in the measurement of the masses of the s-electron and Neutralino, as compared to the currently published estimates.

Zusammenfassung

Der ILC ist ein geplanter Linear Collider , der entworfen wurde, um polarisierte Elektronen und Positronen bei Energien von mehr als 250 GeV, möglicherweise bis zu 1 TeV, zu liefern, die noch nie zuvor an einem Lepton Collider erreicht wurden. Am Wechselwirkungspunkt befinden sich zwei Detektoren, die bei diesen Energien eine hochpräzise Messung durchführen. Um diese Ziele zu erreichen, müssen viele Komponenten über den aktuellen Stand der Technik hinaus entwickelt werden. Darüber hinaus ist eine vorbereitende Simulation und Analyse erforderlich, um zu verstehen, welche Art von Messungen diese Experimente durchführen können und welche Präzision sie erreichen können.

In dieser Dissertation beschäftigen wir uns hauptsächlich mit dem ILD-Experiment, bei dem eine TPC mit großem Volumen als Haupttracker verwendet wird. Der erste Teil dieser Arbeit beschäftigt sich mit dem Design, der Entwicklung und dem Test des ersten Prototyps eines neuen GEM-basierten Auslesemoduls für diese TPC, das auf einem innovativen keramischen Trägersystem basiert, das, verglichen mit traditionellen Lösungen, eine Reduzierung des Totraums im sensitiven Bereich um einem Faktor 3 ermöglicht.

Im zweiten Teil dieser Arbeit werden wir uns auf die Entwicklung einer Computertechnik konzentrieren, um die Position von Kantenähnlichen kinematischen Endpunkten in physikalischen Verteilungen zu messen. Daher wird sich diese Arbeit insbesondere auf die Charakterisierung des Algorithmus konzentrieren, um ein Verfahren zu definieren, mit dem die mit der Messung verbundenen statistischen und systematischen Fehler zuverlässig ausgewertet werden können. An der ILD wäre eine solche Technik besonders nützlich, um den Endpunkt in den kinematischen Verteilungen der Zerfallsprodukte neuer physikalischer Zustände zu messen, wie sie von Supersymmetrie angenommen werden. Um die Leistung des Algorithmus und des Experiments in diesem Szenario zu bewerten, wurde diese neue Technik auf den Prozess $e^-e^+ \to \tilde{e}_R\bar{\tilde{e}}_R \to e^\pm e^\mp \tilde{\chi}^0_1\tilde{\chi}^0_1$ angewendet und die Position der kinematischen Kante in der Impulsverteilung der Endzustands Leptonen gemessen, um die Genauigkeit in der Messung der Massen von s-Elektron und Neutralino im Vergleich zu den derzeit veröffentlichten Schätzungen um einen Faktor 2 zu verbessern.

Contents

Introduction

The Standard Model of particle physics (see § 1.1) is arguably the most successful theory describing the fundamental constituents of our Universe, providing the most precise prediction for a wide array of physical observables. Nonetheless, this theory is known to be only a partial description of the fundamental physics underlying the interactions between the most basic constituents of Nature (see § 1.2). Its validity and limitations have been tested in the last 50 years through hundreds of different experiments but few provide the precision and reliability as those which are performed on particle colliders. Therefore it is likely that the best hints to understand the physics of our Universe beyond the validity range of the Standard Model will come from the measurements performed at experiments using the power of those machines.

The workhorse of collider physics research today is the LHC, capable of creating the most energetic particle interactions artificially produced on Earth, achieved by colliding protons in a circular synchrotron. Those high energies can be reached because, due to the relatively high proton mass, the radiation losses are limited and that makes it possible to use a synchrotron to accelerate the beams. On the other hand, the protons are not elementary particles and this has two important disadvantages: the type of elementary particles which actually collide can not be defined as they can be any quark and gluon with relative probabilities depending on the hadronic form factor which are not themselves known with arbitrary precision; moreover, the centre-of-mass energy cannot be accurately known as the measurable beam momentum only defines the collective motion of all the nuclear components.

The perfect complement of an hadron collider is a lepton collider, where the interacting particles are assumed elementary so their interactions and the centre-of mass energy at which they happen are well defined. Unfortunately the only stable charged leptons which can be easily accelerated[1] are electrons and positrons but, due to their low mass, they lose large amounts of energy through synchrotron radiation as they travel in a circular machine and this limits the maximum energy that can be achieved in those type of particle accelerators. Therefore there are two possible solutions to increase the centre-of-mass energy of a lepton collider beyond that which was already achieved: build a larger ring or get rid of the ring completely and build a linear accelerator. The second path is the one followed by the ILC, currently in advanced design state (see § 2).

[1]The technologies for producing, accelerating and colliding muon beams are currently under study but they are not mature enough for an actual large-scale machine to be built.

In its current baseline design (see § 2.2), ILC aims to collide polarized electrons and positrons at energies up to 500 GeV using two 11 km long linear accelerators. Additionally, the design of a linear collider is versatile enough to allow for a staged construction approach whereby the centre-of-mass energy can be increased in time by increasing the tunnels length and the number of installed accelerating cavities. At the interaction point there will be two detectors, named SiD and ILD, which will share the available beam time. As this thesis was developed in the context of the ILD experiment (see § 3), we will focus on that one in particular. Both detectors, to achieve the performance required to complete their physics programs, need to adopt the so-called particle flow paradigm which aims to reconstruct the momenta of all charged particles in high-resolution trackers and rely on calorimetric measurements only for the neutral particles (see § 3.1). Hence, the tracker system is the keystone of both experiments. In the ILD case, the optimal design choice for the main tracker is a large volume Time Projection Chamber (see § 4.5).

In a TPC, the charge particles to detect ionize a well-chosen gas and the ionization electrons drift towards the anode along the lines of a carefully shaped electric field. By measuring the position and the time of arrival of those ionization cluster to the anode end of the detector, it is then possible to reconstruct the three-dimensional trajectory of the primary particle. Therefore the performance of the detector depend directly on the quality of the position and timing measurement of the readout devices equipping its anode. Traditionally that measurement was performed using multi-wire layers parallel to the anode plane but more modern and accurate detector have been since developed. Many of them can be grouped in the category of the Micro Pattern Gas Detectors or MPGD (see § 4.4.3) and, among them, we will dedicate particular attention to the Gas Electron Multiplier, also known as GEM (see § 5), which combines the desired resolution with high rate capability, robustness and reliability. Even though those technologies have been already used in other TPC detectors they were never used on one of such a scale as the one designed for the ILD. For this reason, an extensive effort of research and development is ongoing, coordinated through a large international collaboration named LCTPC. Because this detector will require the development and optimization of several new technologies, a demonstrator, called the Large Prototype TPC or LP-TPC, and its additional support infrastructure were built and deployed at DESY (see § 6).

To improve the robustness of its design, the readout of the ILD TPC is being developed to be modular, with independent devices equipping a special support structure on the anode end of the detector. Therefore the LP-TPC was also designed with such a modular approach, with several independent readout device that can be installed at the anode end of the detector (see § 6.1.1). The first part of this thesis will focus on the design and test of one of such modules (see § 7 and 8).

One of the most important innovations in our design is the usage of a ceramic frame to mechanically stabilize the GEM foil and, at the same time, to provide the spacing and the electrical insulation between the foils, a technique pioneered in our group at DESY with smaller devices (see § 7.4). To achieve the required resolution, we also designed a specific readout with almost 5000 sensitive pads deployed in a highly dense layout (see § 7.5). Additionally we produced a simplified version of that board which only includes about

1000 sensitive pads in a high density area in the middle of the sensitive surface to perform the initial tests. Those tests were initially performed in our detector laboratory, in a smaller TPC designed specifically for that module, and afterwards on the DESY test-beam line in the LP-TPC (see § 8.8 and 8.9).

The analysis of the data produced during those tests was performed using an extension of the MarlinTPC software, which was designed and developed in the context of the work done for this thesis (see § 9.2). The results presented in chapter 9 focus on the basic characterisation of the setup including: the establishment of the optimal configuration for the electronics used to readout the detector and a procedure to identify anomalous electronics channels in the readout chain, the optimization of the parameters of the data reconstruction and the measurement of the effects of the ceramic grid on the detector efficiency. In particular we noticed a relevant drop of the efficiency at the edges of the sensitive area which was due to the field distortions introduced by the electrostatic interactions with the nearby modules in the anode end-plate (see § 9.6.4).

The second part of this work is dedicated to the development of a new analysis method to identify and precisely measure the position of edge-like kinematic end-points in physically relevant distributions. Those type of features characterise many physical processes, in particular whenever one of the final-state particles cannot be detected by the experiment and the initial-state of the relevant variable is known with sufficient accuracy. That situation is relatively common when studying the possible signatures at particle colliders of theories like the Supersymmetry, shortly described in § 1.3. There the particles produced in the beam collisions are often very shortly lived and immediately decay to a composite final-state made of Standard Model particle and stable or long-lived Supersymmetric particles, typically the lightest one in the spectrum. When that happen, the values of kinematic variables like the final-state energy or the momenta of some combination of the final state particles which are produced in those events will have a well defined range, depending on the initial-state. Because in a lepton collider that initial-state is known with very high precision, the identification and characterization of those kinematic end-points is a powerful tool to understand the properties of the underlying physical processes (see § 10.1).

In the case of the ILC/ILD combination, one of the most important processes where the analysis of such features is relevant, is the production and subsequent decay of the lightest supersymmetric partner of the electron, typically the right-handed s-electron ($\tilde{e}_R$). In an electron-positron collider, if the process is kinematically allowed, those particles are always produced in pairs and the production cross-section is particularly high. As the $\tilde{e}$ cannot be stable, as it would have been otherwise discovered through its electromagnetic interactions, it will immediately decay to a neutral supersymmetric particle, typically the lightest Neutralino, and its Standard Model partner, that is an electron or positron. If that neutral particle is long-lived, the momenta of those leptons will be kinematically limited and by measuring the position of those limits it is possible to calculate the unknown masses of the supersymmetric particles (see § 10.2).

As there is currently no direct evidence of Supersymmetry, the number and range of its characterising parameters is very wide. Therefore most analysis have to choose a

specific point or a limited range in that parameter space to perform detailed analysis, especially when evaluating the full detector performance in that scenario. In our case this benchmark scenario is called STC4 and is described in § 10.3.1. Within that scenario we will use simulated data assuming a 500 GeV ILC with 80% polarized electrons and 30% polarized electrons after accumulating 500 fb^{-1} of data.

The typical way to analyse the above-mentioned distributions is to fit an arbitrary function and to derive the edge position from one of the function parameters. That approach assumes a specific analytic shape for the edge to analyse but that is often not the case as the ideal one can be deformed by effects such as the imperfect knowledge of the initial kinematic state or the detector resolution, hence we decided to develop an algorithm which is simply sensitive to the characterizing feature of an edge, that is the maximization of the first derivative of the function. Unfortunately, the numerical derivative, calculated according to the typical definition, is not robust against noise. Therefore we developed an algorithm, inspired by similar solution used in image processing software, to identify and localize those edges in one-dimensional distributions. The theoretical foundations and the characteristics of that algorithm are described in chapter 11.

Contrary to the case of the image processing where the efficiency in the edge identification is the most important benchmark, we need also to optimize the localization accuracy of the algorithm to be able to quantify the statistic and systematic resolution of our measurement. Therefore, in the second half of chapter 11, we fully characterise the algorithm and describe a systematic procedure to evaluate its localization properties, depending on the values of its steering parameters, and use it on the distribution of the momenta of the electron and positrons generated in the decay of the s-electron produced in the $e^-e^+ \to \tilde{e}_R\bar{\tilde{e}}_R$ process. In this phase we won't include any background and we will not consider any detector effect so that we can evaluate a best-case scenario for our final measurement.

Finally, we added all the background processes and performed a fast detector reconstruction on all data to develop a complete analysis (see chapter 12). That analysis can be divided in three parts: first we developed and characterized a simple electron reconstruction algorithm to identify the isolated electrons in each events, then we performed a dedicated cut-based selection to reduce the background levels at a manageable level so that we can finally apply our edge measurement algorithm to measure the position of the kinematic limits in the momentum spectra of the identified electron and positrons. With those numbers, in § 12.5 we calculated the masses of both the s-electron and Neutralino and, most importantly, the accuracy with which the ILD will be able to measure them using this newly developed algorithm.

Part I

The next generation of high energy physics experiments

Chapter 1

The Standard Model and beyond

The Standard Model of particle physics is a robust and well tested theory that has shown, over the last 50 years, an impressive agreement with a great number of high precision observations. Nonetheless this theory is known to provide only a partial description of the fundamental physics underlying the interactions between the most basic constituents of Nature.

A possible solution to some of the standing issues of the Standard Model comes from an additional, discrete space-time symmetry, called *Supersymmetry*, which postulates the existence of a matching fermion for each boson and vice versa. An experimental evidence for this theory has not been found yet but present and future colliders will be able to test its predictions and verify if this theory is actually realized in Nature.

This chapter will introduce the basic concepts on which the Standard Model is built with a particular focus on the electroweak symmetry breaking mechanism and will justify its claims to validity with a selection of some the most relevant experimental results.

The list of these achievements will introduce the reader to an overview of some of the shortcomings of the model and to some of the hints for new physical phenomena beyond those that it describes (§ 1.2). A particular relevance is given to the *Hierarchy Problem* and to the evidence for *Dark Matter* which can be naturally explained within a Supersymmetric extension of the Standard Model. The simplest Supersymmetric extension of the Standard Model, called *MSSM*[1], is introduced in § 1.3

1.1 The Standard Model of particle physics

Our current understanding of the fundamental behaviour of the basic components of the universe, described by *the Standard Model of particle physics* (see [1] for a complete treatment), is based on the interplay of a set of fermionic fields, called matter, through 3 bosonic gauge fields, that are the forces or fundamental interactions. The interaction of these fields

[1] *Minimal Supersymmetric Standard Model*

with an additional scalar field, known as the Higgs field, gives mass to the particles involved through the Higgs mechanism of electroweak symmetry breaking [2, 3].

The fourth fundamental interaction known in Nature, that is gravity, is neglected in the Standard Model, being too weak at the scale and size that it describes and due to its fundamental difference from all the other interactions, as we understand them today. This model, developed in the 1960s and 1970s, did stand for the last 40 years as "The" theory of particle physics, passing numerous stringent tests. In fact, while many people believe that the standard model is not a complete description of particle physics, it is expected to be incomplete rather than wrong, at worst a subset of the true theory of particle physics.

The Standard Model is a relativistic quantum field theory and, as such, is based on 4 major constraints:

Unitarity: The sum of all probabilities of all mutually exclusive events must be one during the entire time evolution of the Hamiltonian.

Locality: Physics processes must be independent at different point separated by a space-like interval and they must evolve independently, provided no signal is propagated between them. This causality requirement also implies that, for each particle, there exists another one of equal mass and spin, that is its anti-particle, that fulfils the following constraints:

- Anti-particles exist and couple with a strength identical to that of the matching particle. This is called *crossing symmetry*.
- The behavior of particles and antiparticles under symmetries such as gauge or parity transformation are related which, for example, means that the electric charge of a particle is opposite to that of its anti-particle.

This principle together with the fact that fermionic fields are anti-commutative and bosonic fields are commutative implies the spin-statistics theorem: the fermions are half-integer-spin particles and the boson are integer-spin particles.

Poincaré Invariance: Any physically valid theory should be invariant under space-time translations and Lorentz transformations. This means that the Lagrangian density function, through which we describe the model, cannot depend explicitly on the space-time coordinates and must be a Lorentz scalar.

Stability: The final constraint is for the spectrum of the Hamiltonian to be bounded from below, which is necessary to define a meaningful vacuum state as that state of lowest energy. This condition also implies that the Lagrangian is a function of, at most, single derivatives of the fields involved.

A further condition imposed to the Standard Model, not as fundamental as those previously listed, is that of the renormalizability. This criteria is a way to define the validity domain of the theory. It can be expressed saying that there is an energy scale Λ above which the Standard Model is unable to make reliable prediction but that any process above

that scale, of which we do not know the details, can be represented by a finite amount of parameters, such as the mass and charges of the particles involved, that can be measured experimentally in the validity domain of the theory and from which all the other processes can be calculated. One important consequence of the renormalization criteria is that allows only operators of mass dimension $d \leq 4$ to describe the interactions between fields. In general, all such interactions which are consistent with the assumed symmetries must be included in the model.

The Standard Model of Particle Physics is the most general renormalizable theory consistent with those basic principles and with the field content experimentally observed and described in the following section.

1.1.1 Particles and fields of the Standard Model

The strong, weak, and electromagnetic interactions are understood as arising from to the exchange of several spin-one gauge bosons between the spin-half particles that make up matter. The gauge-invariant symmetry group of the standard model, as observed until now by the experiments, is $\boldsymbol{SU_C(3) \times SU_L(2) \times U_Y(1)}$. It is worth noticing that the choice of this symmetry group is an *experimental fact* for which we do not have any deeper understanding. The generators of this group algebra are the fundamental mediator bosons, all massless:

- Eight *gluons*, labelled $\boldsymbol{G^{\alpha}_{\mu}}$, with $\alpha = 1, \ldots, 8$, associated with the $SU_C(3)$ factor. Their coupling constant will be labelled $\boldsymbol{g_3}$. The associated subscript $\boldsymbol{C}$ is meant to denote *colour*. Any particle that transforms with respects to this factor of the gauge group, and thus couples to the gluons, is said to be coloured or to carry colour. This is also called the *strong* interaction.

- Three particles, labelled $\boldsymbol{W^a_{\mu}}$, with $\alpha = 1, \ldots, 3$, are associated with the $SU_L(2)$ group, characterized by the *weak isospin* quantum number, where the $\boldsymbol{L}$ subscripts indicates that only the left-handed fermions transform under this group. The coupling constant of this group will be named $\boldsymbol{g_2}$.

- One particle, labelled $\boldsymbol{B_{\mu}}$, is the generator of the final $U_Y(1)$ group and its coupling constant will be named $\boldsymbol{g_1}$. The $\boldsymbol{Y}$ subscript distinguishes this group, associated with the quantum number called *weak hypercharge*, from the $U_{em}(1)$ group of the electromagnetic interactions described by the *QED*[2].

The four spin-one bosons associated with the factors $SU_L(2) \times U_Y(1)$ are related to the physical bosons that mediate the weak interactions, $\boldsymbol{W^{\pm}}$ and $\boldsymbol{Z^0}$, and to the QED photon

[2] *Quantum Electrodynamics*

$\boldsymbol{A_\mu}$ by the following relations:

$$\begin{aligned} \boldsymbol{W_\mu^\pm} &= \frac{1}{\sqrt{2}}(W_\mu^1 \mp W_\mu^2) \\ \boldsymbol{Z_\mu^0} &= W_\mu^3 \cos(\theta_W) - B_\mu \sin(\theta_W) \\ \boldsymbol{A_\mu} &= W_\mu^3 \sin(\theta_W) + B_\mu \cos(\theta_W) \end{aligned} \tag{1.1}$$

where the Weinberg angle $\boldsymbol{\theta_W} = \tan^{-1}(g_1/g_2)$.

Besides those spin-one particles, we are also aware of a number of fundamental spin-half particles. They are divided in three groups, called families or generations, that couple identically to all the mediator bosons but contain particles with different masses.

Those fermions can also be divided in two sets according to their interactions with the gauge groups:

- The *leptons* ($\boldsymbol{\ell}$) are, by definition, those spin-half particles which do not take part in the strong interactions. Six leptons are known and included in the standard model and are denoted as $\boldsymbol{e, \mu, \tau, \nu_e, \nu_\mu, \nu_\tau}$ (respectively electron, muon, tau and electron, muon and tau neutrino).

- The strongly interacting particles are known as hadrons and their spectrum is rich and varied but they are all described in the Standard Model as the bound states of six *quarks* ($\boldsymbol{q}$), individually denoted, in an increasing mass sequence, as $\boldsymbol{u}$ (up), $\boldsymbol{d}$ (down), $\boldsymbol{s}$ (strange), $\boldsymbol{c}$ (charm), $\boldsymbol{b}$ (bottom) and $\boldsymbol{t}$ (top).

Each fermion field has two chiral components, right- and left-handed, that transform differently in the $SU_L(2)$ gauge group, where the left-handed part is represented by a doublet while the right-handed component transforms as a singlet, i.e. do not interact through that gauge group.

The final component of the Standard Model is the Higgs field ϕ: a scalar, complex, $SU_L(2)$ doublet, which is required to provide mass to the fermions and to some of the gauge bosons of the $SU_L(2) \times U_Y(1)$ group. The key element of the Higgs mechanism to explain the electro-weak symmetry breaking is that, while the field itself is gauge invariant under the $SU_L(2) \times U_Y(1)$ symmetry group, its ground state is not and develops a *VEV*[3] $v \approx 246$ GeV [4]. After the symmetry breaking one of the four bosons mediating the electro-weak interaction remains massless and produces the long range electro-magnetic interaction while the other three become massive, their mass given by the following relations:

$$\begin{aligned} \boldsymbol{M_W} &= \frac{g_2 v}{2} \\ \boldsymbol{M_Z} &= \frac{v}{2}\sqrt{g_1^2 + g_2^2} \end{aligned} \tag{1.2}$$

The Higgs mechanism also implies the relationship between the coupling strengths of the electro-weak gauge fields defined in eq.1.1 and, in particular, the value of the Weinberg angle.

[3] *Vacuum Expectation Value*

The presence of an additional scalar field interacting with the fermions introduces a mass term for them as well through their Yukawa interaction with the Higgs field. This means that the coupling of all fermions and vector bosons to the Higgs field is proportional to the measured mass of the particle. Finally, the mass of the Higgs boson itself, $\boldsymbol{M_H} \approx 125.09\,\mathrm{GeV/c^2}$ [4], is due to the self-coupling of the Higgs field.

1.2 Hints for physics beyond the Standard Model

Even though the Standard Model describes with outstanding accuracy the fundamental physics at least up to the electro-weak scale there are several theoretical problem and some experimental observation that it cannot explain and that would require its amendment or extension.

From the theoretical point of view, one of the most evident shortcoming of the Standard Model is that it cannot describe gravity. In high energy physics the gravitational effects can normally be neglected because, at the energy scales we can experiment with, this force is so weak that its influence on the outcome of any experiment is negligible. The energy scale at which the gravitational interaction should become relevant at the particle level is known as the Planck scale and is of the order of $\boldsymbol{M_P} = 1/\sqrt{G} \approx \mathcal{O}(10^{19})\,\mathrm{GeV/c^2}$. This value, also called the Planck mass, constitutes an hard upper limit for the validity of the Standard Model, which doesn't include a quantum treatment of gravity.

Even before reaching the Planck scale there are hints of new physical processes that could take place at an energy of the order of $\boldsymbol{M_{\mathrm{GUT}}} \approx \mathcal{O}(10^{15})\,\mathrm{GeV/c^2}$. One of those is the running of the value of the three gauge coupling constants. Those parameters vary with the energy scale of the process, and their magnitude tend to unify to the same value at energies of the order of M_{GUT}. If we only consider the processes described by the Standard Model, this unification is only partial, as shown in fig. 1.1, and this might indicate the existence of a new set of currently unknown interactions that becomes relevant at energies between the electro-weak and the M_{GUT} scale.

However the main theoretical problem involved in most extensions of the Standard Model beyond the electro-weak scale is that the Higgs potential is extremely sensitive to any unknown process which would take place at those energies scales. This is what is usually known as the *hierarchy problem*. In fact, in the Standard Model, the mass of the Higgs boson is calculated from the quadratic term in the Higgs potential:

$$\begin{aligned} \boldsymbol{\mathcal{L}_H} &= \mu^2 \phi^\dagger \phi \\ \boldsymbol{m_H^2} &= 2\mu^2 \end{aligned} \tag{1.3}$$

where $\boldsymbol{\phi}$ is the scalar Higgs field. Through first order loop corrections any particle with mass $\boldsymbol{M}$ contributes to $\boldsymbol{\mu}$ for an amount of the order:

$$\boldsymbol{\delta\mu^2} = \frac{\lambda_p M^2}{16\pi^2} \tag{1.4}$$

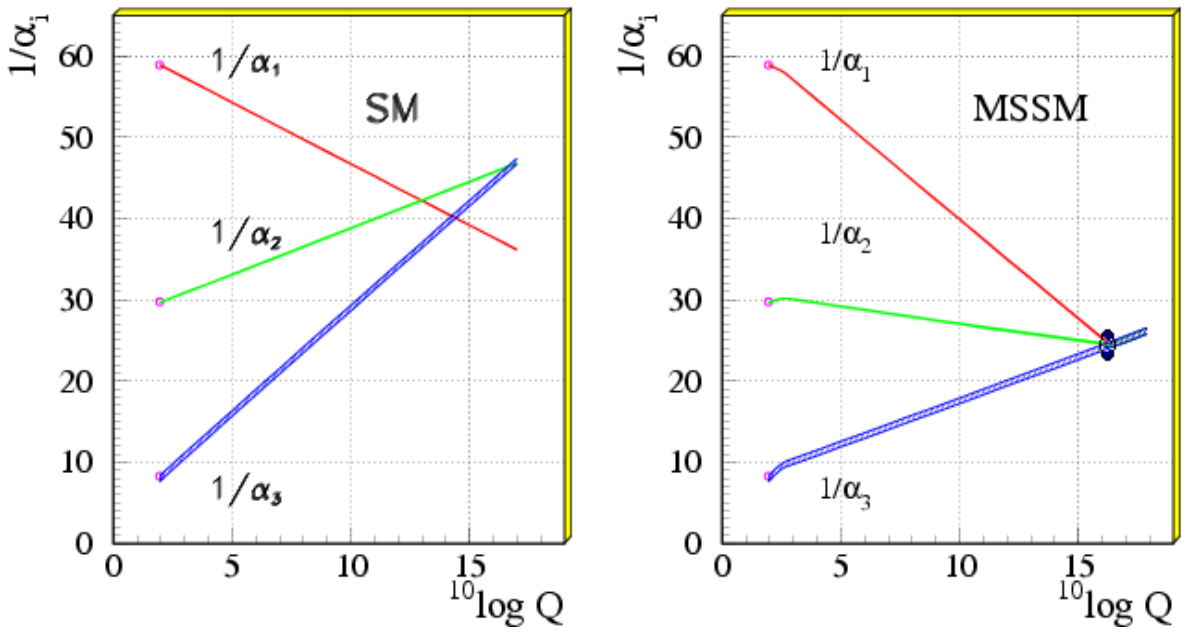

Figure 1.1: Gauge coupling unification in non-SUSY on the left vs. SUSY on the right. The difference in the running for SUSY comes from the inclusion of supersymmetric partners of standard model particles at scales of order a TeV (from [5]).

where $\boldsymbol{\lambda_p}$ is the coupling strength between the particle and the Higgs doublet. Clearly, the larger the mass of the particle, the larger is its contribution to $\delta\mu^2$. If a new physical process introducing new heavy particles takes place at an energy scale of the order of M_P or even M_{GUT} they will contribute huge corrections to the measured Higgs mass at low energies. For that to be of the order of $10^2\,\mathrm{GeV/c^2}$ all those huge contributions must exactly cancel out up to about one part in 10^{34}, if we choose M_P as the scale for new physics[4]. The problem is that, in the Standard Model, there is no fundamental principle which would constrain these contributions to cancel each other out so perfectly and this outstanding event can only be an incredible *accident of Nature*.

There is also an important set of experimental evidences that cannot be explained in a satisfactory way. The most important of those is the astronomical observation that up to 75% of the total gravitational mass of the universe is constituted of weakly interacting, non-relativistic particles which do not match anything contained in the Standard Model. This component of our Universe is called *Dark Matter* [6, 7, 8, 9]. Additionally, if this Dark Matter is constituted by particles that were thermally produced during the initial moments of our Universe that decoupled from the rest of the particle content at a certain temperature, to obtain the observed dark matter density, the annihilation cross section of those particles must be of the order of the weak scale, typically referred to as the *WIMP miracle*.

[4]Independently from the LHC measurements, the Standard Model EWSB mechanism requires the Higgs mass to be of this order of magnitude

Another important experimental evidence of physical phenomena beyond those described by the Standard Model, is the 3.6 σ discrepancy [10] between the measured value of the muon anomalous magnetic moment ($a_\mu = (g-2)$) and its calculated value [11, 12], which depends on the quantum corrections of the tree level diagram predicted by Dirac's theory.

Due to the terrific accuracy level of both measurement and calculations, this quantity is sensitive to new physics processes which could introduce additional corrections to the calculated value, which depend on the mass scale of the new physics processes involved [13]. It is interesting to notice that the measured discrepancy is of the same order of magnitude of the electro-weak contribution to a_μ which hints to the possibility of new physics at the same energy scale.

1.3 Supersymmetry

In the last decades several models were developed to extend the Standard Model and address the issues discussed in the previous section. One of the most thoroughly studied set of extensions of the Standard Model is based on the inclusion of a spontaneously broken symmetry between fermions and bosons, called Supersimmetry or SUSY. The first of these supersymmetric model was introduced in [14] while a detailed summary can be found in [15].

Supersymmetry is not an *internal symmetry* like those that define the gauge fields we described previously, but rather a space-time symmetry[5], and it's the only one that can be combined in a non-trivial way with the Poincaré group in an interacting quantum field theory [16, 17, 18].

When a SUSY transformation is applied to a massless-particle state having an helicity h it generates a new state having $h' = h \pm \frac{1}{2}$. Changing the helicity of half a unit, the supersymmetry generator must be a Weyl spinor $\boldsymbol{Q}_\pm$, which satisfy the anticommutative relation $\boldsymbol{\{Q_a, Q_b\} = 0}$. This means that applied more than once to any given state, the transformation do not generate and endless sequence of states so that massless particles come in *supermultiplets*, containing pairs differing from one another by half a spin unit.

Those supermultiplets that have physical interest are those with helicity pairing

$$(h_1, h_2) = \left(0, \frac{1}{2}\right) \ , \ \left(\frac{1}{2}, 1\right) \ , \ \left(1, \frac{3}{2}\right) \ , \ \left(\frac{3}{2}, 2\right) \tag{1.5}$$

together with those with opposite helicity. Because in a *QFT*[6] the particles must be grouped together with their CPT conjugates, the supermultiplets with opposite helicity must be mixed as one. If we ignore gravitation, we can focus only on the first two of those pairs:

[5] Contrary to the case of the internal symmetries, that leave the Lagrangian invariant, space-time symmetries are those that change the Lagrangian by a total derivative, thus leaving the action invariant.

[6] *Quantum Field Theory*

$$\text{Matter supermultiplets:} \quad \left(0, \frac{1}{2}\right) \oplus \left(-\frac{1}{2}, 0\right) \tag{1.6}$$

$$\text{Gauge supermultiplets:} \quad \left(\frac{1}{2}, 1\right) \oplus \left(-1, -\frac{1}{2}\right) \tag{1.7}$$

An important feature of the supersymmetric Lagrangian is that, among the possible terms, there are several which mix lepton and quark fields as to violate the baryon and lepton number conservation, respectively $\boldsymbol{B}$ and $\boldsymbol{L}$. To address this issue it is possible to introduce an additional discrete symmetry, called the *R-Parity* which forbids that violation. This is done introducing a new, multiplicative quantum number defined as:

$$\boldsymbol{P_R} = (-1)^{3(B-L)+2s} \tag{1.8}$$

where s represents the particle's spin. With this definition the Standard Model particles and the Higgs bosons can be differentiated from their superpartners from the value of P_R, which respectively is $+1$ and -1.

The assumption of this symmetry, has 3 important phenomenological consequences:

- The lightest particle with $P_R = -1$, called the *LSP*[7], must be absolutely stable;
- Each s-particle other than the LSP must eventually decay into a state that contains an odd number of LSPs;
- In collider experiments, s-particles can only be produced in even numbers.

Because SUSY transformations commute with the Hamiltonian, if the symmetry is exact and not spontaneously broken, the particles in each supermultiplet have the same mass. Considering we never observed any of the super-partners of the Standard Model particles, in a realistic SUSY model, we must assume that the vacuum state is not supersymmetric and the spontaneous breaking of the supersymmetry breaks the mass degeneracy within the supermultiplet.

One can parametrize our ignorance about the actual mechanism, including in the Lagrangian all the possible supersymmetry breaking terms. Unfortunately this introduces a large number of free parameters which adds a tremendous degree of arbitrariness to the theory. In fact, the most general Lagrangian including all the possible supersymmetry breaking terms contains 105 new independent parameters [19].

Nonetheless most of this parameter space is already ruled out by the current experimental evidence. In fact, most of the possible parameter configurations would introduce in the model experimentally excluded features like the non-conservation of the single lepton numbers ($\boldsymbol{L_e}, \boldsymbol{L_\mu}, \boldsymbol{L_\tau}$) or the presence of unsuppressed flavour changing neutral currents or imply magnitudes of such observables like the electron and neutron electric dipole moments that are incompatible with the experiments.

[7] *Lightest Supersymmetric Particle*

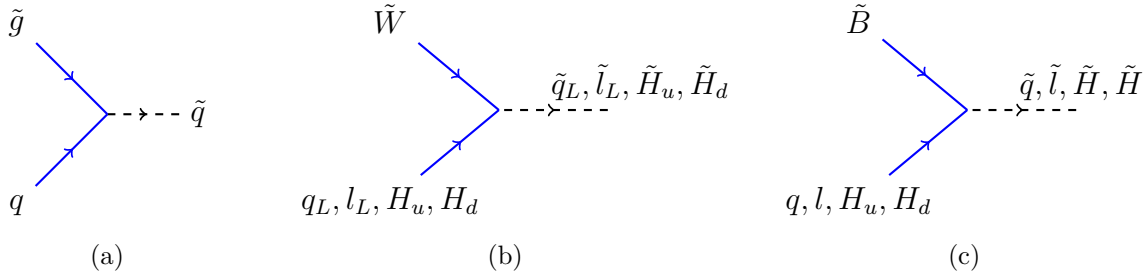

(a) (b) (c)

Figure 1.2: Additional matter-gauge couplings introduced in the supersymmetric extensions of the standard model. In (a) the coloured coupling and in (b) and (c) the electro-weak couplings. For each of the represented diagrams there is another one with the corresponding anti-particles.

1.3.1 The Minimal Supersymmetric Standard Model (MSSM)

The minimal field content of a supersymmetric extension of the Standard Model is obtained adding a super-partner to each of the known fields which leads to the definition of the MSSM. Because in this model the supersymmetry and gauge symmetries commute, the gauge properties of the superpartners must be exactly the same as those of the matching Standard Model fields, in particular their couplings and mixings.

For the gauge bosons this leads to adding a spin-half *gaugino* for each of the gauge generators sharing the same symmetry representation under the $SU_c(3) \times SU_L(2) \times U_Y(1)$ group. Thus we have 8 *gluinos*, three *winos* and 1 *bino*.

Similarly, for each standard model fermion we must add a complex scalar superpartner which has the same quantum numbers of the corresponding left-handed fermion and which are labelled adding an *s* as a prefix of the matching fermion. Thus, for each generation, we have a doublet of *s-leptons* and a *s-lepton* singlet, a doublet of *s-quarks* and two *s-quark* singlets.

Additionally, we need to introduce further matter-gauge Yukawa couplings, mixing the Standard Model fermions with their superpartners and the gauginos. Those couplings can be obtained from the normal Standard model diagrams replacing the gauge field and one of the fermionic field with the corresponding supersymmetric partners and are represented in fig. 1.2. A complete review of the Feynman rules for all the SUSY coupling is published in [20].

Additionally, a minimal supersymmetric model requires the presence of at least two Higgs doublet with identical $SU_C(3) \times SU_L(2)$ representation but with opposite hypercharge assignments, denoted $\boldsymbol{H_U} = (H_u^+, H_u^0)$ and $\boldsymbol{H_D} = (H_d^0, H_d^-)$. Each of these doublets has an *Higgsino* superpartner, with similar symmetry transformations.

Each of those Higgs doublets acquire a non-zero VEV to break the electro-weak gauge symmetry. The two expectations value are usually denoted $\boldsymbol{v_u}$ and $\boldsymbol{v_d}$, for H_U and H_D respectively, and are correlated to the electro-weak parameters by the relation:

$$v_u^2 + v_d^2 = \boldsymbol{v^2} = 2m_Z^2/(g^2 + g'^2) \approx 174\,\text{GeV}^2 \tag{1.9}$$

the ratio of those two quantities, which is a free parameter of the theory, is traditionally

written as:

$$\tan(\beta) \equiv \frac{v_u}{v_d} \tag{1.10}$$

Due to the electro-weak symmetry breaking, three of the eight degrees of freedom of the Higgs doublets are absorbed as longitudinal degrees of freedom of the massive vector bosons. The remaining five mass eigenstates consist of two CP-even neutral particles named h^0 and H^0, one CP-odd neutral state A^0 and two conjugated charged scalars H^+ and H^-.

The electro-weak symmetry breaking also induces the mixing of the Higgsinos with the gauginos. The neutral $\tilde{H}_u^0$ and $\tilde{H}_d^0$ combine with the $\tilde{B}$ and $\tilde{W}^0$ to form four mass eigenstates called *Neutralinos* ($\tilde{\chi}_i^0,\ i = 1,2,3,4$). The charge Higgsinos $\tilde{H}_u^+$ and $\tilde{H}_d^-$ mix with the winos $\tilde{W}^\pm$ to form two *Chargino* mass eigenstates with ± 1 electric charge ($\tilde{\chi}_i^\pm,\ i = 1,2$).

Among the s-fermions, all the scalars with the same charge, R-Parity and colour quantum numbers can potentially mix but the constraint imposed by the suppression of flavour-changing processes among the Standard Model particles, reduces to a negligible level any mixing between different flavours in the SUSY fields as well.

Because the Yukawa couplings of the first and second family are very small, the s-quarks and s-leptons of those two family end up in 7 almost mass-degenerate and unmixed pairs: $(\tilde{e}_R, \tilde{\mu}_R), (\tilde{\nu}_e, \tilde{\nu}_\mu), (\tilde{e}_L, \tilde{\mu}_L), (\tilde{u}_R, \tilde{c}_R), (\tilde{d}_R, \tilde{s}_R), (\tilde{u}_L, \tilde{c}_L), (\tilde{d}_L, \tilde{s}_L)$. On the other hand, the left and right flavour eigenstates of the s-particle of the third family can mix, producing two mass eigenstates for each of the flavours which are denoted $(\tilde{t}_1, \tilde{t}_2), (\tilde{b}_1, \tilde{b}_2)$ and $(\tilde{\tau}_1, \tilde{\tau}_2)$.

The actual masses of all those s-particles depend on the specific supersymmetry breaking scale and mode but, in general, due to the different strength of the coupling involved in the running of the s-particles masses one can expect such a hierarchy between them:

- The masses of the s-quarks higher than that of the s-leptons;
- The s-particles of the third family lighter than those of the other two families
- The R-labelled s-particle lighter than the L-labelled counterpart.

1.3.2 The supersymmetric answer to the Standard Model puzzles

The most attractive feature of the SUSY extensions of the Standard Model is their potential to solve many of the standing issues in our current description of elementary particle physics, some of which were described in § 1.2.

One of the most interesting cases is that of the hierarchy problem. Here, the presence of matching bosons and fermions with the same tree level coupling introduces automatic cancellations in the radiative corrections to the Higgs mass which allows this parameter to be close to the electro-weak scale without specific fine-tunings [15]. In fact, as the Higgs mass radiative corrections are proportional to the squared mass of the involved particle (see eq. 1.4), the most relevant parameters to ensure the correct cancellations are the third generation s-quark masses, and the gauginos and Higgsinos masses which should all be

small enough to avoid excessive fine-tuning of the other parameters involved [21]. Similar cancellations also help in the unification of the gauge coupling if one extends the Standard Model up to the *GUT*[8] scale, as can be seen in fig. 1.1.

The presence of additional particles, especially when they are not very heavy, can introduce tiny additional radiative corrections to low energy observables. In those cases when those observables can be calculated and measured with extreme precision, the corrections can introduce measurable discrepancies, like those in the anomalous magnetic moment of the muon [10].

Finally in the particle spectrum of many SUSY extensions of the Standard Model, it is possible to find a viable Dark Matter candidate. In fact, assuming the conservation of R-parity, if the LSP is a EM- and colour-neutral particle, they could have been produced in the earliest phases of the life of the universe and survived stably since then.

An important requirement to any dark-matter candidate is that its production and decay mechanism in the early universe should be able to account for the precise measurement of the dark matter relic density $\boldsymbol{\Omega_{CDM}h^2} = 0.115 \pm 0.002$, as obtained by the WMAP and Planck experiments [22, 23]. This is typically calculated assuming the dark matter candidate is in a thermal bath until the universe temperature is higher than the particle mass after which its abundance freezes to a value which depends on its annihilation cross-section [24].

In the SUSY case, if the direct annihilation of the LSP to Standard Model particles accounts for the total annihilation cross-section, it is very difficult to find a suitable set of parameters which can generate the measured abundances [25]. If, on the other hand, there are other supersymmetric particles with a mass within about 10% of that of the LSP, annihilation involving those extra particles can significantly change the calculated abundance, reconciling it with the measured value. This scenario is usually referred to as co-annihilation [26].

1.3.3 Direct supersymmetry searches

Supersymmetry has been searched at collider experiments for more than 30 years and no signature was found that could be interpreted as an evidence for a new particle state.

The searches for supersymmetry differ substantially in the cases of lepton and hadron colliders. At lepton colliders, the colourless initial state reduce the QCD background so that the weakly coupled gauginos and Higgsinos, along with the s-leptons, can be produced and detected by the experiments. The initial state knowledge and the possibility to precisely tune the energy and polarization of the primary interacting particles provide powerful tools to constraint the system and perform precise and model-independent measurements. The extreme cleanliness of the experimental environment would even allow to identify the presence of the SUSY states from the tiny discrepancy they will introduce in Standard Model observables, even if the centre-of-mass energy is not sufficient to produce those particles directly. The most recent, precise and extensive searches for supersymmetric

[8] *Grand Unification Theory*

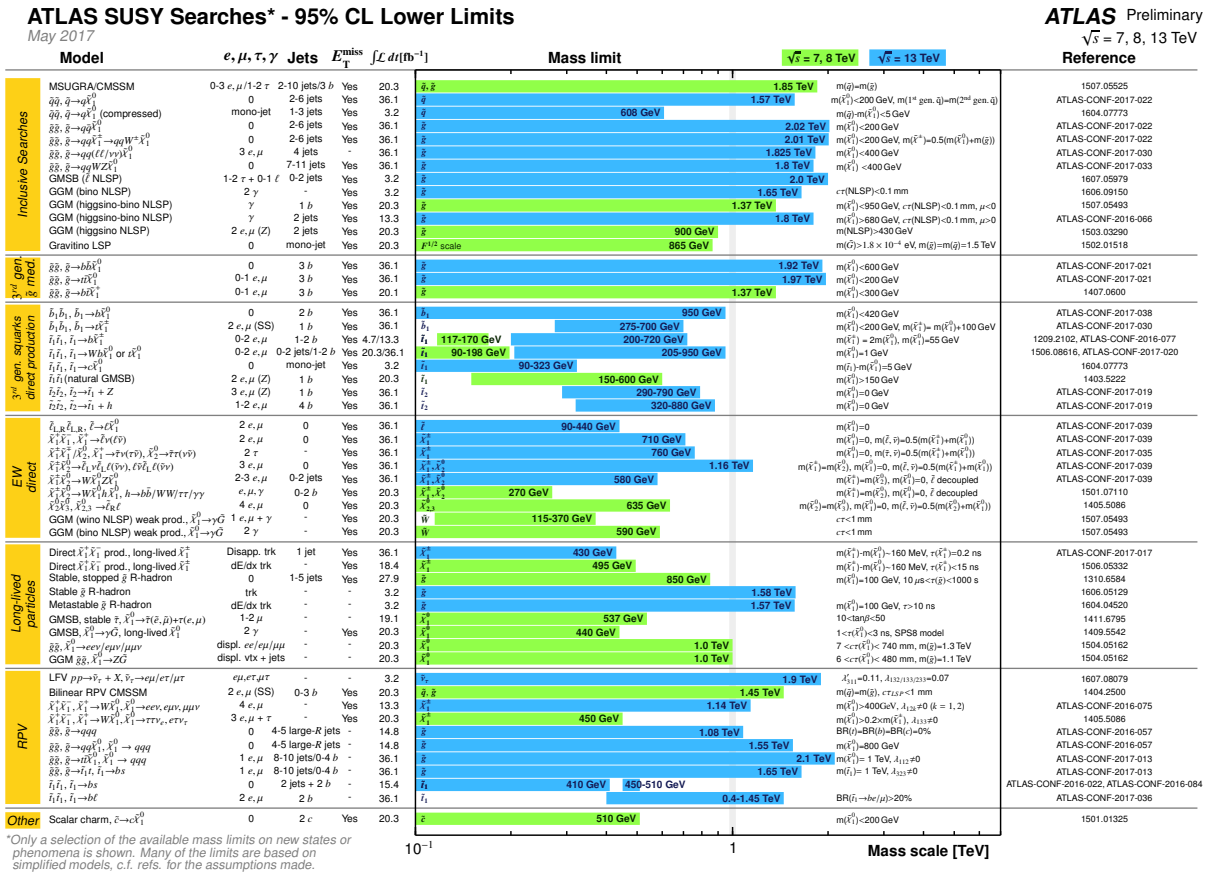

*Only a selection of the available mass limits on new states or phenomena is shown. Many of the limits are based on simplified models, c.f. refs. for the assumptions made.

Figure 1.3: Mass reach of ATLAS searches for Supersymmetry updated to May 2017 from the Atlas public results website. Only a representative selection of the available results is shown.

particles at lepton colliders, in particular s-leptons and gauginos, were performed by the experiments on the *LEP*[9] collider [27, 28, 29, 30, 31].

At hadron colliders the production cross-section is particularly high for coloured s-particles which would be abundantly produced if within the kinematic reach of the accelerator. Unfortunately, the abundance of strong-interacting particles reduces the sensitivity of the experiments to weakly interacting s-particles, in particular when the mass difference between them and their decay products is small.

Both the CMS[10] and ATLAS[11] experiments are performing extensive searches for the many possible supersymmetry signature. A summary diagram showing the most current results of those searches is shown in fig. 1.3. It must be noticed that, due to the complexity of the experimental conditions we mentioned earlier, many of those limits are based on simplified SUSY model, which may leave relevant parts of the full SUSY parameter space unexplored. For that reason the mass limits can vary depending on the specific model used

[9] *Large Electron Positron (Collider)*

[10] https://twiki.cern.ch/twiki/bin/view/CMSPublic/PhysicsResultsSUS

[11] https://twiki.cern.ch/twiki/bin/view/AtlasPublic/SupersymmetryPublicResults

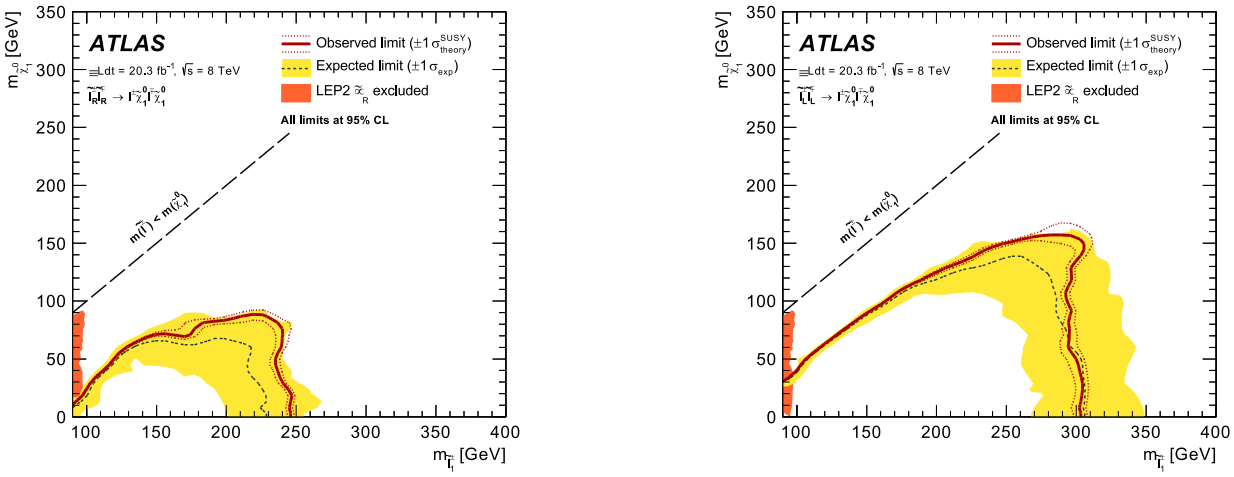

(a) (b)

Figure 1.4: 95% exclusion limits in the $m_{\tilde{\chi}_1^0} - m_{\tilde{l}}$ plane for a right-handed and b left-handed s-electron and s-muon production (from [36]).

to interpret the search results [32, 4].

The most recent LHC searches set limits to the gluinos masses between 700 and 1970 GeV and the first and second family s-quarks between 490 and 1450 GeV [33, 4]. The constraints on the third generation s-quarks are generally much looser. For the s-top in particular, the mass limit is typically of the order of 1 TeV, if $m_{t_1} > m_t + m_{\tilde{\chi}_1^0}$, but can go down to about 235 GeV if that's not the case [34, 35].

Because of the lower production cross-section, the limits on the electroweakinos masses are considerably lower. Indeed, the best limit for the lightest neutralino is still that which was obtained by the LEP experiments which set it to 46 GeV. The situation is similar for the charginos where the most constraining and model-independent results come from the LEP experiments which set lower mass limits to 94 GeV [29].

In the s-lepton sector only recently the ATLAS and CMS experiments started to obtain results which constrain the first and second generation s-lepton masses better than the previous LEP results [37, 38] up to about 300 GeV for left-handed and 240 GeV for right-handed s-leptons (fig. 1.4). The main caveats to those analysis is that they only constrain the s-lepton masses when there is a sizeable mass difference of about 70 GeV between them and the LSP and when their branching ratios to the LSP is 100%. Finally, for the $\tilde{\tau}$, the strictest constraint come from the LEP experiments with a lower mass limit of 81.9 GeV [29].

In the next future those searches will be extended at both hadron and, possibly, lepton colliders. The construction of a linear collider, in particular, will make it possible to extend the LEP searches and complement the results, discovery and exclusion alike, which the LHC may achieve with the next runs at its maximum design centre-of-mass energy. A review of the searches that can be performed in the next years is presented in [39].

Chapter 2

The International Linear Collider (ILC)

The discovery of a new particle compatible with the Standard Model Higgs boson at the *LHC*[1] was the first major accomplishment of a new generation of colliders designed to explore the fundamental laws of Nature at an energy scale of the order of the TeV. The precise measurement of the properties of this new particle will make it possible to clarify its role in the mechanism responsible for the generation of masses predicted by the Standard Model.

Those measurements, together with further explorations of the high energy regime, will be one of the main tasks of the LHC for the next years. However, to increase the precision of many of those measurements, the LHC needs to be complemented by a lepton collider where the well known initial state of the colliding beams, the cleaner event signatures and the lower backgrounds allow for a better understanding of the physical processes involved.

In its baseline design, the *ILC*[2] is designed to be a linear, high-luminosity electron-positron collider, based on superconducting radio-frequency technology, with tunable centre-of-mass energy between 250 and 500 GeV, extendible to 1 TeV [40], and beam polarisation up to 80% for the electrons and 30% for the positrons. To reduce the initial cost a staged approach was proposed to construct the machine [41]. In this thesis we will always refer only to that baseline design, as detailed in the published ILC *TDR*[3] [42, 43, 44, 45, 46], which collects and summarises most of the work in this field of the last two decades.

The first part of this chapter will detail the physics case for this new project, showing the benefits its construction will bring. The second part, that is §2.2, will give an overview of the most relevant characteristics and parameters of this machine.

[1] *Large Hadron Collider*
[2] *International Linear Collider*
[3] *Technical Design Report*

2.1 The Physics case for the ILC

The greater strength of a lepton collider stems from the clean experimental condition arising from the elementary nature of the colliding particles. In particular, the centre of mass energy and the initial state polarisation are known with high precision and can be usually tuned to match the specific experimental needs. Additionally, due to the colour neutrality of the lepton involved, the backgrounds to many interesting processes are several order of magnitude lower than the *QCD*[4] backgrounds that challenge hadron collider experiments.

The main goals of the ILC physics program [47] will be:

- To measure the properties of the Higgs sector, within a precision of a few percent;
- To precisely measure the interactions of top quarks, gauge bosons and new particles;
- To directly and indirectly search for the signatures of *BSM*[5] physics processes and perform measurement in this domain.

2.1.1 Higgs Physics

The discovery by the LHC experiments of a 125 GeV Higgs boson [48, 49] is one of the major accomplishments in fundamental physics of the last decades but is only the first step in the exploration of the Higgs sector. After the LHC, that particle will be studied at the ILC where better precision can be achieved.

The main Higgs production channels at the ILC are the Higgsstrahlung and the vector boson fusion processes. The first process dominates the production cross section at low energies with the second becoming increasingly important as the centre-of-mass energy increases, as shown in fig. 2.1.

The Higgsstrahlung process is particularly important because it allows to study the couplings of the Higgs boson in a model independent way. If the experiments are able to identify with high efficiency the decay products of the Z boson produced in the process, due to the precise knowledge of the initial conditions, it will be possible to measure the mass of the particle it recoiled against, regardless of its decay modes.

By studying the Higgs boson, the ILC can also test many possible BSM scenarios. In the Standard Model, the characterizing feature of the Higgs boson is the perfect linear correlation between the masses of the particles and their Higgs coupling (Fig. 2.2). Depending on the final state and the BSM scenario, these couplings could deviate from the Standard Model forecasts from less than 1% to more than 100% [52].

2.1.2 Top Quark Physics

The top quark, being the heaviest of the fundamental fermions, plays a very special role in the Standard Model. Its large mass affects the prediction of many Standard Model parameters through radiative corrections, including the Higgs mass and the W and Z

[4] *Quantum Chromodynamics*
[5] *Beyond the Standard Model*

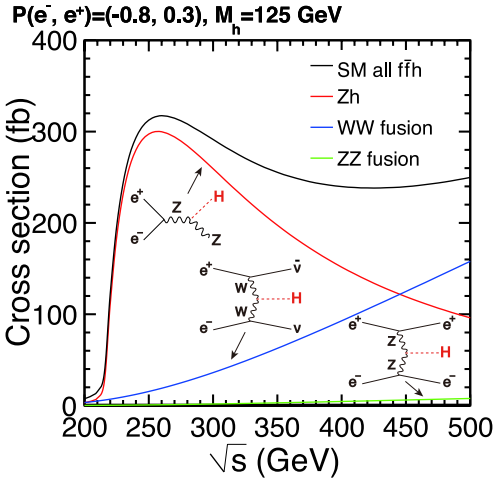

Figure 2.1: Evolution of the Higgs boson production cross-section at an e^+e^- collider in the energy range reachable by the ILC baseline design. The evolution of the different production processes is shown independently, together with their Feynman diagram. From [50].

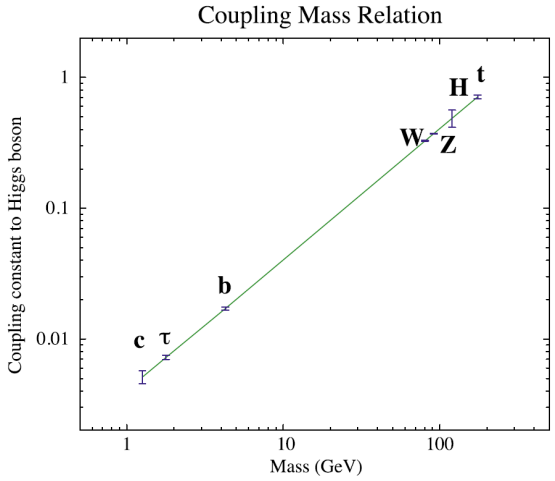

Figure 2.2: Expected relationship between the Higgs coupling to several Standard Model model particles and their masses as can be measured at the ILC [51]. A deviation of those values from the Standard Model as small as a few percent is expected in several BSM scenarios.

coupling, hence high precision measurements of the properties and interactions of the top quark can be sensitive to physics at mass scales much above the EWSB scale. Its short lifetime, shorter than the hadronization time-scale, its also an unique feature that allows to study it as a *bare* particle.

The top quark was discovered at the Tevatron p-$\bar{\text{p}}$ collider [53] and was since copiously produced by the LHC but has been never before studied outside the hadron colliders. The ILC would be the first machine capable to produce this particle from a precisely defined leptonic initial state which will allow the experiments to study its properties with much higher precision.

For example the ILC possibility to control the centre-of-mass energy will allow to perform a threshold scan around the top pair-production energy which will make it possible to measure the quark mass, its width and the Yukawa coupling with a uncertainties respectively of $\boldsymbol{\delta_m} \approx 17\,\text{MeV}$, $\boldsymbol{\delta_\Gamma} \approx 26\,\text{MeV}$ and $\boldsymbol{\delta_g} \approx 4.6\%$ [50].

Additionally, the fact that the top quark production at the ILC will be mediated by the electro-weak interaction will allow the measurements of other observables, like the polarity asymmetries and the weak interaction polarisation of the top, that are potentially very sensitive to new physics processes beyond those described by the Standard Model [47].

2.1.3 Precision EW measurements

In the electro-weak sector, the Standard Model can be theoretically computed with the highest precision and even the smallest deviation from its prediction can be an indication

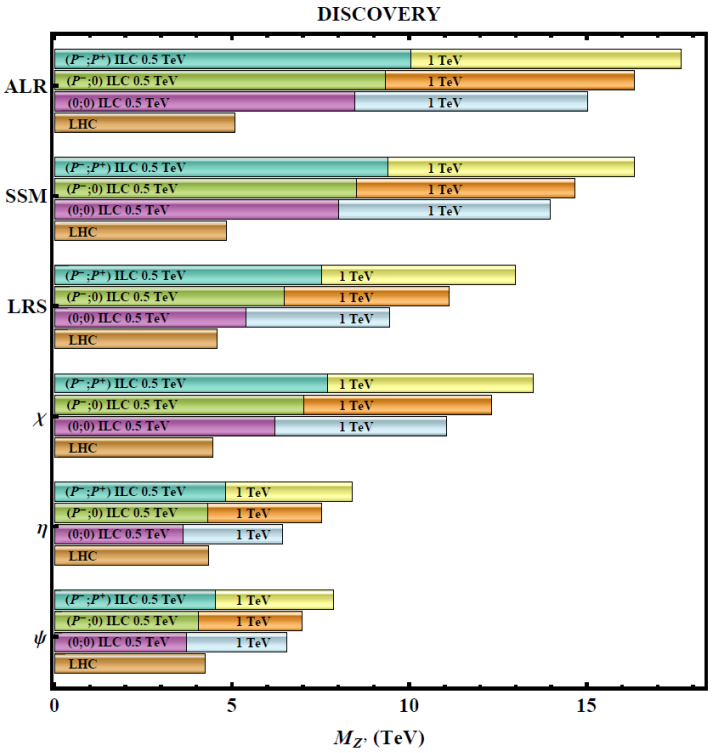

Figure 2.3: Sensitivity of the ILC to various candidate Z' bosons (quoted as 95% confidence level for exclusion), with $\sqrt{s} = 0.5(1.0)$ TeV, $\mathcal{L} = 500(1000)\,\mathrm{fb}^{-1}$ and different polarisation options: both beam polarised, only the electron polarisation and no polarisation. The sensitivity of LHC-14 with $100\,\mathrm{fb}^{-1}$ is shown for comparison. For details see [55]

of new processes beyond those that it describes even when they have an energy scale above that which is directly accessible by the machine.

The major electro-weak processes to be studied at the ILC are the pair production of electro-weak gauge bosons, $\boldsymbol{e^+e^- \to W^+W^-}$ and $\boldsymbol{e^+e^- \to ZZ}$. Due to the $V-A$ structure of the W boson interactions, the polarisation of the initial state beam particles can substantially enhance or suppress their production. The ILC will be the first collider to be able to produce W-pairs in lepton collisions with polarised beams and, due to the possibility of precisely tuning the beam energies, it will be able to perform a scan around the W-pair production threshold to measure the mass of the particle with an accuracy of the order of a few MeV [54].

Additionally the reactions $\boldsymbol{e^+e^- \to f\bar{f}}$, where f could be any fermion, provide a powerful tool to search for and characterise the physics beyond the Standard Model, even if the characteristic particles are beyond the direct energy reach of the accelerator. Those processes are distinguishable by clean, simple final states and precise perturbative predictions of the Standard Model contributions have been calculated up to several orders of loop corrections (see [54] and references therein).

For example many extensions of the Standard Model predict a new, heavy and electrically neutral gauge boson commonly denoted by $\boldsymbol{Z'}$. Searches for such a particle was already performed at LEP, Tevatron and is ongoing at the LHC and they exclude the possibility of on-shell Z' production at the ILC, nonetheless its existence and properties could be inferred through the precise measurement of the $\boldsymbol{e^+e^- \to f\bar{f}}$ processes even if its mass

is an order of magnitude higher than that which will be directly accessible [55] (Fig. 2.3).

2.1.4 Direct searches for new physics beyond the Standard Model

Another important part of the ILC program is the direct search for new phenomena accessible at the machine centre-of-mass energies, complementing the indirect searches that were described in the previous section. In many models extending the Standard Model, there are many electro-weak states that will be difficult to discover or study at the LHC due to their small cross-section or to a topology difficult to isolate in the QCD background. These searches can be grouped in two categories:

- Measurements on states eventually discovered at the LHC where the clean experimental environment and the high precision of the ILC experiments allows a higher accuracy and a better characterisation of the processes involved;
- New direct discoveries of particles not accessible at the LHC.

Of the many ideas that can be used to demonstrate the qualities of the ILC, one of the best known is the Supersymmetry (§ 1.3). This model provides a good example, not only because it is a highly motivated scenario for physics beyond the Standard Model, but also because it provides a rather complete and calculable framework with multiple new scalars and fermions of different gauge charges to be analysed. While the LHC will have a chance to discover any existing coloured sparticles up to several TeV, any colour-neutral state will not be produced as abundantly in an hadron machine. Even though these could be found in cascade decays of strongly interacting super partners, in most cases the discovery potential relies on several model dependent assumptions [56].

On the other hand, at a lepton collider, if enough energy is available at the centre-of-mass, can produce each of these states directly and the clean experimental environment will allow for a precise measurement of their masses, spins and couplings.

2.2 The ILC baseline design

The construction of a lepton collider with the performances required to complete the ambitious experimental plan detailed in the previous section is an exceptional technological challenge that could only be achieved through a world-wide project. This project is taking shape in the ILC. Currently the deployment plan for the ILC is under development[41], therefore here will focus on the baseline design described in the 2013 TDR.

To reach the physical goals detailed in the previous section the ILC was designed with the following operational requirements:

- Centre-of-mass energy continuously tunable between 250 and 500 GeV at optimal luminosity;
- Options to upgrade the machine to reach 1 TeV and to run at optimal luminosity as low as the Z-pole (≈ 90 GeV) centre-of-mass energy;

Centre-of-mass energy	E_{CM}	GeV	500
Pulse Repetition rate	f	Hz	5
Number of bunches in a train	n_b		1312
Bunch population	N	$\times 10^{10}$	2
Bunch interval	Δt_b	ns	554
Luminosity	$\mathcal{L}$	$\times 10^{34}$ cm^{-2} s^{-1}	1.8
Electron polarisation	P_-	%	80
Positron polarisation	P_+	%	30
RMS horizontal beam size at IP	σ_x^*	nm	474
RMS vertical beam size at IP	σ_y^*	nm	5.9
Fractional RMS energy loss to beamstrahlung	δ_{BS}	%	4.5
Fraction of $\mathcal{L}$ within 1% of the nominal E_{CM}	$\mathcal{L}_{1\%}$	%	58

Table 2.1: Summary table of some of the relevant operational parameters of the 2013 baseline ILC design (from [44]).

- Peak luminosity of $\approx 2 \times 10^{34}\,\mathrm{cm^{-2}s^{-1}}$ at 500 GeV centre-of-mass energy;
- Relative energy stability and precision better than 0.1%;
- 80% electron polarisation at the interaction point;
- 30% positron polarisation with an option to improve it to 60%.

The 500 GeV baseline version of the ILC, sketched in Fig. 2.4, will have a footprint of $\approx$ 31 km[6]. At its core it will have two, $\approx$ 11 km long linear accelerators based on superconducting RF niobium cavities operating at 1.3 GHz with an average gradient of 31.5 MV/m, designed to accelerate beams of electrons and positrons to energies up to 250 GeV.

The electron and positron beams are produced in different ways: the electron beams are obtained from a polarised source while the positrons are created via pair-conversion of high-energy photons produced in an undulator. Both beams can be polarised: up to 80% for the electrons and 30% for the positrons [57, 40]. The high luminosity required to complete the ILC ambitious physics programme can only be reached if both electron and positron beams are significantly cooled, compressing their phase space at 5 GeV through a set of 3.2 km long damping rings. The beams will be extracted from the damping rings at a rate of 5 Hz, each bunch-train consisting of 1312 bunches of $\approx$ 500 ns length. The low emittance is maintained by the beam-transport system which brings the bunch trains at the main linac for the final acceleration phase. After that, the beams are guided to the collision point by a 2.25 km long beam-delivery systems, which bring them to interact with a 14 mrad crossing angle and with the optimum parameters to maximise the luminosity. A list of some of the most relevant parameters is given in tab. 2.1.

[6] A recent update of the baseline design increased the total length of the ILC to 34 km. Nonetheless, to keep the description consistent with the parameters used for the data generated for the analysis of the third part of this thesis we will always and only refer to the TDR baseline design.

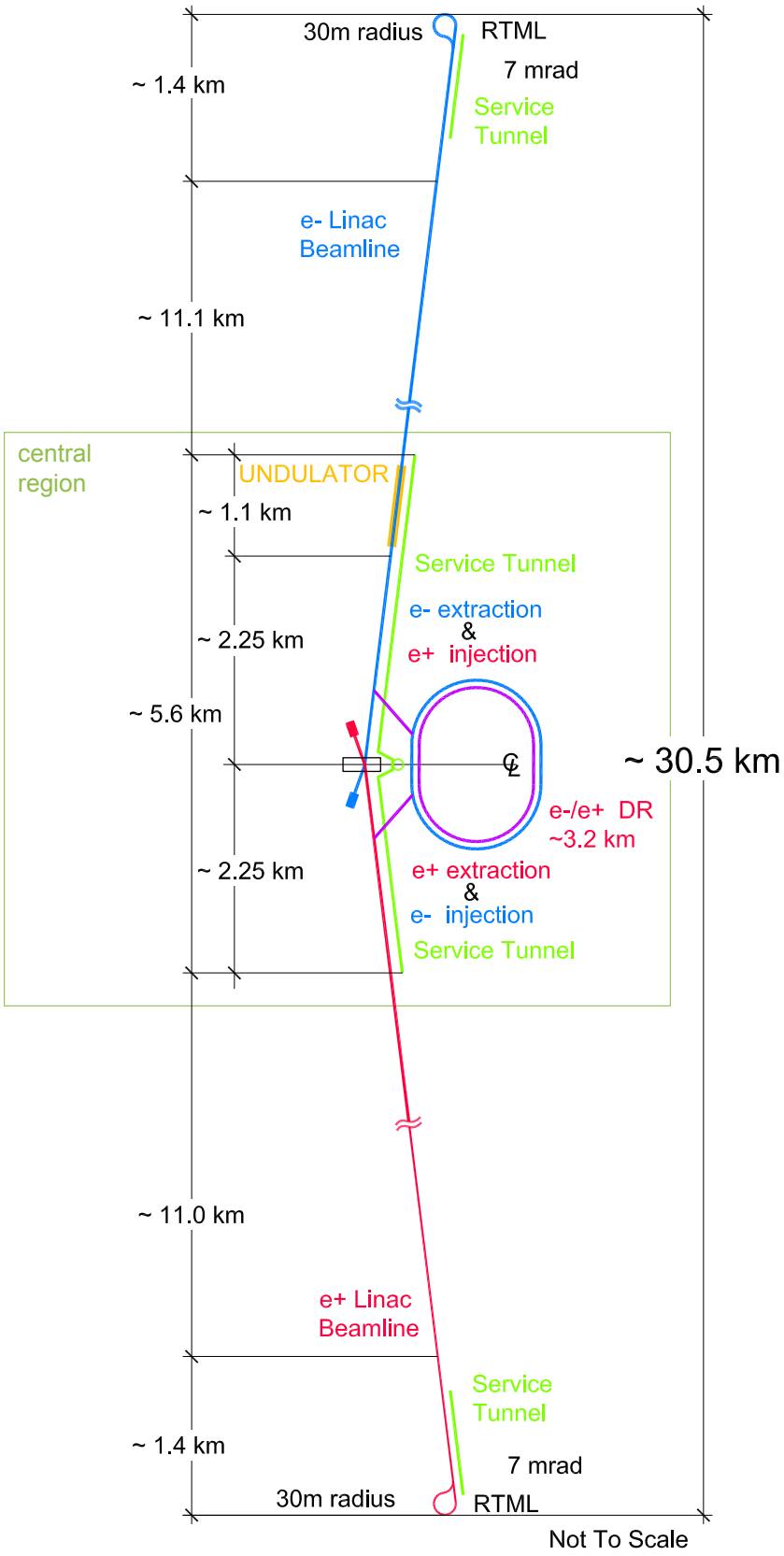

Figure 2.4: Schematic layout of the ILC complex for the 500 GeV centre-of-mass energy 2013 baseline design (from [44]).

2.2.1 High luminosity and beamstrahlung

One key parameter of any high energy lepton collider is the luminosity. Because the total e^+e^- cross section runs proportionally to $\boldsymbol{1/E^2_{CM}}$, the luminosity of the collider needs to increase accordingly. For Gaussian beam shapes, the luminosity can be written as:

$$\boldsymbol{\mathcal{L}} = \frac{n_b N^2 f}{4\pi\sigma_x\sigma_y} H_D \tag{2.1}$$

where all the relevant quantities are listed in tab. 2.1 and $\boldsymbol{H_D}$ is an additional enhancement factor that comes from the intense beam-beam interactions [58].

While in a storage ring this quantity can be kept high increasing the repetition frequency, e.g. 44 kHz at LEP, this is limited in a linear collider to a few Hz for several reasons, including the time required to cool the beams in the damping rings and the filling time of the accelerating cavities. Therefore, to increase the luminosity, it is necessary to reduce the beam size which, at the ILC, will be $\approx 10^6$ times smaller than at LEP. A side effect to this solution is that the large electrical fields produced in such dense charge packets increase the relevance of the low-energy interaction with the other beam.

The beam-beam interactions have two relevant effects: on one hand the influence of the oppositely charged bunch increase the final focusing but, on the other hand, this effect induces the production of additional high energy photons, a process called *beamstrahlung*, which modifies the energy spectrum of the beams at the interaction point so that only part of the total luminosity is available at the nominal centre-of-mass energy of the collider. These additional photons can also collide with the leptons in the beam or with each other producing a low energy background composed of particles with a relatively large transverse momentum that can constitute an experimental challenge.

Chapter 3

The International Large Detector (ILD)

At the ILC interaction point there will be two detectors, ILD and SiD. At any given time only one of the two detectors can be pushed on the beam line for data taking while the other will be parked for maintenance in the so called *push-pull operation mode* [45]. Even though such a configuration presents several technological challenges, the experience at previous colliders demonstrated the advantages of multiple independent experiments that can cross-check any claim, measuring the same observables using different tools with different sources of systematics errors.

To reach the outstanding level of performance required to complete the ILC physics programme both detector are designed to use the particle flow paradigm in the reconstruction of physics events (§ 3.1). This technique requires an efficient and accurate tracking system together with an highly granular and hermetic set of calorimeters.

As the work done in this thesis is related to the ILD, we will describe that detector in more details, with a particular focus on its large volume *TPC*[1] tracker and the electromagnetic calorimeter system which are relevant for the discussion of the rest of this dissertation.

3.1 Detector requirements and particle flow

One of the main requirements of an ILC detector is the ability to efficiently identify and distinguish the neutral from the charged vector boson in hadronic decays. This is relevant, for example, to measure the branching ratio of the $\boldsymbol{H \to WW^*}$ decay in the Higgsstrahlung process or to accurately measure the trilinear Higgs coupling where, due to small cross section of the process, it is important to include all the decay modes of the Z and of the Higgs boson in the search.

This can be done efficiently if the di-jet mass resolution is of the same order of the natural width of the bosons, that is $\boldsymbol{\delta_m/m} = 2.7\% \approx \Gamma_Z/M_Z \approx \Gamma_W/M_W$. Considering that most of the interesting physical processes that are to be studied at the ILC will result

[1] *Time Projection Chamber*

in jets of energies in the range $80 - 350\,\text{GeV}$, the single jet energy resolution needs to be $\boldsymbol{\delta_E/E} \approx 0.3\sqrt{E(\text{GeV})}$ [59].

That requirement, one of the most challenging for ILD, can be met with the implementation of the particle flow paradigm [60]. This technique of energy reconstruction relies on the fact that the majority of the energy in an event is usually conveyed by charged particles whose 4-vector can be accurately and efficiently reconstructed in the tracking system. Once those particles are identified, the energy they carry can be subtracted from the calorimetric measurements which is then used to reconstruct only the energy carried by neutral particles like photons or neutrons. For this type of measurement it is crucial to be able to associate efficiently the correct calorimeter cluster to each charged particle and this can only be done if the calorimeter is highly granular, with a cell size of $\mathcal{O}(10\,\text{mm}^2)$ for the electromagnetic calorimeter and $\mathcal{O}(10\,\text{cm}^2)$ for the hadronic one.

Such a technique relies heavily on the tracking system to accurately measure the momentum of the charged particles, even at high momenta. Additionally most of the Higgs studies relies on the accurate measurement of the di-lepton invariant mass from the process $\boldsymbol{ZH \to \mu^+\mu^- X}$ to reconstruct the mass of the Higgs boson recoiling against the Z.

Those physics-based considerations drive the performance requirements of the whole tracking system which are described by the transverse momentum resolution achievable which needs to be $\boldsymbol{\delta p_\perp/p_\perp^2} < 5 \times 10^{-5}\,(\text{GeV/c})^{-1}$. At the same time the tracking system must be radiation-thin to reduce the interactions of the sampled particles before they enter in the calorimeters.

3.2 ILD Layout

The general layout of the ILD detector, similar to many other omni-purpose detectors for high-energy collider physics, consists of a central, low mass tracker, made of an inner core of silicon detectors and a large TPC surrounding it. All around the trackers there are going to be an electromagnetic and an hadronic calorimeter. All those detectors are embedded in a 3.5 T magnetic field generated by a superconductive solenoid. The return flux of the magnetic field is carried by an instrumented iron yoke that can track the muons that leak through the calorimeters. A schematic sketch of the sub-detectors, as layered in the experiments, is shown in fig. 3.1. All the sub-detectors are designed in a barrel/end-cap layout to maximize the hermeticity of the detector. For the same reason, a forward calorimeter system, named *FCAL*[2], covers the area closest to the beam-line.

At this phase of the experiment design, the specific technology for the sub-detectors is not fixed and several options are still under consideration for most of them. A detailed description of all the sub-detectors is given in [46] and will be only summarised in the remainder of this chapter.

[2] *Forward Calorimeter*

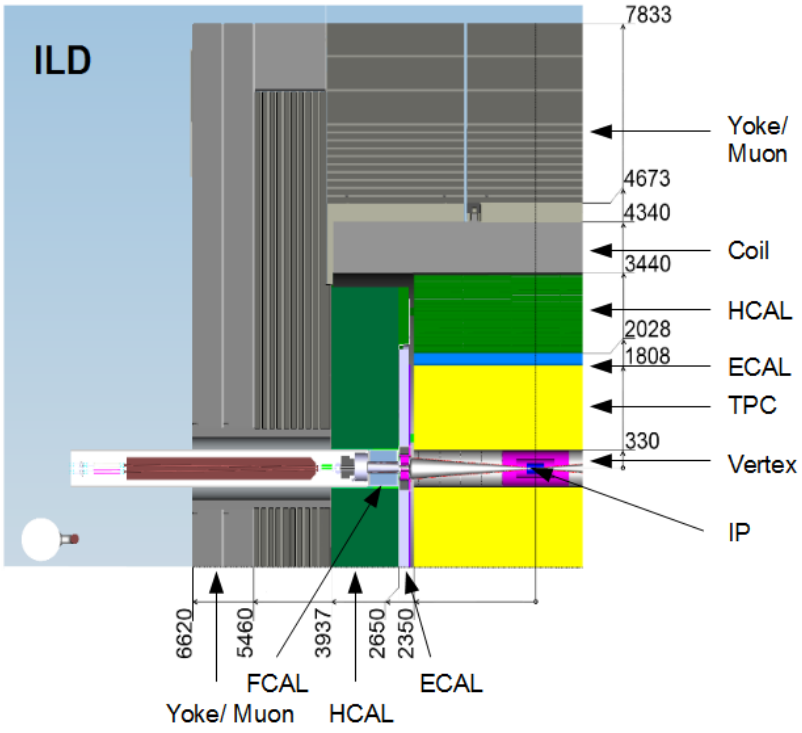

Figure 3.1: Section view of one quarter of ILD showing the placement of all the sub-detectors (from [46])

3.2.1 Inner tracking system

The inner tracker of the ILD is constituted by a silicon-pixel vertex detector surrounded by additional layers of silicon sensors with coarser resolution. The performance of a vertex detection system can be summarised by the precision of the measurement of the impact parameter of the charged particles produced by the collision. This benchmark parameter, for the ILD, is required to be better than $5\,\mu\text{m} \oplus 10/p\sin^{3/2}(\theta)\,\mu\text{m}$. To achieve this requirement the vertex detector must have a point resolution better than $3\,\mu\text{m}$ at 1.6 cm from the interaction point. To ensure the efficiency of the reconstruction the granularity of the detector must be high enough to guarantee an occupancy not exceeding a few %. The complete vertex detector will have a total radiation thickness in the barrel region of the order of 1% of a radiation length.

Surrounding the vertex detector, the ILD will have two double-layer silicon-strip sensors which will provide a few more high-precision samples along a charged particle track. The resolution goal for this sensor is 7 μm, intermediate between the vertex and the TPC, which will help in the extrapolation of the tracks found in the main tracker to those detected in the high-resolution system. This system will also have a total radiation thickness of the order of $1-2\,\%\ X_0$. Here and in the following the symbol X_0 represents the electromagnetic radiation length.

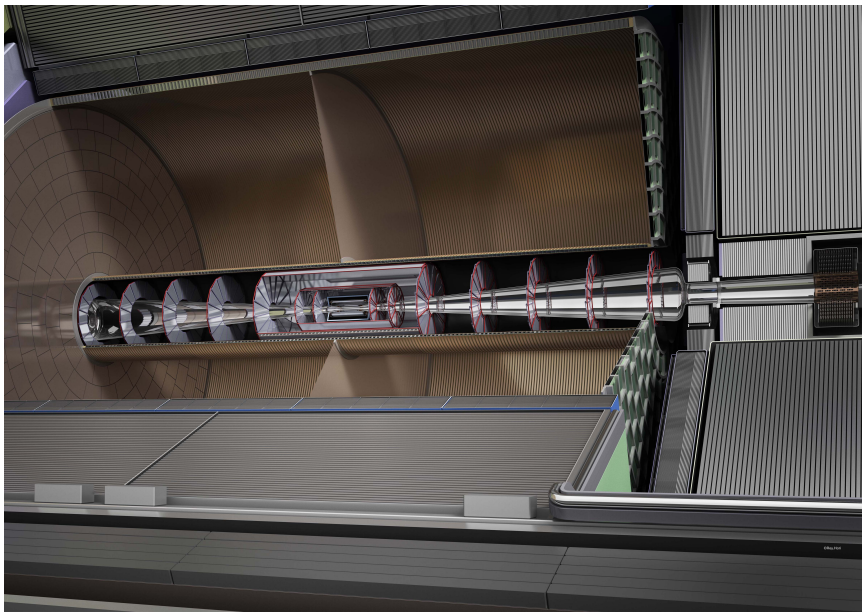

Figure 3.2: 3-dimensional representation of the ILD tracking system. The main visible component is the TPC with the concentric readout modules mounted in the endcap and surrounding the inner silicon-based core (from [46]).

3.2.2 The ILD TPC

The main tracker of the ILD experiment will be a large volume TPC surrounding the inner high precision silicon detectors. The advantage of a TPC in a high-energy collider experiments mainly stem from the possibility to have a very high number of 3-dimensional sample points along each track using a minimal amount of material. Even though the resolution on the position of each of these points is limited, compared to the silicon detectors listed in the previous section, due to the $N^{-1/2}$ dependency of the momentum resolution on the number of samples along the track, it is nonetheless possible to measure the momentum of charged particles with very high accuracy.

The number and continuity of the samples, together with the low occupancy of the detector makes the pattern recognition effort relatively easier even in the presence of relevant backgrounds and for events with several jets, as can be appreciated in fig. 3.3.

The high number of samples along each track also allows to measure the specific energy loss $\boldsymbol{dE/dx}$ of the particle with a precision of $\mathcal{O}(5\%)$ which will improve the particle-identification capability of the experiment.

The mechanical structure of the ILD TPC consists of two end-plates where the readout of the amplified signals take place, and a field-cage built from advanced composite materials. The gas amplification will be performed via an *MPGD*[3] system (see § 4.4.3 for more details) integrated with the readout electronics, the cooling and the power distribution system in one of several readout modules installed concentrically in each end-plate. A three-dimensional representation of those of the complete tracking system is shown in Fig. 3.2. A list of the relevant mechanical and operational parameters of the ILD TPC is given in Tab. 3.1.

[3] *Micro Pattern Gas Detector*

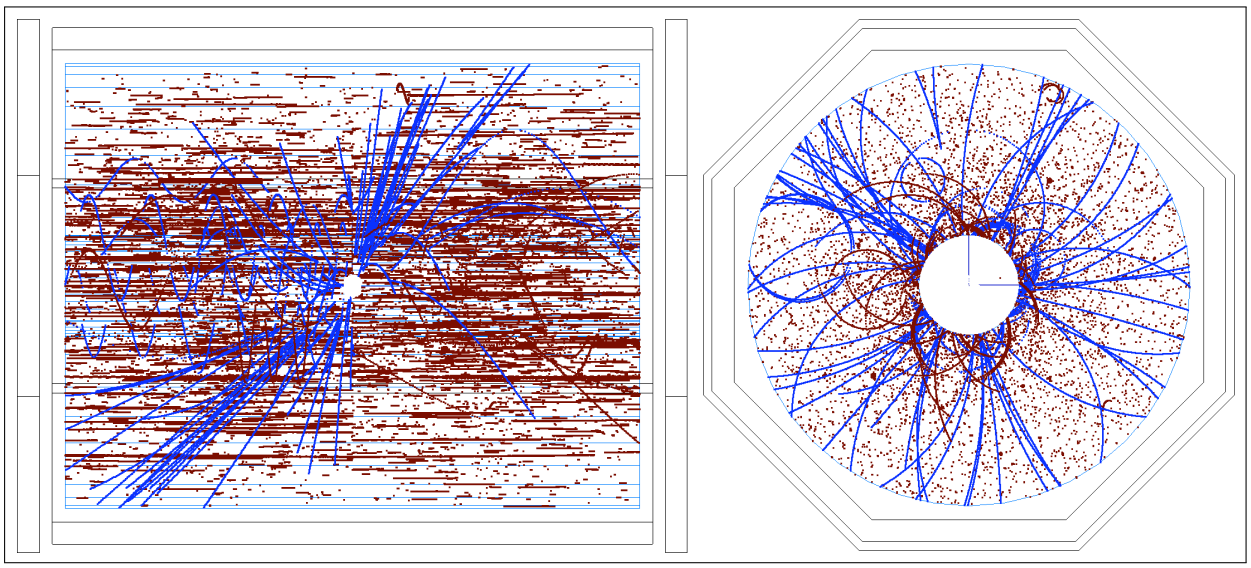

Figure 3.3: The rz and $r\phi$ view of a $t\bar{t}$ event (blue tracks) reconstructed in the ILD TPC in the beam background due to 150 integrated bunch crossings (red tracks). From [59]

TPC design parameters	
Inner radius (r_{in})	329 mm
Outer radius (r_{out})	1808 mm
Half length (z)	2350 mm
Solid angle coverage	$< \lvert\cos\theta\rvert \approx 0.98$
Barrel material budget	$< 5\% X_0$
End-cap material budget	$< 25\% X_0$
Pad size	$\approx 1 \times 6\,\mathrm{mm}^2$
Number of pad rows	≈ 220
Total number of pads	$\mathcal{O}(10^6)$
$\sigma_{r\phi}$	$60 \div 100\,\mu$m
σ_{rz}	$0.4 \div 1.4$ mm
$r-\phi$ double-hit resolution	≈ 2 mm
$r-z$ double hit resolution	≈ 6 mm
dE/dx resolution	$\approx 5\%$
Momentum resolution at 3.5 T	$\delta(p_\perp/p_\perp^2) \approx 10^{-4}/$ GeV/c (TPC only)

Table 3.1: Main design parameters of the ILD TPC (modified from [46])

3.2.3 The calorimeter system

As the particle flow assumes each particle to be individually reconstructed, both the hadron and the electromagnetic calorimeters must have an unprecedented granularity. The ILD calorimeter consists of a cylindrical barrel system and two large end-caps. Both systems are divided in depth in an electromagnetic and hadronic section. To improve the hermeticity at low angles a small dedicated system is placed in the forward direction around the beam pipe.

In all calorimeters the electronics will be integrated within the sensitive layer to locally perform a relevant part of the signal processing thus reducing the amount of data that needs to be transmitted outside the detector. This is necessary due to the large number ($\mathcal{O}(10^8)$) of independent channels to readout.

The electromagnetic calorimeter

The main role of the *ECAL*[4] in the particle flow approach is to identify individual photons in the events, separating them from each other and from other components of the shower, and to measure their energy. To obtain this result the detector must be finely segmented both longitudinally and transversally with respect to the shower.

The baseline design for the ILD ECAL is a sampling calorimeter with 30 sensitive layers interleaved by tungsten absorbers with a total thickness of 24 radiation lengths. The choice of tungsten allows to achieve the desired radiation thickness in a compact design which, in turn, allows to reduce the solenoid magnet size.

The segmentation transversal to the shower is obtained by dividing the sensors in each sensitive layer in 5×5 mm^2 individually read-out cells. That size, smaller than the Moliere radius of the tungsten absorber (9 mm), allows an efficient reconstruction of the shower shape, increasing the isolation of separate calorimeter clusters. The energy resolution is estimated in the TDR from Monte Carlo and test-beam measurements and, depending also on the specific sensor technology, will be of the order of $\mathbf{15\%/\sqrt{E}(GeV)}$.

The hadronic calorimeter

According to the particle flow paradigm, the *HCAL*[5] is optimised to accurately measure the energy carried by neutral hadrons isolating them from each others and from the charged ones in a jet as the momentum of the charged particles will be accurately measured in the tracker. As with the previous case this requires an outstanding segmentation of the detectors the longitudinal and transverse plane of the shower. For this reason the HCAL is designed as a sampling calorimeter with 48 sensitive layers spaced by steel absorbers for a total thickness of 6 nuclear interaction lengths. Each sensor cell of the baseline design is 5×5 cm^2 wide. The stochastic term of the energy resolution of this calorimeter was estimated in the TDR to be of the order of $\mathbf{45\%/\sqrt{E}(GeV)}$.

[4] *Electromagnetic Calorimeter*
[5] *Hadron Calorimeter*

The forward calorimeter

To improve the hermeticity of the most forward regions of the detector, the ILD design includes a set of 3 detectors:

LumiCal Designated to the measurement of the experiment luminosity to an accuracy better than 10^{-3} for a 500 GeV centre-of-mass energy, using the well known Bhabha scattering cross-section as a gauge for the measurement. This detector will cover the polar angle between 31 and 77 mrad from the beam lines.

LHCAL An extension of the hadronic calorimeter to cover the same polar angle range of the LumiCal.

BeamCal To estimate the bunch-by-bunch luminosity correction measuring the energy carried by the photon flux due to the beamsstrahlung, the radiative process due to the soft interactions between the two beams. This detector will also be able to identify single, high-energy photons produced in the initial- or final-state of the e^-e^+ interactions.

3.2.4 Magnet and yoke instrumentation

All the detectors of the inner part of the ILD experiment are contained in a superconductive solenoid magnet which will provide a nominal field in the barrel region of 3.5 T. Such a field will increase the separation of oppositely charged particles in a jet, improve the momentum resolution of the trackers and the general performances of the TPC (see § 4.5 for more details). On the other hand, a TPC is quite sensitive to inhomogeneities in the magnetic field (§ 4.2) which could introduce relevant distortions in the track reconstruction if not taken in account. This implies both a high field quality and its accurate mapping inside the coil.

The return flux of the solenoid magnetic field is conveyed by a massive, instrumented iron yoke which surrounds it and provides the main mechanical structure supporting the detector. Additionally, the yoke also functions as tail catcher for very energetic hadron shower and to help identifying the muon produced at the interaction point. The total calorimeter depth of 6 hadronic interaction lengths, constrained by the magnet cryostat inner radius of 3440 mm, is not sufficient to completely contain the shower produced by hadrons with energies of several tens of GeV, so the volume of the iron yoke immediately behind the coil is instrumented with 10 sensitive layers spaced by 14 cm of iron. Three additional sensitive layers in the barrel region and two in the end-caps, spaced by 60 cm of iron, are used to detect any charged particles leaking through all this material, almost exclusively muons.

Part II

The *GridGEM module*: a new GEM based readout module for a large TPC

Chapter 4

Gas-filled particle detectors and the Time Projection Chamber (TPC)

In the introductory part of this thesis we presented the ILC (§ 2), a new 500 GeV electron-positron collider currently being developed to complement and extend the research performed at the LHC. At the interaction point of the ILC beams there will be two large experiments, ILD and SiD. A general overview of the layout, requirements and performances of the ILD experiment is given in § 3.2.2. The feature of the ILD that is most relevant to the scope of this work is its main tracker: a large TPC (§ 3.2.2).

The main role of a gas-filled detector is the identification of charged particles crossing it using the ionization trail they leave behind in the sensitive gas volume. The fact that the sensitive material is a gas makes it possible to limit the influence of the sensor on the particle to be detected, due to the reduced multiple scattering and radiative energy losses, thus allowing further, precise measurements to be performed, for example by a calorimeter positioned further along the particle path.

To understand such type of device it is important to have an overview of the major physics processes which characterize all gas-filled detectors. Therefore, in this chapter, we will describe the essential features of a gas detector, leading to the specific description of the time projection chambers in § 4.5.

4.1 Gas ionization

When a fast[1], charged particle traverses a gas volume, it ionizes and excites the atoms and molecules of the mixture through a sequence of individual inelastic collisions. Each of these collisions is, in first approximation, independent from the others so the probability of a charged particle colliding $\boldsymbol{k}$ times within a volume of gas of depth $\boldsymbol{L}$ follows a Poisson distribution:

[1] In this context a particle is considered fast if the velocity of the atomic electrons can be considered negligible

$$\boldsymbol{P(L/\lambda, k)} = \frac{(L/\lambda)^k}{k!} e^{-L/\lambda} \tag{4.1}$$

$$\boldsymbol{\lambda} = \frac{1}{N_e \sigma_I(\gamma)} \tag{4.2}$$

where $\boldsymbol{\lambda}$, the mean free path between collisions, depends on the electron density $\boldsymbol{N_e}$ and the total ionization cross section per electron $\boldsymbol{\sigma_I}$, which in turn depends on the relativistic velocity of the primary particle and on the type of gas involved. For example in an Argon based mixture at *NTP*[2], a minimum ionizing particle ($\gamma \approx 3.5$) produces ≈ 28 ionization events per cm [61].

The electrons produced in these events are energetic enough to further ionize the surrounding gas, producing additional ion-electron pairs. Because the range of the primary electrons is usually very low, in most of the cases less than 1 mm, the ionization trail is actually a sequence of ion-electron clusters along the track of the original particle. For this reason two very important quantities characterizing the ionization processes are the cluster size distribution and the amount of energy necessary to produce an ion-electron pair. These quantities are a typical characteristic of the gas mixture where the process takes place and must be determined experimentally [62]. Because this secondary ionization can also involve complex interplay between different components of the gas, e.g. the Penning and the Jesse effects, even small quantities of a secondary component of a mixture can have important effects on its quality.

To further characterize the signal left by a charged particle in a gas volume, it is important to know the amount of energy transferred through its collisions with the atoms of the gas. This can be quantified through a modified version of the Bethe-Bloch formula introduced by Fano [63] which takes in account the Fermi density effect [64] and introduces a cut-off value for the energy transfer $E_{\max}$ which allows to describe the behaviour of electrons and limits the influence of the rare high energetic scatterings on the average energy loss:

$$\boldsymbol{(dE/dx)_{\text{Fano}}} = \frac{4\pi N_e e^4}{m_e c^2} \frac{1}{\beta^2} z^2 \left[\ln \frac{2 m_e c^2 E_{\max} \beta\gamma}{I} - \frac{\beta^2}{2} - \frac{\delta(\beta)}{2} \right] \tag{4.3}$$

This function, represented in fig. 4.1, is characterized by a non relativistic region where the energy loss falls as $1/\beta^2$ up to a minimum ionization region for $\beta\gamma \approx 4$ where a slow *relativistic rise* starts until the *Fermi Plateau* is reached, where the polarization of the dielectric medium crossed by the particle limits the ionization. The magnitude of the relativistic rise is limited to a few percent in liquids and solids but can be as high as $50-70\%$ for noble gases at NTP which makes a gas detector potentially capable of measuring the $\beta\gamma$ factor of a particle in a wide range, thus contributing to distinguish different particle species.

A more detailed model which takes in account the discrete energy levels of the atoms in the gas was derived by Allison and Cobb [65] and allows for detailed Monte-Carlo simulations of the ionization processes in gases [66].

[2] *Normal Temperature and Pressure*

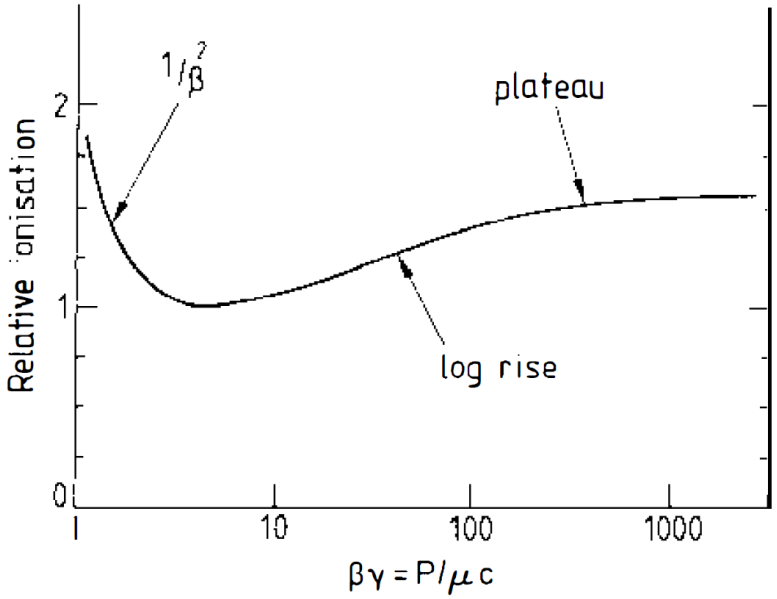

Figure 4.1: The typical dependence of the ionization produced in a gas by a fast charged particle on $\beta\gamma$, commonly known as the modified Bethe-Block distribution (from [65]).

The only other type of particle that can produce a detectable signal in a drift chamber is the photon. Due to its limited radiation length, a gas detector is usually quite transparent to high-energetic photons. When those interact, the product of such an event is a fast moving Compton-electron or an electron-positron pair whose energy deposition can be treated as above. A more detailed review of the physics processes involved in the ionization of a gas with a photon can be found in [67, 68].

4.2 The drift of electrons and ions in gases

After an ionization event, the electrons and ions created during this process move randomly within the gas volume, interacting with the other gas molecules elastically until they are neutralized by an opposite charge carrier. In the case of electrons it is also possible that a neutral molecule with a strong electron affinity may capture it thus reducing its lifetime.

If an electric field is present within the sensitive volume, a collective movement along the field direction will be superimposed to the pure thermal, random motion. The presence of an additional magnetic field can also modify the properties of the collective motion of the particle cloud. Those phenomena can be described by the *Langevin equation*:

$$\boldsymbol{m}\frac{\boldsymbol{d\vec{u}}}{\boldsymbol{dt}} = e\vec{E} + e\left[\vec{u}\times\vec{B}\right] - K\vec{u} \tag{4.4}$$

where $\boldsymbol{m}$ and $\boldsymbol{e}$ are the mass and charge of the moving particle and $\boldsymbol{\vec{u}}$ is its velocity vector. The last term of this equation describes a frictional force caused by the interaction of the particles with the gas molecules, which depends on the gas mixture and its pressure. Defining $\boldsymbol{\tau} = \frac{\boldsymbol{m}}{\boldsymbol{K}}$ which has the dimension of a characteristic time, the solution for $t \gg \tau$

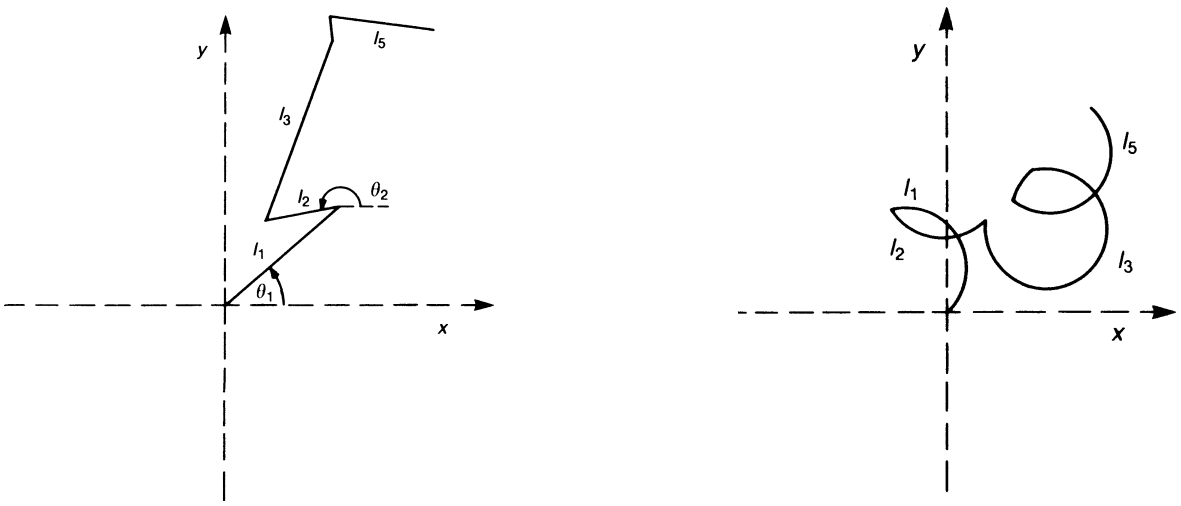

Figure 4.2: Comparison of a free electron random walk in the drift volume of a gas detector without a magnetic field (on the left), and with a strong magnetic field present (right drawing). From [68].

is a steady state for which $\frac{d\vec{u}}{dt} = 0$ and

$$\boldsymbol{u} = \frac{e}{m}\tau \left|\vec{E}\right| \frac{1}{1+\omega^2\tau^2}\left(\hat{E} + \omega\tau\left[\hat{E}\times\hat{B}\right] + \omega^2\tau^2\left(\hat{E}\cdot\hat{B}\right)\hat{B}\right) \tag{4.5}$$

where $\boldsymbol{\omega} = \frac{e}{m}\left|\vec{\boldsymbol{B}}\right|$ is the cyclotron frequency of the carrier.

When there is no magnetic field, that is $\omega\tau = 0$, the carrier velocity is proportional to the electric field and the proportionality constant μ is called the mobility of the carrier in the gas:

$$\boldsymbol{u} = \frac{e}{m}\tau E = \mu E \qquad \boldsymbol{\mu} = \frac{e}{m}\tau \tag{4.6}$$

The presence of a magnetic field can have a strong influence on the motion of the charge carriers and in particular on that of the electrons, as their $\omega\tau$ factor can be orders of magnitude higher than that of the ions.

If we now examine the thermal component of the charged cloud motion in the drift volume and we consider the case of an isotropic diffusion in the medium we know that the mean squared deviation of the carrier position after a certain time t will be proportional to the number of collisions that the carrier underwent during that time. Using again the mean free path λ and the characteristic time between collisions τ that we introduced earlier we have:

$$\boldsymbol{\sigma^2} = \frac{2}{3}n\lambda^2 = \frac{2}{3}\frac{\lambda^2}{\tau}t = \boldsymbol{2Dt} \tag{4.7}$$

where $\boldsymbol{D}$ is a constant. The isotropy condition is a good assumption if the velocity distribution of the carrier after each collision is isotropic, which is a good approximation for

ions in low fields and in general for electrons. Otherwise D is a tensor and the charge distribution will have different widths along each direction.

In presence of an electric field we can convert the time t in the distance L that the carrier travels under the influence of the field. If the electric field and the carrier mobility are constant, as ideally is in the drift volume of a gas detector, it is common to redefine the diffusion constant as:

$$\boldsymbol{\tilde{D}} = \sqrt{\frac{2D}{\mu E}} \tag{4.8}$$

$$\boldsymbol{\sigma^2} = \frac{2DL}{\mu E} = \tilde{D}^2 L \tag{4.9}$$

The presence of magnetic field also has a strong influence on the diffusion of the charge carriers. In this situation the magnetic field forces the carriers to move in helices rather than in straight lines between collisions (see fig. 4.2 which effectively reduces their diffusion in the plane perpendicular to their motion. In the simplified but common situation of collinear electric and magnetic fields, the ratio of the diffusion coefficients with and without magnetic field can be written as:

$$\frac{D_B}{D_0} = \frac{1}{1+\omega^2\tau^2} \tag{4.10}$$

$$\frac{\tilde{D}_B}{\tilde{D}_0} = \frac{1}{\sqrt{1+\omega^2\tau^2}} \tag{4.11}$$

More details and the derivation of these formulas in specific and general cases can be found in [68].

4.3 Signal readout in a drift chamber

In a gas detector, the typical measured signal is the electrical current induced by charged cloud moving towards one of the electrodes. This current is proportional to the amount of charge drifting, the velocity of the carriers and the geometry of the sensitive surfaces. For a generic configuration of electrodes and charges this current can be quantified through Ramo's theorem [69] which states that the current $\boldsymbol{I_n(t)}$, induced on a grounded electrode by a point charge $\boldsymbol{q}$ moving along a trajectory $\boldsymbol{x(t)}$ is:

$$I_n(t) = -\frac{q}{V_w} E_n[x(t)]v(t) \tag{4.12}$$

where $\boldsymbol{E_n}$ is the electric field along that trajectory in the case where the charge q is removed, electrode n is set to voltage $\boldsymbol{V_w}$, and all other electrodes are grounded.

One of the most important consequences of this fact is the difference between ion- and electron-induced signals. Due to the different drift velocities of the two carriers, ion-induced currents develop much slower and can produce long tails in the signals.

In general the sensitive surfaces of a gas detector can be mono-dimensional, like a set of wires, or bi-dimensional. In the second case one of the most common configurations is the pad layout where the surface is segmented in several electrodes, each independently read out by an electronic device. In recent years this concept was brought to its extreme by miniaturizing the pads to the size of a silicon pixel of $\approx 50\,\mu$m [70].

4.4 Gas amplification

In most cases of interest, the ionization produced by the passage of a charged particle in a gas detector is not sufficient to produce a sizeable signal. To enhance it independently from the electronic noise it is therefore important to increase the number of charge carriers inducing that signal.

This can be done inducing an avalanche multiplication of the drifting electrons, called *gas amplification*. To obtain that, it is necessary that the drifting electrons gain enough energy between successive interactions to ionize additional gas molecules. For a fixed gas and electric field, the number of new electron-ion pairs produced by a single electron in a unit length is described by the *first Townsend coefficient* $\boldsymbol{\alpha}$ which depends on the excitation and ionization cross sections of the molecules in the gas mixtures.

The electric field necessary to initiate an exponential electron avalanche in a gas at normal temperature and pressure is of the order of $10^4\,$V/cm. In those conditions the final charge will be proportional to the initial one and the ratio $\boldsymbol{N/N_0}$ between these two quantities is called the *gas gain*.

$$\boldsymbol{G} = \frac{N}{N_0} = \exp\left(\int_a^b \alpha(E)\frac{dE}{dx}dx\right) \tag{4.13}$$

where $\boldsymbol{a}$ and $\boldsymbol{b}$ are the positions where the electric field exceeds the avalanche threshold. As the amplification is, in first approximation, described by the sum of N_0 exponential multiplications, due to the central-limit theorem of statistics, the variance of the final distribution (S^2) is proportional to that of the individual processes ($\boldsymbol{\sigma^2}$) and the mean of the sum ($\bar{\boldsymbol{N}}$) is proportional to the sum of the individual means ($\bar{\boldsymbol{n}}$). Because the variance of an exponential distribution is the square of its mean we can write:

$$\bar{N} = N_0\bar{n} \qquad S^2 = N_0\sigma^2 \tag{4.14}$$

$$\frac{\boldsymbol{\delta G}}{\boldsymbol{G}} = \frac{S}{\bar{N}} = \frac{\sqrt{N_0}\bar{n}}{N_0\bar{n}} = \frac{1}{\sqrt{N_0}} \tag{4.15}$$

If the field is too large, the electron collision will produce also high energetic photons that can trigger secondary discharges in the gas volume which can mar the proportionality

relationship between the initial ionization and the final charge and decrease the localization of the cloud.

When the charge in the avalanche exceeds a value of $\approx 10^8$ electrons, known as the Raether limit [71], the avalanche develops into a *streamer*. In this situation the high space charge at the growing front of the avalanche can produce an electric field as strong as the external field which will induce further growth in the avalanche in a positive feedback loop. When this happens the total charge in the plasma cloud will be almost completely uncorrelated to the initial charge. In many cases this growth can continue until a plasma tube joins two oppositely charged electrodes thus inducing a complete discharge which can, in a best case scenario, nullify the potential difference between them thus blinding the detector until the power supply can recharge them. In some case the energy carried by such a discharge can be so large to damage the electrodes and their support structures and permanently cripple the detector.

4.4.1 Ion backdrift

A common feature of any gas amplification system is the generation of a sizeable cloud of positive charge carriers that will drift back in the sensitive volume of the detector, away from the avalanche region. If the charge density is large enough, this cloud, moving in the sensitive volume, can produce relevant distortions of the electric field.

To get rid of this positive carriers one can rely on the intrinsic features of the amplification system, that will passively annihilate them, or on active systems, usually called gates, where a device can be polarized in two ways, one that leaves it transparent to all charges and the opposite one to absorb them thus removing the positive carriers but also blinding the detector for some time.

4.4.2 Wire amplification

The most common example of a gas amplification device is a single wire, surrounded by a concentric cathode, charged to a sufficiently high potential to generate the electric field necessary to induce the gas amplification of the electrons moving towards it. The amplified electron and ion cloud induces a signal on the wire that can be used to detect and localize the avalanche.

When a plane of several such wires, parallel to each other are placed between two cathodes they act almost as a series of independent simple wire detectors. Segmenting the cathode plane allows to localize the avalanche position with a sub-mm resolution, measuring the current induced by the ions moving away from the wires. The main factor limiting the resolution of such a detector is the minimum distance between two wires in the sensitive plane that, due to the strong electrostatic forces between them, is of the order of 1 mm. To counter those forces it is necessary to apply a strong mechanical tension to the wires which also implies the usage of relatively massive mechanical structure to relieve this tension.

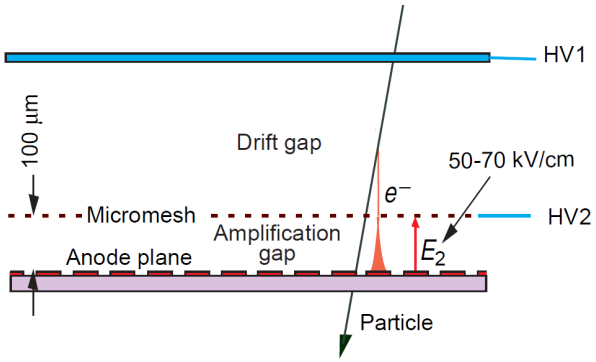

Figure 4.3: Schematic drawing of a Micromegas gas amplification system (from [5]).

Another factor limiting the usage of this type of devices is their performance reduction at high rate when the positive space charge produced during the gas amplification is sufficient to reduce the field around the wire thus reducing the gain. This effect starts being sizeable at a particle flux of approximately 1 kHz/mm at normal operating conditions [5]. At high rate these detectors are also sensitive to ageing phenomena caused by the polymerization of trace gas components on the wire surface which can produce several negative effects from a gain reduction to the induction of continuous, localized discharges. To reduce those phenomena it is necessary to control carefully the gas composition [72].

4.4.3 Micro-Pattern Gas Detectors (MPGD)

In recent years a new group of gas amplification devices, called Micro-Pattern Gas Detectors, was developed to go beyond these limitations and improve the performances of the gas detectors. The most common of those devices can be grouped into two categories: Micromegas [73] and *GEM*[3] [74].

The first type (see Fig. 4.3) creates the high electric field necessary to produce the electron avalanche via a thin metal grid, with a pitch of the order of the tens of μm, placed about 100 μm above the sensitive anode surface. The drifting of the ions produced during the avalanche, and to a lesser extent of the electrons, induces a signal on the sensitive surfaces and, due to the narrowness of the avalanche region, this signal is extremely localized. The high ratio between the electric field in the amplification and drift regions reduces the number of ions produced during the avalanche that can reach the sensitive volume.

In the second type of device, the GEM, the avalanche multiplication happens in holes of the size of the order of about 100 μm, created in a parallel plate capacitor of a similar thickness. Those devices, particularly relevant to this thesis, will be described in better detail in the next chapter (§ 5).

The main advantages of this type of detectors are the increased rate capability, that can

[3] *Gas Electron Multiplier*

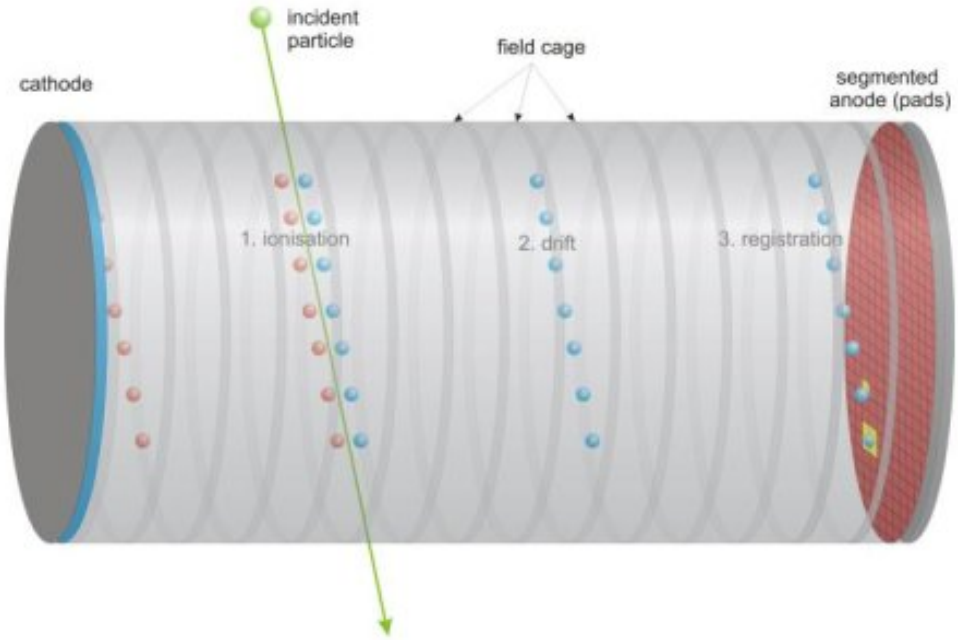

Figure 4.4: Conceptual scheme of a TPC, showing the passage of a charged particle which, ionizing the gas, creates free charge carriers that drift towards the opposite ends of the chamber where, on the anode side, a segmented sensitive plane can be used to localize the track path. From the LCTPC website (http://www.lctpc.org/e8/e57671).

be several orders of magnitude higher than that of a *MWPC*[4], and the reduced distortions they induce in the drift volume due to the micrometric size of the amplifying features which also allow for an improvement in the localization resolution. Moreover most of those devices have intrinsic ion suppression capability which further improves the detector performances.

4.5 The Time Projection Chamber (TPC)

In 1978 a new type of gas-filled detector was proposed to be used on the PEP accelerator at SLAC[5] to perform high resolution and robust 3-dimensional tracking of ionizing particles at high-rate high-energy physics experiments within a relatively compact volume. This detector was called the Time Projection Chamber or TPC [75].

This detector, schematically represented in fig. 4.4, can be conceptually described as a parallel plate capacitor where the space between the two electrodes is filled with a carefully chosen gas. When an ionizing particle crosses the volume between the two plates, the ionization products will drift toward the opposite ends of the detector along the electric field lines. If one of those two areas is equipped with devices capable of recording the time

[4] *Multi-Wire Proportional Chamber*
[5] http://www.slac.stanford.edu/

of arrival of the charge carriers and to localize their position, it is possible to reconstruct the path of the charged particle producing the initial ionization. Because the electron's mobility is much higher than the ion's and because it's much easier to produce the gas amplification of an electron cloud, only the signal produced by the electrons is normally used in a TPC.

The length of the drift volume of a TPC can vary between a few cm to several meters, e.g. the ALICE tracker [76] or the future ILD TPC. When the drift length is so large, it is extremely important to control the quality of the electric field in the detector. To improve its homogeneity, it is possible to use a set of electrodes, called a *field cage*, set at suitable potentials, along the walls of the chamber between the anode and the cathode.

When an additional magnetic field is also present, it is possible to measure the momentum of the detected particle measuring the curvature of the track in a plane perpendicular to that field. Because the amount of material the particle is crossing is relatively low, the influence of multiple scattering on the momentum measurement is reduced accordingly. The magnetic field also improves the localization performances of the detector reducing the diffusion of the charge cloud during its drift in the chamber as we discussed in § 4.2.

On the other hand, if the electric and magnetic field are not parallel to each other, the charge carriers, will be subject to a force perpendicular to the electric field lines (see eq. 4.5) which will produce a distortion in the reconstructed trajectory of the primary particle, unless complex calibration procedures are used to mitigate this problem. The relevance of this effect increases with the drift length of the detector.

Due to the particular sensitivity to any electric field distortion introduced in the drift field, particular care must be taken in designing a TPC to reduce the ion back-drifting from the amplification structures. If the expected event rate is so high that the ions from a previous event are not swept away before the next, this may decrease the system performance. For this reason many TPC use an ion gate and/or an ion-suppressing amplification system like an MPGD.

If the sensors at the end of the detector are also able to measure the amount of energy lost by the charged particle while traversing the chamber, this information, together with its momentum, can be used to distinguish among different particle species as was done, for example, by the ALEPH experiment [77].

The particle identification performance of a TPC, together with its pattern recognition and momentum measurement ability, strongly depend on the number of charge and position samples that can be obtained along the particle path. For example, for a given track length ($\boldsymbol{L}$), sampled $\boldsymbol{N}$ times, in a gas volume at pressure $\boldsymbol{p}$ the accuracy on the ionization measurement [65] varies as:

$$\frac{\boldsymbol{\delta I}}{\boldsymbol{I}} = 0.96 N^{-0.46} (p\frac{L}{N})^{-0.32} \tag{4.16}$$

When the direction of origin of the particles to detect is roughly known it is possible to adapt the segmentation of the sensitive plane accordingly, increasing it in the direction perpendicular to the track. In a collider experiment, for example, it is common to use cyl-

indrical detectors with the sensitive plane perpendicular to the beam direction segmented in concentric rows, each of them divided in small pads. In this case each row will provide a single position and charge sample along the track and the momentum resolution achievable in the plane perpendicular to the magnetic field $\boldsymbol{B(T)}$ is:

$$\frac{\boldsymbol{\delta p_\perp}}{\boldsymbol{p_\perp^2}} = \frac{\sigma_\perp}{0.3BL^2}\sqrt{\frac{720}{N+4}} \tag{4.17}$$

where L is the track length in meters and $\boldsymbol{\sigma_\perp}$ is the position resolution for each of the N sample points.

The single point resolution $\sigma_\perp$ can depend on many factors including the diffusion of the electron cloud during the drift phase, the electronic noise, the track angle and the width of the pads in a row. When all the charge is collected on a single pad of width w this resolution cannot be lower than $w/\sqrt{12}$, the variance of a uniform distribution. When the charge is shared between neighbouring pads it is possible to analyse this distribution to achieve a position resolution an order of magnitude better than the pad width, depending on the number of pads used to reconstruct the position of the charged cloud [78, 79].

It follows that, to increase the detector performances, it is necessary to reduce the pad size, both in height and in width. On the other hand the amount of charge collected for each pad must be sizeable compared to the noise introduced by the system used to measure it which, together with the cost of equipping each pad with an independent readout system, provides a lower limit to the practical pad size.

From this argument it also follows that any dead space in the sensitive area that is parallel to the track direction and will thus result in the loss of multiple samples along that should be avoided more carefully than a dead area perpendicular to that direction which will only result in the loss of a single sample along each track.

4.5.1 Choosing a gas for a TPC

The gas composition in a TPC is a complex choice which impacts strongly the performances of the detector. Due to the very long drift length many effects which can be negligible in other gas detectors have a strong influence on many operational parameters. Ideally a gas mixture to be used in a TPC must have the following features:

Low electron diffusion To improve the localization of the initial ionization. If the chamber is used with an axial magnetic field this can be obtained choosing a gas with a large $\omega\tau$ factor.

High electron mobility To minimize the time necessary to collect the signal relative to one event without using very large electric fields that, due to the large field length will result in extremely large voltage difference between the electrodes.

Saturated drift velocity To reduce the uncertainties on the time of arrival of the charged carriers due to the lack of accuracy and uniformity of the drift field.

Very low electron attachment To reduce the number of charge carriers lost during the drift, particularly relevant for large chambers.

High ionization rate Increasing the number of the primary charge carriers per unit length reduces the fluctuation of this number thus improving both the energy loss measurement and the localization resolution.

High Townsend coefficient To achieve high gas amplification using relatively low electric fields. A lower electric field reduces the probability of an uncontrolled discharge and simplifies the detector operation.

Photon quenching To limit the development of uncontrolled discharges and streamers during the gas amplification (§ 4.4).

No ageing Some components of otherwise efficient gas mixtures, in particular many organic additives, may induce ageing phenomena in the detector, in particular on the gas amplification surfaces or can slowly produce corrosive molecules that can damage the system [72].

Not flammable, toxic or radioactive To simplify the handling.

Most of the gases commonly used in a TPC are mainly composed of a noble gas mixed with one or two more components in lower abundance which can be selected to provide adequate photon-quenching, increase the electron mobility or the ionization rate.

For example, the gas used for the experiments described in this thesis, called *T2K-gas*, is a mixture of 95% Ar, 3% CF_4 and 2% isobutane (iC_4H_{10}). Argon is the most abundant noble gas available on Earth, which reduces the operational costs of a large volume detector. CF_4 is a commonly used quenching gas due to the strong covalent bonds between the Carbon and the surrounding Fluorine atoms which can absorb the photon energy without breaking the molecule, thus converting it in thermal energy. Finally, isobutane is a well known *Penning gas* in combination with Argon and reduces the energy required to produce an electron-ion pair.

Chapter 5

The Gas Electron Multiplier (GEM)

One of the most important parts of any gas detector, and of a *TPC*[1] in particular, is the gas amplification system. This stage of the detector, through a controlled electron avalanche produced in a strong electric field, increases the size of the electron cloud drifting towards the anode and enhance the signal induced there. The physics processes involved in the gas amplification were detailed in § 4.4.

For decades the best performances were obtained with wire-based amplification systems. To fulfil the requirements of the ILD TPC (§ 3.2.2 it is necessary to use a new class of gas amplification devices, collectively named *MPGD*[2]. This chapter will describe the most relevant features of one of the most commonly used MPGD, namely the GEM. After a general description of the technology, we will here discuss the parameters that characterize those devices.

5.1 Overview

The gas electron multiplier, invented in 1997 [74], can be described as a thin parallel plate capacitor pierced by several holes whose size and pitch are of the same order of magnitude as the device thickness. In its most common configuration, the dielectric material of the capacitor is a plastic polymer, for example polyimide, coated with a thin copper layer on both sides. The holes are usually obtained by chemical or laser etching and have a diameter typically between $\approx 20\,\mu$m and $\approx 150\,\mu$m [80].

The gas amplification is obtained charging up the two sides of the device at different potentials which creates a high field between the electrodes. The different permittivity of the gas in the holes and the insulator surrounding them will further increase the field inside them up to the point where the avalanche multiplication can take place. Because this high field is only achieved within the holes the avalanche will have a limited size and its magnitude will remain proportional to the incoming charge, barring a very high

[1] *Time Projection Chamber*
[2] *Micro Pattern Gas Detector*

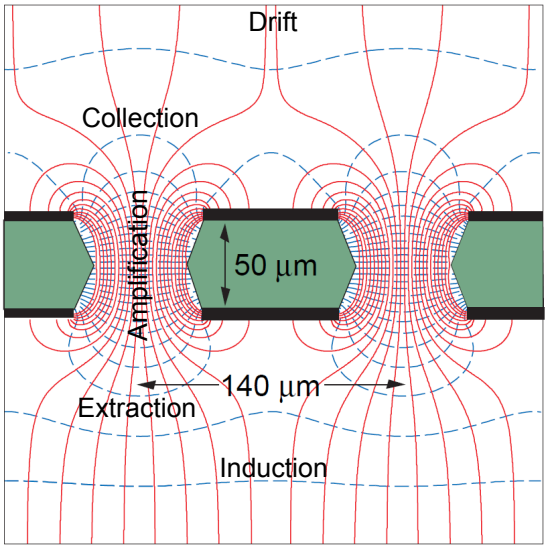

Figure 5.1: Schematic view of a section of a GEM in one of its most common configuration, showing the electric field and equipotential lines. The 5 volumes characterizing the operational configuration of a GEM are also identified. Modified from [5]

initial electron density. In those conditions every hole can be considered as an independent proportional counter which allows the device to stand rates as high as $\approx 10^6\,\mathrm{Hz/mm^2}$ without relevant gain drops [81].

In a typical configuration, like that of Fig. 5.1, the electrons drift from the sensitive volume of the detector and part of them will enter one of the holes of the GEM where they are multiplied. After the amplification, part of the electrons produced will continue drifting in the same direction as before while some will end on the lower GEM electrode. Those electrons that continue their drift will then induce a signal on the sensitive surface or can be further amplified by another GEM or even by a different type of device. On the other hand the ions produced during the amplification will drift back outside the hole towards the sensitive volume but many will end on the top electrode of the foil, thus reducing the ion back-flow.

The possibility of cascading several GEM foils is one of the major advantages of this technology because it allows to achieve a very high total gain, of the order of 10^5, distributing it through several stages, which reduces the chances of an avalanche growing beyond the proportional range in any one of them, causing a streamer and a potentially dangerous discharge.

Finally, because in a GEM based device the current on the sensitive surfaces is induced by the movement of the electrons extracted from the last of the foils, that signal has a fast rise time and a relatively short tail.

5.2 Single GEM characterization

When describing a GEM foil and its performances we can distinguish two sets of parameters: the geometrical parameters which are defined at manufacturing time and the operational parameters which can be adjusted during the device operations.

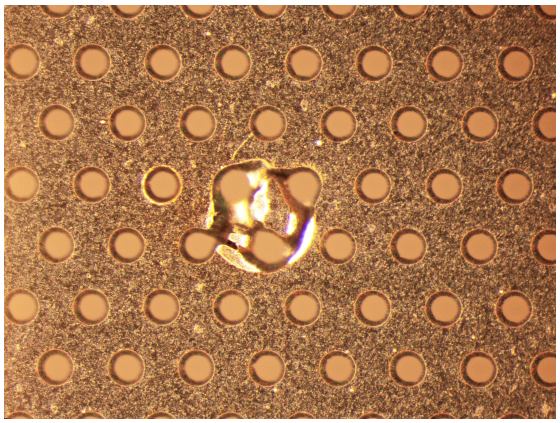

Figure 5.2: Microscopic photo of the surface of a GEM foil. The hexagonal pattern of the holes on the GEM surface is clearly visible. At the center of the photo is also visible the damage to the foil surface produced by a powerful discharge.

The pattern and the shape of the hole in a GEM are the most important geometrical parameters characterizing a GEM foil. Usually the holes are etched in a hexagonal pattern (Fig. 5.2) so that each hole is surrounded, at the same distance, by 6 other holes. The distance between the hole centres, $\boldsymbol{p}$, is what we define as the *hole pitch*.

Due to the manufacturing technique, the holes are not perfectly cylindrical. When they are produced by chemical etching they usually have a double conical shape, depicted clearly in fig. 5.1. The inner and the outer diameter of the hole will be labelled respectively $\boldsymbol{d_i}$ and $\boldsymbol{d_o}$. When no further specification is given, the outer diameter will be implied and labelled $\boldsymbol{d}$.

The "Standard CERN GEM" is the most common configuration in production and will be repeatedly mentioned in this thesis. It has an insulator thickness of 50 μm, with 5 μm copper coating on each side, double conical hole with an inner size of 50 μm and outer size of 70 μm and hole pitch of 140 μm.

The ratio between the holes' surface and that of the electrodes defines the optical transparency of the GEM, that, for uniform hexagonal patterns, can be written as:

$$\boldsymbol{t} = \frac{\pi d_i^2}{2\sqrt{3}p^2} \tag{5.1}$$

For the "Standard CERN GEM " configuration $t \approx 0.12$. Often the same quantity is defined using the outer hole diameter in which case $t_o \approx 0.23$.

5.2.1 Charge transfer and gain

Once the GEM electrodes are charged we can define 5 different volumes, shown in Fig. 5.1:

Drift volume: where the electric field is negligibly influenced by the microscopic structure of the GEM.

Collection volume: where the electric field is distorted by the presence of holes in the GEM and the electrons are guided by the electric fields towards those holes. Some of the electrons, depending on the ratio of the field before and after this volume, can be absorbed by the GEM electrodes while the others continue to drift towards the inner

part of the hole. Similarly part of the ions produced by the gas amplification move towards the drift volume while the others are annihilated at the GEM electrodes.

Amplification region: defined by the volume where the field strength exceeds the gas amplification threshold and an electron avalanche can start and develop.

Extraction region: this starts where the field decreases below the amplification threshold and the electrons produced in the avalanche are further drifted towards the anode of the detector. Only some of the electrons produced in the avalanche will actually end in the next region while the others are absorbed by the GEM anode.

Induction volume: in this area the electric field is again negligibly influenced by the microscopic structure of the GEM and the electrons are freely drifting towards the detector anode.

Assuming a constant field in the drift and induction volume, respectively $\boldsymbol{E_D}$ and $\boldsymbol{E_I}$, the other relevant operational parameter of a single GEM foil is the voltage across the electrodes, $\boldsymbol{V_G}$. Additionally the GEM performances can be influenced by the presence of a magnetic field, $\boldsymbol{B}$.

The most important performance indicator for a GEM foil is the total gain $\boldsymbol{G}$, often called *effective gain*, the ratio between the outgoing and incoming electrons which can be written as the product of 3 factors:

$$G = C \cdot G_i \cdot X = \frac{N_e(I)}{N_e(D)} \tag{5.2}$$

Collection Efficiency: The ratio between the number of incoming electrons from the drift region ($\boldsymbol{N_e(D)}$) and the number of those that arrive to the amplification region ($\boldsymbol{N_e(C)}$) of the GEM holes.

$$C = N_e(C)/N_e(D) \tag{5.3}$$

Intrinsic Gain: The amplification factor in the GEM hole defined as the ratio between the number of electrons immediately after the amplification ($\boldsymbol{N_e(X)}$) and those collected into the hole ($N_e(C)$). This value depends on the Townsend coefficient of the used gas and on the amplification length.

$$G_i = N_e(X)/N_e(C) \tag{5.4}$$

Extraction efficiency: The ratio between the number of electrons that get to the induction volume ($\boldsymbol{N_e(I)}$) and the amount of them in the avalanche as it exits the amplification region ($\boldsymbol{N_e(X)}$).

$$X = N_e(I)/N_e(X) \tag{5.5}$$

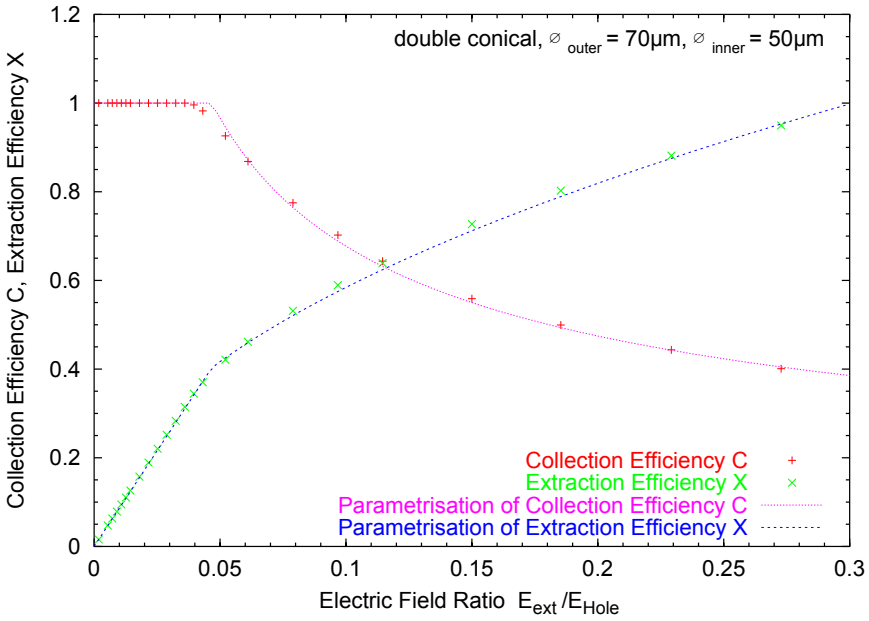

Figure 5.3: Comparison between data and parametrization of the collection and extraction efficiency of a single GEM as a function of the ratio between the field in the drift and induction volume respectively and the field in the hole (from [83]). It must be noted that the field in the hole must be obtained through detailed simulation from the GEM geometry, the external fields and the voltage applied across the GEM electrodes

From the same factors another important quantity can be defined which is the *electron transparency*: the number of electrons that pass through the GEM when we assume no gas amplification.

$$\tau_e = C \cdot X \tag{5.6}$$

The dependency of these factors on the geometrical and operational parameters listed previously is treated in detail in many other publications, for example [82, 83]. It must be noted that in many cases these factors are parametrized as function of the ratio of the field outside and inside the hole (Fig. 5.3). This last quantity cannot be measured directly and must be obtained from simulations. For the gain in particular, an accurate simulation that also takes into account the space charge that accumulates on the GEM hole dielectric material is not yet available and a calibration of the simulation with the experimental results is required.

5.2.2 Discharges in GEM operations

A well known characteristic of all gas amplification devices is the possibility of the development of an uncontrolled discharge between the electrodes. While this phenomenon is not avoidable, an appropriate design of the gas amplification device makes it possible to reduce the rate of occurrence and the damage it will induce on the detector.

When a discharge happens the GEM foils can be susceptible to cumulative and immediate damage. The first type of damage is usually due to the progressive accumulation of a carbon residue in the holes and a detailed description is given in [84]. When the discharges are powerful enough, the plasma can melt the foil substrate and even the copper as can be seen in Fig. 5.2. In both cases the effect is a short circuit between the two electrodes so

that it is no longer possible to reach the amplification voltage.

To reduce the damages caused by the discharge and limit them to the long-term cumulative effects, it is necessary to reduce the amount of energy available in the system. Assuming that the plasma arc is active only until the two electrodes of the GEM reach the same potential, and neglecting any other capacitative load but the one due to the GEM itself ($\boldsymbol{C_G}$), the energy available can be written as:

$$\boldsymbol{E_d} = \frac{1}{2} C_G \cdot V_G^2 \tag{5.7}$$

It follows that, to reduce the discharge energy it is necessary to reduce the GEM capacitance or the potential across the electrodes. For a given area of the sensitive surface of a GEM foil, the first parameter depends essentially on the hole pattern geometry so that we can define a specific capacitance of a GEM as $\boldsymbol{\kappa_G} = C_G/A$, where $\boldsymbol{A}$ is the GEM surface.

A good approximation of this quantity can be obtained calculating the capacitance of a parallel plate capacitor with a surface equal to that of the electrodes of the GEM:

$$\kappa_G = \frac{\epsilon_0 \epsilon_r}{z}(1 - t_o) \tag{5.8}$$

where $\boldsymbol{\epsilon_r}$ is the dielectric permittivity of the substrate and $\boldsymbol{z}$ its thickness. $\boldsymbol{t_o}$ is the optical transparency calculated using the outer GEM hole. With this formula it is possible to calculate the specific capacitance of the "Standard CERN GEM" configuration to be

$$\boldsymbol{\kappa_{CG}} \approx 4.79 \times 10^{-7}\,\mathrm{F/m^2} \tag{5.9}$$

which is compatible with the measured capacitance of a $0.01\,\mathrm{m^2}$ "Standard CERN GEM" of 4.7 nF.

Even though there is no hard upper limit on the capacitance a GEM must have to avoid destructive discharges during operation, years of experience with these devices demonstrated that a high level of reliability can be reached with a foil capacitance of the order of 5 nF.

To cover a wider area than $100\,\mathrm{cm^2}$ but still maintain the same reliability of the "Standard CERN GEM" configuration a common solution is to divide the electrode on one of the two sides of the foil in several sections of $\approx 100\,\mathrm{cm^2}$, powered independently and decoupled from each other. Such a solution was experimented with, for example, by the COMPASS [85, 86] and CMS [87] experiments.

The decoupling of the sectors can be simply done introducing an high-valued resistor, of the order of 10 MΩ, between them and between each sector and any other capacitative load so that the time constant of the discharge of this loads is much longer than the typical time constant of a GEM discharge.

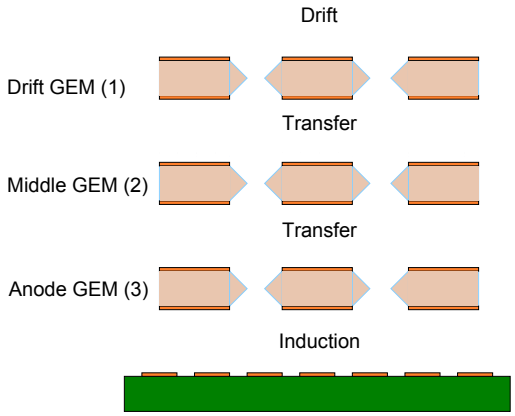

Figure 5.4: Sketch of a three-GEM stack showing the naming conventions used to label the different elements of the stack. The field in the drift, transfer and induction gaps are accordingly named drift, transfer and induction fields. The GEM foils in the stack are named in this document, according to their position, as drift, middle and anode GEM. Another convention, common in literature, is to number them according to the electron drift path. This numbering is shown in parentheses.

5.3 Characterization of a GEM stack

One of the main advantages of the GEM technology is the possibility to stack them above one another to divide the total gain in multiple stages, increasing the final amplification and, at the same time, improving the detector reliability making it less prone to discharges. The most common configurations involve two or three GEM foils in a stack and each of them can have different geometrical parameters.

The other relevant geometrical parameters that characterize a GEM stack is the distance between the stages, called the *transfer gaps*, and between the last stage and the readout plane, the *induction gap*. The size of these gaps and the magnitude of the electric and magnetic field across them define the amount of diffusion the electron cloud will incur while travelling between the stages. The achievement of a diffusion scale larger than the readout scale is one of the main goals of the design of a GEM stack because it will allow to use the charge sharing between neighbouring readout channels to accurately reconstruct the initial position of the electron cloud[3].

From the operational point of view, in a typical three GEM stack, like that sketched in Fig. 5.4, we can identify 8 relevant operational parameters which define the performance of the gas amplification stack: the magnitude of the electric field in the drift volume and in the transfer and induction gaps, the voltage across each GEM foil and the magnitude of the magnetic field.

The total gain of the stack can be written as the product of the gain of the single GEM:

$$\boldsymbol{G_T} = G_D \cdot G_M \cdot G_A = \frac{N_e(I)}{N_e(D)} \tag{5.10}$$

The three individual gains are not uncorrelated though, because the collection and extraction efficiencies of neighbouring GEMs are correlated by the transfer field between them.

The fact that the performances of a GEM stack are influenced by many operational parameters, 7 for a 3-GEM stack, allows to adapt the device to many operational con-

[3]The charge sharing technique and the correlation between the diffusion scale and the size of the readout channels will be discussed in more detailed in 9.1.2

ditions. Some of the most common and relevant optimizations that can be considered are:

GEM voltage optimization. The voltage across the GEM electrodes is the most important parameter to influence the GEM gain. The most obvious configuration for a GEM stack would be to apply an equal voltage difference across each stage to distribute uniformly the gain between them but it is usually better to configure the stack asymmetrically to obtain a higher gain in the drift GEM and a lower amplification in the anode-side device. In fact, because the gain fluctuations are inversely proportional to the square root of the number of initial electrons (eq. 4.15), producing the maximum amplification in the first stage will decrease the relative fluctuations in the following ones. On the other end, the last stage before the induction gap is where the electron density of the cloud is the highest and there a reduced amplification factor improves the reliability of the system.

GEM gaps optimization. To improve the resolution on the measurement of the position of the initial electron cloud it is common to induce its charge on multiple neighbouring pads and calculate the centre of this distribution with a centre-of-gravity method. For this method to be effective the charge must be spread among several neighbouring sensors. Optimizing the gap between the GEMs in the stack allows to match the cloud size with that of the readout elements (pads, strips, pixels). On the other hand a large gap size negatively influences the timing performance of the detector.

Ion backdrift optimization. Even though the GEM have an intrinsic ion suppression capability, it is possible to optimize the stack parameters to further reduce this benchmark quantity. A detailed analysis of this optimization is presented in [83].

All those considerations assume that all the parameters are constant over the detector surface. This assumption is usually not true and the main effect of the variation of these parameters is the non-uniformity of the device gain across the sensitive surface [88]. The two main sources of non-uniformity are the variation in the GEM-hole size due to the manufacturing process and the sagging of the surface of the GEM foil subject to the electrostatic and gravitational forces acting on it.

The first type of systematic can be reduced choosing hole sizes $\approx 70\,\mu$m because the dependence of the gain with the hole size reaches a plateau for diameters lower than that [82]. To reduce the sagging effects we need to develop an appropriate support and stretching system.

5.3.1 Charges and forces on a GEM foil in a stack

The electrostatic force acting on a GEM in a detector can be estimated from first principles from the field configuration. To this end we can consider a GEM foil of surface $\boldsymbol{A}$ as a parallel plate capacitor with capacitance $\boldsymbol{C}$ and thickness $\boldsymbol{h}$, charged with a potential difference $\boldsymbol{\Delta V}$. Using Gauss law we can calculate the total charge on the foil ($\boldsymbol{Q_T}$) and separately on the drift ($\boldsymbol{Q_D}$) and induction ($\boldsymbol{Q_I}$) electrodes.

$$Q_D = E_D A\epsilon_0 - \frac{\Delta V}{h} A\epsilon_r\epsilon_0 = E_D A\epsilon_0 - C\Delta V \tag{5.11}$$

$$Q_I = E_I A\epsilon_0 + \frac{\Delta V}{h} A\epsilon_r\epsilon_0 = -E_I A\epsilon_0 + C\Delta V \tag{5.12}$$

$$Q_T = (E_D - E_I)(A\epsilon_0) \tag{5.13}$$

Where E_D and E_I are the drift and induction fields we defined previously. Using those charges we can calculate the total force on the foil ($\boldsymbol{F_T}$) as the sum of the electrostatic forces on each of the electrodes, which we will label $\boldsymbol{F_D}$ and $\boldsymbol{F_I}$:

$$F_D = (E_D A\epsilon_0 - C\Delta V)\,(E_D + \Delta V/h) \tag{5.14}$$

$$F_I = (-E_I A\epsilon_0 + C\Delta V)\,(E_I + \Delta V/h) \tag{5.15}$$

$$F_T = A\epsilon_0(E_D^2 - E_I^2) + C\Delta V(\epsilon_r^{-1} - 1)(E_D - E_I) \tag{5.16}$$

It is worth noticing that $\boldsymbol{\epsilon_r}$ is not the dielectric constant of any of the particular material used in the GEM construction but an effective quantity that can be calculated from the following relation:

$$\epsilon_r = \frac{C \cdot h}{A\epsilon_0\epsilon_r} \tag{5.17}$$

For a $0.01\,\mathrm{m}^2$ wide "Standard CERN GEM" of $\approx 4.7\,\mathrm{nF}$ capacitance, $250\,\mathrm{V}$ across its electrodes, $3\,\mathrm{kV/cm}$ induction field and $1.5\,\mathrm{kV/cm}$ drift field, a typical configuration for the anode GEM in a stack, this force amounts to $1.22 \times 10^{-1}\,\mathrm{N}$ in the drift direction. This is several times larger than the GEM weight of $\approx 2\,\mathrm{g}$, which makes the electrostatic force the dominant one in a GEM stack which causes the sagging of the foils towards each other.

5.3.2 GEM support systems

Because A GEM is typically composed of a thin polymer foil which is not by itself mechanically stable it is necessary to install each foil in a support system. The main requirements for such a system are:

- Ensure the correct and stable positioning of the foils in relation with the readout devices that lie beyond them.
- Create the necessary spacing between the amplification stages in a stack guaranteeing that each one is electrically insulated from the others.
- If the GEM foils are stretched to improve their flatness, the support structure must be able to sustain the load without relevant deformations.
- Introduce as little material and dead space as possible in the detector.

Commonly this is done through a plastic frame, usually made of *GRP*[4], glued on the outer part of a stretched foil. A description of such a system as used in the GEM detectors of the COMPASS experiment can be found in [86]. A more recent application of the same concept to a larger area system was done for the high-η muon chambers of the CMS experiment [87].

In all these cases a strong stretching of the GEM foil is necessary to achieve a sufficient flatness. A novel approach to the problem which limits the amount of stretching necessary was developed at DESY and tested on a small TPC prototype using a 100 cm^2 triple GEM stack [88]. This technique is the basis of the support system that is used for the amplification stack of the readout module described in this thesis.

[4] *Glass Reinforced Plastic*

Chapter 6

The infrastructure for TPC R&D

To complete the ILC physics program, it is necessary to develop a new generation of particle detectors that will enable the experiments to reach the performances described in Tab. 3.1. For this reason each sub-detector is undergoing a phase of development and optimization that will lead to the choice and validation of the technologies to be used. For the large TPC that will be the main tracker of the ILD experiment, this process was organized within an international scientific collaboration called *LCTPC*.

The main goal of this developments phase is to provide an answer to several questions relevant to the development of a large scale TPC detector for a lepton collider experiment:

- How to build an MPGD based readout structure that covers the whole sensitive surface of the anode end of the ILD TPC ($\mathcal{O}(10\ m^2)$) homogeneously and with as little dead area as possible?
- What is the best design for a data acquisition system capable of reading out up to about 20 channels per cm^2?
- What is the best solution to operate a TPC with such high performances in a slightly non-homogeneous magnetic field?
- What solutions can be devised to minimize the material budget of the TPC end-plate?

This chapter is dedicated to the description of the infrastructure that was put in place at DESY to answer those questions with a particular focus on the *LP-TPC*[1], the prototype TPC built to perform this R&D. The LP-TPC is part of a test beam infrastructure which is installed at the 7 GeV T24 electron beam-line of the DESY II accelerator. This infrastructure was realized in the framework of the EUDET project and became available in November 2008 and since then it was used by several institutes [70, 89].

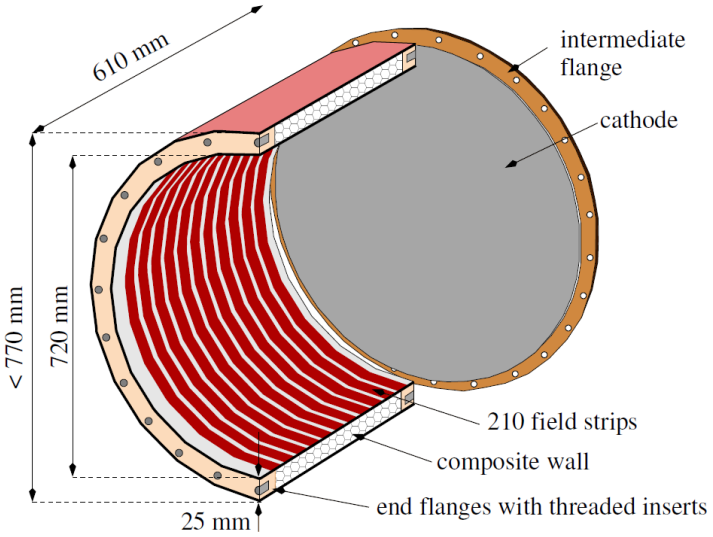

Figure 6.1: Cut-away section of the Large Prototype field cage with the mounted cathode (from [90]). The relevant dimensions of the detector are highlighted in the figure. The anode end-plate is not included and is considered as a separate component.

6.1 The Large Prototype TPC (LP-TPC)

The LP-TPC [91, 92, 90] was built in 2008 at DESY to validate the different technologies needed for the ILD TPC. The LP-TPC construction itself was a validation test for some of those technologies, namely a lightweight *field cage* built with composite material and a modular and lightweight end-plate.

The LP-TPC is made of three main components:

- A cylindrical field cage made of composite materials to limit the multiple scattering and built with high mechanical accuracy to limit the field distortions.
- An adjustable cathode with an engraved pattern that, when illuminated with UV light, will emit primary electrons used to study the field distortions in the field cage.
- An anode end-plate to house up to seven different and interchangeable readout modules.

The LP-TPC has a total length of 61 cm with a drift distance of ≈ 57 cm and an inner diameter of 72 cm, similar to the design size of the inner field cage of the ILD TPC. This size allows the LP-TPC to fit inside the PCMAG superconductive magnet (§ 6.2.2) leaving some space between the outer wall of the field cage and the inner wall of the magnet to mount an additional high resolution tracking detector, e.g. a silicon detector, as an external reference to measure the position of the incoming particles. A cross-section of the field cage including the detector dimensions can be seen in Fig. 6.1.

[1] *Large Prototype TPC*

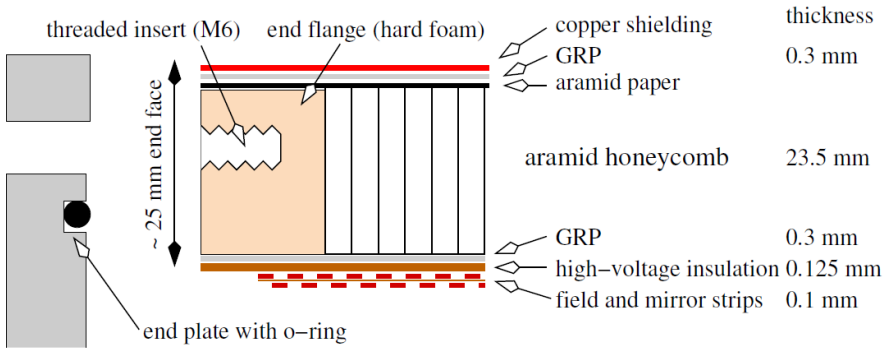

Figure 6.2: Cross-section of the Large Prototype field cage showing the different material layers composing the wall (from [90]).

Figure 6.3: Schematic cross-section of the LP-TPC resistor chain (from [90]).

6.1.1 The LP-TPC field cage and end-plates

To reduce the material budget, the LP-TPC field cage wall (Fig. 6.2) was designed as a composite structure made of an honeycomb core, reinforced by *GRP*[2]. The radiation thickness of the field cage wall was estimated to be 1.21 % of a radiation length (X_0) which is close to that required for the inner wall of the ILD TPC.

The LP-TPC was built to achieve an electric field uniformity better than $\frac{\Delta E}{E} \lesssim 10^{-4}$. The layout of the electric field shaping system is depicted in Fig. 6.3. It is made of 210 parallel copper strips, concentric to the axis of the chamber, printed on a flexible circuit board, glued on the inner side of the field cage. The copper strips are connected to one another via a chain of identical resistors. The 1^{st} and 7^{th} strip are connected to the outside via two custom high-voltage power plug. The 7^{th} strip of the field cage is aligned with the anode termination plate described later while the next-to-last field strip is aligned with the cathode and electrically connected to the same potential.

The cathode of the TPC is installed on one side of this field cage, mounted on a moving flange that allows the alignment to the anode. The cathode plate is made out of aluminium, covered with a copper layer and is electrically connected to the outside through a special high-voltage power plug. In order to help the calibration of the readout modules, the copper layer is removed in specific positions revealing the aluminium underneath. Due to the lower work function of aluminium as compared to copper, an ultraviolet light source tuned to the correct wavelength can extract electrons exclusively from the engraved pattern in the cathode. Comparing that pattern with the one detected at the anode end it is possible to

[2] *Glass Reinforced Plastic*

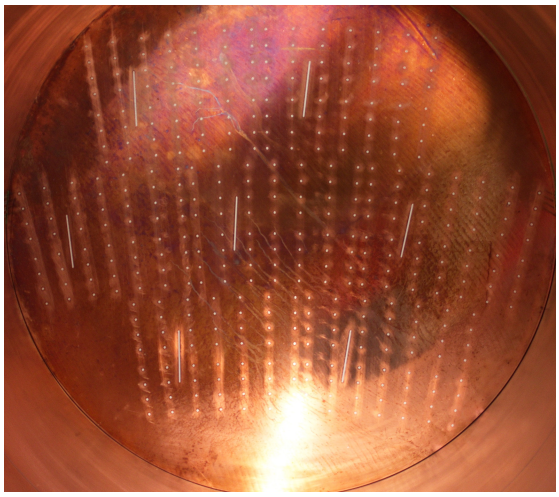

Figure 6.4: Photo of the cathode of the Large Prototype, showing the engraved pattern that, when illuminated by an UV light of the right wavelength, will emit photoelectrons that can be detected at the anode end of the TPC.

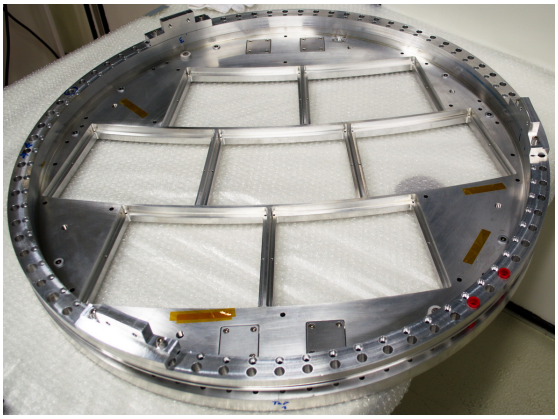

Figure 6.5: Photo of the naked aluminium structure of the anode end-plate of the LP-TPC. The 7 major holes can host a readout module each. The red pieces on the lower right of the photo are the high voltage plugs used to power the 1^{st} and 7^{th} strip of the field cage.

detect and measure the distortions in the electric and magnetic field (Fig. 6.4).

On the opposite side of the field cage, that is the anode side, the LP-TPC hosts up to 7 readout modules in a lightweight end-plate. This end-plate is composed of a circular base structure made of aluminium alloy [3], that includes seven identical cornerstone shaped holes each of which can house a readout module of similar shape (Fig. 6.5). Each module is fixed to the end-plate with a mounting bracket (Fig. 6.6) that also ensures its correct alignment with the end-plate itself. This end-plate was designed and built at Cornell University, USA, for the LCTPC collaboration.

Because the readout modules do not cover the entire circular section of the TPC several additional elements, visible in fig. 6.6 are installed on the inner surface of the anode end-plate. Those elements, collectively called *termination plate*, are connected through the end-plate to several high voltage plugs. The termination plate and the drift facing surface of each module are aligned with the 7^{th} strip of the field cage (Fig. 6.7) and, if connected to the proper potentials, define an equipotential surface.

It is relevant to notice that, because the anode equipotential surface is made of several independent components, there are small gaps, of the size of about 1 mm, between each of those. The presence of this small gaps can create relevant distortions in the electric field in proximity of the anode potential surface. Moreover the drift field quality is directly correlated with the alignment of all the components forming the anode equipotential surface.

[3] Alloy Type: 6061-T651

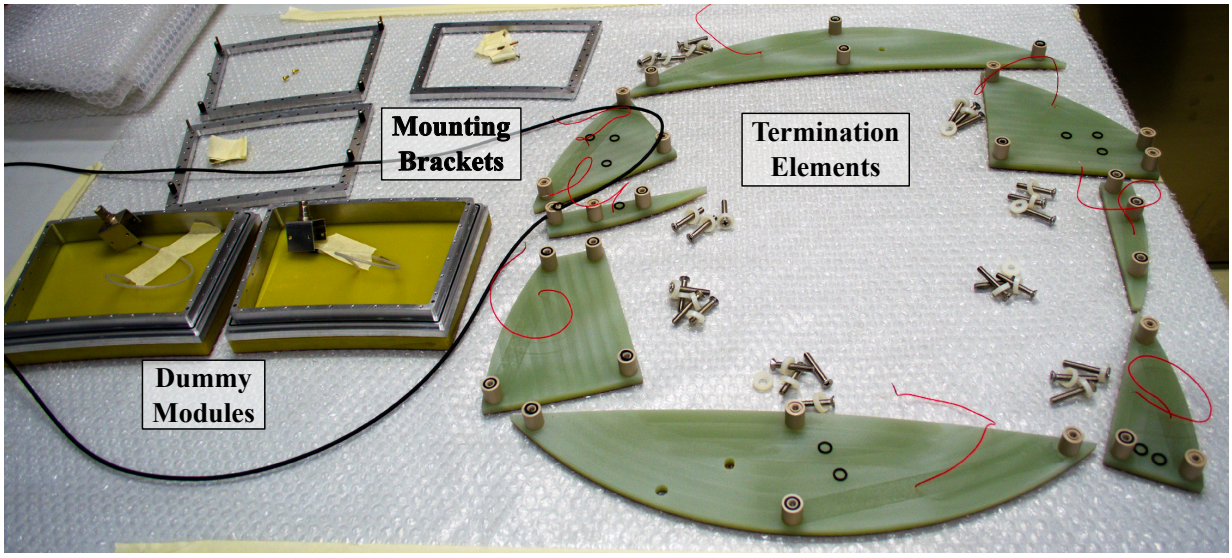

Figure 6.6: Components of the anode end-plate. On the right-hand side the different pieces of the termination plate are visible which complete the circular equipotential surface around the readout modules. On the left side two dummy modules with their mounting brackets are visible in the photo, along with the big O-ring ensuring the gas tightness of this end-plate.

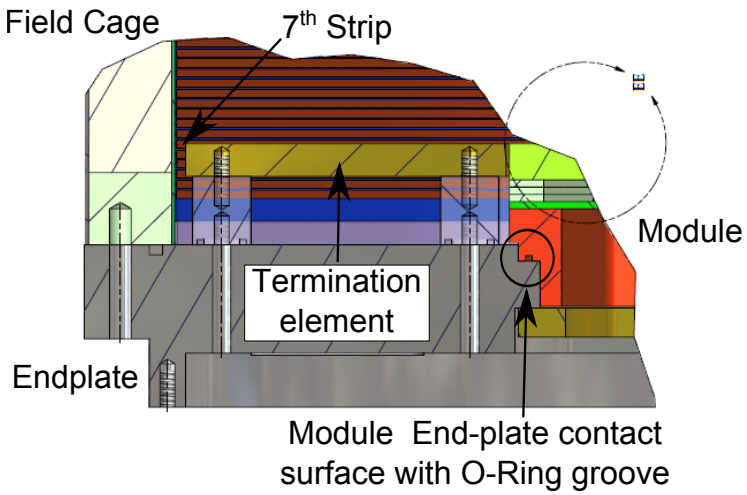

Figure 6.7: This drawing shows how the modules, and the termination plate are aligned with the seventh strip of the field cage (actually the sixth visible in this drawing) to form a single equipotential surface inside the TPC. An O-ring, placed in a groove at the interface between the module and the end-plate ensures the gas tightness of the whole system (Courtesy of Dan Peterson of Cornell University).

6.1.2 Modules for the LP-TPC

Any readout module for the LP-TPC must comply with several mechanical and functional requirements dictated by the geometry and the concept of that drift chamber and, in particular, by the design of the anode end-plate that will host the readout module:

Each module must fit Each module is allotted a well defined area on on the end-plate called *bounding box* (see page 220 for a detailed drawing). No module should exceed the allotted area to avoid colliding with those neighbouring it. On the other hand, the shape and size of the module should be as close as possible to the bounding-box to reduce the gaps between modules that will create a distortion in the electric field in the drift region of the TPC. The surface of each bounding box is $\approx 377\,\mathrm{cm}^2$.

Each module must be gas tight To ensure the gas quality of the TPC each module must be designed to avoid any gas leakage through its interface with the end-plate.

Alignment with the termination plate The drift facing surface of each module must be aligned with the termination plate and powered to that same potential to avoid introducing distortions in the drift field.

The basic type of module for the LP-TPC, designed contextually with the detector and complying with these requirements and none more is called a *dummy module* (Fig. 6.6) and is composed of an aluminium frame, called *back-frame* on top of which a thick copper-coated GRP plate is glued. The back-frame (see page 221 for the detailed drawings describing this element), ensures a gas tight fit in the LP-TPC end-plate and the mechanical stability of the system.

6.2 The DESY test–beam infrastructure

In order to use the LP-TPC with particles other than cosmic rays, the LCTPC collaboration developed a test infrastructure, installed at the T24 test-beam line of the DESY II synchrotron in Hamburg. The construction of this infrastructure was partly financed by the EUDET project [93].

The main components of this infrastructure are:

- A superconductive solenoidal magnet, called PCMAG, that can fit the LP-TPC in its bore;
- A movable stage that carries the magnet and the TPC allowing to change their position with respect to the beam;
- Two separate trigger systems: one to detect the beam activity and the other optimized for cosmic ray particles;
- A DAQ system based on the ALTRO digitizer chip and a programmable preamplifier (PCA16) (§ 6.3).

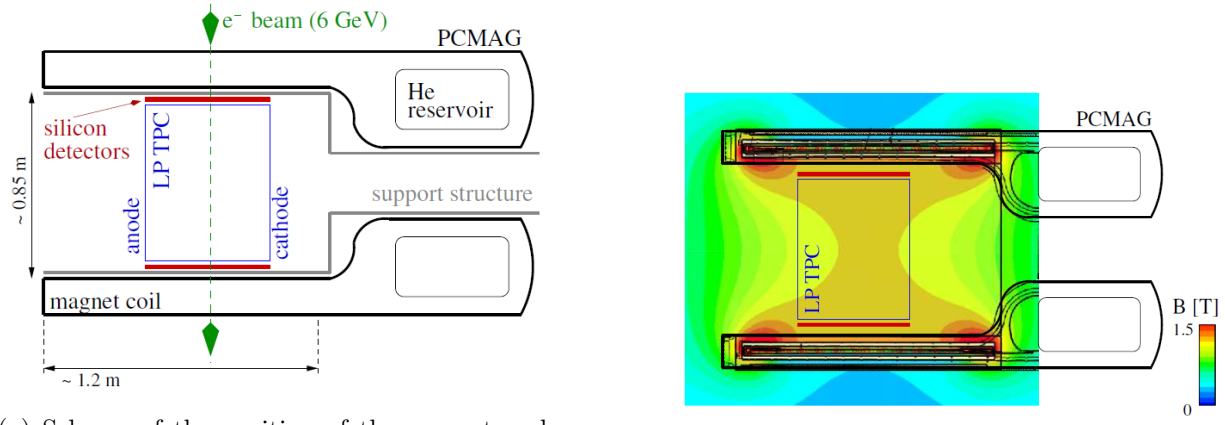

(a) Scheme of the position of the magnet and the detector relative to the beam incoming from the DESY II T24 beam line.

(b) Map of the magnetic field generated by PCMAG and the position of the LP therein.

Figure 6.8: Schematic view of Large Prototype in the DESY test-beam setup (from [90]).

6.2.1 DESY II test beam

The DESY II machine is a 7 GeV electron and positron synchrotron which can be used as a source of several particle beams used for test purposes. The beams are obtained from the conversion of a highly energetic photons into pairs of electron/positrons. A spectrometer is used on the secondary beam to select the desired energy for the experiment.

The final beam has a width of several mm and an energy spread at the collimator of $\approx 4\%$ over the nominal energy. The particle rate at the collimator also depends on the beam energy, peaking at ≈ 2.7 GeV at the T24 beam-line [94, 95]. To reach the experimental area after the first collimator, the beam has to cross an air gap of about 20 m and a second collimator further reducing the particle rate and degrading the energy spectrum. The final trigger rate in the experimental area is approximately in the range $10 - 30$ Hz, depending on the fill status of the accumulation ring.

6.2.2 The Persistent Current Magnet (PCMAG)

Even if not strictly necessary to the successful operation of a TPC, a magnetic field parallel to the electric field of the chamber considerably improves the performances of the detector. For this reason one of the most important systems of the test-beam infrastructure at DESY is the superconductive magnet called PCMAG.

This device was developed to carry instrumentation in balloon borne cosmic-ray experiments and for this reason is very lightweight and carries its own independent liquid helium reservoir that guarantees several days of continuous operation[4]. It has a usable diameter of about 85 cm, usable length of about 130 cm and can produce a magnetic field with an intensity of up to 1.25 T in its centre

[4] In 2012 the magnet was modified to work with an external cooling system which increased its reliability and eliminated the necessity of a periodic refill of liquid helium [96]

Due to its short length as compared with the diameter and the absence of a return yoke the field is homogeneous within $\approx 3\%$ of the nominal intensity only in a region of about 30 cm at the center of the magnet. The magnetic field in that region was mapped [97] and the optimal position of the LP-TPC in the magnet was established (Fig. 6.8b). Nonetheless the edge of the TPC, being as long as 61 cm will always be partially outside of the homogeneous region. This will necessarily introduce distortions in the detected signals that must be taken in account during the analysis of the data.

6.2.3 Movable stage

Many measurements, important to validate the different detector technologies, require the particle beam to pass through the TPC at different depths, positions and angles. Because the beam path through the experimental area is fixed, and the area where the magnetic field produced by PCMAG is limited, is necessary to move the entire experimental set-up with respect to the beam. This is achieved by mounting the whole magnet on a movable stage.

This movable stage has three degrees of freedom: it can move in both directions perpendicular to the beam and can rotate around the vertical axis. It can be steered remotely from the control room, external to the experimental area.

6.2.4 Trigger Systems

To trigger the electronics, the area is equipped with two separate systems: the beam and the cosmic trigger. The beam trigger is constituted by a telescope with two pairs of small scintillator slabs with a sensitive surface of $\approx 3 \times 3$ cm^2, positioned just after the second collimator along the beam line. The coincidence of the signals produced by all four scintillators produces the trigger input for the readout electronics. The cosmic trigger, on the other hand, is composed by 3 sets of scintillator tiles, placed above and below the magnet, movable to match the position of the TPC inside the magnet.

6.3 The LCTPC ALTRO based DAQ system

One of the tasks of the LCTPC collaboration is to develop a readout system for the ILD TPC that allows the detector to achieve the design performances required by the experiment [99, 100]. A first version of this system was delivered and successfully used in several experimental campaigns by the members of the collaboration to test different readout modules [70]. The system is based on a modified version of the ALICE TPC front end electronics [101].

The first processing stage is a programmable charge pre-amplifier, named PCA16 [99]. This device can be configured with different gains (12, 15, 19, and 27 mV/fC) and different shaping times (30, 60, 90 and 120 ns) for either positively or negatively polarized signals. After the amplification, the signal is transferred to the ALTRO chip where it is digitized

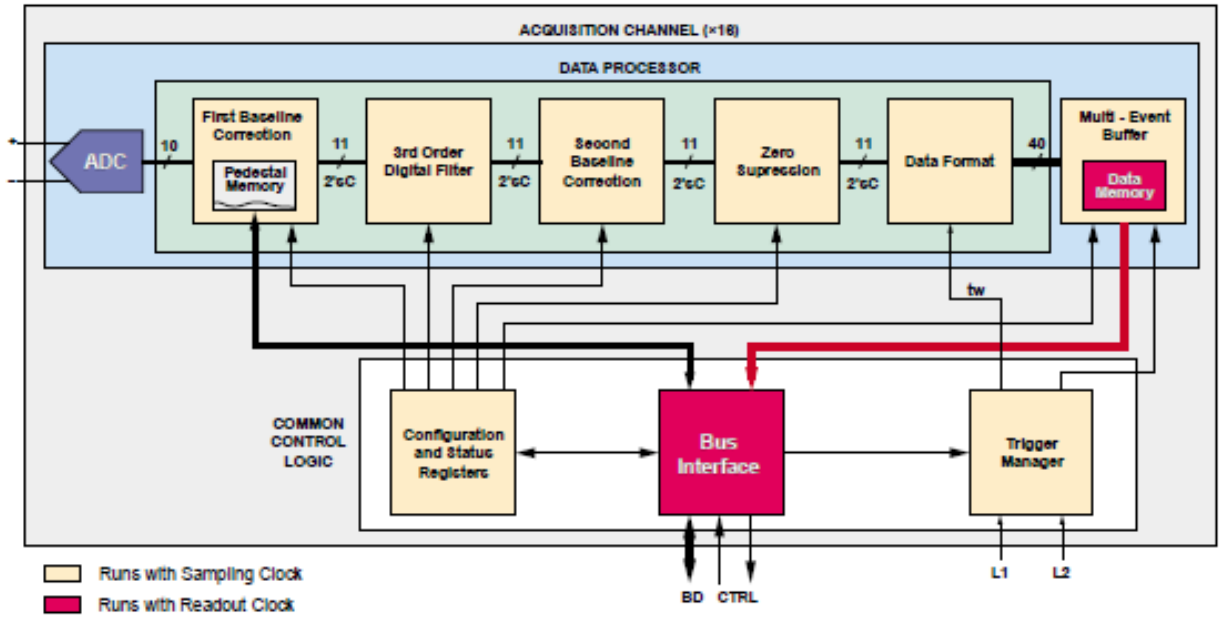

Figure 6.9: Details of the processing of the digital signals performed by the ALTRO chip for each of 16 readout channels (from [98])

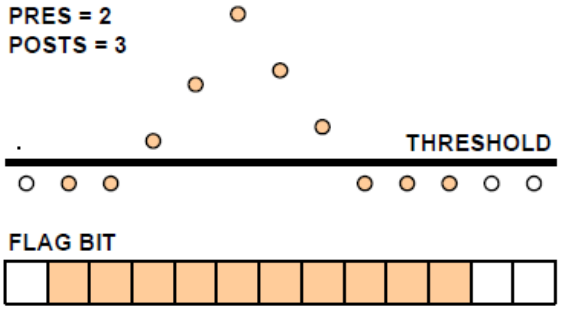

Figure 6.10: Sketch of the zero suppression processing step of the ALTRO chip (from [98]). Each digital sample is represented by a small circle and those colored are saved in the chip memory. In this case all of those over the threshold value and 2 additional samples before the first one over threshold and 3 in the tail are saved.

by a 10-bit *FADC*[5]. The digital signal is further elaborated in the same chip (Fig. 6.9), separately for each of the readout channels. The most relevant steps in this processing are the first baseline correction, also called pedestal subtraction, and the zero suppression (Fig. 6.10).

Those components are mounted on a *FEC*[6]. Each FEC can process the signals from 128 readout channels. Up to 32 of them can be connected to a single *RCU*[7], the device in charge of collecting, serialize, and transmit all the data streams to the *DAQ*[8] computer.

After the signal processing the data are placed in a memory buffer large enough to contain 16 samples. The whole data processing can be clocked at 20 or 40 MHz and is performed continuously, independently from the triggering system. When a trigger signal is received the data samples are transmitted to the output circuit during a user defined time window. Recovering the samples contained in the buffer memory it's possible to obtain up to 15 samples recorded before the arrival of the trigger signal. Further information on the ALTRO chip can be found in [98].

To link the FEC to the detector, each board has four 40-pin plug connectors (model JAE WR-40S-VFH05-N1), each carrying 32 signal lines and 8 ground lines. Those connectors are mated to their receptacle counterparts (model WR-40P-HF-HD-A1E) mounted on a flat and flexible cable. A similar receptacle is installed on the other side of this flat cable and can be connected to a compatible plug on the detector side

[5] *Fast Analog to Digital Converter*
[6] *Front End Card*
[7] *Readout Control Unit*
[8] *Data Acquisition*

Chapter 7

Design of the *GridGEM module*

The LP-TPC, that stands for Large Prototype TPC, is a lightweight detector with a modular gas amplification and readout stage with seven slots for as many independent and replaceable modules. This feature allows to develop several technologies in parallel and test them on a single test-bench. This chapter will describe the design of one of the LP-TPC modules, which uses a triple GEM amplification stack, supported by a new type of ceramic mounting system, on a pad-based readout board. This device is called *GridGEM module*.

This project was developed by the FLC-TPC group at *DESY*[1], in collaboration with the *Helmholtz Gemeinschaft*, the LCTPC collaboration, EUDET, and partly financed by the Marie-Curie Action FP7 project MC-PAD ITN.

7.1 A new module for the LP-TPC

The first step in the design of the module is the definition of the requirements the system will have to satisfy. Several constraints were imposed by the designed of the LP-TPC end-plate and those were already listed in § 6.1.2. Additionally we defined a few other functional requirements that would characterize our design:

- The TPC equipped with such modules should be able to demonstrate a point resolution better than 100 μm for drift distances up to $\approx 2m$, the length of half of the ILD TPC, in a 4 T magnetic field.
- The gain across the module surface should be uniform enough to allow the achievement of the ILD dE/dx resolution goal of the order of 5%.
- The hit detection efficiency should be higher than 90% so that more than 200 samples could be collected along a track crossing completely the barrel of the ILD TPC.
- The material budget should be reduced as much as possible to reduce the multiple scattering of particle crossing the end-cap.
- The dead area introduced by supporting material should be minimized, in particular in the radial direction, parallel to the tracks that we aim to detect.

[1] *Deutsches Elektronen Synchrotron*

- The system should be scalable so that it can be built on the semi-industrial scale required for the ILD TPC.
- A sub-detector installed in such a complex experiment like the ILD will not be easily accessible at any given time without incurring in long experimental downtimes, thus we must ensure the system can be highly reliable. In particular the discharge rate should be kept low and the device must be robust against these discharges.
- Even though an MPGD gas amplification system can significantly reduce the ion drifting back to the sensitive volume, this reduction might be insufficient for the experimental conditions and the performances we plan to reach at the ILD. For this reason the module must be designed with the possibility to add a gating stage on top of the amplification.

Many of those listed are long-term requirements for the final ILD TPC readout system. The prototype system that was developed within the scope of this thesis was aimed to start a development process towards the complete fulfilment of those requirements. In particular we intend to show that the usage of a triple-GEM stack module with an integrated ceramic support system, requiring limited foil-stretching will be a viable solution to equip the ILD TPC end-plate.

7.1.1 Gas amplification: the case for GEMs

The first requirement for the design of the *GridGEM module* implies the usage of an MPGD gas amplification technology, the only one available that can potentially reach the resolution goals set for the ILD TPC. The most mature micro pattern gas amplification technologies at that time were the Micromegas and the GEM (§ 4.4.3). From the functional point of view the most important differences between these two technologies are:

Readout board integration The Micromegas is usually integrated with the board carrying the sensitive surfaces required for the signal readout. The GEM is usually a completely independent component that can be installed on top of the readout board.

Stacking Multiple GEM foils can be stacked above one another to increase the gain and the reliability of the gas amplification system. This is not possible with Micromegas;

Charge sharing In a Micromegas, due to the very short distance between the mesh and the readout board, the amplified electron cloud cannot diffuse for more than few hundreds μm. In a GEM system, the size of the electron cloud inducing a signal can be one order of magnitude greater.

Operating voltage The operating voltage of a the drift-side electrode of a GEM-based gas amplification system is of the order of few kV. The maximum necessary voltage to operate a Micromegas system is of the order of a few hundreds Volts.

Flexibility of operation A Micromegas based amplification system has 2 relevant operational parameters that define its behaviour: the amplification gap and the mesh voltage. A multi-GEM stack can be tuned more accurately to the specific requirements through the variation of many operational parameters.

Figure 7.1: Exploded view of the *GridGEM module* module showing the different components stacked one after the other. From the right is possible to see the back-frame, followed by the PCB, 3 ceramic components spacing the first GEM of the stack. The other 2 GEM are similarly spaced by other ceramic components including a grid shaped inner element to reduce the sagging of the foils due to the electromagnetic and gravitational forces involved.

Discharges Micromegas probability for discharges in an hadron beam is of the order of 10^{-7} per particle [102] while in GEM setups, for the same gain of $\approx 10^4$ this can be lower than 10^{-12} per particle [103]. On the other hand the Micromegas are very robust against discharges and, provided the readout system is as robust, a spark will only cause a short dead time while in a GEM system a discharge could actually destroy the amplification foil. If the readout system is not robust, e.g. when is based on silicon pixels, a Micromegas discharge can reach the sensitive parts and damage them. This probability is much lower in a GEM system.

In general a GEM system is more difficult to optimize and operate due to the large parameter space available for its configuration but the same feature makes it more versatile so that is possible to choose the best compromise between performance benchmarks like gain, ion back-drift, charge spreading on the readout system, energy resolution and more.

Moreover, because the gas amplification is decoupled from the specific readout system in use, it is possible that a solution not yet mature like a pixel readout system can be integrated in a GEM-based device developed for a simpler pad readout [70]. The versatility of a GEM system even allows to use part of the amplification stack as an active gating device to further reduce the amount of ions drifting back in the drift volume.

Even though discharges can be potentially dangerous for a GEM setup, the lengthy and unfailing operation of a system like that used in the COMPASS experiment [86] demonstrated the reliability of the technology.

For these reasons we believe that GEM-based gas amplification system is a very promising technology for the development of an ILD-sized TPC detector and it's the one chosen for the *GridGEM module*.

7.1.2 *GridGEM module* overview

the *GridGEM module* consists of several components, listed from the outside of the detector towards the drift volume and represented in fig. 7.1):

- An aluminum support, called back-frame, providing a gas tight fit of the module in the LP-TPC anode end-plate, a mechanically stable platform above which to build the rest of the module and the means to align the detector to the end-plate and thus to the rest of the experimental setup;
- A *PCB*[2], with one side segmented in pads as small as 1.26×5.85 mm^2. Each of these pad is routed through the board to a connector compatible with the ALTRO based DAQ system (§ 6.3). This board is glued on one side of the back-frame;
- A stack of up to 4 GEM used as gas amplifiers and/or gate devices, each of them mounted in a ceramic support structure that stiffens and keeps the GEM foils stretched and flat and provides the spacing between the different GEMs in the stack.

The advantages of a multi-stage amplification system were already described in §5.3. The main reason why we choose to have as many as 4 stages is to be able to test a single- or double-stage GEM gating. This system was not developed for this first prototype described in this thesis but the modularity of the *GridGEM module* and the versatility of the GEM technology will make it possible to easily implement it after the basic functionalities of the *GridGEM module* are well understood. Without a gate the *GridGEM module* will use a triple-GEM amplification stack which allows the required charge sharing, high gain and reliability.

7.1.3 A note about naming

It is common in the literature to label the stages of a GEM stack with a number sequentially increasing, starting with the drift side stage. The personal opinion of the writer is that this type of numbering can sometimes lead to misunderstandings, thus I decided to label the GEM stages differently.

Throughout this work the GEM in the stack closest to the readout board will be named *Anode GEM* (**GA**). The middle stage in a triple-GEM stack will be named *Middle GEM* (**GM**). Finally the GEM foil facing the drift volume is called *Drift GEM* (**GD**). If an optional gating GEM is installed above the *Drift GEM* this is called *Gating GEM* (**GG**).

When referring to a specific electrode of a GEM foil in the stack this label is suffixed with an **A** for the anode or with an **C** for the cathode.

In §6.1.2 we introduced the concept of *Bounding Box* as the total surface ideally available for each module: this area has the shape of a cornerstone (see page 220). Describing any component of that shape, unless otherwise stated, we will always refer to the arc with the greater radius as the upper arc and the one with the lesser radius as the lower arc of the component while any straight line parallel to the radius of the cornerstone will be referred as the radial part of the component.

[2] *Printed Circuit Board*

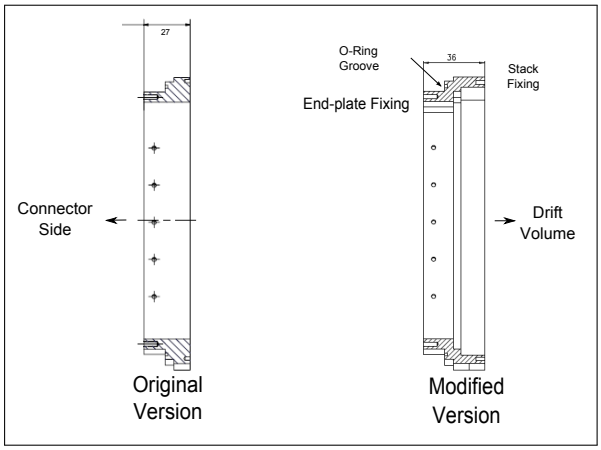

Figure 7.2: Comparison of the original design of the back-frame used for the dummy modules of the LP-TPC with the modified version used for the *GridGEM module*. Some material was removed from the drift side of the back-frame, where the readout PCB is going to be glued, thus increasing the space available for the electronics component to be mounted on the connector side of that board

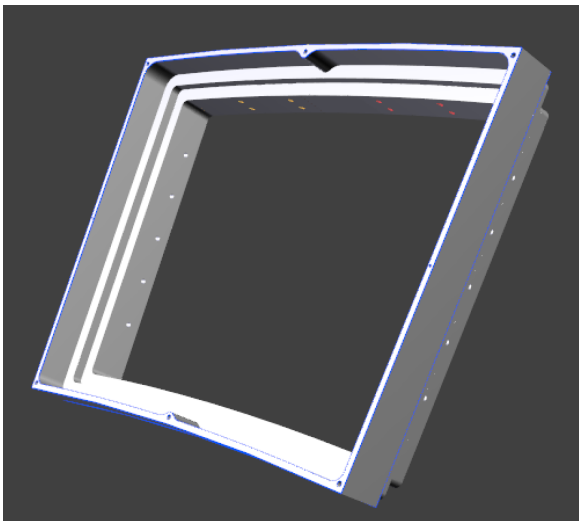

Figure 7.3: 3-dimensional rendering of the *GridGEM module* back-frame as seen from the drift side. It can be noted the presence of the 6 screw-holes on the corners and in the middle of the two arcs and the 2 small dowel holes in the middle of the side walls.

7.2 Modules back-frames

To ensure a gas tight fit and the mechanical stability of a LP-TPC module, the active part of the device must be installed on an aluminium structure, commonly called a back-frame (§ 6.1.2). A standard design for this element was available and used for the dummy modules. The actual back-frame used for the *GridGEM module* is derived from that model (a detailed drawing is included at page 222). The main difference can be appreciated in fig. 7.2. Considering that the readout PCB is glued on the drift side of the back-frame, its new design *increases the space available on the connector side of the board*.

Furthermore the modified back-frame includes, on the drift side, six screw-holes, to fix the whole detector stack, and two 1 mm dowel-holes to align the readout board to the back-frame. The back-frame is, in turn, aligned to the LP-TPC end-plate through a set of dowel holes on the connector side. To fix the back-frame to the LP-TPC end-plate and apply an uniform pressure on the sealing O-Ring, on the connector side there are 30 screw holes. A 3-dimensional rendering showing the drift side of the improved back-frame is visible in fig. 7.3.

7.3 The design of the GEM foils

In recent years a thorough study was performed in the FLC group at DESY to evaluate and compare GEM foils with different layouts geometrical characteristics and produced by different manufacturers [104, 88]. As a result of this studies we decided to choose CERN as

provider for our foils. In fact, not only the quality of a CERN GEM is measurably higher but, due to strong collaborative connections, they usually provide a prompt feedback and advice, useful in designing custom products and prototypes.

The CERN GEMs are produced by chemical etching on a 50 μm thick Apical polyimide film[3] coated with a 5 μm thick copper layer. The CERN workshop can provide GEM foils with a custom shape [105] and with user defined geometrical parameters. For the *GridGEM module* we decided to use the "Standard CERN GEM" configuration, described in § 5.2, due to demonstrated quality and reliability of the design.

As mentioned in [105] the CERN workshop has, by now, developed a very promising single mask etching technique to produce GEMs. When inquired about it, the CERN workshop replied that for the GEM size to be used in the *GridGEM module* it was more efficient and economic to resort to the standard double mask technique, thus all the GEM foils used for our system were manufactured using a traditional double-mask technique.

7.3.1 GEM sectioning

The total available surface for each module, as defined by the *Bounding Box* (see page 220), amounts to 377, 00 cm^2. This number defines the upper limit for the sensitive surface of any module for the LP-TPC.

The first feature to define in the design of a new GEM amplification system is the segmentation of the GEM electrodes necessary to achieve the desired reliability. As we noted in § 5.2.2 the capacitance of each foil should not be higher than $\approx$ 5 nF, corresponding to that of a 100 cm^2 "Standard CERN GEM". Considering the available surface is about four times as big as that we decided to segment our foil in 4 electrically independent electrodes.

To simplify the layout, reducing the number of independent HV lines to route only, one of the two sides of the GEM foil is segmented while the other is kept whole. This solution is successfully used in many other detector systems pioneered by the COMPASS experiment [86], where a similar layout is working reliably since several years.

Therefore, this layout requires 5 independent HV power channel for each GEM foil. To produce a module with 4 stages it is necessary to provide an high voltage power distribution system with 20 independent lines capable of standing up to about 4 KV. Each of these power line must be routed through the PCB to a different position in the outer region of the sensitive area with a sufficient clearance from the read-out pads and from the other power lines. The definition of the layout of the power lines of the GEM foils was driven by the following considerations:

- To minimize the dead area parallel to the direction of the tracks (§4.5), the two sides of the module should not be used.
- To further reduce the dead areas introduced by the HV lines, only the top or bottom edge of the sensitive area should be used so that in only one of the two areas it will

[3] http://www.kaneka.com/kaneka-americas/products/apical

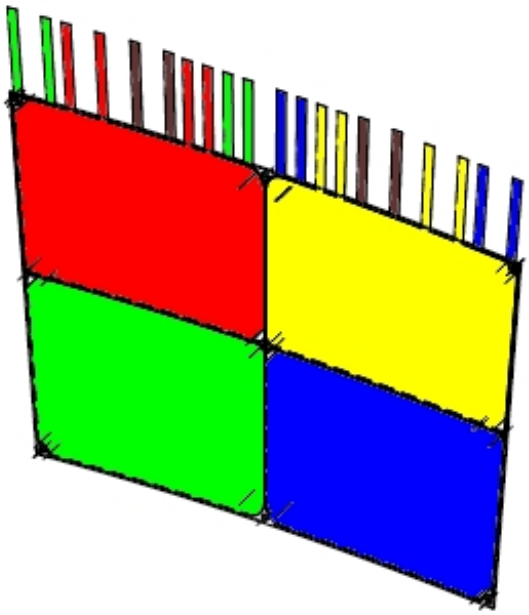

Figure 7.4: Sketch of the layout of the sectioned side of the GEM showing in different colour each sector and the group of electrodes connected to that sector. The 4 black electrodes are those connected to the back side of the GEM.

be necessary to clear enough room to avoid discharges between the power lines and the readout pads.

- Additionally, to avoid discharges between adjacent modules without increasing the gap between them, the electrodes of one module should not face those of another.

Considering the greater length of the top arc we decided to place all the power electrodes in that area. Because the biggest fix cost in the production of a new GEM is the creation of a photo-lithographic mask to be used during the etching process, we decided to place all the 20 possible electrodes on each foil. At assembly time the unnecessary electrodes will be severed. Additionally, prior to the final assembly, each GEM can be assigned to equip any position in the stack.

To be able to test the effect of both radial and transversal gaps on the detector efficiency, we chose to section each GEM foil as shown in fig. 7.4. A detailed drawing of both sides of the foil can also be found in the appendix in page 227.

Because all the electrodes are positioned on the top arc but 2 of the 4 sectors are not adjacent to that area, a set of copper tracks is routed through the radial gaps in the middle and at the edges to connect those two sectors to their respective electrodes.

The actual positioning of the electrodes, which are not uniformly distributed along the edge, was established taking in account the likely potential difference between each electrode and its neighbour. For example, starting from the left side, the 2^{nd} and the 3^{rd} electrode are positioned quite close to each other because they will connect 2 different sectors on the same stack layer, which are powered to the same potential

7.4 Ceramic support structure (S^3 System)

The most common system to provide a support system for a GEM foil in an amplification stack is to have a wide and thin GRP external frame glued to the stretched foil and to pile several of this assemblies using the frame themselves or some additional component to space the amplifying elements. If the sensitive area is too big, it is common to add some material in the sensitive area supporting the foil, to reduce the sagging of the foils and increase the gain uniformity [86].

In the current design of the LP-TPC end-plate, the whole surface of each module is part of the ideal sensitive area and the common solution of a wide frame in the outer regions of the module will actually introduce a sizeable dead area. For example, a 7 mm wide rim like the one used for the COMPASS experiment will introduce a 14% dead area in the sensitive volume. To reduce this dead area one solution is to use a different material, stronger than the GRP, which will make it possible to build a similar system of smaller size.

Considering a straight, homogeneous beam, with a rectangular cross section under an uniform load perpendicular to the beam axis, the maximum deflection compared to the unloaded configuration can be evaluated through eq. 7.1

$$w_{\frac{l}{2}} = \frac{5}{32}\frac{ql^4}{Ehb^3} \tag{7.1}$$

where $\boldsymbol{l}$ is the length of the beam, $\boldsymbol{h}$ the thickness of the beam, $\boldsymbol{b}$ is its width parallel to the applied load $\boldsymbol{q}$ and $\boldsymbol{E}$ is the Young Modulus of the material. This means that, to obtain the same deformation and assuming the same thickness and length of the beam, its width scales as the inverse of the cubic root of E.

Additionally, to be suitable for a GEM support system, any material must be insulating to avoid short circuiting the electrodes of the foil, with a high dielectric strength to avoid any electrical breakdown, and should not outgas any chemical that can reduce the lifetime and performances of the chamber. Because the element is going to be used in a tracking detector, where the material budget is important, it is also preferable to use materials with high radiation length.

An ideal candidate which fulfils all the requirements is the ceramic which is among the strongest industrial materials, as can be seen in the plot of fig. 7.5. In particular, when compared to commonly used composite materials (tab. 7.1), we observe that ceramic can be more than an order of magnitude stiffer than the GRP. Using the scaling law we mentioned earlier we can estimate that a ceramic element can be almost 3 times smaller than a similar one made from a composite material.

In addition, any fibre reinforced material, has inhomogeneous mechanical properties with much greater strength in the direction of the fibre. The presence of fibres extruding out of the epoxy matrix can also introduce local effect which can be avoided only by a careful processing of the material. Both these problems are not present in a ceramic compound.

Therefore we developed a new type of support system for GEM based TPC readout

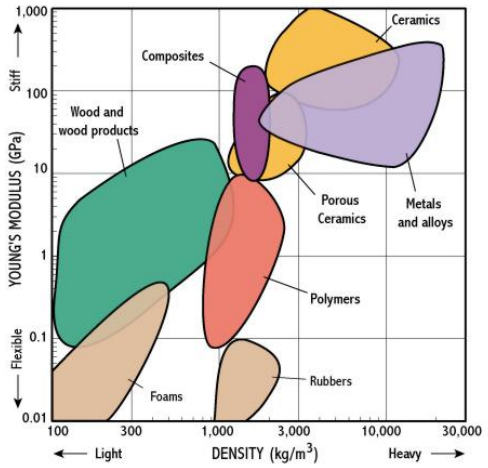

Figure 7.5: Material selection chart showing the correlation between Young's modulus and density for several material classes (from http://www-materials.eng.cam.ac.uk/mpsite/physics/introduction)

	G10 (BASF Ultradur B4040)	**Alumina 96% (CeramTec Rubalit 708 S)**	**Alumina 99.6% (CeramTec Rubalit 710)**
Dielectric Strength (kV/mm)	≈ 30	> 20	> 20
Resistivity ($\Omega \cdot$ cm)	$> 10^{13}$	$> 10^{13}$	$> 10^{13}$
Young's Modulus (GPa)	16.5	340	350
Radiation Length (cm)	≈ 13.3	≈ 7.4	≈ 7.2

Table 7.1: Comparison of the relevant properties of several materials usable for the construction of a GEM support system. In parentheses, alongside the common name, we listed the commercial name of a material of that type.

systems, called the S^3 system[4]. This system is built around a very thin ceramic frame which supports the GEM weight and the electrostatic forces between the foils, relieving also the tension of a limited stretching of the foils. Those ceramic components additionally act as spacer between the different GEM foils removing the need of any additional device.

7.4.1 The design of the S^3 system

The optimal solution to reduce to a minimum the dead areas in the direction parallel to the radius of the TPC will be the complete elimination of any element in the supporting system not concentric with the bounding arcs of the module. This would imply leaving

[4] S^3 stands for: Supporting, Spacing and Stretching

the two sides of the GEM unsupported and stretching the foils only when assembling them on their readout board. This would, in turn, make it difficult to control the GEM flatness and considerably increase the complexity of the system which should include a stretching device integrated in the readout board. As one of our requirements is to develop a module that can be produced reliably and consistently in large numbers we decided not to pursue this possibility.

The next best solution is to use a frame as thin as possible all around the GEM, supporting it from all sides. This basic structural component is named *Simple Frame* and a detailed technical drawing is available on page 223. This component has a total surface in the sensitive plane of $\approx 7.8\,\mathrm{cm}^2$ corresponding to $\approx 2\%$ of the available space, which can be compared to the 14% we previously calculated for a traditional GRP frame.

To further reduce the required tension we can introduce some element in the inner region of the module, supporting the foil in that area which is a strategy pursued by many other experiments that use a traditional GRP frame. The cost to pay is an increased amount of material and dead areas in the sensitive volume. Such a components with an internal ceramic pattern is named *Supporting Frame* and can be further distinguished by the design of the internal elements.

A relevant way to minimize the dead areas of the readout system is to match those introduced by the necessary sectioning of the GEM foil with those due to the design of the S^3 system. For this reason the internal elements of the *Supporting Frames* must be carefully aligned with the sectioning gaps of the foils. Because the GEM foil of the *GridGEM module* is divided in 4 sectors, any *Supporting Frame* should not divide the sensitive volume in more than 4 parts.

To reduce the negative effects introduced by the presence of this additional material we can choose the configuration of the internal supporting elements to avoid those perpendicular to the module arcs. We called this the *4-arcs design* which is available as a detailed drawing at page 224. The total surface of this element is $\approx 16\,\mathrm{cm}^2$ corresponding to $\approx 4.2\%$ of the available surface.

Another one that is compatible with the 4 partition constraint is shown in a detailed drawing at page 225 and is called the *Grid Design*. It has a total surface in the sensitive plane of $\approx 11.7\,\mathrm{cm}^2$, corresponding to $\approx 3.1\%$ of the total sensitive surface. This design, albeit not optimal to reduce the dead spaces in the radial direction, allows to test all the component of the system and evaluate the effect of the radial elements on the module performances and is more robust and easy to manufacture than the optimal one and was therefore chosen for the initial prototype of the *GridGEM module*.

To align the GEM stack with the readout board and the back-frame we included two, 1.0 mm wide holes in the middle of the side of the frame. To fix the whole stack to the back-frame without using any glue, 6 holes are placed on the 4 corners and in the middle of each of the arcs.

Additionally, the S^3 system is to provide electrical insulation between the grounded readout pads and the high potential power pads. Without any insulation, in an Argon based gas like those used in our detector, to avoid discharges from an high voltage pad powered to about 3 kV to the a ground pad one would need a clearance of $\approx 1\,\mathrm{cm}$ that would

introduce a dead area of the order of 10% of the available sensitive surface. Interposing one ceramic element will reduce the clearance to that strictly necessary for the positioning of the element itself which is ≈ 1 mm. For this solution to be effective, the ceramic must be perfectly glued on the readout board between the high voltage and readout pads.

7.4.2 Production and assembly

The most common technique to produce complex micro-structures in a thin ceramic plate is to cut away the unwanted material with a powerful laser out of a mother-plate of the desired thickness [106]. Unfortunately this procedure can introduce strong thermal shocks in the materials that can crack during the process.

The probability of this occurrence is correlated to the internal stresses of the original plate and the amount of material the heat can disperse into. One thing which is particularly difficult is to create structures where the aspect ratio between the thickness and the width of an element is lower than 1 : 1, e.g. to create arcs thinner than 1 mm in a 1 mm thick plate. The risk also increases with the length of the element to produce so, after some trial performed by a specialized company we decided to produce our ceramic frames with an element width of 1.4 mm in a 1 mm thick plate. In fact, the final decision to increase the element width to 1.4 mm, after some unsuccessful attempts with 1 mm wide elements, was taken after the GEM foils were produced. Therefore the width of the GEM gaps, that is 1 mm, is slightly smaller than of the matching frame elements.

Other possibilities to produce ceramic structures of complex shape is the sintering of the piece directly in its final form using a mould or a fast prototyping machine. Neither of these techniques were further explored during the development to verify their usability because this knowledge was not acquired until later in the development phase.

To ensure the best mechanical properties, all the internal elements of the *Supporting Frames* must be glued to the GEM. If the ceramic is well aligned with the sections gaps, the glue application would not damage the foils or reduce the detector performances, assuming that one can avoid any overflow from reaching the sensitive region. On the other hand is important to reduce to a bare minimum the distance between the first set of amplifying holes and the ceramic to reduce the dead areas caused by the section gaps. We choose this distance not to exceed 0.3 mm which requires a very good control of the flow of the glue to avoid an excessive deposition leading to dangerous overflows.

The most common ceramic available on the market is made of Aluminum Oxide (Al_2O_3) and called Alumina. There are many production grades of this material, with the main distinction being the concentration of Aluminium oxide in the mixture. In tab. 7.1 we listed two of such materials: the Rubalit 708 S[5] with 96 % of Alumina and the Rubalit 710 with 99.6 % of Alumina. With similar electrical properties, the Rubalit 710 is only marginally stronger but much more expensive to purchase thus we decided to use the former as base material for the development of the module prototypes.

[5] http://www.ceramtec.com/

7.5 Pad readout board

The last important component of the *GridGEM module* is the readout board. It has 2 important functions: it must route the high voltage power to the GEM foils and include the sensitive surfaces on which the signals are induced. In our module, those sensitive surfaces are thin pads, laid out in 28 rows, concentric to the boundary arcs of the module. Each of those pads is electrically coupled to a pin of a connector placed on the external part of the board which can be connected to an external DAQ system like the one described in §6.3.

The readout board was designed in collaboration with Jochen Kaminski of the University of Bonn as a contribution to the LCTPC and *Helmholtz Gemeinschaft*. This device is an 8 layer PCB with blind vias connecting the outermost layers of the stack to the inner core to avoid any gas leakage. The layer of the PCB containing the readout pads and in direct contact with the drift volume is called *Pad Layer* while the one on the opposite side housing external connector is called the *Connector Layer*. All those in between are called *Mid Layers* and numbered from 1 to 6 starting from that adjacent to the *Pad Layer*

7.5.1 The power distribution scheme

For the reasons described in §7.3.1, the GEM foils are powered through 20 electrodes laid out on the top arc of the sensitive area (Fig. 7.4). The main challenges to address when designing such a system are:

- Define a radial clearance small enough to reduce the dead spaces but sufficient to avoid discharges.
- Insulate the power connection from the grounded areas and the readout pads to avoid discharges.
- Route the power lines in such a way through the board as to avoid discharges between them.
- Have a protection resistor for each of those power lines.
- Provide a safe and simple connection of the high voltage distribution in the board to a standard power supply.

The sketch in fig. 7.6 shows the solution that we devised to solve this problem. To reduce the space necessary for this connection the ideal solution is to solder the 4 mm wide GEM electrode to the board perpendicularly but this solution would be mechanically very unstable. For this reason we designed a 2 mm deep slot as large as the electrode and 1 mm wide[6], going from the *Pad Layer* to the *Mid Layer 6*, which is the last before the *Connector Layer*. The walls of this slot and its floor are completely metallized and connected to the

[6]Due to a design change in the slot width from 0.7 mm to 1.0 mm required by the manufacturing company when all the other components of the module were completed, the ceramic component slightly overhang on the slot. If the gluing is performed according to a standard procedure we established, this issue do not cause performance problems.

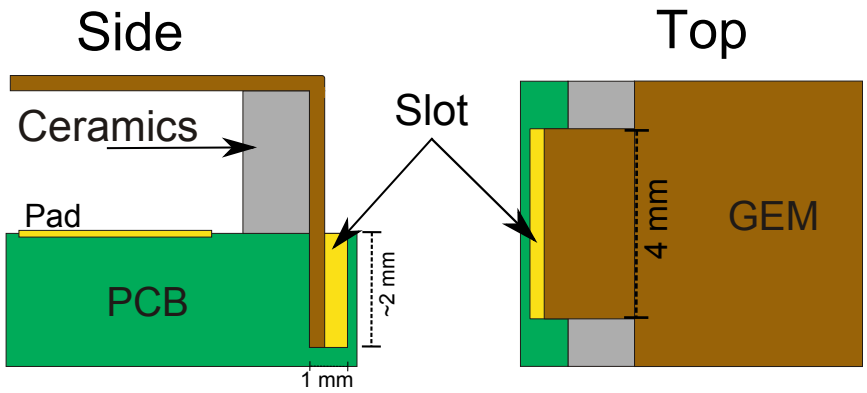

Figure 7.6: Scheme of the connections between the GEM electrode and the PCB power line. The GEM electrodes, in brown is inserted in a slot of the PCB that is filled with solder to fix the connection. To reduce the necessary clearance between the high voltage connection and the sensitive (grounded) pads, the ceramic frame is interposed.

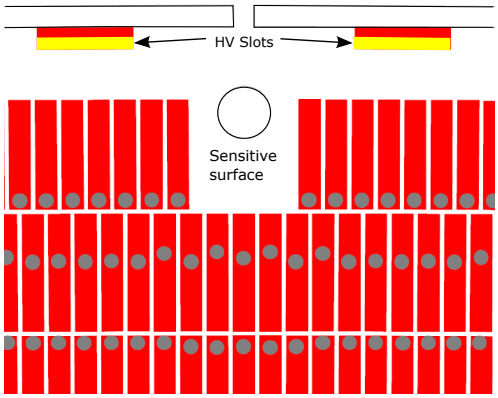

Figure 7.7: Drawing of the central area of the top border of the readout board. It shows the HV slots separated from the readout pad by a gap large enough to fit a ceramic component. It is also visible, in the center of the sketch, the through hole used to fix the S^3 system to the back–frame.

remainder of the power distribution system. In this way the GEM electrode can be fit inside the slot and fixed with enough solder as to fill completely the slot. This solution demonstrated its validity and reliability during 2 years when none of those connection failed even after repeated replacement of the GEM connected to a given slot.

Because the grid is also used as insulator between the high voltage connections and the sensitive area to avoid discharges, the necessary gap between the high voltage slots and the last of the sensitive pad rows can be limited to the width of the ceramics elements (see fig. 7.7 and 7.9 for details). To obtain a good insulation, it is very important to carefully and reliably glue the top arc of the first ceramic component of the S^3 system on the readout board. For production reason the minimal distance between the power slot and the border of the board is limited to 0.6 mm which makes the total distance between the edge of the readout board and the first of the sensitive rows 3.5 mm.

To power the whole stack, in case of a complete 4 GEM stack, one needs to provide a total of 8 voltage levels, 2 for each GEM. For each of these 8 voltage levels the board provides a separate distribution network. The terminations of this network on the con-

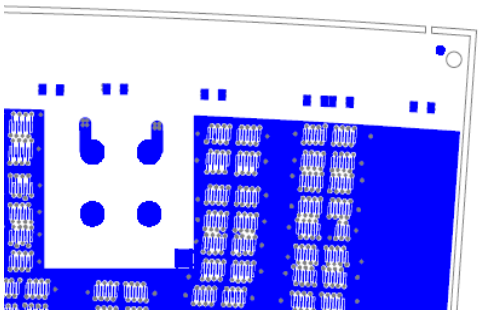

Figure 7.8: Drawing of one of the corners of the connector side of the readout board. The 4 large round pads are the end of 4 of the 8 high voltage distribution networks. The small square pads in that region are the designated areas for the installation of the protection SMD resistors.

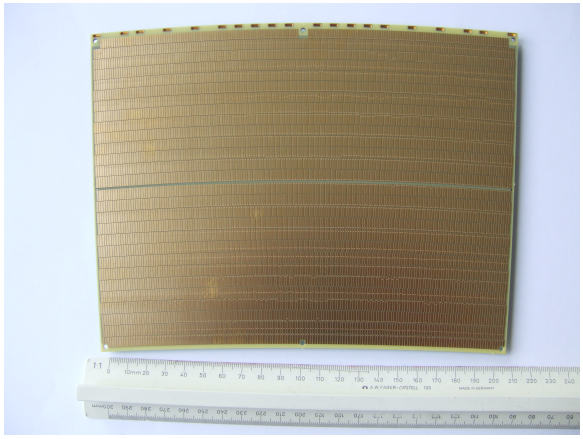

Figure 7.9: Photo of the *Pad Side* of the readout board of the *GridGEM module*.

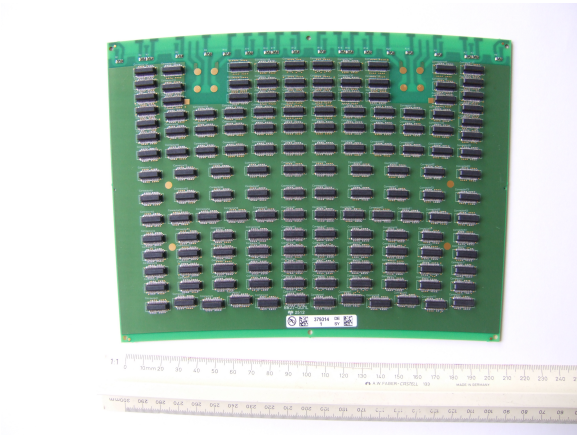

Figure 7.10: Photo of the *Connector Side* of the readout board of the *GridGEM module*.

nector side of the board are grouped in two areas matching the size of the quadrupolar high voltage connector chosen to connect the board to an external power supply[7]. Those connectors are rated to stand up to 7.5 kV DC and are relatively small with a maximum diameter not exceeding 20 mm, allowing to considerably reduce the amount of space on the connector side of the board dedicated to the high voltage distribution (fig. 7.8 and 7.10).

To decouple each GEM sector from each other and from any external capacitive load the board integrates a protection resistor. The 20 resistors necessary are *SMD*[8] components in the 1206 form factor and are positioned on the top region of the connector side of the board. This solution allows to save space on the central part of the board to install all the necessary connectors interfacing the readout pads with the external electronics system.

7.5.2 The sensitive area and electronics connections

To ensure an accurate reconstruction of the position of the amplified electron cloud the sensitive area is segmented in thin pads. In the case of the *GridGEM module* we want to develop a system that could achieve a point resolution better than 100 μm in a 4 T magnetic

[7] Fischer, model D104 Z062

[8] *Surface mounted device*

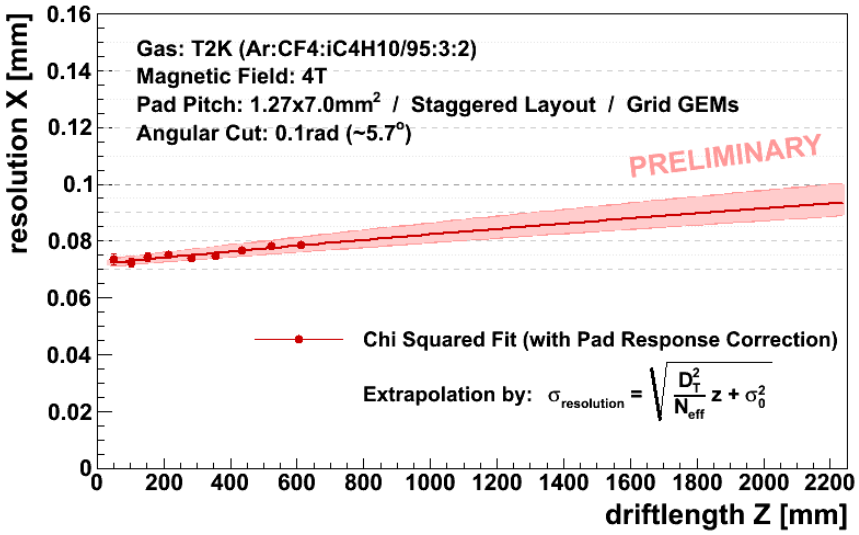

Figure 7.11: Point resolution of a GEM based medium size prototype in a 4T magnetic field. The resolution beyond ≈ 600 mm could not be measured directly due to the limited length of the detector and is estimated using the formula visible in the lower right corner.
To be published, courtesy of Ralf Diener.

field. In the previous years a set of measurements was performed at DESY with a medium sized prototype, called *MediTPC*, using a GEM amplification system and a magnet capable of reaching a magnetic field intensity of 4 T. Those measurements were performed using a staggered rectangular pad layout and showed that with a pad pitch of 1.27 mm, the point resolution can be lower than 100 μm for the entire drift length foreseen for the ILD TPC (fig. 7.11).

This result led us to choose a pad width similar to that used for that study. While a smaller pitch can potentially further improve the resolution it will decrease the amount of charge collected by each pad, thus increasing the significance of the electronic noise, and would increase the pad density which will make the routing of the electronic signals through the board more complicated. Because the shape of the sensitive area is that of a cornerstone, the readout pads have a similar shape with the top side slightly wider than the lower one.

Another important feature to be established that will influence the behaviour of the detector is the staggering of the different rows. For a cornerstone shaped sensitive area, a non-staggered layout implies a different pad size for each of the module rows which will make the induced response of the pad to the incoming charge different for every row. On the other hand a constant pad size implies necessarily a staggering but its amount (S) is constrained by the ratio of the difference between the inner and outer arc length of a row

and the pad pitch(P):

$$S = \frac{(R_{\mathrm{Out}} - R_{\mathrm{In}}) \cdot \theta}{P} \tag{7.2}$$

where θ is the angular length of an arc on the sensitive surface. Inverting this equation is possible to calculate the optimal row pitch for a given pad pitch and staggering ratio. Considering that the ILD TPC design goal is to have more than 200 samples for tracks crossing the whole barrel region[59] and that the ILD TPC end-plate can host 8 rows of modules similar to the *GridGEM module*, each of them should have at least 25 pad rows, possibly more to allow for some unavoidable inefficiency.

Given those data, we designed the pad layout of the readout board of the *GridGEM module* with the following features:

Pad Pitch (min-max) $1.26 - 1.265\,\mathrm{mm}$
Row Pitch $5.85\,\mathrm{mm}$
Number of rows 28
Staggering 0.66, 2 pads every 3 rows
Number of pads 4827

Additionally the gap between the 14^{th} and 15^{th} was enlarged to match the size and position of the central arc of the *Supporting Frames* of the S^3 system. To simplify the routing the board, is symmetric relative to the central meridian.

Excluding those areas dedicated to the HV connectors and the protection resistors necessary for the power distribution system, the remaining surface of the connector side of the board is occupied by 152 connectors (type JAE WR-40S-VFH05-N1, see page **??** for a detailed drawing), which allows the module to be connected to the ALTRO DAQ system (§ 6.3).

To reduce the noise picked up by the electric tracks linking the readout pads with the electronics connectors, those were kept as short as possible placing the connector almost exactly on the opposite side of the group of pads it is connected to. This is impossible at the edge of the module, where the presence of the back-frame does not allow the placement of these connectors and is particularly difficult on the top arc where the HV connectors occupy some of the available space. In these area the connectors are more tightly packed than elsewhere.

To further reduce the noise that could be picked up by the electric lines, all the surface not occupied by a via or a signal track in every layer of the board is occupied by a conductive surface connected to the ground potential which is also connected to the ground pins of the signal and HV connectors. In fact the *Mid Layer 1* and *Mid Layer 6*, which are those inner layers closer to the exterior of the board, are essentially large ground planes protecting the long signal lines in the other inner layers from crosstalk and noise. This configuration, assuming all the other devices are properly connected should avoid the presence of ground loops in the systems.

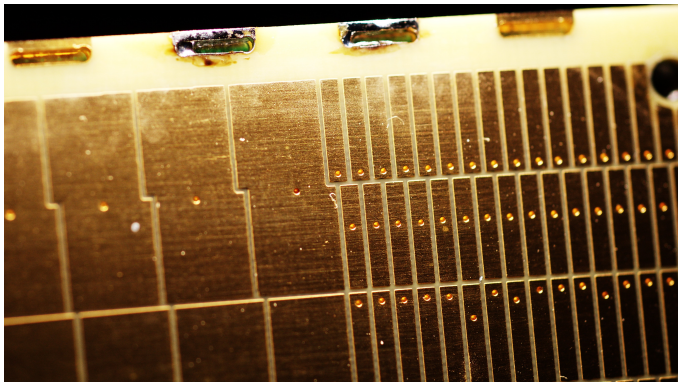

Figure 7.12: Photo of the upper central region of the pad side of the simplified board where it is possible to see the nominal size pad surrounded by the enlarged ones.

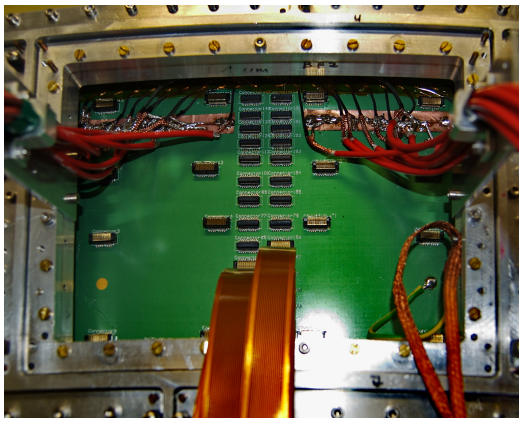

Figure 7.13: Back side of the simplified board showing the reduced connector occupancy and the ad-hoc high voltage connections.

7.5.3 The simplified pad board

The design and production of the board described in the previous section was lengthy and complex. To validate some of the design solutions, namely the system to connect the GEM foils to the power distribution system (§ 7.5.1) and the internal signal routing, and to test the installation procedure and prepare a working module in time for the test-beam campaign we planned for Summer 2011, we decided to initially produce a simplified version of the readout board.

In this simplified board only 31 or 32 pads in the central region of each row, that is 883 of them, have the nominal size of $\approx 1.25 \times 5.85\,\mathrm{mm}^2$. Outside this region, groups of 8 pads are joined in a single sensitive surface thus reducing the total number of channels especially in the corners and reducing the total amount of required signal connectors.

The other main difference between the simplified and the final board is the power distribution system. While the slot to connect the GEM foils to the power distribution are almost identical, being just 0.7 mm wide instead of 1 mm, the power lines that come from those elements are routed directly outside to 20 soldering pads on the connector side where short (1.5 m) high voltage cables are fixed as visible in fig. 7.13. Additionally the protection resistor for each of the power channels were not integrated in the board but installed in a distribution box connected at the other end of the high voltage cables.

This choice allows to connect the electrodes of the GEM in any way deemed useful and to power the different sections of the GEM foils independently. Both of these features proved useful to understand and solve some of the early reliability problem of the high voltage distribution system.

7.6 Final detector assembly

With all components produced and tested the assembly of the detector proceeds as follow:

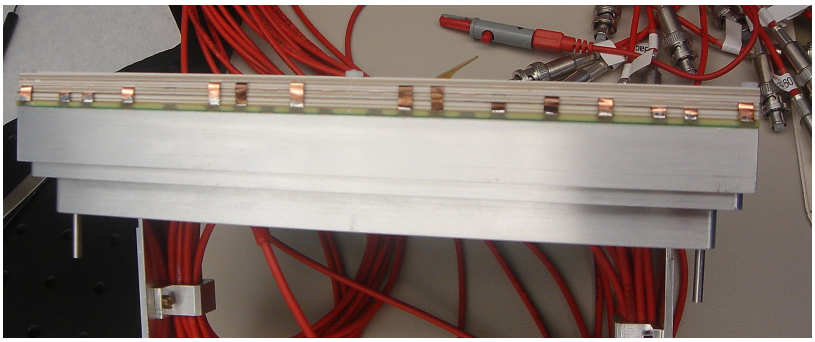

Figure 7.14: Top arc of the *GridGEM module* at the end of the installation procedure showing the electrodes coming from the different layers in the GEM stack soldered to the readout board.

- The first of the S^3 system ceramic elements is glued to the readout board, with particular care to completely seal the gap on the top arc where a discharge between the readout pads and the power slots can happen.
- The pad board is glued to the back-frame using the two dowel holes on the side of both components to ensure a precise positioning.
- The GEM foils are glued to the ceramic elements of the S^3 system on one or both sides and the useless electrodes are cut away. To avoid discharges from the stumps of the removed electrodes a thin layer of glue is placed on them.
- Six headless nylon screws are fixed to the back-frame, through the readout board, in the corners and in the middle of the top arc.
- The stretched GEM foils and any other ceramic element are piled above the readout board using the headless screw to guide them.
- After each GEM is positioned, the five electrodes are soldered in the power slots.
- With all the GEM installed a nylon nut is screwed on the top of the headless screw to fix the stack in position.

To avoid any distortion that may be caused by the sector gaps the drift facing GEM is installed with its unsectioned side facing the drift volume. The other GEM foils can be installed in either direction and they are usually installed in the same direction as the drift facing amplification stage.

The usage of a nylon nut on top of the stack, extending for a few millimetres in the drift volume can possibly cause field distortions when, during the chamber operations, it may charge up. Nonetheless this solution allows for a simple way to install the amplification stages and eventually replace them if damaged and this feature was deemed more important, at the current prototype stage, than the removal of a possible distortion source limited to few restricted areas.

Chapter 8

Building procedures and test of the *GridGEM module*

The *GridGEM module*, described in the previous chapter, consists of a mechanical support structure, called back-frame, on which to install a PCB board that integrates the power distribution system and a pad-based signal readout network for a modular stack of up to 4 GEMs installed above it.

To ensure the reproducibility, performances and reliability all the components, they must be tested at several stages of the assembly procedure. The most important measurements and control procedures, described in this chapter are:

- Survey of the position of the alignment holes of the back-frames (§ 8.3);
- High voltage test of the power distribution system (§ 8.4);
- Selection of the ceramic mother-plates most suitable for the GEM frames production (§ 8.5);
- Testing and training of the GEM foils used for the amplification stage of the module to ensure their reliability and stability under high-voltage condition (§ 8.6).

Once all the components to be used for the module construction were selected and certified through those tests we assembled the system. After the assembly and the test of the *GridGEM module* in a small TPC built ad-hoc, we performed a test-beam experimental campaign.

8.1 Tooling for the components tests

To perform many of the procedures required for the assembly of the *GridGEM module* and for the quality and performance tests of many components we had to prepare an adequate tool set. Some of those tools are commercial products, many were custom built to address our specific goals.

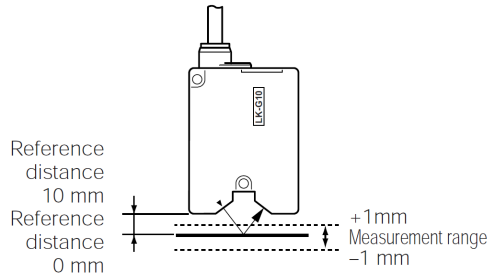

(a) Sketch of the configuration of the LK-G10 Laser displacement sensor installed to perform a profile measurement.

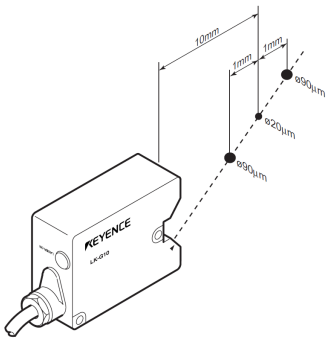

(b) Sketch of the laser beam spot produced by the LK-G10 displacement sensor on a target surface at different distances from the measuring head.

Figure 8.1: Schematic view of the LK-G10 sensor and its measurement range (from [107]).

8.1.1 The LK-G10 laser displacement sensor

The LK-G10 [107] is a high speed, high accuracy sensor that allows to measure the displacement of a target surface from an ideal plane placed at a fixed distance from the measuring head as shown in Fig. 8.1a. Moving the head above the target surface or vice versa, the system allows to measure the one dimensional profile of the object along the movement path. The size of the surface sampled by the device, that is the beam spot of the laser on the target, varies between 20 μm at the reference distance and 90 μm at the extremes of the measurement range (Fig. 8.1b). The resolution achievable by this device can be as good as 0.01 μm.

Each measurement is obtained averaging a configurable number of displacement samples, acquired at a customizable frequency down to a minimum period of 20 μs. The obtained values can also be filtered automatically within the controller using one of these algorithms:

- High-pass filter with customizable cutoff frequency;
- Low-pass filter with customizable cutoff frequency;
- Moving average filter with customizable window size.

8.1.2 The 3-axis moving robotic arm

Both the flatness measurements and the precise gluing of the ceramic elements on the GEM foils require an automated and accurate moving system that can carry the laser displacement sensor or a glue dispenser over the target surface. To this end we used a moving arm with 3 translational degrees of freedom (Fig. 8.2) powered by 3 independent linear micro-stepping motors. Each of the 3 axes has a moving range of $\approx$ 30 cm.

The 3 motors are driven by a single LSTEP/PCI controller[1] [108] that can achieve a micrometric positioning resolution. To increase the reproducibility of the device positioning

[1] http://www.lang.de

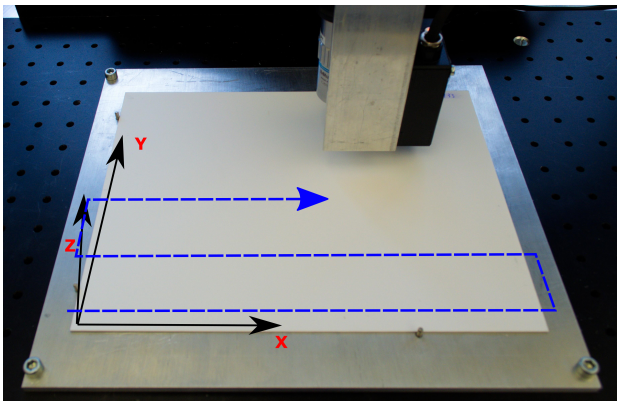

Figure 8.2: Picture of the 3D-roboting arm with the LK-G10 displacement sensor. Superimposed to the picture the three direction of motion are indicated and the meander path that is possible to execute using the Win-Commander program.

Independent channels	12
Output voltage	$0 \div -6\,\mathrm{kV}$
Voltage set resolution	$0.5\,\mathrm{V}$
Voltage monitor resolution	$\pm 0.3\% \pm 1\,\mathrm{V}$
Maximum output current	$200\,\mu\mathrm{A}$
Current monitor resolution	$\pm 2\% \pm 0.1\,\mu\mathrm{A}$

Table 8.1: Relevant operational parameters of the CAEN SY2527 power supply mainframe equipped with one A1832N board. The A1832N board is configured on its *low range* setting

the motor has a feedback measurement system. The controller is installed in a common PC through its PCI interface and can be steered through a C++ or Labview API.

The proprietary software provided by the hardware producer does not to allow to perform a meander on a vertical plane, which is necessary to measure the flatness of a GEM foil as installed in the detector, or to follow a curved path like the shape of the ceramic element of the S^3 system that we need to glue to the GEM foils (see for example the drawing at page 225). Therefore we developed a Labview program that extends the standard functionalities of the provided software to perform a meander in any arbitrary plane and follow curved paths.

8.1.3 CAEN SY2527 power supply

To power the high voltage circuitry of the *GridGEM module* we used the combination of a CAEN SY2527 Power Supply Mainframe[2] equipped with one CAEN A1832N plugin board[3]. This system allows to power independently up to 12 high voltage channels up to -6 kV and can also be used to monitor the voltage and the current independently on each channel. The relevant parameters of the system are listed in Tab. 8.1.

Each channel of the system can be configured with a different trip threshold. When the current reaches this threshold the power supply acts like a current supply for a configurable

[2] http://www.caentechnologies.com/csite/CaenProd.jsp?parent=20&idmod=123
[3] http://www.caentechnologies.com/csite/CaenProd.jsp?parent=20&idmod=171

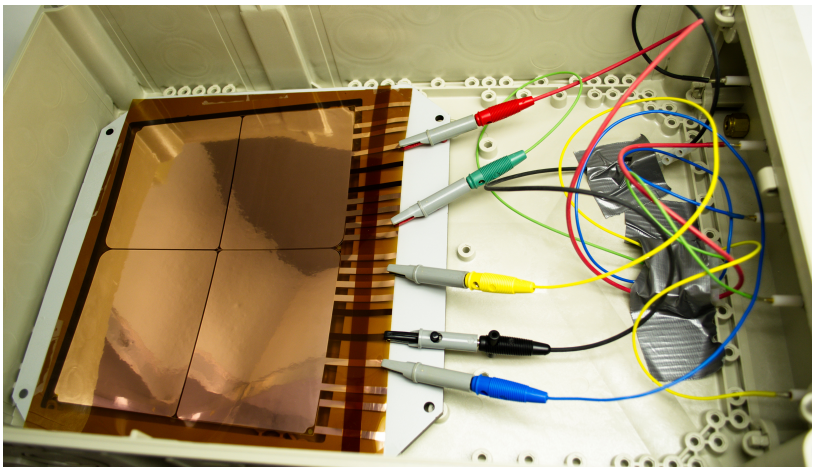

Figure 8.3: Photo of the open HV test-box with a GEM foil installed for the initial validation test and training procedure. Each sector of the GEM is connected to a different channel identified by a cable of different color. A protection resistor is installed on each of these cables, protected by the tape visible in the photo, to reduce the probability of a discharge damaging the GEM.

time variable from 0 to infinity. When the system remains in this configuration for a longer time the channel is automatically switched off (*tripping*).

8.1.4 Sealed containers for HV measurements

Many components of the *GridGEM module*, e.g. the GEM foils and the pad readout board, must be tested to ensure their high voltage stability even before they can installed in a real drift chamber and at different stages of the module assembly. To perform this type of tests we prepared a set of simple gas tight boxes with several high voltage lines feeding through replaceable front-ends.

The main component of this boxes is a commercial distribution box for electric installations produced by Hensel GmbH[4] (Mi-9210 or Mi-9310). These boxes have a simple foam O-Ring between the main plastic enclosing and a transparent cover that ensure a decent sealing. The walls of these boxes can be replaced by a removable cover that can be customized to install different connectors and components for different applications.

The most common configuration we built, visible in fig. 8.3, has five high-voltage and two gas connectors. The gas tightness of the container is good enough to achieve an oxygen content in the container better than $\approx 100\,\text{ppm}$ with a gas flow of $20\,\text{l/min}$. At the end of the high voltage connectors we installed a wire which includes a $10\,\text{M}\Omega$ protection resistor, ending with a crocodile clamp that is used to connect the power distribution to the component to test.

8.2 The *Single Module TPC* (SM-TPC)

The LP-TPC was developed to test the ultimate performances of the readout systems developed for the ILD TPC but, before those tests, it's necessary to evaluate the basic

[4] http://www.hensel-electric.de

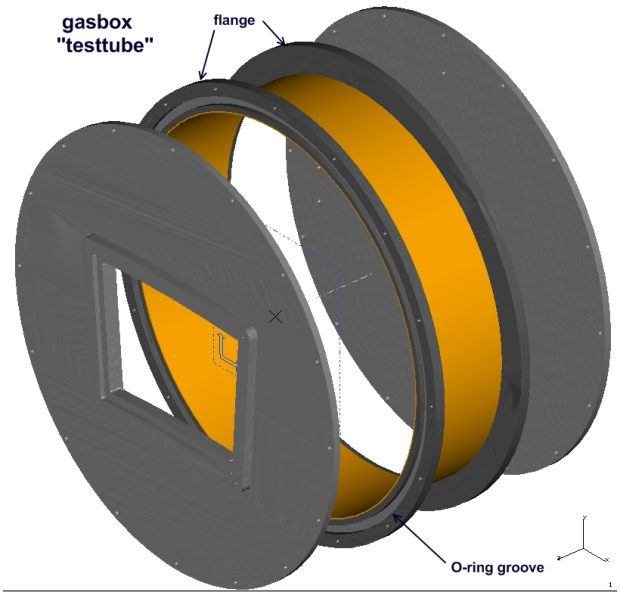

Figure 8.4: 3-Dimensional representation of the gas container and mechanical support structure of the SM-TPC.

functionality of the modules. There are several reasons why it is inconvenient to use the LP-TPC for the initial tests of any module prototype:

- The LP-TPC, being used by all members of the LCTPC collaboration, is often scheduled for other users.
- Because of its large volume, the time it takes to reach a gas quality good enough for any test after a module exchange is about one day.
- There is no way to install a radioactive source inside the chamber to be able to perform gain uniformity measurements. Circulating a radioactive gas is not a viable option as well due to the DESY safety regulations.
- The LP-TPC is a delicate, expensive and not easily replaceable tool and should not be used in the early phases of development and testing of a module in case a problem in the readout system may damage the whole TPC

To perform this preliminary tests, we designed and built a smaller, robust and versatile TPC, able to house a single LP-TPC readout module and several radioactive sources. This device is called SM-TPC.

The main components of the SM-TPC are the gas container and the field cage. The gas container is a steel cylinder with an inner diameter of 435 mm, a height of 120 mm and a total inner volume of $\approx 17.8\,\mathrm{l}$. Two steel flanges are welded to the outer surface of this cylinder to fix it to the two end-plates that seal the chamber. Those two flanges have a groove along the whole circumference to house an O-ring that ensures the gas tightness of the system. A 3-dimensional representation of this device is presented in fig. 8.4 while a more detailed drawing is included in the appendix at page 231. To avoid possible discharges the inner surface of the cylinder is coated with a Kapton foil.

The end-plate on the cathode side only include one feed-through hole for the inlet gas connector, the holes necessary to fix it to the gas container and 6 blind holes necessary to

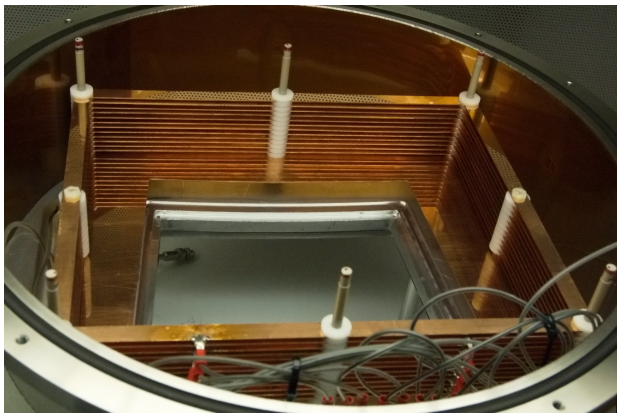

Figure 8.5: Photo of the field cage of the SM-TPC, without the cathode plate. The 6 posts over which the structure is built are visible on the 4 corners and in the middle of the long side. The bottom plate of the field cage has an hole of the same size and shape as the bounding box of an LP-TPC module. The wires going from the field rings to the resistor divider board are visible in the lower part of the photo,

fix the field cage in place. The anode end-plate, on the other hand, is more complex (a detailed drawing is included at page 232). At the centre of this end-plate there is a hole shaped to install the LP-TPC modules. Additionally there is the outlet gas connector and five HV connections that can be used to power the inner field cage. On the inner side of the end-plate there are 6 blind holes, matching those available on the cathode side, used to fix in place the field cage.

The field cage of this device has a rectangular shape of inner size of $245 \times 305\,\mathrm{mm}^2$. The corners of the field cage are rounded to reduce the possibilities of corona discharges in any of the device elements. This field cage is built as a stack of a variable number of copper rings, 1 mm thick and 12 mm wide, spaced by plastic washers. On the anode side, the field cage is closed with a termination plate shaped to match the LP-TPC module bounding box. The termination plate is not fixed and can be aligned with the module surface to reduce the field distortions at their edges. On the other side of the field cage it is possible to install different types of cathodes. The standard one is a simple copper plate but that could be replaced by a mesh or a membrane if necessary. To fix the field cage inside of the gas container, 6 posts are installed between the matching blind holes in the anode and cathode end-plates and these are used as guides to build the ring stack. The field cage of the SM-TPC is powered through a resistor divider built on a board installed inside the gas container, in the space left between the field cage and the walls of the chamber. The three termination of this divider, one for the cathode, one for the termination plate and the third for the ground potential are wired to as many high-voltage connectors installed in the end-plate. Considering that the field cage has a variable number of field rings, the resistor divider was designed to allow the user to connect and remove them from the chain easily. A picture of the open field cage, without the cathode plate, is shown in fig. 8.5.

In the configuration that we commonly use for this detector, we install 12 rings with a 3 mm spacing between each other to create a maximum drift length of 51 mm. Because there is not enough space to do otherwise, the SM-TPC must be opened and the cathode removed each time to replace the module. This procedure is usually performed in a clean environment to avoid damaging the module.

To be able to use radioactive sources to illuminate the drift volume we also built a support structure to install them in the drift chamber, as close as possible to the cathode

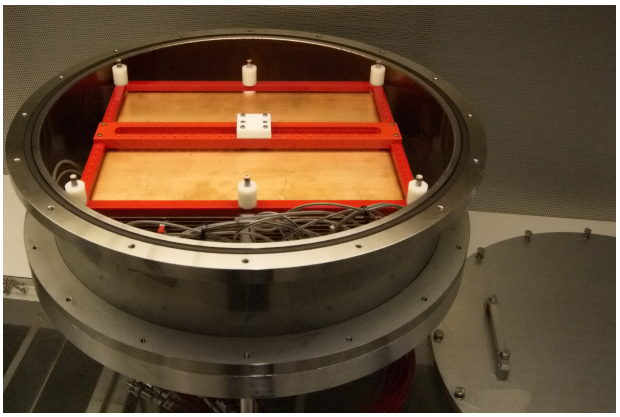

Figure 8.6: Photo of the open SM-TPC showing the complete, closed field cage with the radioactive source support mounted on top. The outer frame is piled on the same structure that supports the field cage. On top of this frame it is possible to install several rails in several positions, one of which is shown in this photo. On this rails one can install several source containers, the white box in the photo, that are only opened on the side facing the cathode, thus shielding the operator during the installation.

(Fig. 8.6). The system is constituted of three components, all made out of plastic:

- An outer frame that can be installed on the same support posts as the field cage.
- A set of rails that can be mounted on top of this frame.
- Several containers where the radioactive source, shaped like a coin, can be installed. The container has a small hole in the bottom from which the source can emit radiation in the direction of the cathode.

8.2.1 Commissioning

After the chamber was built we tested its gas tightness and high voltage stability. These tests were performed installing a dummy module (§ 6.1.2) on the anode side.

To evaluate the gas tightness, the chamber was filled with nitrogen at the maximum design overpressure of 10 mbar and sealed, with a gauge monitoring the internal pressure. This configuration was kept for three days and no gas leak were identified in the system. Additionally we installed an oxygen sensor on the gas line coming from the chamber and verified that, after a few hours flushing, the oxygen content in the chamber would asymptotically reach a value lower than 10 ppm, the actual value depending on the flow rate of the gas in the chamber.

To verify high voltage stability of the system we powered the field cage to −6 kV at the cathode. This voltage was kept for several days without any discharge being recorded by our instruments.

8.3 Back-frame production and survey

The back-frames used for the *GridGEM module* were built with a stress-relieved aluminium alloy, known as DOGAL 5080, machined into shape with a *CNC*[5] device. The standard back-frames, used for the dummy modules, were produced using a complex multi-step

[5] *Computer Numerically Controlled*

Back-frame ID	Dowel-holes Av. Dev.	Dowel-holes Max. Dev.	Screw-Holes Av. Dev.	Screw-Holes Max. Dev.
BF1	0.01	0.02	0.21	0.40
BF2	0.01	0.02	0.08	0.08

Table 8.2: Results of the survey of the *GridGEM module* back-frames. The position of the connector-side dowel-holes and the stack-fixing screw-holes was measured and the average and maximum deviation from the nominal position is reported in the table. All the deviations are measured in mm and measured with a resolution of 10 μm

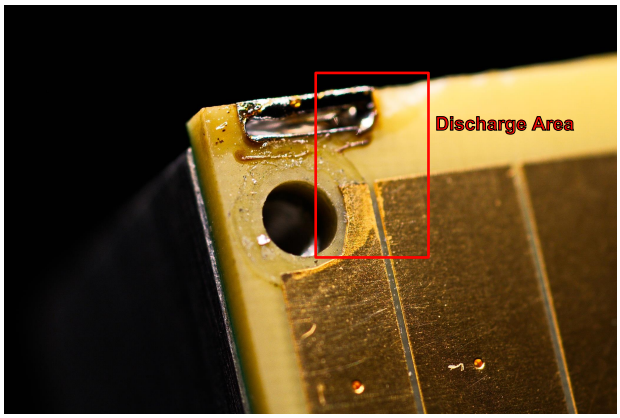

Figure 8.7: Photo of the corner of the readout board where, due to the insufficient gluing of the first ceramic component, a discharge between the high voltage slot and the readout pad happened

technique involving several cold shocks in liquid nitrogen to relieve the material of internal stresses and improve the quality of the final product. The back-frames produced for the prototype of the *GridGEM module* were manufactured without the use of cold shocks to simplify the construction procedure and make it more economic.

Two such back-frames were produced at DESY for the first prototype of the *GridGEM module* and their quality was surveyed at the DESY Qualitätssicherung Department after the production to evaluate possible deformations of the component. The results of such a survey are presented in tab. 8.2. It is noteworthy that the deviation of the actual position of the dowel-holes used for the alignment of the module with the end-plate from the nominal position is, in the worst case, less than 20 μm.

8.4 Tests of the *GridGEM module* readout board

The key measurements necessary to ensure that the readout board can reliably be used in the detector are:

- Connectivity test for the HV and signal channels verifying the absence of short or open circuits.
- Test of the power distribution system to verify that each of the high voltage line is correctly insulated from all other high voltage and signal line.
- High voltage test of the power distribution connection slots to verify the absence of discharges between them and between these areas and the grounded surfaces like the

back-frame and the signal pads.
- Gas leakage test of the board–back-frame assembly.

The connectivity test was performed by the manufacturing company that produced the piece and which provided a quality certification of the product, therefore it was not performed again.

The detailed drawing of the inner layer 6 included at page 228 shows both the high voltage line and the ground plane lie on the same board layer at close distance between each other. A similar situation is realized in all the inner layer of the board. Ideally the two groups of lines are separated from one another by the insulating material that keeps the layer of the boards together but if this insulation is damaged a high voltage discharge can develop inside of the board. The second set of test aim to exclude this type of defect.

The test is performed in the sealed container described in § 8.1.4, powering each of the high voltage distribution line up to 4 kV for a few minutes in Nitrogen while keeping all the other lines connected to the ground potential. The ground line is monitored to verify that the leakage current is not above 1 nA. The usage of Nitrogen reduces the probability of a discharge happening in the gas volume but does not affects the phenomena happening within the board thus allowing us to decouple the eventual source of any detected discharge.

Afterwards, the sealed container is filled with an Argon based gas and each of the high voltage distribution line is powered up to 3 kV for a few minutes while the current on all the other electrodes, connected together to the ground voltage, is monitored. The test is considered successful if there are no discharges during the power time and if the leakage current remains below 1 nA.

During this last set of tests we verified experimentally the importance of an accurate gluing of the first of the ceramic components of the S^3 system to the readout board. In fact the insufficient sealing of one of the corners of the first prototype we prepared (see Fig. 8.7) caused the discharge of some of the high voltage slots to the nearest pad at a voltage of $\approx 1200 - 1500$ V. This problem was solved improving the sealing at the interface between the board and the ceramic component.

When the electrical stability of the board is verified the system composed of the board glued to the back-frame is installed inside the SM-TPC and a gas leakage test is performed.

8.5 Evaluation of the internal tensions in the ceramic mother-plates

One of the factors influencing the probability of a ceramic component to crack while laser-cutting is the presence of internal stresses in the mother-plate. A good estimator of this quantity is the curvature of the plate without any load. To evaluate this property we measured the profile of the plate laying on an horizontal surface using the Keyence LK-G10 displacement sensor installed on the robotic arm described in § 8.1.2.

To perform this measurement we aligned the plate sides to the X and Y movement directions of the table and, starting from one corner the table is moved in a meander in

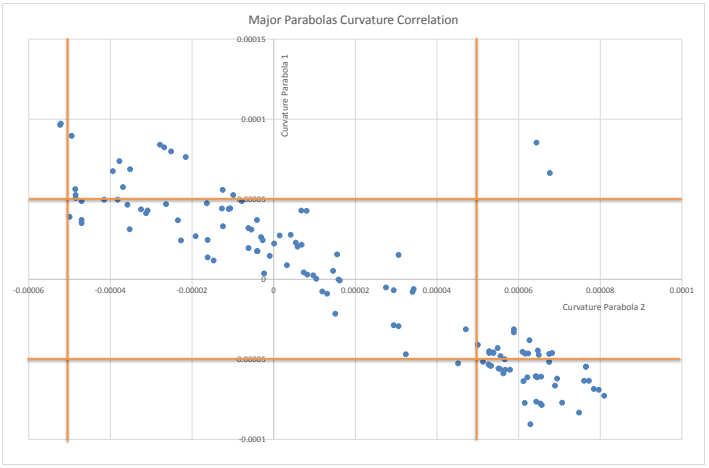

Figure 8.8: Correlation of the curvature of the ceramic plates along the two major axes of the fitted paraboloid surface. Superimposed to the plot, the red line represent the threshold for the selection of the plates. The curvature is expressed in mm^{-2}

the X-Y plane (fig. 8.2). Care is taken to make sure that the Y component of the meander is always performed outside of the plate surface. The meander is usually configured to perform 6 passages over the plate moving in the X direction. During the time it takes to complete this path the displacement sensor performs a continuous measurement. After the measurement the data are fed to a program, written in Labview, that performs the analysis of those data.

Before the actual analysis this program separates, within the data, the set of measurements that were taken above the plate from those that were acquired outside of it, recognizing the discontinuity in the measurement profile at the edge of the plate. Knowing the starting point of the measurement, the total plate size along the X direction and the distance between the lines of the meander path, the program associate to each displacement measurement an X and Y position value to obtain an array of 3-dimensional points.

To remove any effect due to the tilt of the plate under measurement the data are interpolated with a plane and the best fitting surface is subtracted from the measured set. Subsequently, to characterize the curvature of the plate, we assumed that the surface could be represented by a generic paraboloid:

$$Z = a_{11}X^2 + a_{12}XY + a_{22}Y^2 + a_{13}X + a_{23}Y + a_{33} \tag{8.1}$$

This function is used to fit the data set and we used the quadratic terms to form a symmetric 2×2 matrix which identifies the type of paraboloid. This matrix is diagonalized to obtain the two real eigenvalues. This operation is equivalent to a rotation along the Z axis which will bring the X and Y axis parallel to the major axis of the paraboloid and the two eigenvalues represent the curvatures (κ_1 and κ_2) of the generating parabolas.

After consulting with the manufacturing company in charge of laser cutting the ceramic plates, we defined an acceptance threshold for the plate curvature along each of the major axis of $5 \times 10^{-5}\,\mathrm{mm}^{-2}$. A plot of the measured curvatures of each of the analysed plate

Total delivered	29
Dead on arrival	3
Nitrogen test passed	21
Nitrogen test not executed	5
Damaged on gluing tests	4
Passed T2K testing	22
Damaged during operation	8

Table 8.3: Results of the acceptance tests executed on the *GridGEM module* GEM delivered between 2010 and 2012

is shown in Fig. 8.8. With this threshold we were able to accept 64 out of 132 measured plates.

8.6 The GEM foils testing and training

The GEM foils, being the active components of the *GridGEM module*, are a key element to ensure the reliability of the entire device and needs accurate testing and preparation. For this reason each foil is tested several times at different stages of the module assembly: when the foils are delivered, after gluing the ceramic components of the S^3 system and after the installation on the module. In any case the test procedure can be summarized in three steps that are usually executed sequentially:

- An initial training in dry nitrogen that removes most of the pollutant with minimal risk for the foil integrity.
- The training of the foil in the counting gas to reach the required performance.
- The long term testing in the same counting gas to verify the reliability of the device.

Keeping the foils in a dry atmosphere for long times also allows their plastic base material to expel most of the humidity that they could have absorbed during the storage periods which, in turn allows them to operate more stably during the actual measurements. All the testing performed on standalone foils are executed in our high voltage test boxes. When the foils are installed on a *GridGEM module*, the tests are performed in the SM-TPC.

The training of a GEM foil, mentioned for example in [86], is a common procedure used to remove any microscopic debris, usually dust particles, residuals chemicals of the GEM production or microscopic imperfection of the holes. This procedure is performed ramping up the voltage across the foil electrodes up to a point when the above-mentioned imperfections trigger an arc discharge. During this discharge the impurity is burned away and a higher working point can be reached. To avoid permanent damages to the foils is important to execute this procedure first in dry nitrogen where it is possible to achieve higher voltages without triggering an avalanche multiplication.

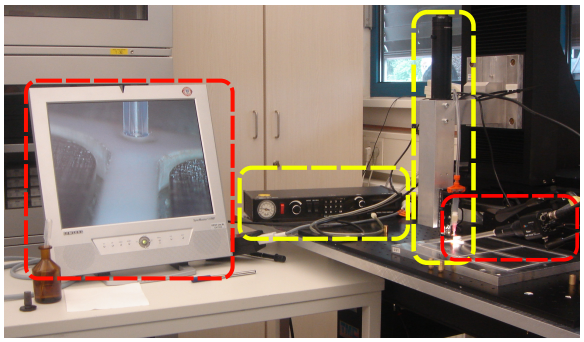

Figure 8.9: The set-up for gluing the GEM foils on the ceramic elements. In the red boxes it is shown the microscope and the connected display used to monitor the dispenser operation. In the yellow boxes the actual dispenser with the connected pump.

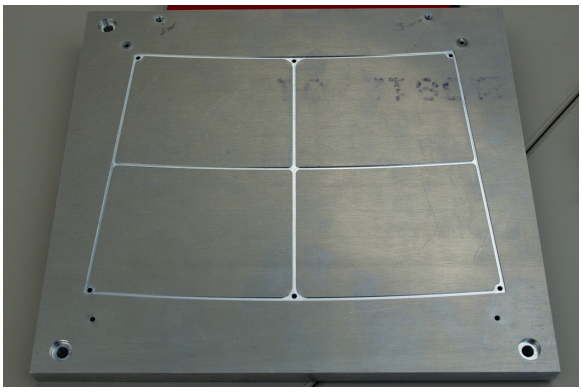

Figure 8.10: Photo of the ceramic element alignment plate. This device is position under the 3D-moving robotic arm and aligned to it.

In our case, to accept a GEM foil to be used as an amplification stage for the *GridGEM module*, we required that:

- Each sector of each foil stands 600 V in Nitrogen for about 10 minutes without discharging and with a leakage current lower than 10 nA.
- Each sector of each foil stands 300 V in the T2K counting gas [109] for $>$ 12 hours (*overnight test*) without discharging and with a leakage current lower than 10 nA, without any drift and induction field.

The results of those tests are listed in tab. 8.3.

8.7 Stretching the GEM foils on the ceramic support

The most delicate and time consuming task of the *GridGEM module* assembly procedure is the stretching and gluing of the GEM foils on the ceramic elements that will support them. What makes this task particularly delicate is the limited width of the S^3 system components (1.4 mm) and the small distance between the ceramics and the closest GEM holes (0.3 mm). To avoid the holes to be covered or filled by the glue it is necessary to control very precisely its flow and to design a mechanical system that allows an accurate dispensing of the glue on the surface of the ceramics. This situation is made even more complex by the shape of the ceramic elements.

The set-up to stretch and glue the GEM foils on the ceramic elements of the S^3 system is composed of the 3D-moving robotic arm on which we installed a glue dispenser which is made of a 3 cc syringe with a Teflon tipped needle of 0.15 mm (6 mils) diameter, connected to a pump which allows to exert a controllable pressure on the syringe's piston. To monitor the operation of the dispenser, that is to verify the the amount of glue is uniform along

the path and that the dispenser follows it accurately, a microscope camera is focused on the tip of the syringe and connected to an external display. This setup is shown in fig. 8.9.

This system is used to put the glue on the surface of a ceramic element. To align the ceramic element with the glue dispenser, we prepared a special grooved plate (fig. 8.10) where the component is positioned during the operation and aligned through the 6 fixing holes common to all the ceramic components. On a second plate, after aligning it using the same 6 holes, the GEM foil is stretched and fixed.

After this operation, the glue is dispensed over the ceramic component on a path programmed in the 3D-robotic arm. This program allows to follow precisely the arcs of the ceramic components. The whole glue dispensing operation takes 10-15 minutes, depending on the component to glue, and is important that the viscosity of the glue remains constant during this time.

Immediately afterwards, the stretching plate with the fixed GEM foil is placed and pressed above it to allow the two parts to adhere to each other. To ensure a precise matching of the two elements it is possible to install three alignment pins on the grooved plate that serve as guides during the operations.

To avoid introducing tensions between the two parts the curing of the glue is performed at room temperature for at least 12 hours. Afterwards, when the parts are fixed to one another, the whole system of the two plates with the parts to glue is put in an oven at 40 °C for 2 more hours to ensure the complete polymerization of the glue. After this final step the two plates are carefully separated and the GEM foil, glued to the ceramic component is extracted.

When it is necessary to glue a second ceramic component on the other side of the GEM foil, it is possible to follow the same procedure without stretching the GEM foil already glued to the stretching plate. In this case the component is simply aligned and fixed on the stretching plate.

The requirements for the glue we need for our detector, and in particular to fix the GEM foils to the ceramic components of the S^3 system can be summarized in the following list:

No outgassing of molecules that can influence the properties of the counting gas mixture or reduce the performance of the detector in the long term.

Medium viscosity to reduce the possibility of the glue flowing away from the interfaces between the foil and the ceramics. On the other hand an excessive glue viscosity could limit the accuracy with which we can control its flow.

Room temperature curing to avoid introducing tensions between the materials that could cause a deformation in the assembly.

Long pot life, of the order of 1 hour, to allow for the time to mix it and dispense it on the entire ceramic component without any appreciable viscosity change.

To comply with the first criteria we choosed our material among those listed in [72] that were tested to have no dangerous effects on gas detector. Among this material we

Surface	N^2 Training	Ar Training	Connector Test	Driftless	Sub-nominal	Nominal	Test-Beam Nominal
Anode	0	0	0	0	0	0	0
GA_A	600	300	1200	900	900	900	900
GA_C	600	300	1200	1140	1100	1140	1150
GM_A	600	300	1800	1440	1400	1440	1450
GM_C	0	0	1800	1690	1600	1690	1700
GD_A	0	0	2400	1990	1900	1990	2000
GD_C	600	300	2400	2250	2100	2250	2250
Cathode	600	300	2400	2250	5000	5000	14775

Table 8.4: Voltages of the different potential surfaces during the different static tests of the *GridGEM module* in the SM-TPC. All potentials are given in V, the labelling of the GEM surfaces follows the convention established in § 7.1.3. The transfer gaps between the GEM foils are of 2 mm each, the induction gap 3 mm and the drift length was set to 51 mm.

evaluated the Araldite AY-103 mixed with the hardener HY-991[6] and the STYCAST 1266 A/B[7] and choose the first one because of its higher viscosity.

8.8 Testing the *GridGEM module* in the SM-TPC

After the assembly of the *GridGEM module*, it is necessary to evaluate its performances as a whole in the SM-TPC before proceeding to install it in the LP-TPC. Two type of tests should be performed on each module before installing it in the LP-TPC. On one hand it is necessary to make sure that the system is stable when powered to the nominal conditions. Additionally one should verify the basic performances of the system, and in particular measure the gain and gain uniformity of the *GridGEM module*. Unfortunately it was not possible to perform this second type of tests due to the lack of a DAQ system for the SM-TPC.

All the voltage configurations used to perform the high voltage stability tests are listed in tab. 8.4. The first goal of those tests is to verify that every GEM foil, when assembled in the complete system, remains as reliable as when it was previously tested standing alone. To this end each GEM is brought in similar operating conditions as in the standalone training.

If all the foils pass this first test the system is brought in the *Connector Test* operating condition. The goal of this test is to verify that the power distribution system can stand the

[6] http://www.huntsman.com/advanced_materials/a/Home/Adhesives
[7] http://mccombe.physics.buffalo.edu/lab-manuals/stycast.pdf

required potentials. In this case the two side of the foil are brought at the same potential to make sure that any eventual discharge is not caused by the foil itself and reduce the possibility of damaging the foils in any such event.

Finally the GEM foils are brought to the nominal operational voltages in three steps: First the foils are brought to the nominal potential but the drift field is kept to 0 to reduce the probability of discharges due to an excessive gas amplification, then the voltage across the foils is slightly reduced but the drift field is brought to the nominal value and finally everything is set to the operational conditions to be used in a measurement test.

8.9 Testing the *GridGEM module* in the LP-TPC

From June 27^{th} to July 9^{th} 2011 the first prototype of the *GridGEM module* was installed in the LP-TPC at the DESY II T24 Test-Beam facility to be tested. The goals of this tests were to verify the quality of the design, pinpointing eventual weak points to further optimize, and to measure the basic operational performances of the device. This test-beam campaign involved a multinational team of $\approx$ 20 people from several institutes of the LCTPC collaboration.

To verify the design quality of the *GridGEM module* we needed to make sure that:

- The system could be reliably operated in configuration that allows high enough gain to achieve a good signal-to-noise ratio at the end of the electronics chain.
- The width of the readout pads is small enough to guarantee a sufficient charge sharing between neighbouring channels at all drift distances.
- The module can be operated reliably at nominal voltages in beam conditions, in other words that the discharge rate is no higher than ≈ 1 per day.
- The electric field distortions in the sensitive area due to the module are small enough that their effect can be corrected during the reconstruction.

Furthermore we planned the test-beam to collect enough data to measure its performances and in particular:

- The proportionality of the GEM amplification stack.
- The gain uniformity and the hit efficiency.
- The point and track resolution at different drift distances with and without magnetic field.
- The effect of the track angle to the track resolution.
- The effect of the S^3 system on the hit efficiency.
- The dependency of the drift velocity on the drift field in the T2K gas to be compared with the theoretical simulations.

For that campaign we prepared a single prototype module with a simplified board for the signal readout and a three layer amplification stage. The induction gap between the readout board and the anode GEM was set to 3 mm while the transfer gaps between the other GEM foils was set to 2 mm. Unless otherwise specified the foils where powered to

Parameter	Value
Electronics Gain	12 mV/fC
Shaping time	120 ns
0-Suppression Threshold	3 ADC counts
0-Suppression Length	2 Samples
Pre-Threshold Samples	3 Samples
Post-Threshold Samples	7 Samples
Pre-Trigger Buffer	15 Samples
Events per run	20000

Table 8.5: Nominal configuration of some relevant parameters of the ALTRO electronics during the test-beam.

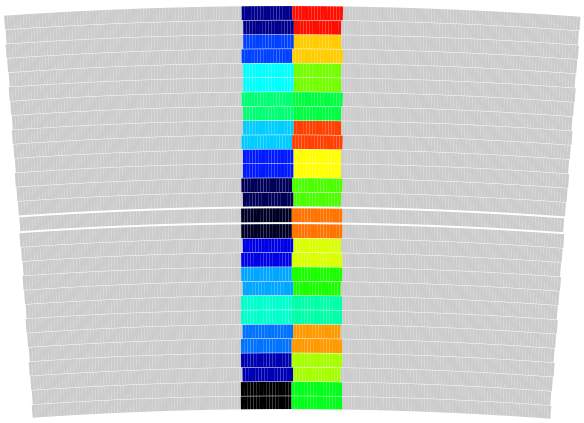

Figure 8.11: Mapping of the different pads of the module to the electronics connectors during the 2011 test-beam campaign.

the nominal test-beam configuration described in tab. 8.4 which accounts for a transfer field of 150 V/mm and an induction field of 300 V/mm. The cathode potential of the LP-TPC was set to achieve a drift field of 220 V/mm. It is noteworthy that in the test-beam configuration all the GEM foils were powered with the same potential difference between the electrodes. This was done as a precautionary measure to reduce the gain in the first stage after the drift GEM was damaged by a discharge during the set-up of the system (§ 8.9.1).

Each GEM was installed between two *Supporting Frames* but for the one facing the drift volume that was stretched over a single *Supporting Frame*. The remaining 2 mm gap between the anode GEM and the readout board was bridged by 2 *Simple Frames*, one of which was glued to the board itself. The module was installed in the central slot of the LP end-plate while the other 6 slots were occupied by dummy modules.

All 883 pads of the high-resolution, central area of the simplified board were connected to the ALTRO DAQ system (§ 6.3) while the large pads surrounding this central area

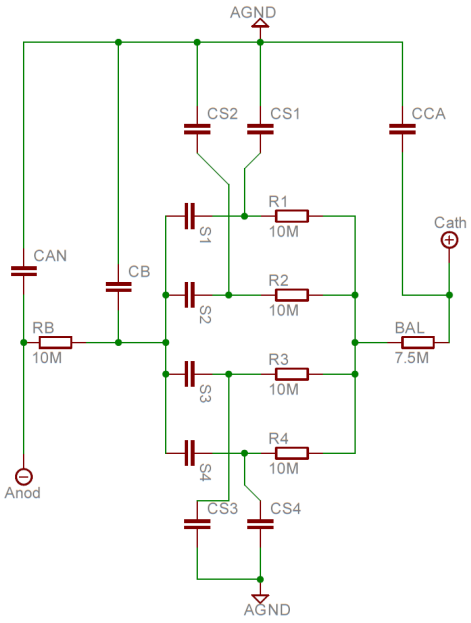

Figure 8.12: Scheme of the power distribution to one of the GEM foils of the *GridGEM module* as installed in the test-beam. The other two foils are powered through a similar circuit. Each GEM foil sector is represented as a capacitor labelled S1-4 and is connected to a protection resistor of 10 MΩ labelled R1-4 and RB. To balance the resistivity along the discharge path from each sector through the power supply an additional *balancing resistor* of 7.5 MΩ was placed in series to the 4 connected to the sectioned side of the foil. The cable capacitance towards ground is represented by 7 additional capacitors in this scheme.

where connected to the ground potential and were not read-out (see fig. 8.11). The nominal configuration of some relevant parameters of this electronics are listed in tab. 8.5.

To power the module, the HV cables were connected to a distribution box where the protection resistors for each GEM electrode were mounted. Each HV line was powered by one of the 12 independent channels of the A1832N module of the CAEN SY2527 power supply without using any resistor divider. To keep the same discharge rate on the two side of the GEM foil we also added a balancing resistor in series with those of the sectioned side. A schematic of the power distribution circuit of one of the three GEM foil is provided in fig. 8.12, with the other two being identical and connected in parallel to this.

What can be noticed in the previously mentioned schematics is that the short high voltage cables between the GEM sectors and the protection resistors add an additional capacitance towards ground to the sector itself. This factor can be relevant when evaluating the effects of a discharge on the foils.

During our campaign the test-beam line was set-up as to provide a 5 GeV beam. At that energy, in the T24/1 area, behind all the collimators, we could achieve a trigger rate of 10-15 Hz.

8.9.1 Magnet availability and discharges at the test-beam

During the test-beam campaign there were two relevant events that negatively influenced its outcome. The first one was a problem with the cooling of PC-MAG (§ 6.2.2) when a frozen air clog blocked the helium circulation within the internal piping of the system. This forced us to warm up the magnet before cooling it down again and did not allow us to excite it until the final days of the campaign, thus limiting the amount of data we could collect with the magnetic field on.

Overlapping with this issue we had two major discharges which damaged the GEM foils of the *GridGEM module*. Each of these discharges destroyed, in a single event, two independent sectors of the drift-most GEM foil and, in one case, even a third sector in the middle GEM foil, that is they created a short between the two sides of the foil. Luckily the simplified power distribution of the readout board allowed to re-route any power channel independently and we could continue to use the *GridGEM module* even after those events. To do that, the two short-circuited electrodes were connected to the same voltage, which disabled the gas amplification in that quarter of the module, and the value of the resistors in the *distributor box* were changed accordingly.

8.9.2 *GridGEM module* reliability and discharge protection

One of the most noteworthy experiences during the test-beam was the realization that, even though the discharge rate in the GEM foils of the *GridGEM module* was very low, that is less than 1 every 2 days, a single event could be as destructive as to damage several electrodes of the device. After careful examinations we realized several possible sources of such a problem.

On one hand, because the simplified board was not provided with an integrated protection resistor for each channel those where installed at the end of about 1.5 m of high voltage cable. The importance of this cables capacitance was underestimated, in particular considering that several of them will be charged up to more than 2 kV thus carrying a considerable energy. In fact, considering a 50 Ω impedance, 1.5 m long coaxial cable, with a silicone ($\epsilon_r \approx 3.6$) dielectric, we can calculate the additional capacitance to each GEM sector to be:

$$C_c = 3,33610^3 \frac{\sqrt{\epsilon_r} L}{Z} \approx 190\,\text{pF} \tag{8.2}$$

If this cable is powered at 2250 V, that is the highest potential on any GEM foil, the additional charge stored and available to fuel a discharge is ≈ 427 nC which is half of the charge stored in a *GridGEM module* GEM sector.

This problem would explain why a single discharge would kill a GEM sector or even the same GEM sector on two adjacent GEM foil in the stack if the discharge was propagating in the transfer gap but cannot explain why several sectors of the same GEM where damaged in the same catastrophic event. To explain this behaviour we should analyse the power distribution circuit in fig. 8.12 noticing that the balancing resistor labelled BAL was not installed in the initial system. In case of a discharge when the power supply automatically switches off, all the electrodes are connected to the ground. In this situation the one side of the foil that is divided in sectors discharges through a parallel circuit of four 10 MΩ resistors while the other side discharges through a single, similar valued resistor which means that the sectored side will discharge much faster than the other side. As the discharging goes on an increasing potential difference develops between the two sides of the foil, possibly triggering secondary discharges that can damage the foil. For this reason, after the first

Data Set	Number of runs	Avail. Sectors	Magnetic Field
Setup Runs	2	All	0T
Working Point Adjustment	20	S2 + S3	0 T
Electronics Scan	6	S2 + S3	0 T
Z Scan 0 T	27	All	0 T
ϕ Scan	1	All	0 T
Electronics Scan	5	S2	0 T
Working Point Adjustment	6	S2	1 T
Z Scan 1 T	6	S2	1 T
Drift Field Scan	18	S2	1 T
Total Runs	91		

Table 8.6: List of the data sets acquired during the test-beam campaign of June-July 2011. The table lists, for each of the data set the number of 20000 events runs acquired, the available module sectors that were available, that is not damaged by discharges, during the acquisition period and the magnetic field strength.

damaging discharge we proceeded to install the balancing resistor in the power distribution circuit.

Nonetheless, even after these solutions were adopted and in a later test-beam campaign performed using the full board we observed similar problems when a single discharge damaged multiple sectors. After further tests we finally discovered another cause for this problem that was due to the LP-TPC set-up itself and the dummy modules that surround the active one. The dummy modules were not provided with a protection resistor and have a very limited capacitance. When the power supply is switched off their potential goes to 0 almost immediately while the *GridGEM module* drift GEM foil is still fully powered at more than 2000 V. Because the closest distance between the dummy and the drift GEM is less than 2 mm the voltage across this gap can easily exceed the Roether limit triggering a powerful discharge.

Once all this problem were addressed, using the full board with integrated resistors, balancing the discharge circuit of the system, adding a protection resistor to the dummy modules and addressing some of the HV instability issues of the field cage we could operate the module for several days without discharges and without damaging the module.

8.9.3 Test-beam acquired data sets

Even though the problems we described limited the available time, during the test-beam campaign of June-July 2011 we managed to collect almost 2 millions triggered events in 91 data runs, each totalling 20000 events. These runs can be grouped in several sets listed

in Tab. 8.6:

Setup Runs Initial test to verify that all the systems were working correctly and that the sensitive area was correctly aligned with the beam. We were able to collect data at the first trial after installing the *GridGEM module* and the electronics in their default configuration.

Working point adjustments Each run in this data set was collected powering the GEM foils at different potentials to evaluate the best configuration to achieve a high enough S/N ratio without overflowing the dynamic range of the electronics at the minimum electronics gain. The drift, transfer and induction field were kept constant. The optimal configuration that we choose in the end was identical to that which was previously used on smaller prototypes with a 3 GEM readout in the same gas. Using this data set would also be possible top measure the gain linearity of the system as the GEM potential were changing. These data sets were only acquired with 1 or 2 available sectors on the module.

Z Scan With the nominal setup we acquired data aiming the beam parallel to the anode plane and the *GridGEM module* radius, in the same position relative to the central axis of the module but at different drift distances. We acquired this data set with and without the magnetic field but in the second case with only one available sector. The Z scan without magnetic field was the only complete data set that was acquired with all the 4 sectors available for the readout.

ϕ Scan Once again aiming the beam parallel to the anode plane and the *GridGEM module* we planned to scan the sensitive volume in the direction parallel to the rows of the readout board. Unfortunately the *GridGEM module* was damaged by a discharge at the beginning of this scan that made the sectors 1 and 4 insensitive and forced us to stop it.

Drift Velocity Scan With the nominal *GridGEM module* and electronics configuration we varied the cathode potential to modify the drift field in the sensitive volume to be able to measure the drift velocity and diffusion curves and compare it with the simulated values for this quantities. To perform this measurement, for each drift field value, we acquired 2 data runs at 2 different distances of the beam from the anode. The beam was directed parallel to the anode plane and perpendicular to the rows of the readout board and only one sector was available for this measurement.

Electronic parameter scan Keeping the nominal *GridGEM module* configuration we changed several electronics parameters such as the gain, the shaping time and the zero suppression thresholds while keeping the beam in a fixed position in the sensitive volume.

Chapter 9

Reconstruction, analysis and *GridGEM module* performances

In the previous chapter we described the design of the *GridGEM module* and the tests we performed to validate the design and evaluate the detector performances. Those tests culminated in a test-beam campaign on the DESY II electron beam where we collected roughly 2 millions events. In this chapter we will use those data to verify the functionality of the detector and validate some of the most relevant choices which were described earlier in this thesis. A complete analysis of the data collected during this first experimental campaign was performed within the scope of another graduate project in our group [110].

The first step of the analysis of the data acquired in a TPC is usually called *data reconstruction*, and consists in the processing of the raw data acquired to obtain physically meaningful quantities up to the parameters of the trajectory of the primary particle in the TPC.

9.1 From raw data to reconstructed tracks in a pad based TPC readout

The task of the reconstruction software in a TPC detector is to process the raw data acquired by the electronics to form a set of increasingly complex object that will finally combine to the trajectory of the initial charged particle that crossed the detector.

The first step is to recognize and characterize, in each of the independent electronic readout channels, the signals induced by the moving electron cloud produced by the gas amplification system, usually called *pulses*. Afterwards, these are clustered in space and time to produce 3-dimensional *hits* that can be finally combined in *tracks* and used to determine the best parameters to describe the trajectory of the primary particles.

9.1.1 Pulse finding

In a system where the signals are digitized through a set of ADC, the raw data are a sequence of integers between 0 and a predefined maximum value that depends on the specific digitizer used. For example, the ALTRO based DAQ used for the *GridGEM module* test-beam, has a 10 bit sampling range which fixes the maximum value to 1023. Each element in the sequence is usually called a *time slice*.

The actual signals induced by the gas amplified charge cloud on the detector sensitive surfaces are superimposed on a quasi-constant electronic noise, usually called *pedestal*. The fluctuations of this baseline on time scales comparable with the sampling period of the ADC constitute the sample noise for the signals to detect. We can characterize those fluctuations with their standard deviation around the pedestal mean value and call them the *pedestal width*.

The first task of the pulse finding is to separate the random noise fluctuation from the real signal. If the signal to noise ratio is large enough this can be done with a simple, threshold based discrimination. The relevant information carried by the pulses are the total charge induced to the readout pad, which is, ideally, proportional to the primary ionization charge, and the pulse time, which is correlated to the time of arrival of the primary cloud to the amplification region.

When using a charge sensitive pre-amplifier the first quantity is proportional to the maximum value of the pulse [68]. When the pulse rises from a well defined baseline and the response of the pre-amplifier is linear, the integral under the pulse can also be used to measure the pulse charge. This type of information can often be computationally easier to obtain and is therefore often used in the pulse reconstruction algorithms.

To define the pulse time, it is necessary to identify a feature in the signal that is not subject to strong time-walk effects, that is a feature whose position relative to the *true* arrival time of the signal has minimal correlations with the pulse amplitude.

Ideally, in the case of a charge pre-amplifier on a delta-like signal, the peaking time is fixed by the electronics configuration, independent from the signal amplitude, and that would be a perfect candidate to measure the pulse time. In practical applications though there is a measurable dependency between the peak time and amplitude.

An alternative is to use the inflection point of the rising edge of the pulse to define its time. This feature is also stable in time for a delta-like pulse, depending only on the pre-amplifier impulse response, and is easy to calculate using the mean of the derivative on the rising edge. The typical shape of a signal pulse recorded by our detectors is represented in fig. 9.1.

9.1.2 Hit reconstruction

The task of the hit-finding algorithms is to cluster the pulses selected in the previous step to define 3-dimensional space points, called *hits*, which lie on the trajectory of the primary particle. Each hit is therefore characterized by its 3-dimensional position and by the total charge deposited in that cluster.

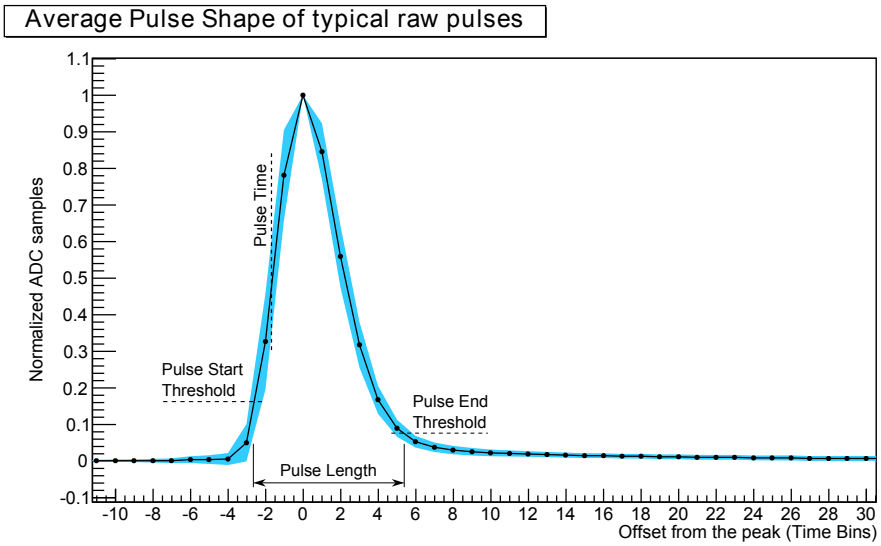

Figure 9.1: Average shape of a typical raw data pulse produced by the ALTRO-based DAQ system with pedestal subtraction and zero suppression. A typical pulse finding system, used in the data reconstruction, selects signals based on two thresholds, the peak height and the length of the pulses between the thresholds. To associate a time to the pulse one of the most reliable method is to identify the inflection point in the pulse shape. The charge can be calculated using the peak height or the integral below the pulse. The trailing edge of the pulse often falls back to a level higher than the baseline giving rise to a long tail in the pulse.

In a readout system where the pads are laid out in rows, either parallel to each other or concentric (see fig. 9.2), the clustering is often done separately for each row, considered as an independent sampling layer. In this case the coordinate along the row direction, $\boldsymbol{x_h}$, can be estimated by calculating the centre of charge of the cluster, that is the average of the pulse position weighted with their respective charge.

$$x_h = \frac{\sum_{i=k}^{k+w} q_i x_i}{\sum_{i=k}^{k+w} q_i} \tag{9.1}$$

Where $\boldsymbol{w}$ is the number of samples in a layer used to determine the hit position and is

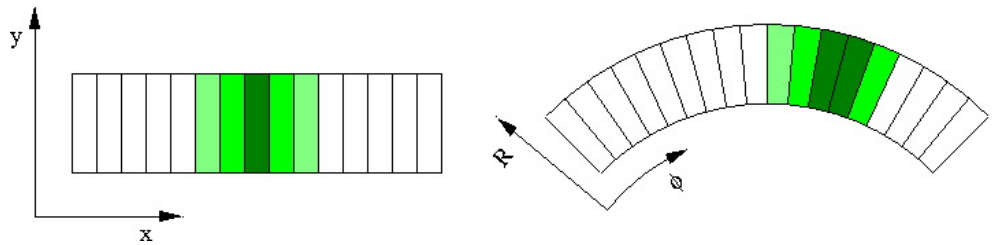

Figure 9.2: Row-based hit reconstruction in a rectangular (left) and circular (right) pad readout system (from [110]). In such algorithms neighbouring pulses are merged to determine the total hit charge and the centre of gravity is used to define the hit position along the row.

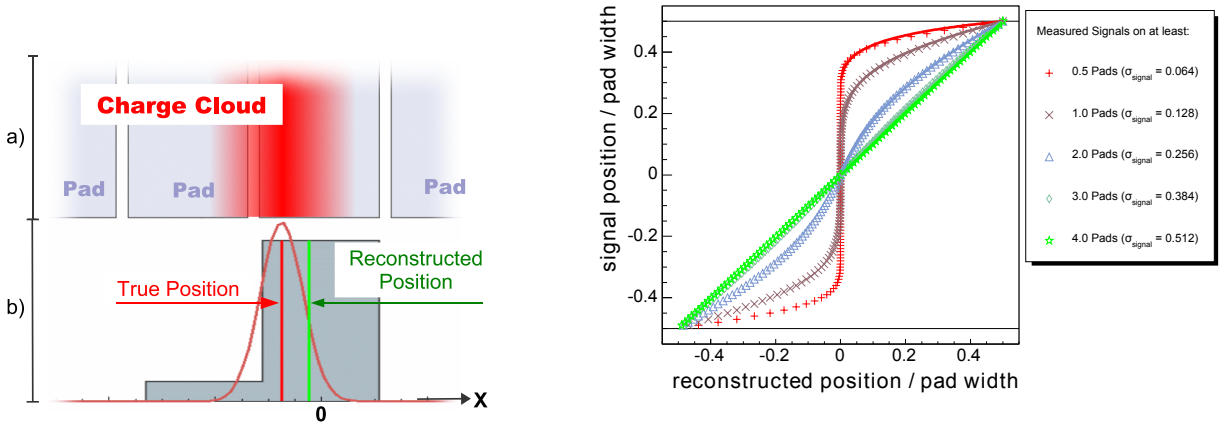

(a) (b)

Figure 9.3: When a hit is reconstructed from a small number of samples the calculated position is biased towards the sample of greater magnitude (a). This systematic error becomes negligible if 3 or more samples are used in the reconstruction (b). The pictures are extracted from [78].

called the *hit width*. When the hit width is small, this estimator is biased towards the pad with the maximum collected charge (fig. 9.3a). To minimize this effect the charge should be spread over three or more pads (fig. 9.3b).

The second hit coordinate, in the direction perpendicular to the sampling layer, is obtained directly from the geometrical position of the pads.

Finally, the third coordinate, along the drift path, is obtained from the time of arrival of the largest pulse in the cluster. The reason for this choice is that the different pulses on the neighbouring pads used to form a hit usually peak at slightly different times but, on average, the electrons in the core of the cloud are those that strayed less from the ideal path due to diffusion in the drift volume, thus taking a smaller time to reach the anode. This effect is amplified further during the transfer between the different amplification stages. Additionally, because of the larger signal-to-noise ratio on the pulse with the largest charge, the measurement of the time of arrival on this pulse is more accurate than the same measurement on the smaller surrounding signals.

9.1.3 Track reconstruction

The last step in the processing of the data obtained with a TPC, is the combination of the hits reconstructed in the previous stage to build one or more *tracks*, the representation of the trajectories of the primary particles in the detector. When the energy losses of the primary particles in the detector is negligible and we can ignore the multiple scattering, the track can be represented by a helix or straight line, respectively if there is a magnetic field or not. Due to the minimal material density in the sensitive volume of a TPC, these assumptions are usually valid. If one wants to consider these additional effects, it is usually possible to approximate locally the track to a helix or line segment and define the final

trajectory splicing those segments.

The track reconstruction algorithm is usually divided in two parts: *finding* and *fitting*. In the first phase all the possible hit combinations are considered to group those that are likely to be created by the same primary particle. Depending on the total number of hits to process there are several different possible algorithms that can perform this task. They can generally be divided in global techniques, which consider all the hits at the same time and on the same footing, and local procedures which start the search in a sub-domain of the sensitive volume, expanding it to only include areas where new candidates are expected.

The second phase of the tracking is the determination, from the hit candidates, of the best parameters to describe the particle trajectory. Given a reference point, e.g. the centre of the experiment, a straight line can be represented in space by three parameters while a helix requires five independent quantities [111, 112]. There are several algorithms developed for such a task which mainly differ in the way they deal with the parameter variation as the particle crosses the detector. A deeper treatment of the different algorithms used for the track reconstruction is provided in [110]

9.2 Reconstruction and analysis software

To process the data produced for the validation of the ILC detectors, either as results of experimental campaigns or Monte Carlo productions, the Linear Collider Collaboration developed a software framework called ILCSoft[1]. Within ILCSoft one can find several tools, mostly written in C++, that are used to perform the reconstruction of TPC raw data. The relevant packages necessary to perform the reconstruction of the TPC data are LCIO[2] [113], Marlin[3], MarlinTPC[4] [114, 115], GEAR[5] and LCCD[6].

LCIO provides the data persistency model of the framework. Each data file is composed of a general header containing the metadata and a set of numbered objects called *Events*. Each *Event* is made of a set of *Collections*, sequential containers of a single predefined type, e.g. pulses, hits or tracks. Because each *Event* is a self-contained object, they can be processed in parallel.

Marlin defines a unified framework to process LCIO data and to facilitate the modular development of reconstruction and analysis algorithms using LCIO as data container. The base component of a Marlin module is the *Processor*. It defines a set of standard callbacks that the user should implement in their subclasses. A steering file mechanism allows to activate the required processors at runtime. The processors can thus

[1] http://ilcsoft.desy.de/portal
[2] http://ilcsoft.desy.de/portal/software_packages/lcio/
[3] http://ilcsoft.desy.de/portal/software_packages/marlin/
[4] http://ilcsoft.desy.de/portal/software_packages/marlintpc/
[5] http://ilcsoft.desy.de/portal/software_packages/gear/
[6] http://ilcsoft.desy.de/portal/software_packages/lccd/

be chained in a custom sequence to elaborate the data contained in each event of the LCIO file, usually creating a new collection containing the results of this elaboration.

GEAR is designed to describe the detector geometry for the ILC reconstruction software. For a TPC, for example, it provides the position of all the sensitive surfaces within the detector and the length of the drift volume.

LCCD provides an interface between the reconstruction software and a special SQL database containing the description of the experimental conditions. This package manages the condition data as LCIO collections thus unifying the data treatment. In the case of our test-beam campaign these parameters are: the pedestal information, the electronic configuration used during the data acquisition, the mapping between the electronic channels and the geometric position of the connected sensitive surface as described by the GEAR package, the gas condition inside of the TPC and the voltage settings of the TPC and the readout modules.

MarlinTPC contains the tool for the reconstruction and analysis of TPC data. Its main building blocks are several Marlin processors and a number of standalone tools and applications.

9.2.1 The ILC Analysis Library

To define a unified and reusable framework to analyse data produced with the ILCSoft tools, we developed an additional library called the *ILC Analysis Library*. This library defines a class hierarchy and a set of interfaces through which it is possible to create analysis packages sharing a similar structure and common tools, thus simplifying the maintenance of the software and the sharing of some components among different analysis.

One of the goal of this library is to allow the user to use either the original LCIO files or a ROOT[7] tree as source for the analysis algorithms. In this way it is possible to prototype the analysis algorithm using the latter and then publish it to the rest of the community using the LCIO data type as input.

9.2.2 The Test-Beam Analysis package

Based on the *ILC Analysis Library*, we developed a software, called the *Test-Beam Analysis package* (TBA): a collection of algorithms and tools used to quickly analyse the reconstructed data collected in a test-beam campaign for the off-line monitoring of the data-taking conditions.

The processing algorithms are written in C++ and steered through a set of Python[8] and Bash[9] scripts which are also used to generate the ILCSoft steering files and execute

[7] http://root.cern.ch
[8] http://www.python.org/
[9] http://www.gnu.org/software/bash/

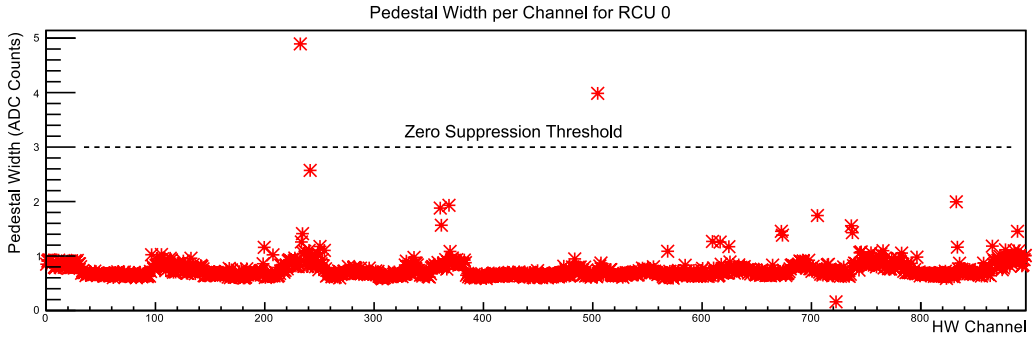

Figure 9.4: Measurement of the pedestal width for each connected channel in a typical test-beam session. Superimposed on the plot there is the zero suppression threshold that was set in that session. The channels with abnormal pedestal fluctuations are clearly visible. It is also possible to identified substructures in the bulk of the distribution due to the grouping of the signals on different readout chips, carried on independent cables.

the data reconstruction. Some of this algorithms are embedded in Marlin processors to perform the analysis tasks directly on the LCIO file in the most efficient way.

9.3 Electronics noise and dead channels

The first element we will evaluate to establish the quality of the *GridGEM module* is the correct interface with the electronics. This means quantifying if and how many read-out channels should be marked as defective.

We can divide the defects that we are looking for in two categories: dead channels where a negligible signal is detected by the electronic set-up, and noisy ones, characterised by the abnormal fluctuations of the signal baseline. In this section we will show how to identify these types of defects using the pedestals and raw data, without any further post-processing necessary.

In fact, the noisy channels can be identified from the analysis of the pedestal oscillations where they appear as large-valued outliers compared to a more uniform bulk. The measurement of the pedestal width for all the channels used in a typical test-beam run is shown in fig. 9.4.

From that plot it is possible to visually identify a handful of isolated noisy channels but it is also possible to notice additional features in the bulk of the distribution. The most relevant observation is the presence of groups of neighbouring channels with different pedestal widths as compared to the surrounding area. A more detailed analysis shows that each of these groups is readout by a different chip in the DAQ system and that the signals to each of these chips are carried by an independent cable. The difference between different groups is at most of the order of 20% and it is negligible compared to the typical signal amplitude and to the zero suppression threshold used during the data acquisition.

Due to their prominence, the noisy channels can also be automatically recognized by an appropriate outlier rejection algorithm. A very simple implementation, for example,

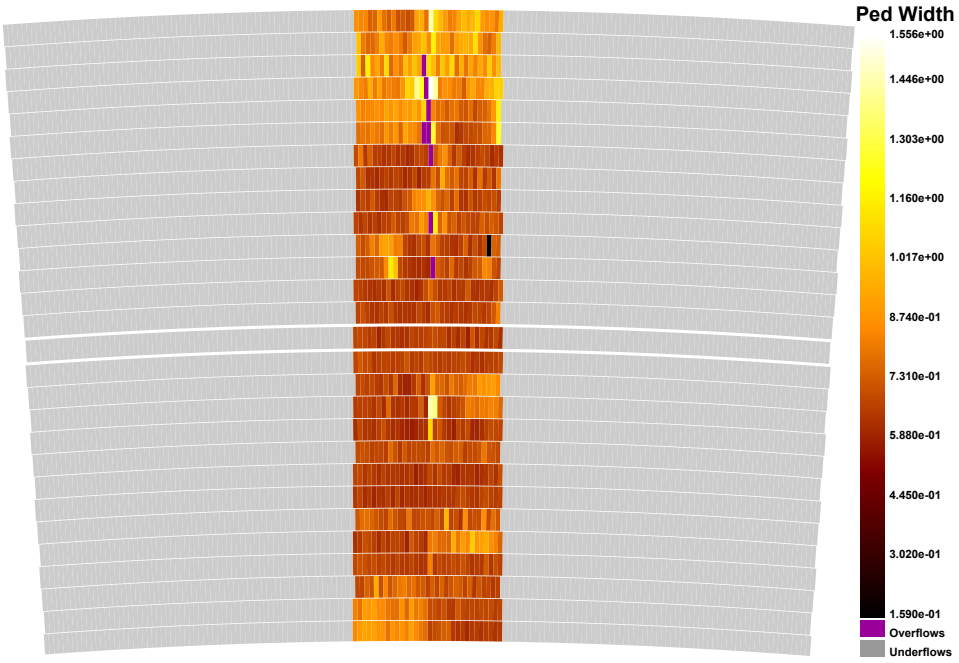

Figure 9.5: Map of the pedestal widths on the *GridGEM module* pads. The noisiest 1% of the channels are grouped in the overflow bin to allow an easier visualization and discrimination of the others. The dead channel due to the faulty electronics is the isolated black pad on the map.

characterises as noisy a fixed fraction of the channels with the highest pedestal width. This implementation is used to mark the last percentile of the channels shown in fig. 9.5 as overflowing. A more complex algorithm should be implemented in future that consider the actual statistical distribution of the signals to identify those abnormally high.

In that plot, the pedestal widths are mapped to their geometrical position on the readout board. It is possible to notice that these noisy channels are not randomly distributed on the readout surface but seem to cluster along the medial line. Because reconnecting the system changes the distribution of the noisy channels it is possible that this noise is partially due to signal picked-up by the cables connecting the electronics to the board. In fact, these cables, about 20 cm long, are not electromagnetically shielded.

Nonetheless, even in the case of the noisiest channels, the average fluctuation is at least one order of magnitude lower than the amplitude the typical signals which, as we will see later, is of the order of 100 ADC counts. In fact, the influence of that white noise is removed already in the pulse reconstruction step, as can be observed comparing fig. 9.6 and 9.7, which plot the total collected charge in a run before and after that reconstruction phase. This result also allows to set an appropriate threshold for the integrated zero suppression algorithm, highlighted in fig. 9.4.

Another way to understand the electronic noise is to study the correlation between the signal amplitude and the time at the peak, shown in fig. 9.8. As expected, most of the signals are clustered in a narrow area representing the beam spot. The number and the amplitude of the signals decrease steadily until around the time bin 165 where their

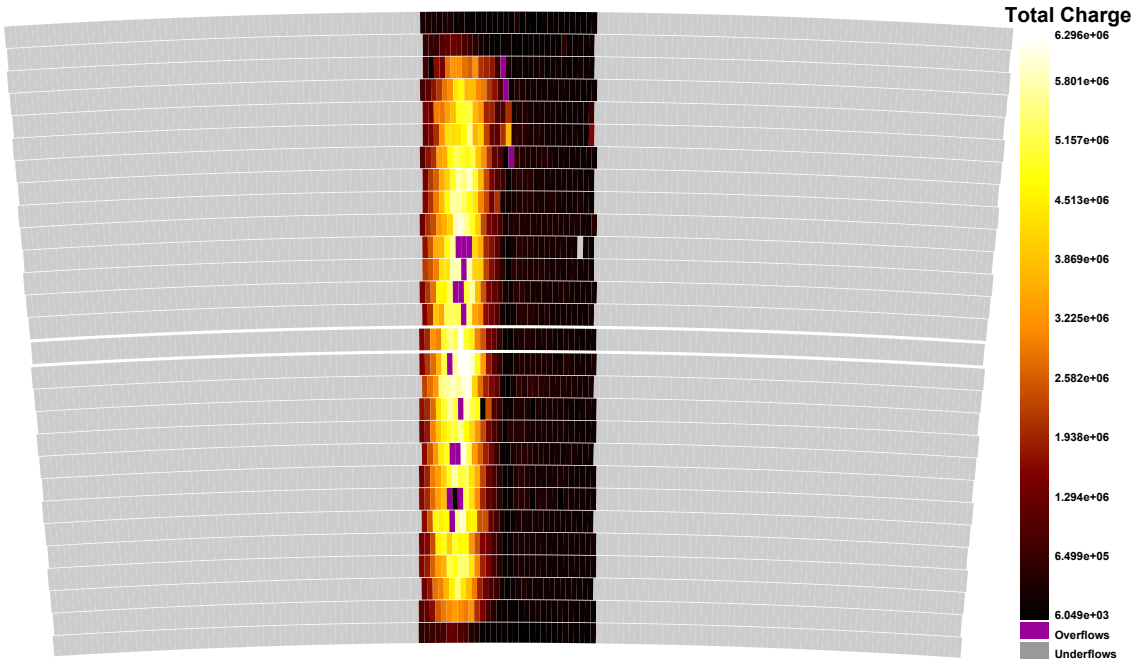

Figure 9.6: Geometric map of the *raw signals* amplitudes integrated in one run. The region crossed by the beam is clearly evident. The most evident feature is the charge deficiency at the edges of the module. It is also possible to clearly notice the presence of noisy and dead pads.

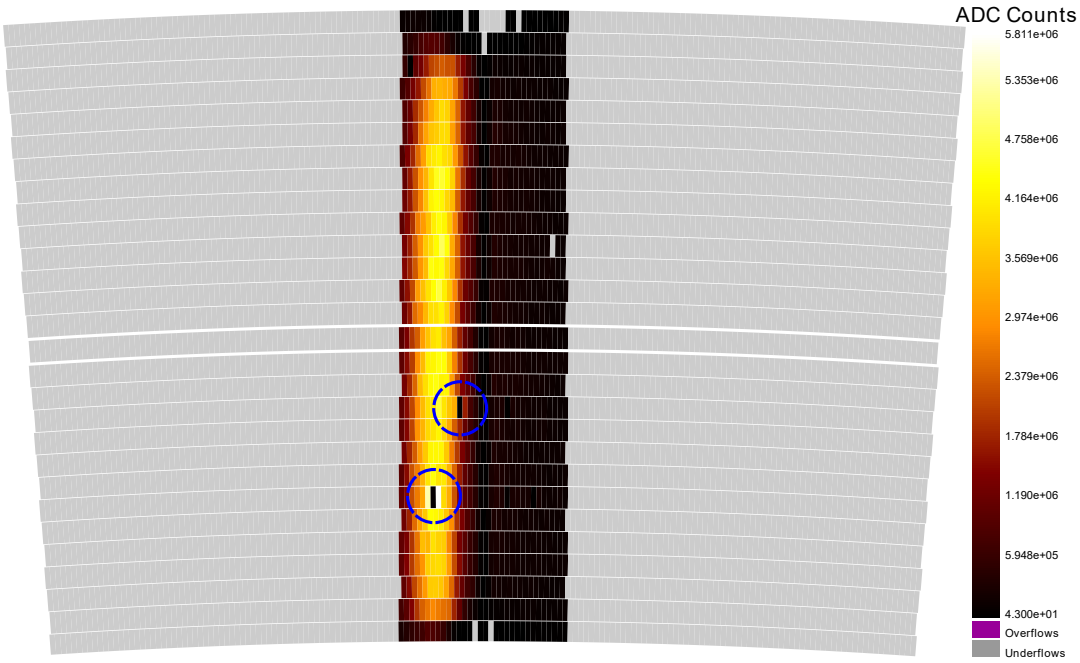

Figure 9.7: Geometric map of the integrated pulse charge in a test-beam run. Comparing it to the similar plot in fig. 9.6 it is possible to notice how the effect of the noisy pads was removed. Circled in blue are the dead pads recognizable on the sensitive surface exposed to the beam.

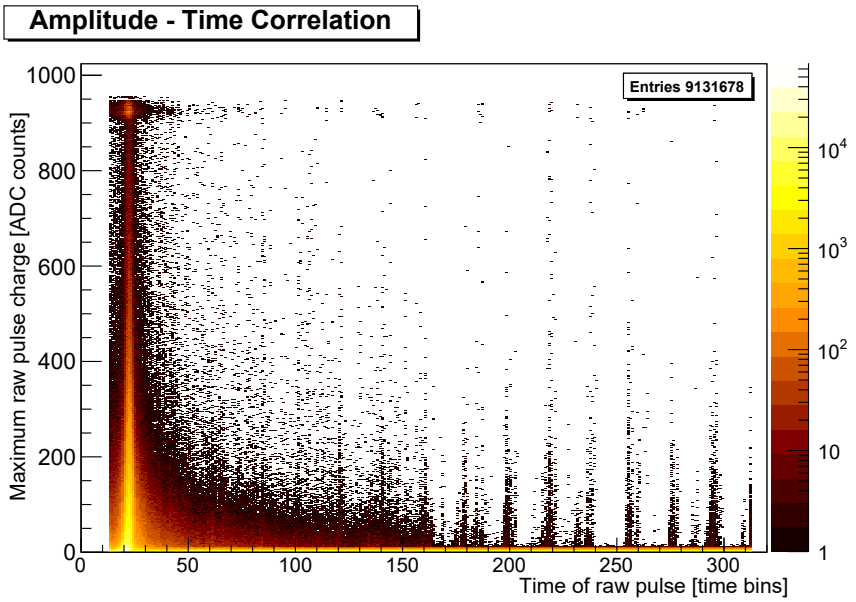

Figure 9.8: Amplitude-Time correlation of the *raw signals*. The beam position is clearly defined and is possible to see the number of recorded pulses steadily decrease farther from that region. Also an abrupt decrease of the amount and amplitude of the *raw pulses* is visible around time bin ≈ 165 and a repetitive pattern after that time.

number decrease abruptly.

This sudden drop is a rough estimate of the position of the cathode from which it is possible to obtain a rough estimate of the drift velocity. In fact, considering that the measured length of the TPC ($\boldsymbol{L}$) is 569.37 mm, that the first 15 time bins are buffered before the trigger signal and that the electronics was operated at a readout frequency of 20 MHz, which means a period $\boldsymbol{\Delta t}$ of 50 ns per time bin, it is possible to evaluate the drift velocity to:

$$\boldsymbol{v_d} = \frac{L}{N_b * \Delta t} \approx 76 \pm 1\,\mu\text{m/ns} \tag{9.2}$$

where $\boldsymbol{N_b} \approx 165 - 15$ is the time length of the TPC. The error was evaluated considering an absolute error of ± 2 time bins on N_b.

This value should be compared to the value of $75.24\,\mu$m/ns obtained through more accurate measurements [110]. In that case the time at the cathode was calculated to be $8.09\,\mu$s, corresponding to approximatively 162 time bins, compatible with our very rough observation.

Ideally after the cathode position one would expect a roughly constant amount of noise but, as can be seen in fig. 9.8 superimposed to this constant, low-amplitude noise, there is a periodic shot-noise of large amplitude. The frequency of this component is ≈ 1 MHz which corresponds to the revolution frequency of the DESY synchrotron, whose beam line passes a few meters away from the detector. This led us to think that this was noise picked-up from that source.

9.3.1 Dead channels

The dead channels which are insensitive due to faults in the amplifier can also be observed in the pedestal data of fig. 9.4 and 9.5. There they appear as channels with a lower than average pedestal width. Only one such defect can be observed in the above-mentioned plots.

The channels that are not sensitive due to a faulty electric connection, on the other hand, should be detected in the actual data samples as the main source of noise is the thermal noise in the electronics and the pick-up from the cables.

This analysis was performed using the Z-scan dataset (see tab. 8.6) observing the total charge integrated on each electronic channel represented in plots like that of fig. 9.7. Excluding the top and low edge of the sensitive area, where the charge inefficiencies are due to field distortions to be discussed later, it is possible to clearly identify 2 dead pads among the roughly 300 of those which collected enough charge. An additional feature that is interesting to notice, is how the two pads in the same row surrounding the dead ones show an increased charge collection. This can be interpreted assuming the dead pad to be floating, thus creating a local field distortion funnelling the charge towards its immediate neighbours. This implies that the cause of the pad inefficiency is a broken electrical connection to the electronic system.

9.4 Electronics characterisation

We already discussed, in the previous section, of the optimization of the zero-suppression level of the ALTRO-based electronics using the recorded pedestal widths to determine a reasonable threshold. The other two relevant settings of the readout-system are the pre-amplifier shaping time and its gain.

Longer shaping times improve the collection of the incoming signal thus increasing the accuracy of the measurement of the collected charge. A longer shaping time also reduce the electronic white noise, acting as an integrator on the random fluctuation on the baseline. On the other hand a long shaping time can induce long tails in the signal, thus reducing the rate performance of the system.

The typical pulse shape recorded by the test-beam DAQ system for different shaping times is shown in fig. 9.9. In these plots it is possible to evaluate how the typical number of relevant samples in the rising edge of the signal decreases from around 3 for the 120 ns setting to about 1 for the shortest available shaping time of 30 ns. Because these samples are normally used in the pulse reconstruction to define the pulse time, it is important for the signals to be long enough, compared to the ADC sampling time, to perform an accurate measurement of that observable.

Looking at the signal tails we can also observe two more effects. First of all the shorter shaping time induces a quicker drop of the signal to the baseline. For the longest shaping time it is actually possible to verify from those plots that, after 15 time bins, the signals is still higher than the initial baseline. The difference amounts to about 1-2 % of the

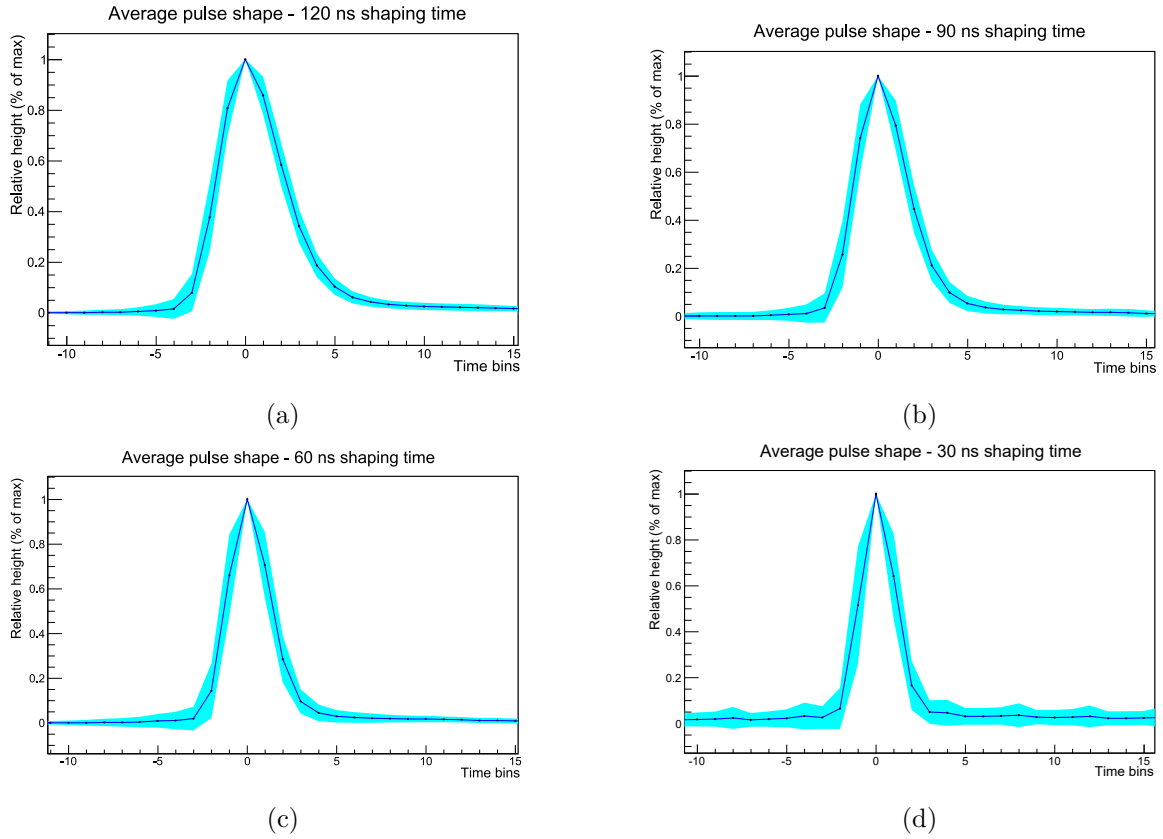

Figure 9.9: Comparison of the typical shapes of the signals recorded for different electronics shaping times. The other settings of the readout system were kept to the nominal values listed in tab. 8.5 and the GEM settings were the test-beam nominal values listed in tab. 8.4. The signal profile was obtained averaging all signals with an amplitude between 100 and 200 ADC values and normalizing the samples to the maximum signal height. 1 time bin corresponds to 50 ns. The shaded area surrounding the profile represents the standard deviation of each group of samples.

maximum amplitude reached by the pulse. Considering a zero suppression threshold of 3 ADC counts, this means that, for an amplitude larger than roughly 150 ADC counts, the signal never falls back under that threshold. We will notice the effects of such a behaviour later.

The second effect we observe is that a very short shaping time causes a large increase of the baseline white noise, which can observed in the width of the shaded area on the baseline of the pulse shape obtained at a shaping time of 30 ns in fig. 9.9d. The same increased noise can be observed on the spectrum of the typical pedestal widths shown in fig. 9.10d.

Finally we can evaluate the effects of the different settings on the hit time resolution. The hit time in the current implementation of the reconstruction algorithms, is defined by the time of the pulse with the largest charge in the set used to create the hit. In the configuration we used to perform this electronic setting scans, only two of the four GEM sectors were available (see tab. 8.6).

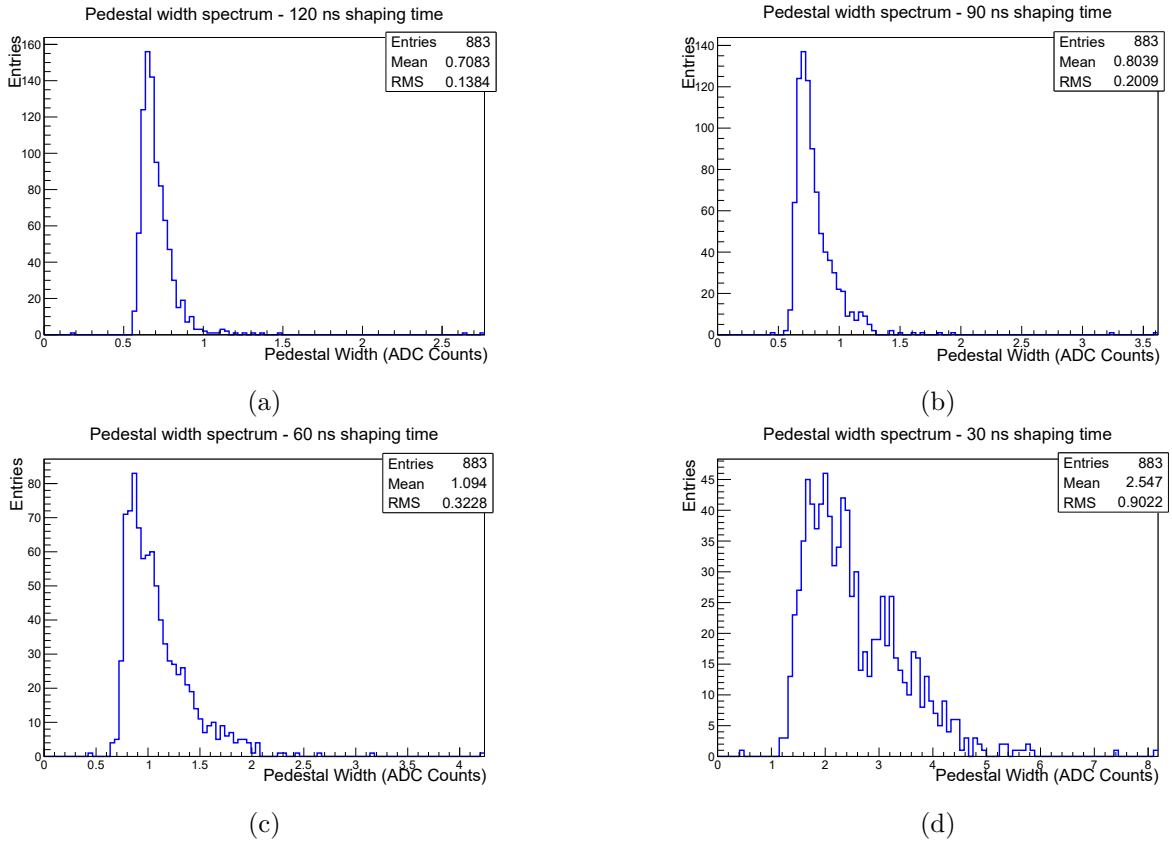

Figure 9.10: Comparison of the pedestal width spectra for runs recorded with different electronics shaping times. The other settings of the readout system were kept to the nominal values listed in tab. 8.5.

Due to the fact that, during each run, the position of the TPC was kept stable, relative to the beam line, we expect a hit distribution peaked at a fixed distance from the anode. From the width of this distribution it is possible to evaluate the effect of the different shaping times on the measurement of the hit coordinate along the drift direction.

To perform this comparison we plot the coordinate along the drift direction of all the hits reconstructed by our software framework using the steering parameters included for reference in the appendix at page 237. We can then fit a Gaussian function on the highest peak of this distribution and use the σ parameter of the fit result to characterise the different configurations. The plots used for this observation are shown in fig. 9.11.

Comparing this results we can appreciate that the longer shaping time allows for a more accurate measurement of the drift time but a remarkable negative effect is only visible in the sample take with the shortest shaping time. In fact, for the samples taken at 90 ns and 120 ns no relevant difference is observed.

From a comparison of all these relevant benchmark parameters, summarized in tab. 9.1, it is possible to draw the following conclusions:

- The 30 ns setting introduces a relevant white noise and, due to the longer sampling period of the ADC (50 ns) produces signals with a really short rising edge which

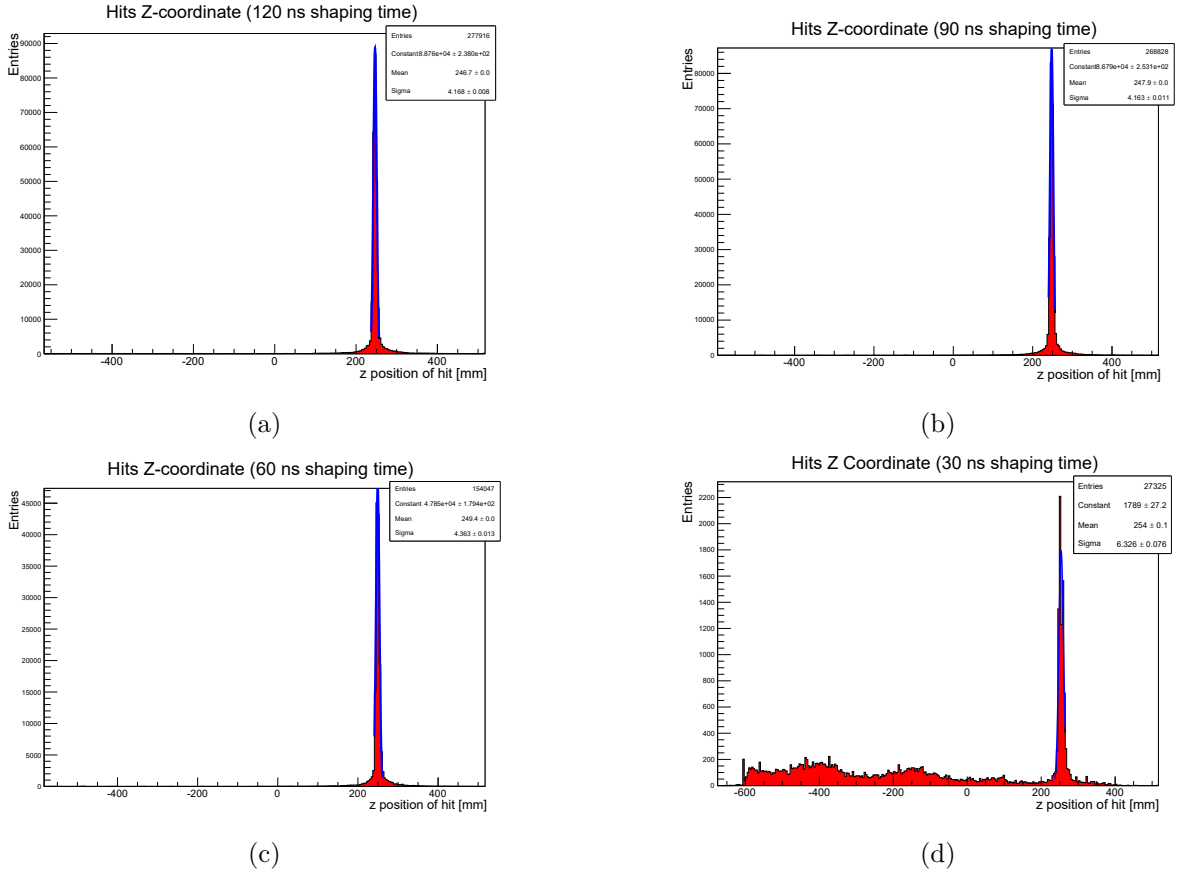

Figure 9.11: Comparison of the reconstructed z-coordinate of the hits for different shaping times. The other settings of the readout system were kept to the nominal values listed in tab. 8.5. We did not apply any selection to the hits collection. The highest peak in the distribution was fitted with a Gaussian function.

Shaping time	**Samples on rising edge**	**Pedestal width mean**	**Hit Z σ**
120 ns	≈ 4	0.7	4.2
90 ns	≈ 3	0.8	4.2
60 ns	≈ 3	1.1	4.4
30 ns	≈ 2	2.5	6.3

Table 9.1: Comparison of the relevant benchmark measurements for different electronics shaping times.

reduces the overall pulse-time resolution which, in turn, determines the hit drift coordinate. For these reasons this setting should be avoided.

- The 60 ns configuration produces a relevant increase in the detected white noise but, considering that the typical signal amplitude is several times higher, the pulse reconstruction is able to efficiently filter out this noise signals as can be seen by the absence of additional background hits in fig. 9.11. Nonetheless the shorter rising edge seems to induce a measurable worsening of the measurement resolution of the hit drift coordinate, that is the hit time.

- The two longer shaping times, that is 90 ns and 120 ns, are substantially equivalent, with the latter slightly less noisy, as expected.

- Due to the lack of an appropriate data set it was not possible to evaluate experimentally the double track resolution of the different settings. Nonetheless, considering that to reliably separate two peaks it is necessary for the second to arrive on the declining edge of the first it is possible to speculate that the shorter time settings would allow better performances according to this benchmark alone.

- All considering the best shaping time configuration for our set-up is 90 ns.

The second relevant setting of the DAQ set-up is the electronic gain. This can be changed in 4 steps: 12, 15, 19 and 27 mV/fC. If the electronic system is working correctly we should observe a linear correlation between the amplitude of the signals and the gain.

To perform this measurements we scanned the different electronics gain settings planning to keep all the other parameters, including the GEM potentials constant. To avoid excessive overflows at high electronic gain settings we reduced the GEM potential by 10 V in each amplification stage, compared to the nominal set-up described in tab. 8.4. Thus the potential difference at the three amplification stages in this measurement set is 230 V, 240 V and 250 V for the anode, middle and drift GEM respectively.

Unfortunately we only realized after the end of the data taking that for the lowest gain settings (12 mV/fC) we didn't acquire a measurement set with the identical GEM potential configuration that we used for the other electronic settings of the scan. Nonetheless we recorded measurements at a similar working point where the sum of the GEM potentials is the same, that is 230 V, 250 V and 240 V for the anode, middle and drift GEM respectively. Moreover some of the measurements described in this section can be performed observing the pedestal width alone, which should not be influenced by the amplification stage. In fact, because most of the white noise is produced within the pre-amplifier itself we expect it to be amplified differently at the different gain settings and the recorded values be linearly correlated to the electronic gain.

To optimize the dynamic range, the baseline reference of the ADC stage has a different value at each of the gain settings, thus the absolute value of the pedestal is not a valid figure of merit for this comparison but the pedestal width is.

The spectrum of the pedestal width at each of the gain settings is shown in the plots of fig. 9.12. In fig. 9.13 the mean value and the RMS of each of those distribution are shown

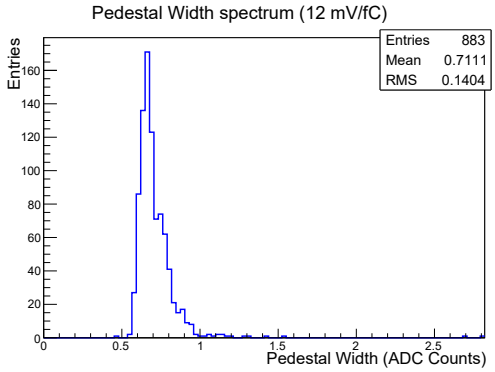

(a)

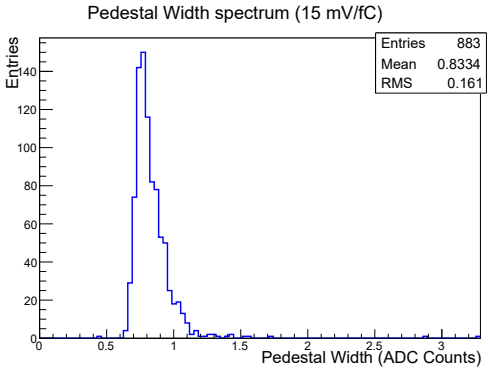

(b)

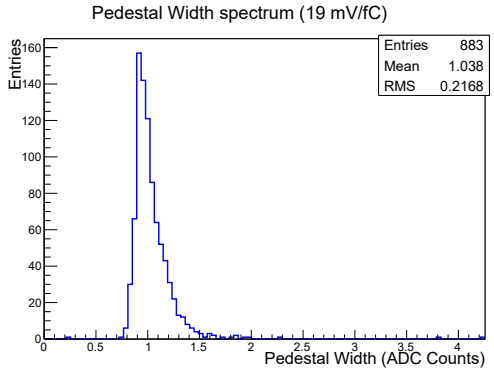

(c)

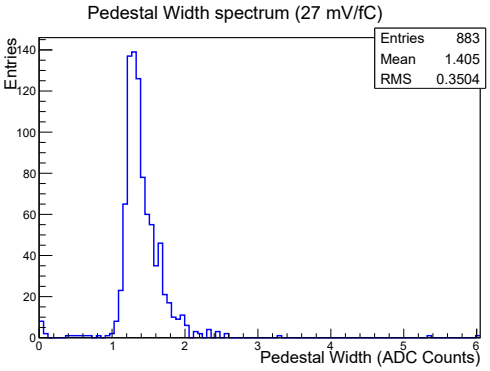

(d)

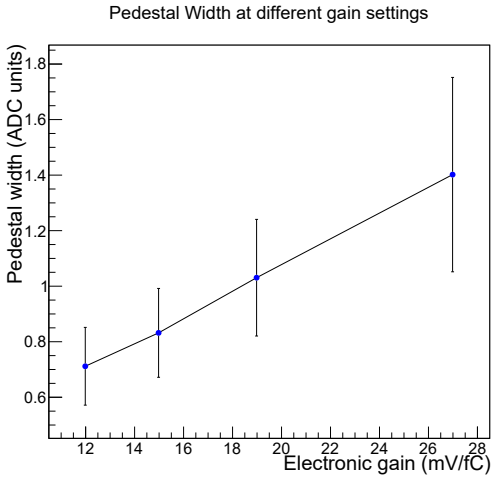

(e)

Figure 9.12: Comparison of the pedestal width at different electronic gain settings. The other settings of the readout system were kept to the nominal values listed in tab. 8.5. The graph in e shows the tendency of the pedestal width mean at the different settings. The error bar represents the RMS of the data.

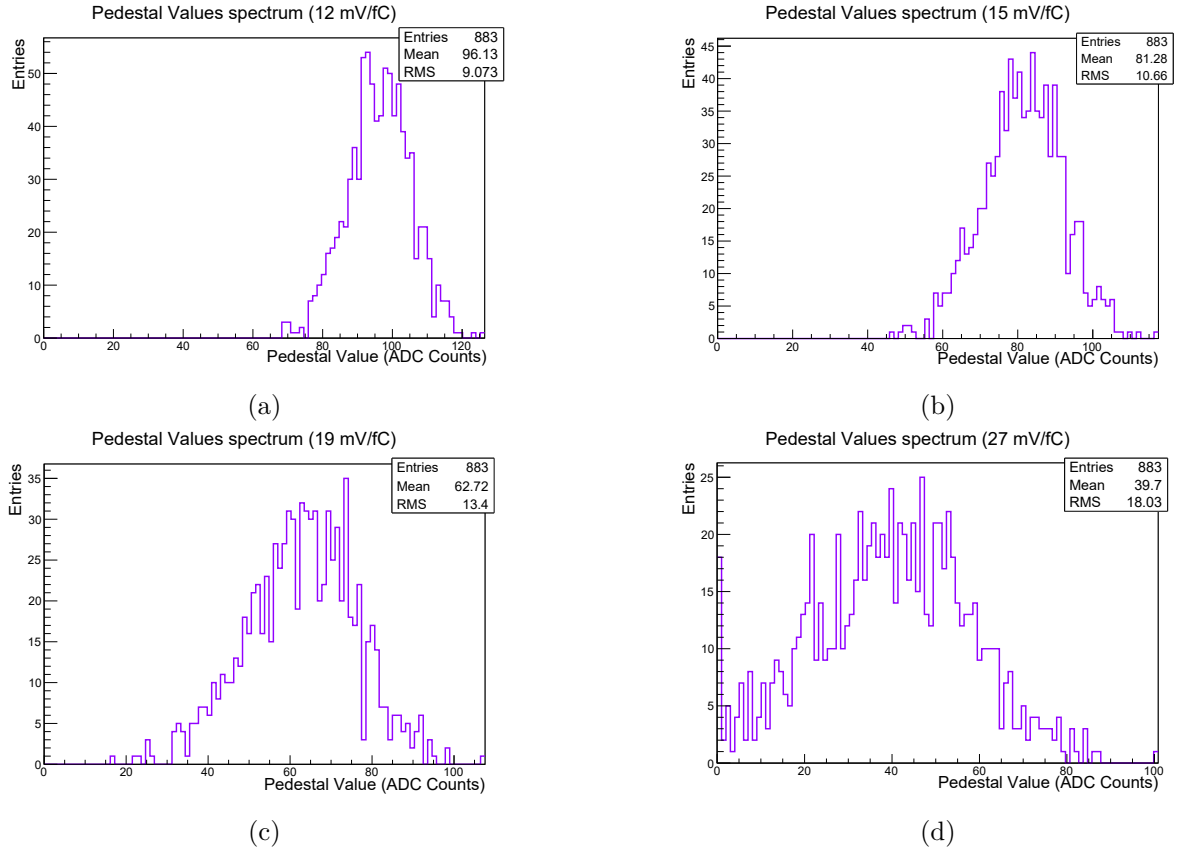

Figure 9.13: Comparison of the pedestal values recorded at different electronic gains. The other settings of the readout system were kept to the nominal values listed in tab. 8.5.

together to highlight the expected linear correlation between the electronic gain and the average pedestal width.

An interesting feature though, is to observe an increased number of channels with a very low pedestal width. This can be explained looking at the absolute value of the pedestals, plotted in fig. 9.13.

As mentioned before this baseline varies at the different settings to enhance the dynamic range of the system. It can be observed that at the gain of 27 mV/fC the baseline is too low and for several channels is falling below 0, which is shown by the large value of the first bin of the histogram. For this reason the 27 mV/fC gain setting configuration can be considered unreliable and should not be used in further tests unless this effect is taken into account.

To verify the linearity in the pre-amplifier response in normal operating conditions we also compared the average energy deposition per hit in an event. Because only 2 of the sectors of the GEM were functional during those runs, we only consider the hits recorded in the lower right of the sensitive area. We also ignored the first three rows, where the hit efficiency is relatively low, as will be shown later, and the seventh row where a dead pad in the middle of the sensitive area usually splits the hits.

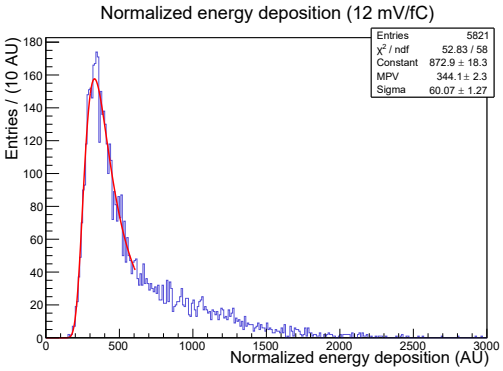

(a)

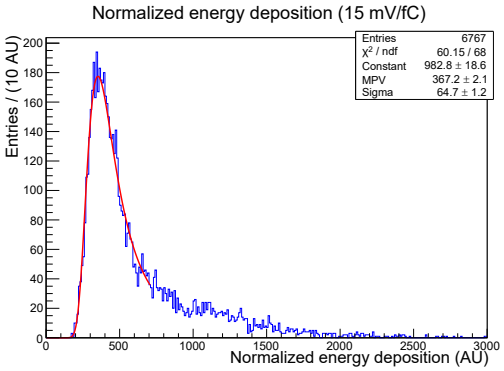

(b)

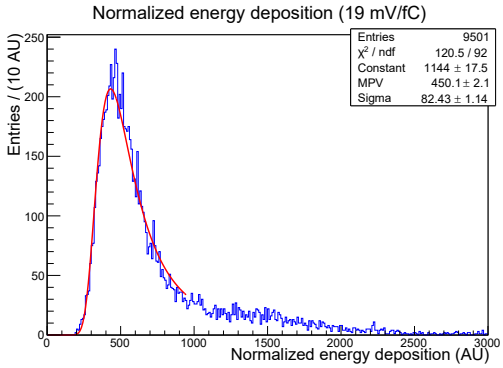

(c)

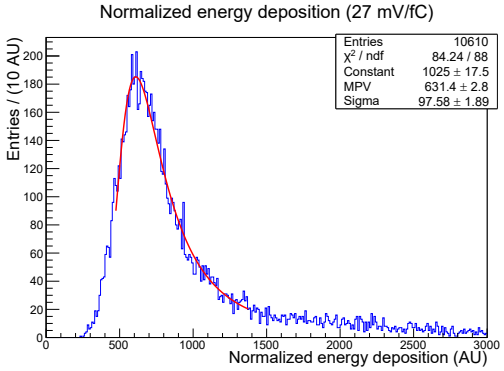

(d)

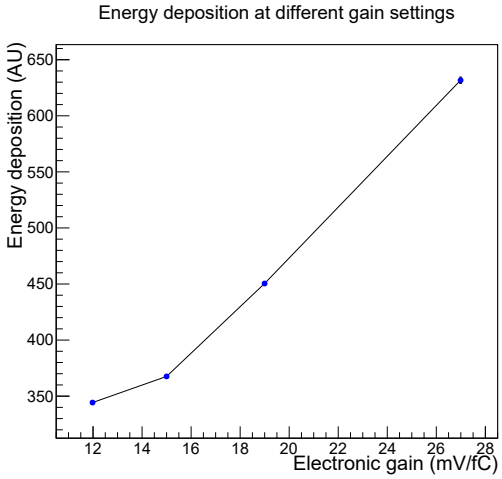

(e)

Figure 9.14: Comparison of the recorded energy deposition of the hits for different shaping times. The other settings of the readout system were kept to the nominal values listed in tab. 8.5. We did not apply any selection to the hits collection. The highest peak in the distribution was fitted with a Landau distribution.

Electronic gain	**Pedestal width mean**	**Energy deposition MPV**
12 mV/fC	0.71	344.1 ± 2.3
15 mV/fC	0.83	367.2 ± 2.1
19 mV/fC	1.03	450.1 ± 2.1
27 mV/fC	1.40	631.4 ± 2.8

Table 9.2: Comparison of the relevant benchmark measurements for different electronics shaping times.

The distribution of these quantities for the four gain settings are shown in fig. 9.14. To compare them we fit a Landau distribution to them and considered the most probable value of the resulting function.

As can be seen in the tendency graph on the bottom of fig. 9.14, the response of the electronic looks reasonably linear in this case as well, especially taking into consideration that the first of the four data point was acquired at a slightly different gas amplification setting.

The summary of these measurements for the four gain settings is contained in tab. 9.2. As we mentioned before, the highest gain setting should be avoided due to the inappropriate baseline reference value. Otherwise the appropriate setting for a measurement campaign should be chosen depending on the gas amplification of the device. It is in general preferable to keep the electronic gain as low as possible and rely on the gas amplification to increase the signal-to-noise ratio.

9.5 Correlation between the signal peak and integral

In a charge-sensitive pre-amplifier, like the PCA16 model used to process the signals induced on the *GridGEM module* sensitive surfaces, the total charge collected on a channel is proportional to the height of the output pulse of the amplifier. When consecutive pulses are not overlapping, if the output pulse shape is independent from the pulse amplitude, it is possible to reliably use the pulse integral to measure the total collected charge.

Additionally, if the amplified signal is sampled by an ADC, to be able to accurately measure the signal amplitude it is important to have several samples in the peak region. If the ADC sampling period is not small enough, compared to the amplifier shaping time, the peak might be characterised by a single sample. In this case using the pulse integral can provide a more accurate charge measurement.

As we already stated, though, the main assumption necessary to use the signal integral to perform a charge measurement, is for the signal shape to be independent from its amplitude so that the peak value and the pulse integral are linearly correlated.

To study this characteristic we plotted, in fig. 9.15, the correlation between the signal integral and the height of the maximum sample in it. At a first approximation these two quantities are linearly correlated, as expected, at least up to the overflow threshold of the ADC. Nonetheless, at a deeper inspection we can observe two sets of signals which show

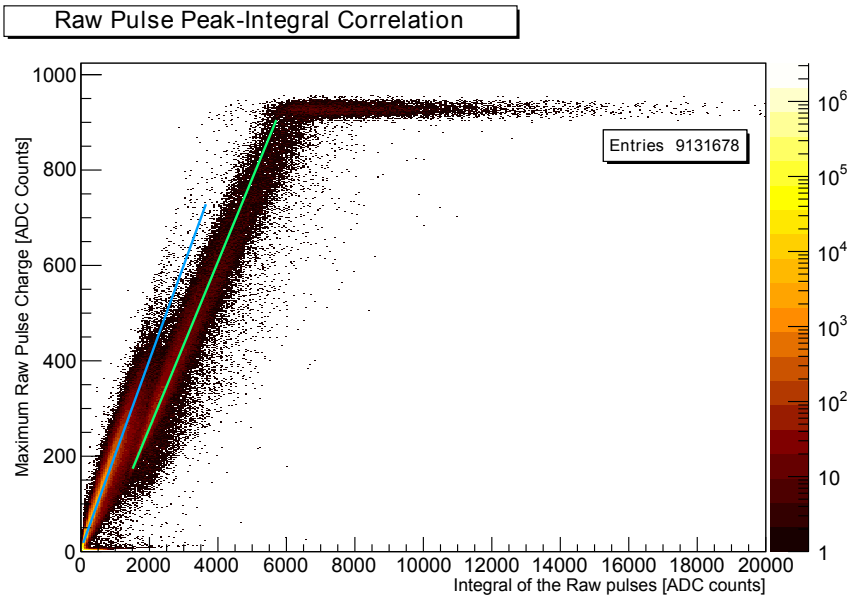

Figure 9.15: Amplitude-Integral correlation for *raw data pulses*. Two groups of them are visible, each with a different linear correlation between the observables.

different correlation characteristics, highlighted in that plot with lines of different colours. According to our hypothesis those two groups would correspond to signals with different shapes, one dominant at low amplitudes, while the other characteristic of the larger signals.

The difference between these two groups was identified in the different behaviour of the long tails of the recorded signals, a phenomenon we discussed earlier in § 9.4. When the signals are small, in fact, they decay quickly below the zero-suppression threshold and the electronics cuts them off efficiently. For signals of amplitude larger than roughly 150 ADC counts, the pulse tail often decays to a baseline that is larger than the zero-suppression threshold. In these cases the signals can be as long as the entire acquisition window.

This effect can be observed in fig. 9.16, where the correlation between the signal amplitude and its length is plotted. Here it is very easy to observe the expected behaviour that is how, for signals larger than about 150 ADC counts, the tail extends for the whole length of the acquisition window, giving rise to very long pulses, grouped on the far right of the plot.

For this reason, when integrating the signal over its full length above the zero-suppression threshold, we are effectively adding a constant offset which explains the presence of the two separate group of recorded signals.

This problem is solved in the pulse reconstruction process by defining a high enough cut-off threshold for the pulse trailing edge and by using an algorithm to effectively eliminate the signal tails when the difference between successive samples is smaller than the intrinsic electronic noise.

The effect of the pulse reconstruction algorithm on this benchmark can be observed in fig. 9.17. Here we consider only those signals reconstructed by the pulse finder algorithm and we measure their amplitude and integral with the same methods used for the raw data.

In this case we can observe a very good linear correlation between the two quantities

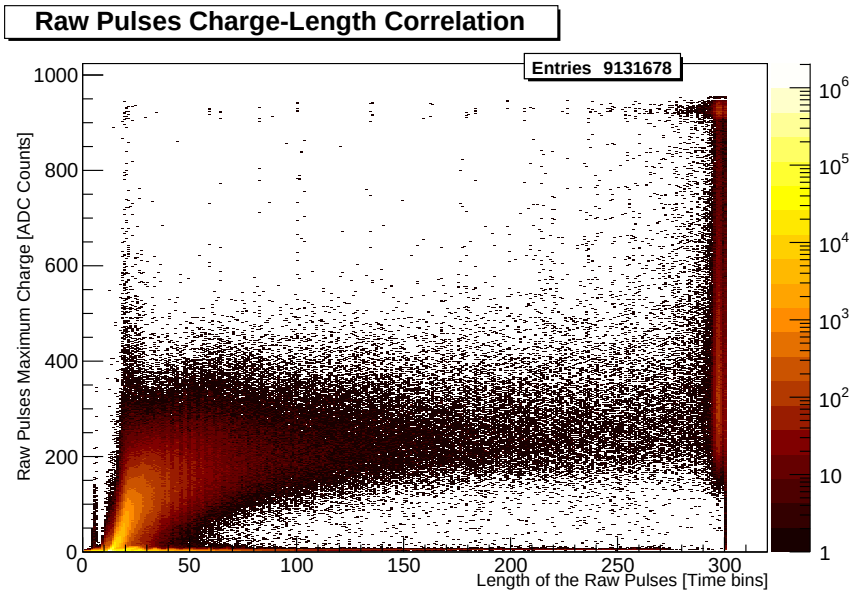

Figure 9.16: Amplitude-Length correlation for *raw data pulses*. It is possible to see here as well how the signals are divided in two categories with the *raw pulses* of larger amplitude also being as long as the maximum allowed.

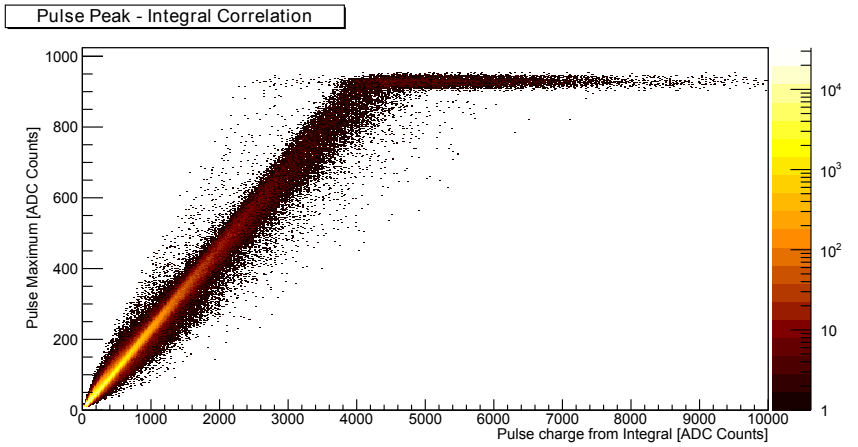

Figure 9.17: Correlation of the amplitude and the integral of the pulses recognized by the reconstruction software. The two quantities are recalculated from the spectrum of the signal used by the pulse finder with the same algorithm used for the raw data.

that justifies the usage of the simpler integral method to calculate the pulse charge.

9.6 *GridGEM module* detection efficiency

One of the more relevant feature that can be observed in the data is the important charge deficiency at the edge of the *GridGEM module*. This effect can be qualitatively appreciated in both figs. 9.6 and 9.7, representing the total charge accumulated on each pad in the raw signals and reconstructed pulse data respectively. In this section we will quantify this effect comparing the related measurements at different drift lengths.

To perform this analysis we are going to use the data reconstruct up to the hit level of the 0 T Z-scan set (§ 8.9.3). We are going to use these data to do two types of measurements:

- We will first evaluate the row-wise detection efficiency, that is the probability, for

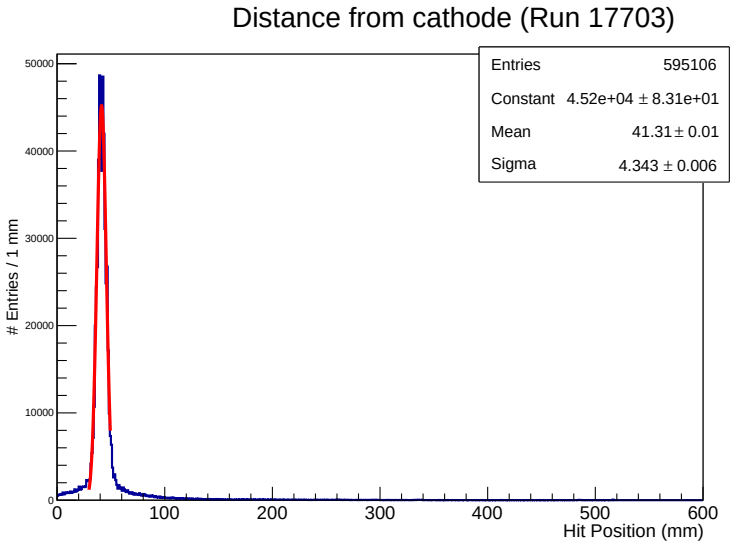

Figure 9.18: Distribution of the hit coordinate along the drift direction for a test-beam run. The peak of the distribution was fit with a Gaussian function to measure the beam position and width.

each of the sensitive pad-rows, to reconstruct a hit in single track events.

- Afterwards we can measure, for each sensitive row, the charge collection efficiency, that can be defined as the typical amount collected in that row in an event.

After describing the algorithm used to select the required single-track events, we are going to describe all the measurements and the observable features in the analysed data and finally attempt an interpretation of those data,

9.6.1 Event selection

For this analysis we are going to use data reconstructed up to the hit level but we want to identify single-track events. Additionally we need this tracks to be parallel to the sensitive surface to be able to measure the intended quantity at a fixed distance. Finally we require the track to be in the centre of the sensitive area, far from the central longitudinal element of the ceramic support to avoid any disturbance due to that element.

To avoid being biased by the rows with low efficiency the 3 rows closer to each of the edges are not used in the selection process (row 0 to 2 and 25 to 27). We also excluded the seventh and eleventh row, where we previously detected a dead pad in the sensitive area and the fourteenth and fifteenth which are next to the transverse element of the ceramic support structure.

Using all the hits thus selected we measure the beam position localizing the maximum in the hit-position distribution like that shown in fig. 9.18 and, after fitting a Gaussian function to the peak of the distribution, we select the hits within 3σ from the maximum. This selection limits the number of tracks tilted on the plane perpendicular to the sensitive one.

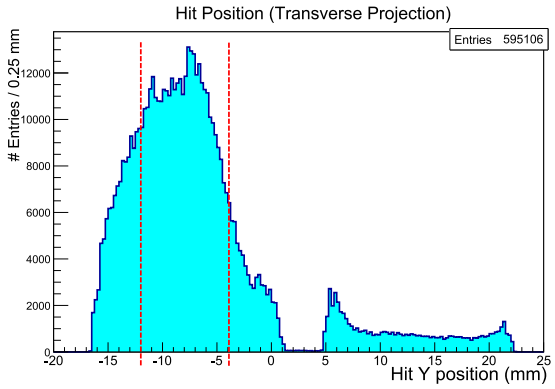

Figure 9.19: Distribution of the hit coordinate along the direction parallel to the pad-rows. The red lines mark the edges of area selected for the hits used in the hit efficiency analysis. These hits are far enough from the edges of the sensitive areas and from the longitudinal ceramic support to avoid a bias.

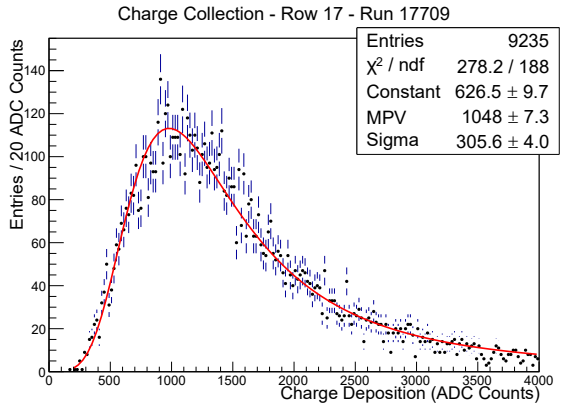

Figure 9.20: Distribution of the charge collected in one of the sensitive rows of a typical test-beam run. We fit the distribution with a Landau function, superimposed to the histogram, to evaluate the most probable charge deposition.

The next step in the selection process is to remove those tracks tilted in the plane parallel to the anode and crossing the radial element of the ceramic support. This selection is based on the radial coordinate of the hits that is shown in fig. 9.19.

The most relevant feature in this distribution is, in fact, the wide gap visible in the middle. About 3.5 mm in width, this gap matches the position of the radial ceramic element and the size of this effect is compatible with what previously observed and reported in [88].

Considering that most of the hits recorded in a 0 T test-beam run are built using the signal of no more than 6 pads, as we will describe in more detail later, we will remove all the hits closer than 5 mm to either the central longitudinal support or to the edge of the sensitive area. The red lines in fig. 9.19 limit the selection region.

To eliminate multiple-track events we then required at most one hit to be recorded in each of the sensitive rows and we finally select an event if at least 12 of the 18 relevant rows recorded a hit.

In the following analysis we will assume that this selection will give us a pure sample of single track events. From fig. 9.18 we can estimate that the background due to noise hits is negligible, considering we required 12 of such noise hits in a limited volume.

The other possible background is due to a double track merged into one due to the proximity and parallelism of the two trajectories above the whole sensitive surface. Without an external reference it is not possible to accurately quantify this effect but we can evaluate

its relevance looking at the energy deposition in one of the rows in the middle of the sensitive area after applying the selection described previously (fig. 9.20). If the sample contains a relevant amount of double-track events we would observe a significant deviation from the ideal Landau distribution which is not observed in the selected data.

9.6.2 Detection efficiency

The first of the two measurements that we performed on the selected single-track sample is the evaluation of the detection efficiency of each of the sampling layers of the detector, that is for each of the pad rows. We defined this quantity as the probability of recording a hit in the analysed row in a single-track event. If we assume, as we previously justified, that our selected sample has a purity close to 1, we can measure the detection efficiency by the ratio of the recorded hits in a row to the total number of selected events.

The plots showed in fig. 9.21 show that measure for each of the sensitive rows at three different distances of the beam from the anode of the TPC. In general it can be appreciated that the detection efficiency over most of the sensitive surface is close to 100 %. On the other hand, it is easy to notice the relevant drop of the detection efficiency in the rows at the edge of the active surface, that is the first 2 and the last 3, as we previously notice from the charge collection maps.

To better understand the behaviour in those areas we can study the detailed scan of the detection efficiency over the whole drift length in those areas (fig. 9.22). The most relevant characteristic of these plots is the drop of the efficiency as we move towards larger drift length up to about 20 mm after which that quantity remains constant.

Another noticeable feature in fig. 9.21 is the limited efficiency drop in the 7^{th} pad-row, where we previously detected a dead pad in the middle of the analysed area. A detailed scan of the detection efficiency in this specific row, labelled *Row 6*, compared to the two neighbouring layers is shown in fig. 9.23. This plot shows that the effect of this dead pad is relevant only for relatively short drift length and becomes negligible for distances larger than about 200 mm.

The last area in which we want to evaluate the detection efficiency in more details is the one around the transverse ceramic element of the support structure. For this we generated a plot of the detailed scan of the detector efficiency at different lengths, analogous to those previously presented, which is shown in fig. 9.24. From this plot we cannot observe any relevant effect of that support element on the detection efficiency.

9.6.3 Charge collection efficiency

The second and complementary benchmark measurement that can be done on the same data set is that of the charge collection efficiency. We previously defined this quantity as the typical amount of charge collected in each row in a single track event.

The amount of charge collected in a sampling layer is a statistical quantity that, for thin enough materials should follow a Landau distribution. The 5.8 mm deep gas layer sampled by each row qualifies as thin, from this point of view, and we can fit the observed

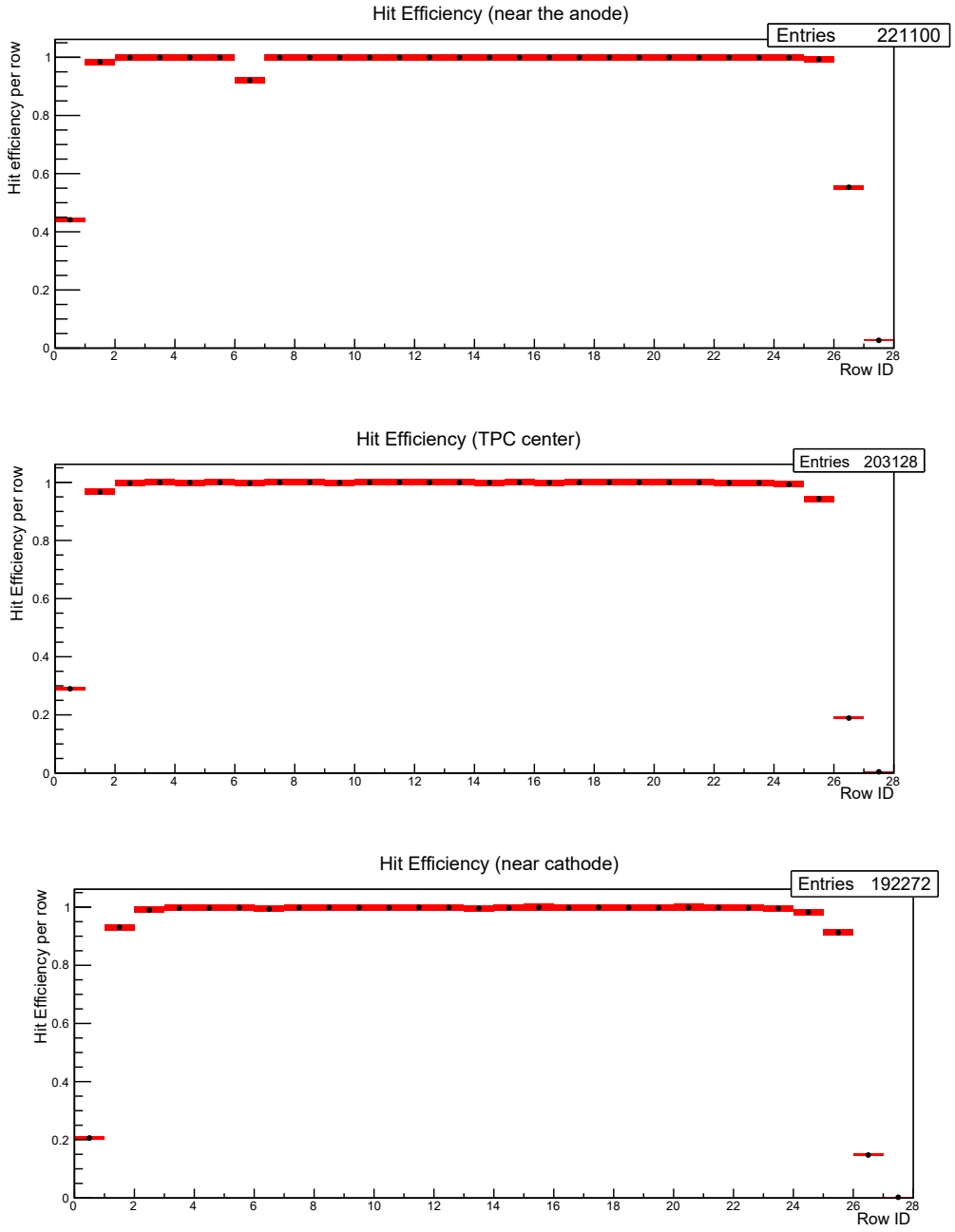

Figure 9.21: Hit detection efficiency for each of the sensitive pad-rows. The red box around each data point identifies the statistical error of the measurement. The three measurements were performed with the beam crossing the TPC at different distances from the anode.

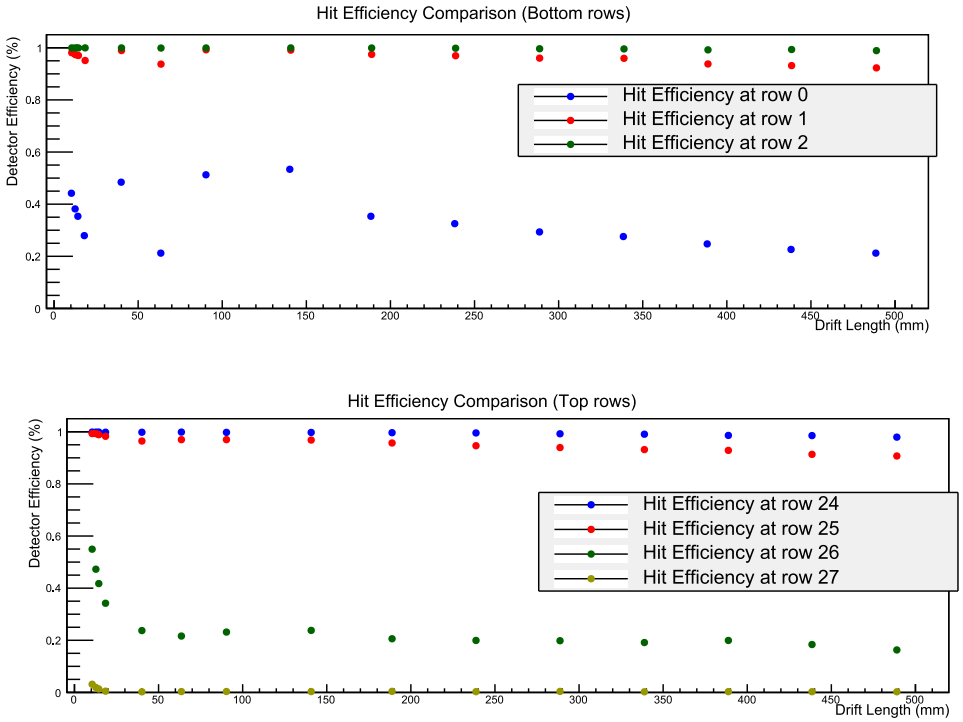

Figure 9.22: Hit efficiency for the lower 3 rows of the sensitive surface (upper plot) and for the top 4 (lower plot). The error bars, when not visible, are smaller than the marker. The abscissa of each point is determined using the position of the peak in the distribution shown in fig. 9.18.

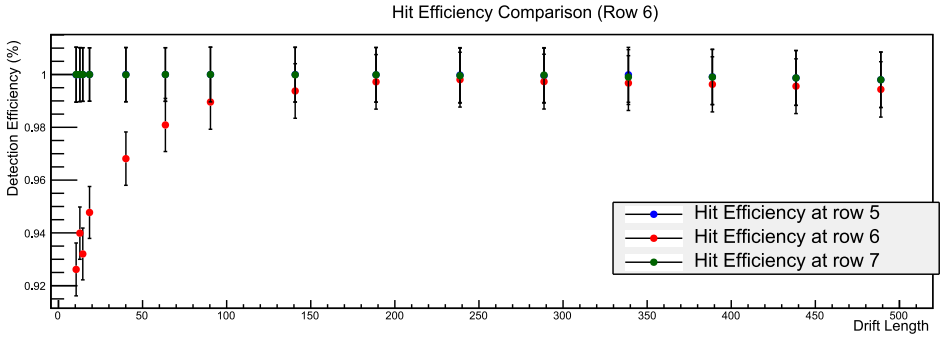

Figure 9.23: Comparison of the hit detection efficiency of the seventh row of the module and the two neighbouring ones. In the seventh row a dead pad was detected previously. The abscissa of each point is determined using the position of the peak in the distribution shown in fig. 9.18 to measure the distance from the cathode.

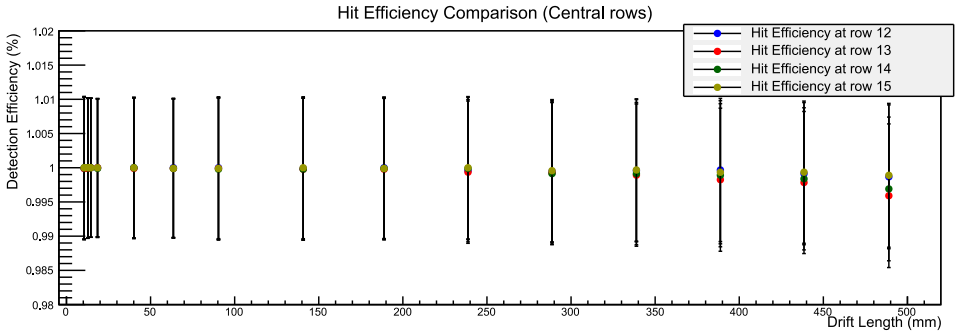

Figure 9.24: Comparison of the hit detection efficiency for the rows closer to the concentric ceramic support structure. The abscissa of each point is determined using the position of the peak in the distribution shown in fig. 9.18 to measure the distance from the cathode and the total length of the TPC to get the drift distance.

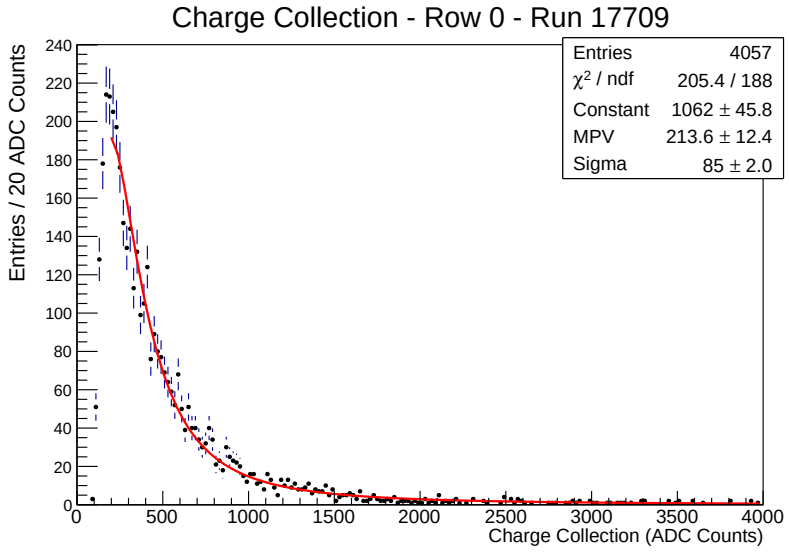

Figure 9.25: Distribution of the charge collected in one of the sensitive rows at the edge of the active surface in a typical test-beam run. Because of the limited efficiency in that region, the most probable value of the landau fit falls below the detection threshold which is roughly between 150 and 200 ADC counts per hit.

distribution with a Landau function to extract the most probable value and the statistical error on the determination of this value to characterize the measurement in each row.

An example of such a plot for one of the rows in the central area of the sensitive surface was previously shown in fig. 9.20 and it is easy to observe a good agreement between the fit and the data.

On the other hand the same method is not as reliable when applied to the first (*Row 0*) and to the last two rows (*Row 26* and *Row 27*). In that case, as visible in fig. 9.25, due to the charge deficiency we observed, the most probable value of the Landau distribution falls below the hit detection threshold that, depending on the hit width stands between 150 and 200 ADC counts. For this reason, even though the automatic fitting procedure is often able to converge to a result, the value obtained shows larger statistical errors and can be potentially biased towards higher absolute values.

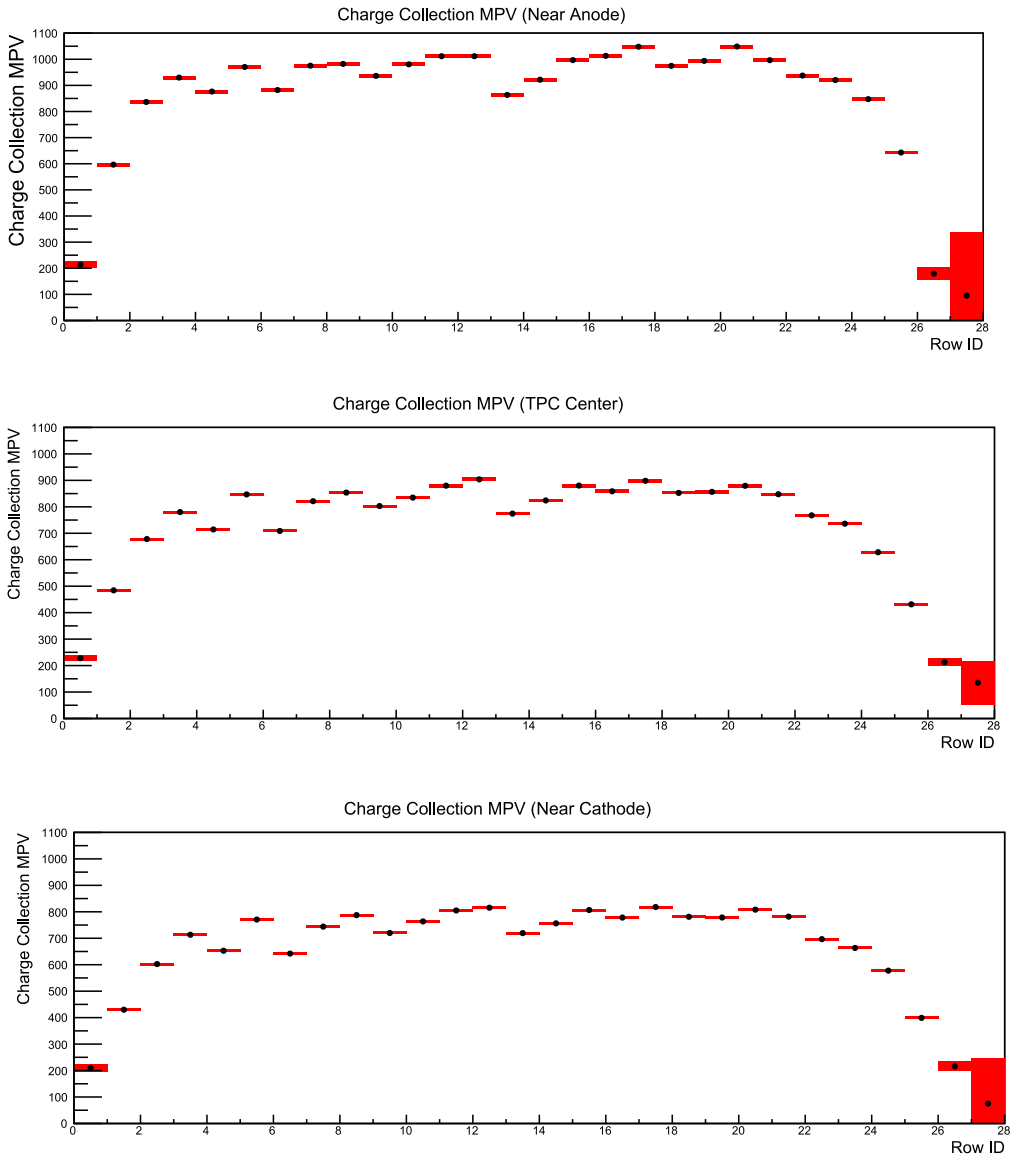

Figure 9.26: Comparison of the charge collection efficiency at different drift length for all rows. The plotted value is obtained extracting the most probable value from the fit of a Landau function to the charge collection distribution. The error for each value is obtained from the fitting procedure. The value in the first and in the last two rows must be considered unreliable due to the most probable value falling below the charge detection sensitivity threshold.

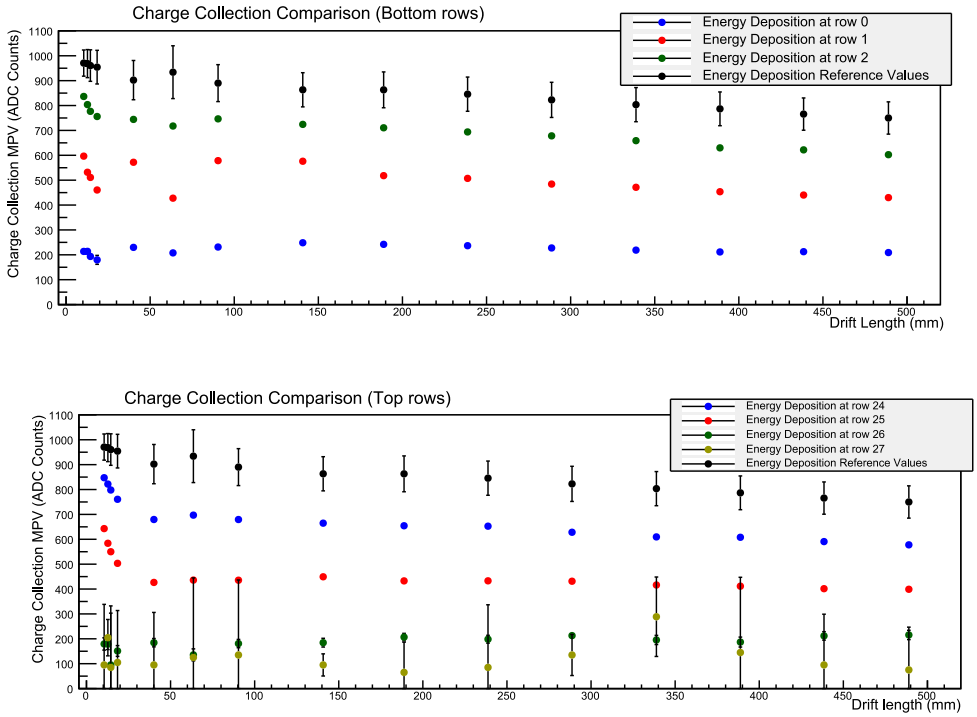

Figure 9.27: Comparison of the charge collection efficiency for the lower 3 rows of the sensitive surface (upper plot) and for the top 4 (lower plot) at different drift lengths. The error bars depicted in the plot only include statistical errors. The algorithm to calculate the reference points is described in § 9.6.3. The abscissa of each point is determined using the position of the peak in the distribution shown in fig. 9.18 to measure the distance from the cathode.

As we did previously for the detection efficiency measurement, we can plot the charge collection efficiency for all the sensitive rows at three relevant positions inside the TPC (fig. 9.26). If we exclude those rows at the edges, the fluctuation on the charge collection is of the order of 10% at all drift lengths.

Because we do not have an absolute reference to compare our measurement of the charge collection, due to the lack of an absolute charge calibration of the electronic system, we need to extract a reference measurement from the data themselves to evaluate the charge collection deficiency. We will compute this reference from the mean of the charge collection in the rows we used for the selection process. The error on each reference measurement is the standard deviation of the same sample.

As before we can start looking at the region at the edge of the sensitive surface where we noticed a clear charge deficiency (see fig. 9.27). In the edge rows we observe the charge collection efficiency dropping in the few centimetres closest to the anode, after which it remains almost constant up to the cathode. In the reference plot, on the other hand, the rate of change of that variable is roughly constant at all drift lengths, the expected behaviour if that charge deficiency is only due to the recombination of the primary

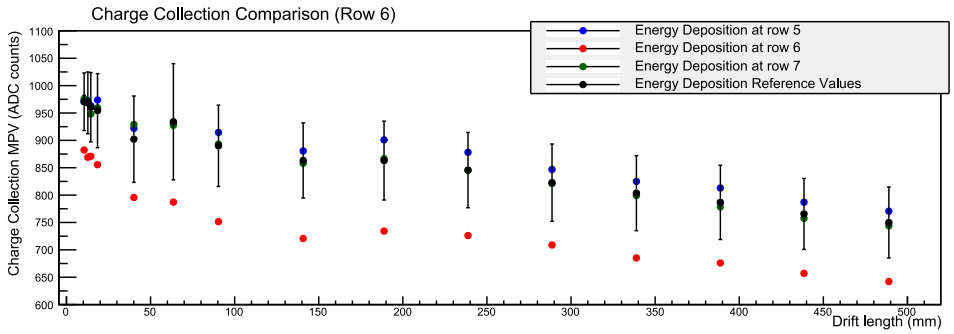

Figure 9.28: Comparison of the charge collection efficiency in the seventh row of the sensitive area and in the two neighbouring rows. In the seventh row a dead pad was previously detected. The error bars depicted in the plot only include statistical errors. The algorithm to calculate the reference points is described in § 9.6.3. The abscissa of each point is determined using the position of the peak in the distribution shown in fig. 9.18 to measure the distance from the cathode.

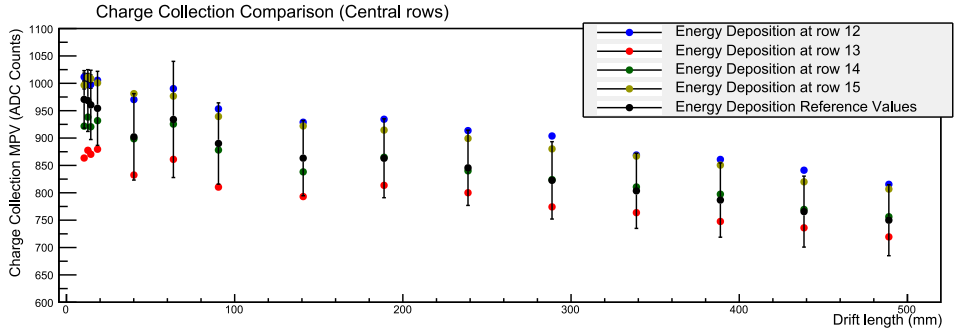

Figure 9.29: Comparison of the charge collection efficiency in the 4 rows closer to the concentric ceramic support element. The algorithm to calculate the reference points is described in § 9.6.3. The abscissa of each point is determined using the position of the peak in the distribution shown in fig. 9.18 to measure the distance from the cathode.

ionization electrons in the drift volume. We will try to give an interpretation to this observation at the end of this section.

The second area we need to analyse is that surrounding the dead pad in the seventh sensitive row. The comparison between the charge collection efficiency in that row and in the two neighbouring ones is presented in 9.28. In this case we record a sensible charge deficiency, uniform between 10% and 20%, in the row with the dead pad.

Finally, using the same type of analysis, we can take a look at the collection efficiency in the neighbourhood of the central, concentric element of the S^3 system. In this case it is very interesting to notice that the support element seems to have a small, almost negligible effect on the charge collection. For one row the measurement is perfectly in line with the mean value of the reference data, while the other shows a systematic deficiency smaller than the standard deviation of the value measured in all the other rows.

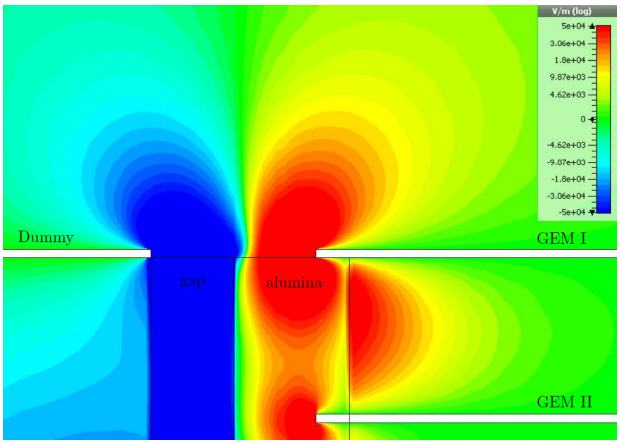

Figure 9.30: Electrostatic simulation of the gap between the *GridGEM module* and the neighbouring dummy module. The microscopic structure of the GEM is not simulated. The contour lines between different colours represent the equipotential line of the electric field component parallel to the GEM layer. The spatial scale can be deduced from the distance between the GEM layers which corresponds to 2 mm. From [116].

9.6.4 Field distortions and detector efficiency

The measurement that we described in the first part of this section allowed us to characterise and quantify the charge collection deficiency we clearly noticed in the raw data (see fig. 9.6). An important conclusion we can reach observing the available data, is that this effect is unlikely due to the mere presence of the ceramic support structure. In fact we noticed that the central transverse element has no relevant effect on both the detection and charge collection efficiency.

In a TPC, a well known and common cause of similar effects is a distortion of the electric and/or magnetic field inside the drift volume. In our case all the observations were performed without a magnetic field, thus we can completely discount its influence.

We can also observe that the missing charge at the edges of the module is not compensated by an increased collection in the immediate neighbouring rows which implies that those missing electrons ended up on a non-sensitive surface. Considering the radial development of the observed phenomenon we can assume that the electrons are somehow deflected in the radial direction, away from the sensitive volume. Those considerations lead us to hypothesize that the observed charge deficiency could be due to the distortions of the electric field in the drift volume caused by the gap between neighbouring modules.

To verify this hypothesis we performed an electrostatic simulation of the gap region using a simplified model of the interface between the bottom edge of the *GridGEM module* and the neighbouring dummy module. We choose to model the bottom edge instead of the top one, where the deficiency is more severe, because of the absence of any high voltage power line in that region which would make the simulation more complex and more difficult to interpret.

The results of this simulation, described in detailed in [116], are visually represented in fig. 9.30 where we can observe the magnitude of the radial component of the electric field in the proximity of the module gap region.

In a perfect configuration this component should be negligible everywhere in the sensitive volume, compared to the field component perpendicular to the GEM layers. In our

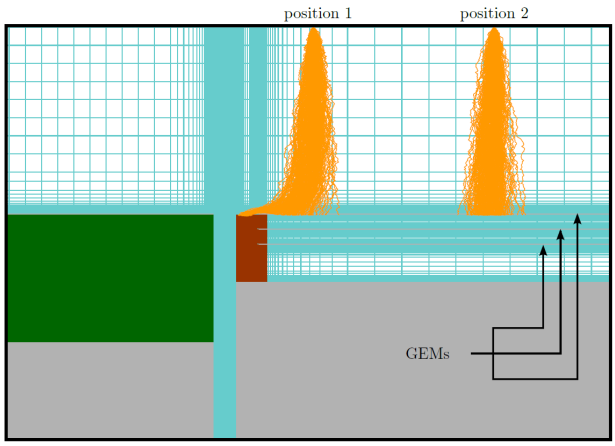

Figure 9.31: Simulation of two electron bunches drifting in the vicinity of the edge of the module (position 1), and outside of the influence of the gap distortions (position 2). The electrons are then further propagated through the GEM layers without amplification. From [116].

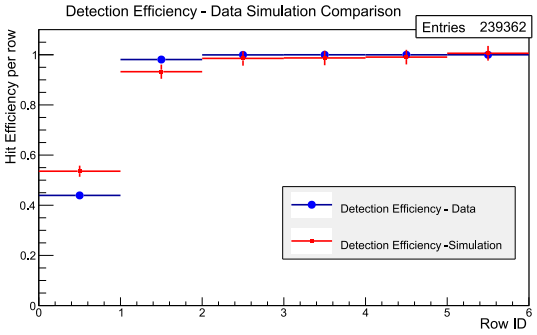

Figure 9.32: Simulation of the effect caused by the field distortions on the amount of charge collected by the detector. The simulation do not include the charge amplification within the GEM layers. The data used in this comparison were acquired in the anode's proximity. The simulated data were generated by K. Zenker.

case we observe fields that are more than twice as large as the nominal drift field[10] and extending for several mm within the drift volume.

The field-map thus obtained is then used to simulate the drift towards the anode of several group of electrons, starting at different radial positions. The results can be seen in fig. 9.31 for two different positions above the sensitive surface. This result could explain the observation of a steep decrease of the charge collection efficiency within the first cm, while approaching a constant behaviour after that. In fact, if the primary electron cloud is originally generated in the proximity of the first GEM layer, the charge carrier will be drifting in the radial direction for a shorter length, thus reducing the observed deficiency.

Finally we can compare the results of this simulation with the data we acquired in the test-beam campaign. This comparison is presented in fig. 9.32 and it can be seen that the simulation reproduce the data quantitatively with good accuracy.

9.7 Charge sharing

An important benchmark to evaluate the quality of our design is to measure the charge sharing among neighbouring pads. As we discussed in § 9.1.2, to eliminate the bias in the position determination obtained with the centre of gravity method, it is necessary to

[10] 500 V/cm as compared to 220 V/cm

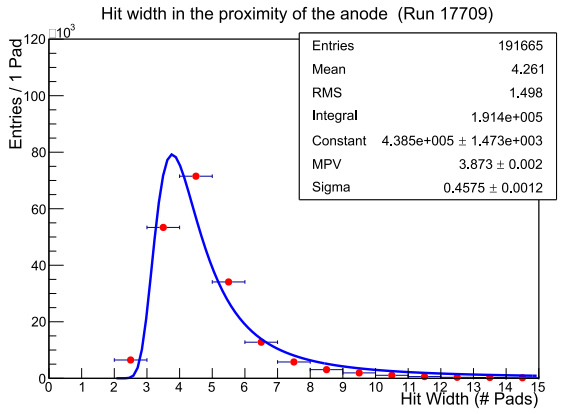

Figure 9.33: Spectrum of the hit width in the vicinity of the *GridGEM module* anode, corresponding to a drift length of 49±10 mm. The hit selection algorithm is described in the text. Superimposed to a data point we fit a Landau distribution.

spread the charge among at least 3 neighbouring pads. The relevant observable in this case is what we previously called the hit width (see eq. 9.1): the number of pads in a row used to reconstruct the hit.

To avoid the influence of the field distortions we previously identified, we are going to only select those events that pass the selection algorithm described in § 9.6.1. Within these events we only select hits in rows where we didn't record any appreciable charge deficiency.

The spectrum of the width of the selected hits selected is shown in fig. 9.33 for a drift length of 9 ± 6 mm, corresponding to the data set closer to the anode. In these conditions, which are the worst case scenario for this type of measurement we can observe that almost the totality of the recorded hits have a width of 3 pads or more, which ensure an unbiased centre-of-charge reconstruction.

We can also assume the hit width to be correlated to the energy loss in the primary ionization event. In fact the range of the electrons directly knocked out by the incoming particle is proportional to the energy transfer in the ionization event. For this reason we can attempt to fit a Landau function to the hit width distribution and we can indeed notice a very good agreement with the data.

To evaluate the behaviour of the hit width at difference drift lengths we plotted the most probable value of the Landau distribution we fit to the data at different drift lengths. The result of such process is shown in fig. 9.34.

Theoretically the hit width is determined by the size of the primary electron cloud, which depends only on the ionization processes, and by the random-walk diffusion of such a cloud while it drifts towards the anode (§ 4.2). The spread of the diffusion cloud is described by eq. 4.9, thus the hit width should be described, in first approximation by a function of the type $p_0 + p_1\sqrt{x}$, where p_0 represents the constant diffusion within the amplification stage while p_1 is proportional to the diffusion constant $\tilde{D}$. Fitting this function to the observations we obtain a value for the constant term of $p_0 = 3.34 \pm 0.01$ pads $= 4.18 \pm 0.01$ mm compatible with what we observed in fig. 9.33.

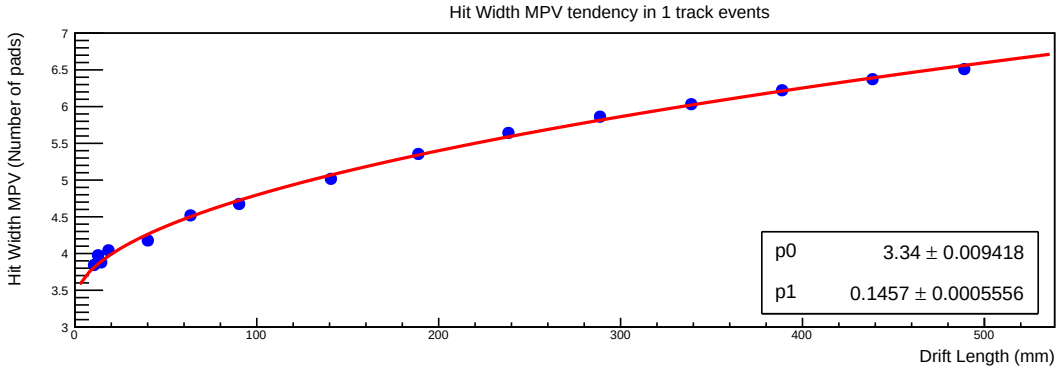

Figure 9.34: Most probable value of the hit width at different drift lengths. Each data point is obtained from the MPV of a Landau function fit to the hit width distribution recorded for a single test-beam run. The error bar, smaller than the marker, is the statistical error on the determination of the MPV from the fit. The algorithm to select the hits is described in the text. The points were fit with the following function: $p_0 + p_1\sqrt{x}$

Conclusions and outlook for future optimizations

The main topic of this part of the thesis is the description of the design, development and test of the first prototype of a new readout module for a large TPC, itself a prototype of the larger tracker designed for the ILD experiment at the ILC (§ 2 and § 3).

This readout system, called the *GridGEM module*, consists of a pad readout board with an extremely high channel density, necessary to achieve the position resolution of better than 100 μm over the entire drift length, required by the ILD TPC. This readout structure was designed to be operated with up to 4 GEM, used to achieve the gas amplification, integrating the HV power supply of the GEM stack in the most compact way possible inside the same board hosting the sensitive surfaces.

One of the most relevant innovation of our design is the introduction of a ceramic-based support system for the GEM foils which acts at the same time as a spacer between the layers, as a tension relief for the stretched foils and as the main mechanical support for the assembled stack. Additionally it provides the necessary insulation between the high voltage connectors and the signal pads on the drift-side of the readout board surface. This design, called the S^3 system, is described in details in § 7.4. Using it we were able to reduce the dead area in a single module from about 15% necessary with a traditional GRP frame to less than 5%. Additionally, the optimized version of this design does not have any ceramic element perpendicular to the pad-rows, excluding the framing at the very edge, and, as we demonstrated in § 9.6, those spacing elements that are concentric with the readout rows do not reduce the detection efficiency of the *GridGEM module*.

Another important goal of the project was to design a system that could be produced on a semi-industrial scale so that could be used to equip the readout surface of the ILD TPC. To achieve this goal we established a precise set of assembly and test procedure for our detector which could be automated and improved to achieve a good uniformity in the performances of the single components and of the detector as a whole.

Those assembly procedures were summarized in § 7.6 and the details of the most important steps where provided in § 8. It is remarkable to notice that, once all the preliminary gluing processes are completed, it is possible to assemble a complete module in about an

hour.

One of the most delicate and important steps of the whole procedure is the stretching and gluing of the GEM foils on the ceramic support elements. To perform this task in a reliable and repeatable way we developed an automated procedure, described in § 8.7. While the glue disposal and the assembly of the foil with the ceramic component is working reliably and efficiently, one step of this procedure should be further optimized and that is the stretching of the foil prior of the gluing. At the moment this is done manually and requires a certain degree of manual ability from the operator. In the future a more sophisticated procedure should be devised that allow a better control on the tension applied to the foil.

We validate our design through two sets of tests. On one hand every component of the assembly undergoes a specific testing procedure to make sure that it performs as good as required. After the assembly we tested the whole detector, first without any radiation source in a drift chamber specifically built for that purpose, and finally at the DESY test-beam infrastructure, installed in the LP-TPC.

This test sequence is particularly important for the GEM foils to evaluate and test their reliability and reduce the probability of discharges which can depolarize or damage the foils. For this reason the foils are subject to a lengthy test at every step of their assembly in the detector and this allowed us to reach high levels of reliability with a detected discharge every few days.

The final and most important test of our detector was the operation of the system at the LCTPC test-beam infrastructure at DESY. During that campaign we managed to acquire more than 2 million events which allowed us to perform the initial characterization of the *GridGEM module*. Unfortunately the amount of data that were acquired was limited by some technical problems affecting the *GridGEM module* and the test-beam infrastructure.

The most severe of those problems was the realization that, when mounted in the LP-TPC, even a single discharge was able to destroy one or more sectors of the GEM foils of the *GridGEM module*. This serious problem allowed us to identify several potential problems in the discharge protection system of our detector and to improve our design to mitigate those potential issues. Nonetheless, as the same type of discharges appeared again later while using the improved design, we also realized that the main source of those discharges was the LP-TPC itself, and this experience allowed us to improve that detector as well.

The analysis of the test-beam data was performed within the scope of this project and of another thesis published within our group [110]. To perform this analysis and to evaluate the basic performances of the system already during the data taking, I developed a software package, integrated in the wider scoped ILCSoft framework. In this document I evaluated the basic performances and operational parameters of the *GridGEM module* name including:

- The efficiency of the readout system in terms of noise and dead channels;
- The optimal operational parameter of the ALTRO DAQ applied to our detector;
- The detection and charge collection efficiency of the prototype;

- The correct choice of the GEM stack operational parameters, allowing an optimal charge sharing between the readout pads.

The last two points of that list deserve a few more words in this section, as they can be considered the most relevant benchmarks of the low level performances of the *GridGEM module*.

The measurement of an hit width larger than three pads even at the shortest drift distances and without magnetic fields, confirms the appropriate choice of the readout board pad width in relation with the geometry of the GEM stack. Those measurements were performed using a simplified board layout and their results gave us confidence to produce the more complex board that is to be used in the next tests.

The most relevant feature that is clearly visible even without any analysis or reconstruction is a remarkable deficiency in the charge collected near the edges of the board, in the first pair of rows on each side. After an accurate measurements, and with the support of an electrostatic simulation of those areas, we concluded that those inefficiency were caused by the electric field distortions due to the sizeable gap between neighbouring modules. After our measurement a similar phenomena was also noticed on several other types of LP-TPC modules. The field distortions could be reduced introducing some type of field shaping structure on the side of the ceramic support facing the gap. This improvement is under consideration for the next iteration in the development of the *GridGEM module*[11].

[11] This part of this thesis was completed and written in 2013. Since then the development of the *GridGEM module* continued but the writer didn't work on it any longer. Therefore the presented outlook represents the view of the author at the time of the completion of the experimental work, that is in 2013

Part III

A new algorithm for the measurement of the kinematic edges positions in SUSY decays decays.

Chapter 10

Supersymmetry at a lepton collider

In recent years the experimental signatures of supersymmetry were searched for at many high-energy particle accelerator experiments. Nonetheless no direct indication of any new particle described by any of the supersymmetric extensions of the SM has been found. This scenario could radically change in the next years with the new experimental runs of the LHC and with the construction of a new electron-positron collider, currently under design, that is the ILC.

As discussed in § 1.3.3 and 2.1, due to the different nature and entity of the background processes, a lepton collider like the ILC is able to perform accurate measurements of the masses and the couplings of several particles that might be discovered by the LHC and will have the potential to discover other particles that would be invisible at the LHC due to its experimental conditions [117, 50]. In particular, because the production cross-section for coloured particles is relatively higher at the LHC, the ILC will be more sensitive than the the hadron collider to any s-lepton within its kinematic reach.

As supersymmetry is experimentally unverified, the values and even the number of its free parameters depend on the specific model one chooses to study and those assumptions on which the model depends. Nonetheless, in any supersymmetry model there must be one particle which is the lightest, the *LSP*[1]. Assuming it is stable or at least long-lived on the time scales of the typical particle physics detector and assuming it is at most weakly interacting it will leave the detector undetected. Therefore, if a supersymmetric particle produced in a collider experiment decays in the LSP and in one or more Standard Model particles, the event kinematics is underconstrained and the masses of the unknown particles must be inferred from the position of the end-point of specific kinematic distributions.

In this chapter we will discuss the importance of those kinematic endpoints to infer the parameters of the supersymmetric particles produced in a collider experiment and we will specifically analyse the case of an s-electron production and decay at a lepton collider like the ILC where the masses of both the s-lepton and the final-state Neutralino can be calculated measuring the position of the edges in the momentum distribution of the final-state electrons. Finally, to be able to evaluate the performance of the ILD in a

[1] *Lightest Supersymmetric Particle*

concrete experimental scenario, in § 10.3 we described how the benchmark model to test SUSY predictions are defined and we will give more details on a specific one, called the $\tilde{\tau}$ *coannihilation scenario*, used to evaluate the performance of both the ILC and the LHC experiments.

10.1 Kinematic endpoints in SUSY analysis

If we assume R-parity conservation, the LSP of any Supersymmetric model must be stable and, because it was never detected, should be, at best, weakly interacting. This implies that, when Supersymmetric particles are produced in a collider experiment, the LSP will escape detection. In those cases, to measure the masses of those unknown particles, it is necessary to use the endpoints of some kinematic observable of the visible decay products like their invariant masses or, when the initial centre-of-mass energy is known, the momenta of those particles. This is a commonly used technique which is applicable at hadron colliders like the LHC as, for example, in [118, 119, 120, 121] and many others, as well as at lepton colliders like the ILC as was done, for example, in [122, 123, 117].

The typical method to determine the position of edges and end-points in those analysis is to fit an arbitrary function in the pre-identified edge region and correlate one of the fit parameters to the observable position to measure. Even assuming that the preliminary identification of the regions of interest could be done with perfect efficiency, the major conceptual problem of this approach is that the actual shape of the edges or of the end-points can be strongly dominated by effects that have little to do with the initial theoretical distribution which lead to the choice of a specific fit function.

It is therefore important to develop a technique to precisely measure the position of edges or end-points which, avoiding modelling the shape of those features, can be robust against eventual distortions which cannot be analytically described. An example of such effects can be those induced by unknowns in the initial state or in the detector reconstruction. To keep the model independence, the optimization procedure should also be data driven up to the determination of a calibration factor relating the actual measurement to a particular model dependent observable. Theoretically the identification of the characterizing feature, i.e. the kinematic edge, and the optimal measurement of its position can be performed independently but it would be desirable to perform both tasks with the same technique.

Such technique would be particularly useful when applied to processes where the feature shape is strongly distorted by effects which are unrelated to the particular physical process under study and where the experimental conditions enhance the importance of a model independent approach and the utmost measurement precision is required.

One such a process is the decay of a light s-lepton produced at a lepton collider in a neutralino and the matching Standard Model lepton. There the determination of the masses of the Supersymmetric particle involved can be done by measuring the position of the kinematic edges in the spectra of the momenta of the visible decay products. Among the three flavours, due to the particularly high production cross-section and the relevant

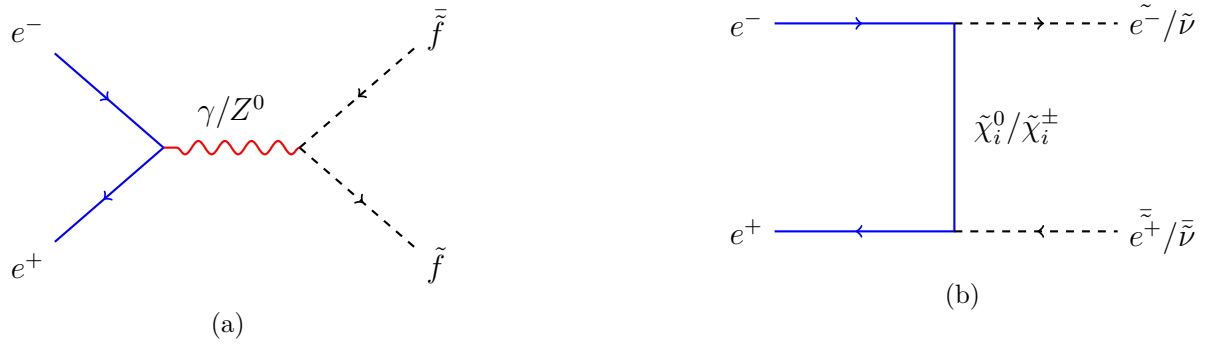

Figure 10.1: Comparison of the sfermions production processes. In a the annihilation process produces all kinematically accessible sfermions in a "democratic" way. In b, the exchange diagram is available only for the production of $\tilde{e}$ and $\tilde{\nu}$

distortions caused by detector effects and by the intrinsic uncertainties in the centre-of-mass energy, we choose the electronic sector as our favourite benchmark by analysing the production of a pair of $\tilde{e}_R$ at the ILC and their subsequent decay in a pair of $\tilde{\chi}_1^0$ and a pair of $e^\pm$.

We would like hereby to notice that, while this analysis was being developed, another method was applied to the same problem which satisfies most of the requirements I described in this section [123]. In that work, the edges position is determined by sub-dividing the full data sample in smaller sub-sets. In each sub-set the most and least energetic lepton are identified after eliminating the most extreme outliers. The size of each sub-set and the outlier rejection fraction is optimized to yield the lowest possible variance in the endpoint determination. The resulting measurement has a well defined bias compared to the true simulated value and that bias is corrected by means of a toy Monte Carlo calibration procedure which also determine the SUSY masses uncertainty. Using that method the authors claim an achievable mass resolution of $210\,\mathrm{MeV/c^2}$ and $160\,\mathrm{MeV/c^2}$ for the $\tilde{e}_R$ and the $\tilde{\chi}_1^0$ respectively.

Just like the algorithm we are going to describe in this work, that procedure does not require a predefined model for the edge shape and only requires the optimization of a small number of free parameters which can be performed within a data-driven approach. Lacking additional details, the writer cannot evaluate whether this technique is particularly sensitive to a changing background shape and amplitude but it allows to obtain the best published estimation of the s-electron and neutralino masses at a lepton collider and will be therefore used as a comparison benchmark for the algorithm which will e presented in the following chapters.

10.2 $\tilde{e}$ production and decay at the ILC

In an e^+e^- collider, like the ILC, almost all the supersymmetric particles are produced through the s-channel annihilation of incoming leptons in a vector boson, as described by

the diagram in fig. 10.1a. Additionally, for $\tilde{e}$, $\tilde{\nu}$, $\tilde{\chi}_i^0$ and $\tilde{\chi}_i^\pm$, the tree level pair production can happen through the t-channel exchange of, respectively, a $\tilde{\chi}_i^0$, $\tilde{\chi}_i^\pm$, $\tilde{e}$ or $\tilde{\nu}$, like the one shown in the Feynman diagram of fig. 10.1b. In the case of the s-fermion production, the two diagrams interference is constructive leading to a relevant enhancement of the cross-section. As one of the supersymmetry's corner-stones is that any SM particle must have the same couplings and mixing angles as the corresponding s-particle, the cross-section is determined by defining the centre-of-mass energy and the masses of the particles to produce. The detailed formulae for the calculations of all those cross-sections can be found in the literature, for example in [124].

Another important difference between the two processes is that, through the s-channel annihilation we can only create particle-antiparticle pairs with the same chirality index, e.g. $\tilde{e}_R\bar{\tilde{e}}_R$ and $\tilde{e}_L\bar{\tilde{e}}_L$. On the other hand, through the exchange process, the outgoing s-particles chirality is correlated to the incoming particles polarization which means that we can also produce pair of $\tilde{e}_R\bar{\tilde{e}}_L$ or the matching anti-couple. Therefore we can use the beam polarization to selectively enhance some t-channel processes as can be appreciated in tab. 12.1.

10.2.1 The distribution of the $\tilde{e}$ decay products

One of the most important features of the processes involving the lightest charged s-leptons ($\tilde{\boldsymbol{\ell}}$) in a scenario like those of the STC family, is the exclusive two-body decay of the produced s-particle in a neutralino and the matching Standard Model partner.

Such a constrained kinematic configuration, assuming the knowledge of the initial condition, that is the centre-of-mass energy $\boldsymbol{E_{CM}}$ and the masses of the $\tilde{e}$ and the $\tilde{\chi}_1^0$, respectively $\boldsymbol{M_{\tilde{e}}}$ and $\boldsymbol{M_{\tilde{\chi}_1^0}}$, allows to calculate analytically the distribution of the decay products.

We will start by defining $\boldsymbol{S_{\tilde{e}}}$ as the rest frame of the $\tilde{e}$ with the z-axis oriented along the direction of the electron emission. In this frame, the $\tilde{e}$ 4-momentum $\boldsymbol{P_{\tilde{e}}}$ is simply defined by its mass:

$$P_{\tilde{e}} = (M_{\tilde{e}}, 0, 0, 0) \tag{10.1}$$

and we can calculate the electron and neutralino 4-momenta, $\boldsymbol{P_e}$ and $\boldsymbol{P_{\tilde{\chi}_1^0}}$ respectively, imposing energy and momentum conservation. As the electron mass is several orders of magnitude smaller than all the other masses and energies involved in the process we can neglect it:

$$E_e + E_{\tilde{\chi}_1^0} = M_{\tilde{e}} \qquad \text{energy conservation} \tag{10.2}$$

$$E_e^2 - M_e^2 = E_{\tilde{\chi}_1^0}^2 - M_{\tilde{\chi}_1^0}^2 \qquad \text{momentum conservation} \tag{10.3}$$

$$\boldsymbol{E_e} = \frac{M_e^2 + M_{\tilde{e}}^2 - M_{\tilde{\chi}_1^0}^2}{2M_{\tilde{e}}} \overset{M_e=0}{\approx} \frac{M_{\tilde{e}}^2 - M_{\tilde{\chi}_1^0}^2}{2M_{\tilde{e}}} = p_e \tag{10.4}$$

$$\boldsymbol{E_{\tilde{\chi}_1^0}} = \frac{M_{\tilde{e}}^2 - M_e^2 + M_{\tilde{\chi}_1^0}^2}{2M_{\tilde{e}}} \overset{M_e=0}{\approx} \frac{M_{\tilde{e}}^2 + M_{\tilde{\chi}_1^0}^2}{2M_{\tilde{e}}} \tag{10.5}$$

$$\boldsymbol{P_e} = (p_e, 0, 0, p_e) \tag{10.6}$$

$$\boldsymbol{P_{\tilde{\chi}_1^0}} = \left(E_{\tilde{\chi}_1^0}, 0, 0, -p_e\right) \tag{10.7}$$

Then we can rotate the reference frame to align the third axis in the boost direction in the centre-of-mass frame ($\boldsymbol{S_{\mathrm{CM}}}$) and boost it to obtain its representation in that reference frame. We will call the rotation angle $\boldsymbol{\rho}$ while $\boldsymbol{\gamma}$ and $\boldsymbol{\beta}$ are the Lorentz boost parameters. In S_{CM} the 4-momenta of electron and neutralino become:

$$\boldsymbol{P'_e} = (\ \gamma p_e(1 + \beta\cos\rho) \quad , p_e \sin\rho \quad , 0 \quad , \ \gamma p_e(\beta + \cos\rho)\ ) \tag{10.8}$$

$$\begin{aligned}\boldsymbol{P'_{\tilde{\chi}_1^0}} &= \left(\ \gamma E_{\tilde{\chi}_1^0} - \gamma\beta p_e\cos\rho \quad , \ -p_e\sin\rho \quad , 0 \quad , \ \gamma\beta E_{\tilde{\chi}_1^0} - \gamma p_e\cos\rho\ \right) \\ &= \left(\ \frac{E_{\mathrm{CM}}}{2} - \gamma p_e(1+\beta\cos\rho) \quad , \ -p_e\sin\rho \quad , 0 \quad , \ \frac{\beta E_{\mathrm{CM}}}{2} - \gamma p_e(\beta+\cos\rho)\ \right)\end{aligned} \tag{10.9}$$

assuming

$$\gamma = \frac{E_{\mathrm{CM}}}{2M_{\tilde{e}}} \tag{10.10}$$

From these calculations we can observe two important features of the momentum spectrum of the observable electron:

- The spectrum has two end-points which are a function of the centre-of-mass energy and of the masses of the SUSY particles involved:

$$\max(E'_e) = \boldsymbol{E_e^+} = E'_e(\cos\rho = 1) = p_e(\gamma + \beta\gamma) \tag{10.11}$$

$$\min(E'_e) = \boldsymbol{E_e^-} = E'_e(\cos\rho = -1) = p_e(\gamma - \beta\gamma) \tag{10.12}$$

- Because the $\tilde{e}$ is a scalar particle, there is no preferential direction in the decay process so $\frac{dN}{d\cos\rho}$ is constant.

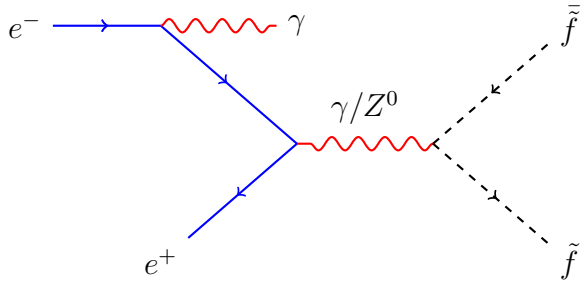

Figure 10.2: Feynman diagram of the ISR process in $\tilde{f}$ production by annihilation.

From those considerations we can deduce that, in the ideal case of a fixed centre-of-mass energy and neglecting any inaccuracy in the reconstruction of the electron's energy, the energy spectrum of the decay products of the $\tilde{e}$ is a uniform distribution between the calculated end-points. We should also notice that the presence and position of such end-points follows from the process kinematics alone and not from the specific production channel of the $\tilde{e}$.

Inverting the equations we can also see that, to calculate the $\tilde{e}$ and χ_0 masses, we need two observables related to that distribution. For example we could choose the position of the two end-points or, alternatively, the width (W_e) and the centre (C_e) of the distribution.

$$\boldsymbol{W_e} = E_e^+ - E_e^- \qquad = 2p_e\beta\gamma \tag{10.13}$$

$$\boldsymbol{C_e} = \frac{E_e^+ + E_e^-}{2} \qquad = \gamma p_e \tag{10.14}$$

$$\frac{1}{\gamma^2} = 1 - \frac{W_e^2}{4C_e^2} \qquad = 1 - \frac{(E_e^+ - E_e^-)^2}{(E_e^+ + E_e^-)^2} \tag{10.15}$$

$$\boldsymbol{M_{\tilde{e}}} = \frac{E_{\mathrm{CM}}}{2}\left(\sqrt{1 - \frac{W_e^2}{4C_e^2}}\right) \qquad = \frac{E_{\mathrm{CM}}}{2}\left(\sqrt{1 - \frac{(E_e^+ - E_e^-)^2}{(E_e^+ + E_e^-)^2}}\right) \tag{10.16}$$

$$\boldsymbol{M^2_{\tilde{\chi}_1^0}} = \frac{E_{\mathrm{CM}}^2}{4\gamma^2} - \frac{E_{\mathrm{CM}}C_e}{\gamma^2} \qquad = \frac{E_{\mathrm{CM}}^2}{4}\left(1 - \frac{(E_e^+ - E_e^-)^2}{(E_e^+ + E_e^-)^2}\right) + \\ - \frac{E_{\mathrm{CM}}}{2}\left(E_e^+ + E_e^- - \frac{(E_e^+ - E_e^-)^2}{E_e^+ + E_e^-}\right) \tag{10.17}$$

10.2.2 A realistic momentum distribution

In the previous section we calculated the momentum distribution of the decay products of the $\tilde{e}$ assuming a fix centre-of-mass energy at the accelerator design value. In the actual experimental conditions, the centre-of-mass energy can be very different as compared to the nominal value we assumed previously due to two important phenomena:

Initial State Radiation In general one or more real photons can be irradiated from one of the incoming leptons thus reducing the energy available at the actual production

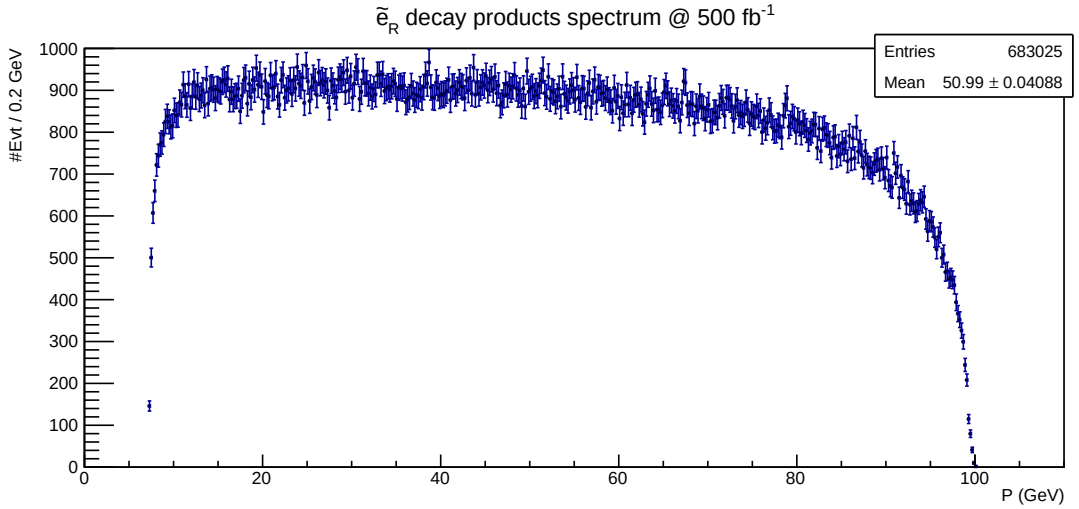

Figure 10.3: Momentum distribution of the electron and positrons produced by the decay of a $\tilde{e_R}$ pair, generated using a realistic beam energy distribution. The masses and cross-section are calculated with the tools described in § 12.1. The momentum is directly extracted from the generator files, before any detector reconstruction is applied. The amount of simulated data corresponds to 500 fb^{-1} at 500 GeV with a 80% right-polarized electrons and 30% left-polarized positrons

vertex (fig. 10.2). In most cases the photon is emitted in the forward direction and cannot be identified by the detector. This is a well-known radiative correction to all QED interaction and its probability with respect to the emission angle can be calculated accurately [125].

Realistic beam spectrum The actual energy of the incoming beam particles depends on the energy distribution within the accelerated bunches which is influenced by the acceleration process, the final focussing and the interaction with the particle bunch approaching from the opposite direction. This last process, in particular, leads to the emission of several highly energetic photons which reduces the available energy in the centre-of-mass.

The net effect of both those processes is a reduction of the centre-of-mass energy which typically cannot be reconstructed on an event-by-event basis as that energy is usually carried away by photons propagating in the very forward direction, that is outside of the geometric acceptance of the detectors. On the other hand those losses can be analysed from a statistical point-of-view and they result in a relevant and asymmetric smearing of the kinematic distribution edges, which can be appreciated in fig. 10.3.

This smearing is further enhanced by uncertainties in the detection process: in addition to the intrinsic detector uncertainties, for electrons and positrons the radiative losses as the particles pass through the detector layers can be relevant. To achieve an accurate measurement of the momentum of the primary particles it is important to reconstruct the correlated products of the radiative events and cluster them together with a specific algorithm.

10.3 SUSY benchmark models

Due to the large number of free parameters of the supersymmetric extensions of the SM it is necessary to apply strict constraints, reducing the dimensionality and extent of the parameter space, to study the phenomenology implied by the chosen model and consequently look for the relevant signatures in the experimental data.

Many of those constraints can be motivated by the general need to ensure the consistency of the SUSY model with the existing high precision measurement of the SM processes (e.g. Proton stability, lepton magnetic moments, CP violation, see [15] and references therein). To further simplify this scenario and choose physically suitable point in the parameter space two general approaches are usually followed:

Top-down or high-energy: In this case one imposes a specific structure to the model at extremely high energies (Planck and/or GUT scale) and evolves it towards the electroweak scale, deriving in this way the low-energy parameters. In most cases the high-energy constraints are derived from a well-defined set of assumption about the supersymmetry breaking mechanism. A popular example of such a model family is *mSUGRA*[2] [126].

Bottom-up or low-energy: In this second approach one starts by choosing a set of low-energy observables that are phenomenologically viable, usually imposing a certain number of additional constraints to avoid the appearance of un-physical features in the model. The full model and, in particular, the s-particle masses and couplings and their high-energy running are then calculated from those assumptions. This approach allows to explore a much wider portion of the parameter space but also involves a much larger number of free parameters and does not imply anything about the actual mechanism of super-symmetry breaking.

A relevant example of the second type is the *pMSSM*[3] model family, described in [127], and used to evaluate the significance of the currently available data and the possible reach of the LHC experiments [128], that reduces the number of free parameters 22 assuming the following constraints:

- All the SUSY-breaking parameters are real and do not introduce new sources of CP-violation, when compared to the SM;
- The matrices of the s-fermion masses and the trilinear couplings are all diagonal, implying the absence of flavour-changing neutral currents at the tree-level.
- First and second s-fermion generation universality at low energy to cope with the severe constraints from $K_0 - \bar{K}_0$ mixing and other similar evidences. This is also motivated by the observation that the masses of the first and second generation fermions are too small to have any relevant effect on the running of the SUSY-breaking parameters.

[2] *Minimal Supergravity*
[3] *Phenomenological MSSM*

Parameter	Value	Parameter	Value
$\tan\beta$	10	$m_{\tilde{\chi}^0_{1,2}}$	95.58, 206.2
μ	400	$m_{\tilde{\chi}^0_{3,4}}$	407.5, 422.7
m_A	384.0	$m_{\tilde{u}_{L,R}}$	2029, 2026
m_h	123.4	$m_{\tilde{t}_{1,2}}$	293.1, 1530.5
m_H	400.6	$m_{\tilde{d}_{L,R}}$	2030, 2026
$m_{H^\pm}$	408.3	$m_{\tilde{b}_{1,2}}$	794.8, 1510
$m_{\tilde{g}}$	2044	$m_{\tilde{e}_{L,R}}$	213.1, 126.2
$m_{\tilde{\chi}^\pm_{1,2}}$	206.0, 423.3	$m_{\tilde{\tau}_{1,2}}$	106.2, 219.0

Table 10.1: Mass spectrum of the SUSY particle in the STC4 benchmark point.

Even after applying those constraints, the parameter space is so wide that it cannot be analysed analytically to study its phenomenological implications so it is necessary to define relevant benchmark points in that space which should be chosen in such a way as to represent an interesting and representative scenario.

10.3.1 $\tilde{\tau}$ coannihilation benchmark scenario

The ongoing analysis of the LHC data improved the constraints on the SUSY parameter space, stimulating the definition of new sets of benchmark scenarios compatible with those new data, among them several relevant for the ILC capabilities [32]. All those benchmark point include several particles which can be accessed by the ILC and are not yet excluded by the LHC searches.

One family, called *STC*[4], in this set is characterized by the small gap between the LSP and the *NLSP*[5], of the order of 10 GeV, with the two particles being, respectively, the lightest neutralino and the $\tilde{\tau}$. Such a benchmark family can be obtained with the pMSSM using the input parameters described in [32], producing the SUSY mass spectrum listed in tab. 10.1. The benchmark scenarios of the STC family differ from each other only for the mass parameter of the right-handed third generation s-quarks at 1 TeV. Thus, when that parameter is set at 400 GeV as in the relevant case for this analysis, we will label the specific scenario STC4. From the theoretical point of view this scenario has several relevant motivations: for example it provides an efficient dark-matter co-annihilation mechanism due to the low $\tilde{\tau}$ mass (see § 1.3.2), it reconciles the experimental value of the anomalous muon magnetic moment and of the branching ratio $b \to s\gamma$ with the theoretical calculations.

In the STC scenarios the masses of s-quarks and s-leptons are not correlated which results in the possibility of a heavy set of $\tilde{q}$, which would have defied the LHC efforts, and a light set of $\tilde{l}$, accessible at the ILC energies yet invisible at the LHC due to its complex environment (see § 1.3.3). In particular, in the case of the 500 GeV ILC, all s-leptons and the lighter set of electroweakinos defined in those scenarios are kinematically

[4] $\tilde{\tau}$ *coannihilation*

[5] *Next-to-Lightest Supersymmetric Particle*

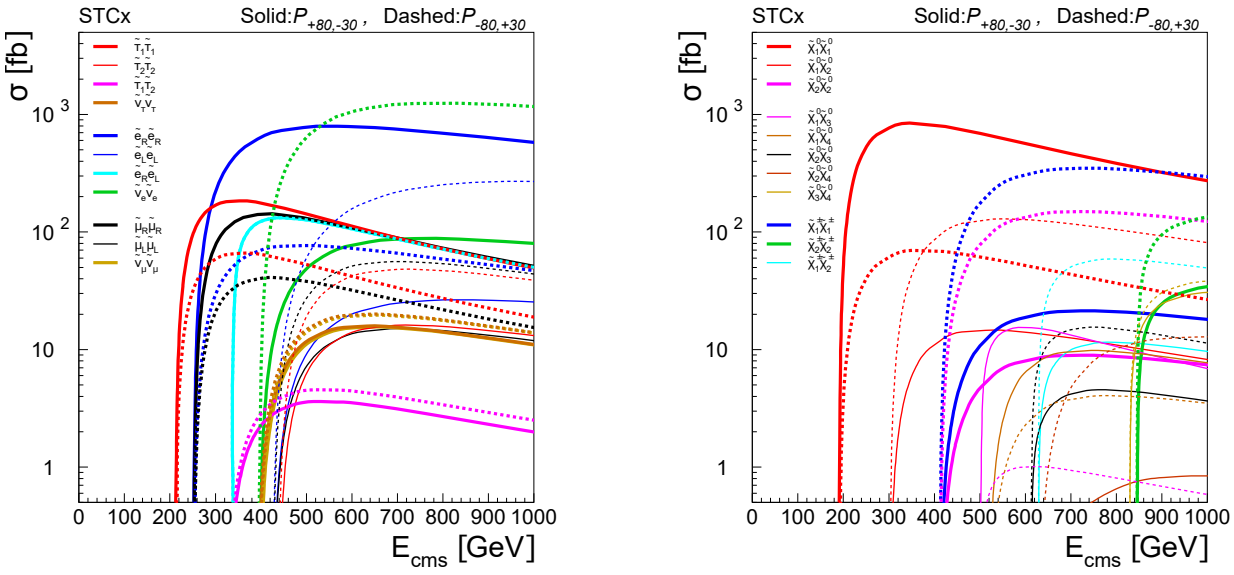

(a) (b)

Figure 10.4: Production cross section of the SUSY processes from the STC benchmark family accessible at the ILC up to a centre-of-mass energy of 1 TeV, separated between the sfermions in a and electroweakinos in b. From [123].

accessible (fig. 10.4) and only the left-handed s-leptons are currently excluded by the LHC searches. An important feature of this model family is that, even at relatively low energies, many s-particles can decay through several different modes in potentially long chains (i.e. fig.10.5a). That can make the analysis challenging and a true benchmark for the ILC experiments capabilities.

10.3.2 The s-lepton sector of the STC benchmark family

In recent years the STC benchmark family was used as a proving ground to verify the performances of both LHC at ILC and understand what type of results could be expected by either experiment. A summary of most of those study is presented in [123]. In this section we will focus in particular on describing the characteristics of the s-lepton sector in the STC models and the current status of the ILC studies involving it.

Considering that the main feature of the STC benchmark family is a light s-lepton spectrum, which are also those which are more abundantly produced at a lepton collider, the understanding of those processes is a natural benchmark for the ILC experiments design and an important experimental goal if such a scenario would be the natural occurring one.

At the ILC, the possibility to precisely control the centre-of-mass energy would allow to perform both threshold scans for each of the relevant particles, and fixed-energy analysis for all the processes within its reach. Additionally. the possibility to control both beam polarizations, will allow the ILC experiments to enhance the production of specific processes improving the precision of all experiments [57].

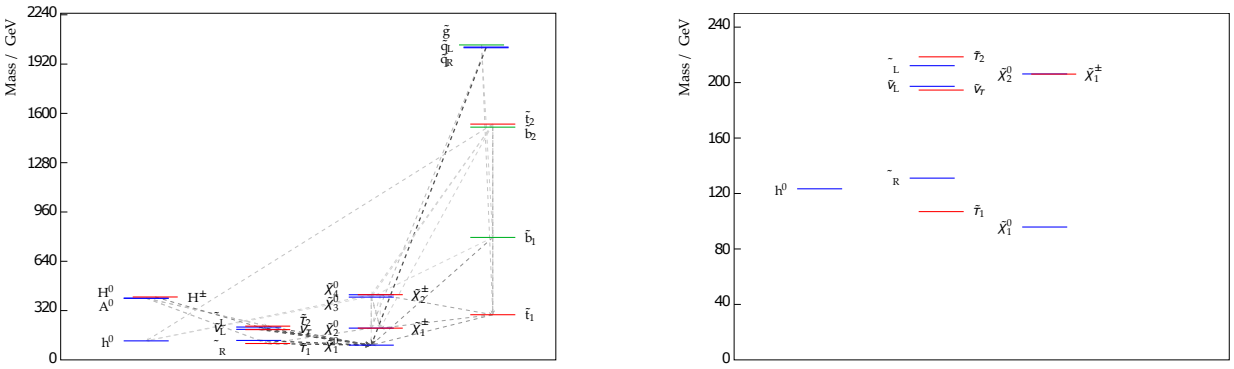

(a) (b)

Figure 10.5: a: Full Spectrum of the STC4 benchmark scenario with highlighted decay modes with a branching fraction of at least 10%. b: Lighter part of the spectrum of the STC scenarios, relevant to the ILC capabilities ([129]).

Moreover the lightest particle of each s-lepton family is usually lighter than any neutralino or chargino other than the LSP so their decay proceed exclusively towards that particle reducing any dependency of their measured properties on the specific details of the rest of the SUSY spectrum, thus achieving the model independent simplification described in the previous section.

In the STC scenarios, the $\tilde{\tau}_1$ is the NLSP and its properties are important to estimate the dark-matter co-annihilation rate which is one of the main motivation behind the design of those models. The small difference, of the order of 10 GeV, between that particle and the LSP is what makes the co-annihilation possible but also makes it more challenging to study. Specifically, such a small mass gap means that the energy of the τ produced in the $\tilde{\tau}_1$ decay is between 2.5 GeV and 45 GeV. Furthermore each τ will promptly decay softening the spectrum of the observable particles even more and making the suppression of the SM background events more challenging. Nonetheless the ILC experiments project to be able to measure the $\tilde{\tau}_1$ mass with a precision of 200 MeV, assuming an uncertainty of 100 MeV on the LSP mass. Similarly, the mass measurement resolution for the $\tilde{\tau}_2$ particle will be 5 GeV.

The study of the s-electrons and s-muons is easier than the previous one due to the greater mass difference between the parent and daughter particle in the decay and due to the higher efficiency in the identification of electrons and muons, as compared to the τ. This makes it possible to measure their kinematic end-points with much higher precision, even in challenging experimental environments. In this sense, the STC4 benchmark scenario is particularly well suited to evaluate the performances of the ILC experiments in this sector. In the s-electron channel in particular, the two kinematic edges of the $e^-e^+ \to \tilde{e}_R\bar{\tilde{e}}_R$, located at $E^+ = 99.362\,\mathrm{GeV/c}$ and $E^- = 7.298\,\mathrm{GeV/c}$[6], present very different backgrounds so that an effective analysis of this scenario can be used as a general benchmark for the potential

[6]The edge positions can be calculated from the masses listed in tab. 10.1 using the equations 10.11 and 10.12.

performances of the ILD in this context.

In recent years the LHC experiments were able to exclude the left-handed s-leptons of the STC scenarios [37, 38] but they are still insensitive to the right-handed partners as the small mass difference with the LSP, of the order of 30 GeV, will not produce enough missing energy in the events to be able to distinguish them from the Standard Model background. At the ILC all of them can be successfully studied by measuring the position of their kinematic edges.

Chapter 11

Computational edge detection

As we discussed in the previous chapter, if a process like $\tilde{\ell} \to \tilde{\chi}_1^0 \ell$, where ℓ is any Standard Model lepton and $\tilde{\ell}$ is its supersymmetric partner, is kinematically accessible at the ILC, to measure the masses of the unknown supersymmetric partners we must precisely measure the position of the edges in the momentum distribution of the final-state leptons.

The characterizing feature of an edge in any function or distribution is the local maximization of the first derivative but in the case of an experimental distribution we need to take in account the presence of noise in any sampling we perform. As we will show in § 11.1, the differential operator is not robust against noise, in the sense that a small change in the input parameters induces large changes in the solution. Therefore a more sophisticated algorithm should be used to accurately measure the position of a differential feature in a noisy environment. Moreover, to be able to use the results of the algorithm for an experimental measurement, we need to be able to reliably evaluate the experimental errors associated to that result.

In this chapter we will describe the development and characterization of an algorithm to identify and localize the position of edge-like features in a monodimensional binned distribution in presence of arbitrary noise. After describing the algorithm we will define the criteria to characterise it and, using those criteria, we will develop a data-driven procedure to choose the optimal parameter set for a given measurement. Furthermore we developed a Monte Carlo technique to evaluate the statistical and systematic errors to associate to the results obtained with the algorithm. Finally, in § 11.4, we will apply all those techniques to the distribution of the final-state momenta of the electrons produced in the decay of the s-electrons produced in the $e^- e^+ \to \tilde{e}_R \bar{\tilde{e}}_R$ process, as obtained from a Monte Carlo simulation which does not include backgrounds or detector related effects. That measurement will be used both to demonstrate the performance of the algorithm and to provide us with a best-case measurement to compare with further measurements presented in the next chapter.

11.1 Computational edge detection

In the general case of a continuous function $\boldsymbol{g(x)}$, an edge-like feature is characterized by a local maximum or minimum in $\boldsymbol{g'(x)}$ and a zero-crossing in $\boldsymbol{g''(x)}$. Unfortunately, in the case of experimental data, the physical signal is disturbed by noise and the differential operator is not robust against noise. For example, given the functions $\boldsymbol{t(x)}$ and $\boldsymbol{\tilde{t}(x) = t(x) + \epsilon \sin(\omega x)}$, they are very close for any ω for most typical metrics, provided ϵ is sufficiently small. On the other hand $\boldsymbol{t'(x)}$ may be very different from $\boldsymbol{\tilde{t}'(x)}$ if ω is large.

One of the methods to regularize such a problem is to convolve the target function $\boldsymbol{g(x)}$ with an appropriate function $\boldsymbol{f(x)}$ before the differentiation stage [130]. Assuming $\boldsymbol{f}$ is differentiable and absolutely integrable, and $\boldsymbol{g}$ absolutely integrable, we can write

$$\frac{d}{dx}(f(x) * g(x)) = \frac{df(x)}{dx} * g(x) = h(x) * g(x) \tag{11.1}$$

and we can robustly identify edge-like features in $g(x)$ from the maxima of $h(x) * g(x)$ or the zero-crossings of $h'(x) * g(x)$. In this context $\boldsymbol{h(x)}$ is usually called the *Impulse Response* (IR) of the algorithm. Because that function can unambiguously characterize the algorithm we will often refer to the former as a shorthand for the latter and call either the *convolution filter* or *differential filter*.

Assuming an isotropic domain where the search is applied, the filter function should be either odd or even. If we are interested in searching for the extrema of the response the filter should be an odd function. If the search algorithm looks for zero crossings in the response then we need to use even functions. In any case, to avoid false edge detections, the filter function should have the least number of zero crossings, with the optimal situation being one crossing for an odd function and zero for an even one[130].

To quantify the performance of those filters to detect an edge of amplitude $\boldsymbol{A}$ in presence of a random noise with $\mathbf{RMS} = \boldsymbol{n_0}$, we can define a set of three criteria [131] which depend only on the shape of the *CIR*[1] $\boldsymbol{h_c(x)}$:

Good detection The probability of not identifying real edges should be minimized as well as the probability of falsely marking non-edge points. Since both these probabilities are monotonically decreasing functions of the output signal-to-noise ratio, this corresponds to maximizing that parameter:

$$\text{SNR} = \frac{A}{n_0} \cdot C_{c1} \quad \text{with} \quad \boldsymbol{C_{c1}} = \frac{\int_{-W}^{0} h_c(x)dx}{\left[\int_{-W}^{+W} h_c^2(x)dx\right]^{\frac{1}{2}}} \tag{11.2}$$

Good localization The distance between the point marked as edge by the operator and the „real“ edge position should be minimized:

$$L = \frac{A}{n_0} \cdot C_{c2} \quad \text{with} \quad \boldsymbol{C_{c2}} = \frac{|h_c'(0)|}{\left[\int_{-W}^{+W} h_c'^2(x)dx\right]^{\frac{1}{2}}} \tag{11.3}$$

[1] *Continuous Impulse Response*

Suppression of multiple responses There should be a single identification for each edge. This parameter can be quantified by the mean distance between two maxima when $A = 0$:

$$x_{\max} = \boldsymbol{C_{c3}} = 2\pi \left[\frac{\int_{-W}^{+W} h'^2_c(x)dx}{\int_{-W}^{+W} h''^2_c(x)dx} \right]^{\frac{1}{2}} \tag{11.4}$$

According to those criteria the optimal filters for detecting an edge-like feature in a noisy environment is a linear combination of 4 exponentials, called *Canny filter*. That function is very similar to the first derivative of a Gaussian (FDOG) which has only slightly worse performances according to the above-mentioned criteria. On the other hand, sampling a Gaussian distribution is very efficient computationally and for practical application it can effectively replace the Canny filter.

11.1.1 Optimization criteria for a discrete function edge finder

The mathematical formulation of the Canny criteria was derived in the continuous domain. In the realistic cases we are interested in, the physical function is actually sampled as an histogram in the discrete domain and the convolution filters have to be defined in the same domain.

The straightforward extension of the edge detection optimization criteria to a discrete function is not possible, in particular due to the usage of the response function's derivative which appears in the definition of the second and third criteria. Hence it is necessary to redefine those criteria for discrete filters, with *DIR*[2] $\boldsymbol{h_d(k)}$, and to develop an operational procedure to evaluate the algorithm performances. Additionally that procedure can be used to quantify the benchmark parameters for edge detection algorithms which are not based on differential convolution filters, e.g. an *FFT*[3] based algorithm. Some of the concept used to develop this procedures are also described in [132].

Scale Factor The first parameter we need to define is a meaningful *scale factor*. This parameter allows us to compare the response of different algorithms, filters or parameters. We define the scale factor, also named the algorithm *response size*, as the RMS of its response to an ideal step function.

Efficiency The good-detection criteria is equivalent to the determination of the algorithm efficiency in detecting a edge-like feature in the distribution. This can be evaluated by defining the detected edge position as the global maximum in the algorithm response. Using this definition we define the *algorithm efficiency* as the probability that the global maximum is also the one which is the closest to the *true* edge position.

[2] *Discrete Impulse Response*
[3] *Fast Fourier Transform*

Localization power We can define this parameter as the mean ($\hat{\boldsymbol{L}}$) and standard deviation ($\boldsymbol{\sigma_L}$) of the distance between the *true* edge position and the closest peak in the detector response. The σ_L value is particularly relevant to our goal as it allows to define the uncertainty in the edge position measurement. We will often refer to this parameter as the *localization error*. The mean value of this value, provides a measurement of the bias of the method.

Multiple response Finally we can define the *multiple response criteria*, which we will label $\boldsymbol{C_{d3}}$, as the mean distance between the detected edges on a constant noisy function, similarly to the definition in the continuous domain. This parameter allows to evaluate the smallest feature size the algorithm is able to detect individually. Two similar features closer than this distance will be likely be identified as a single, merged edge by the algorithm. On the other hand, a filter with a small C_{d3}, offers a limited robustness against noise as multiple features can be detected within the domain of a single, extended edge.

11.2 Implementation of a discrete convolution edge finder

To perform the search and characterization of edge-like feature on a discrete function we developed a flexible algorithm contained in a C++ library. The algorithm identifies edge-like feature on a discrete function convolving the input with a custom filter and detecting the peaks in the convoluted function.

11.2.1 Peak finding algorithms

One of the key components of the algorithm we developed is the peak-finding procedure. All the classes that perform this operation are based on the same interface to detect peaks with both positive and negative polarity and can be easily replaced and compared.For this work we developed and used three different peak-interpolation algorithms: barycentric, quadratic and Gaussian, listed in order of computational complexity. The performances of those algorithm will be analysed in the context of the more general evaluation of the edge finder parameters in the next sections.

All three algorithm are based on a three-point interpolation, evaluating the values of the bin at the local extreme and its nearest neighbour in each direction. If we assume those three points are samples around the apex of a parabola, calling $\boldsymbol{f(i)}$ the samples of a function with a local maxima at $\boldsymbol{i = k}$, then the peak position $\boldsymbol{P_x}$ and its value at the peak $\boldsymbol{P_y}$ can be calculated using the quadratic interpolation as:

$$P_x = k + \frac{f(k+1) - f(k-1)}{2(2f(k) - f(k-1) - f(k+1))}$$
$$P_y = f(k) - \frac{(f(k-1) - f(k+1)) \cdot P_x}{4} \tag{11.5}$$

For the Gaussian and barycentric interpolation we also need to estimate the peak amplitude A from a reference baseline $\boldsymbol{B = f(k) - A}$, which we defined as the difference between the function value at the interpolated peak and that at the nearest extreme.

The Gaussian interpolation algorithm stems from the consideration that the logarithm of a Gaussian is indeed a parabola so that is possible to apply the quadratic interpolation to the logarithm of the function values around the peak. Defining $\boldsymbol{\ell(i) \equiv \ln(f(i) - B)}$ the peak coordinates are:

$$P_x = k + \frac{\ell(k+1) - \ell(k-1)}{2(2\ell(k) - \ell(k-1) - \ell(k+1))}$$
$$P_y = B + \exp\left(\ell(k) - \frac{(\ell(k-1) - \ell(k+1)) \cdot P_x}{4}\right) \tag{11.6}$$

Finally the barycentric interpolation estimates the correction on the peak position as the weighted average of the values of the function around the peak. In this case it is not possible to also estimate the peak amplitude but defining $\boldsymbol{y(i) \equiv f(i) - B}$ we obtain:

$$P_x = k + \frac{y(k+1) - y(k-1)}{y(k-1) + y(k) + y(k+1)} \tag{11.7}$$

11.2.2 Sample functions

To test and characterize the developed algorithm we also defined, through a common interface, a set of step-like sample function with well defined parameters. Each of those functions is characterized by a baseline value $\boldsymbol{B}$, amplitude $\boldsymbol{A}$, and step position $\boldsymbol{P}$. Additional white noise of predefined amplitude $\boldsymbol{N}$ is overlaid to the ideal functions and we define the *Signal-to-Noise ratio* as the ratio between maximum derivative of the ideal function and the noise RMS. We also define the step width $\boldsymbol{W}$ as the integral interval between the 10^{th} and the 90^{th} percentile of the total amplitude. Two of those functions were finally used for the algorithm characterization described later:

Ideal step characterized by the following function with P being an integer in the function domain:

$$\begin{aligned} f(k) &= B \quad \text{for} \quad && k < P \\ f(k) &= B + A/2 \quad \text{for} \quad && k = P \\ f(k) &= B + A \quad \text{for} \quad && k > P \end{aligned} \tag{11.8}$$

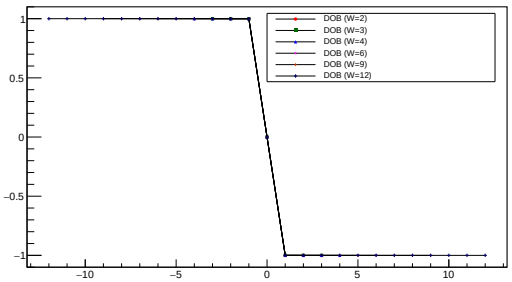

(a) DOB filter DIR

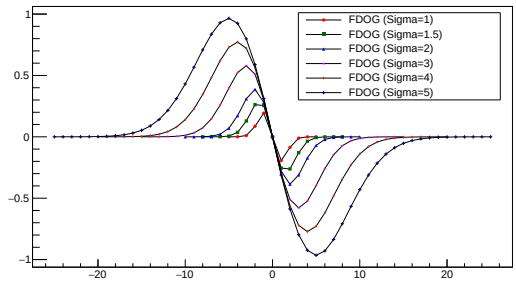

(b) FDOG Filter DIR

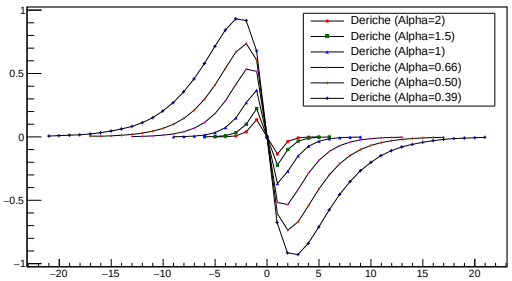

(c) Deriche Filter DIR

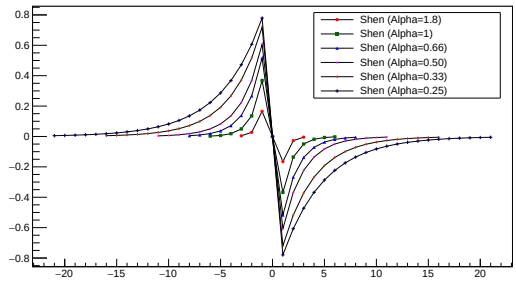

(d) Shen Filter DIR

Figure 11.1: Impulse response of different convolution filters. For each of them we plot this function for different values of the characterizing parameter.

In this case the *Signal-to-Noise ratio* is defined as $\mathbf{A/N}$ and the width is always equal to 2.

Smooth step that is an ideal step smoothed by convolving it with a Gaussian function. The width of this function is equivalent to the full width at 10% of the maximum of the smoothing function, that is $\boldsymbol{W = 2\sqrt{2\ln(10)}\sigma}$.

11.3 Edge finder characterization

To understand the properties of the edge finding algorithms we developed and to optimize the parameter's choice, we compared, according to criteria described in § 11.1.1, four different convolution filters:

Difference of Boxes (DOB): This filter is equivalent to the performance of a moving average in a window of size $2N + 1$ prior to the derivative stage. The characterizing parameter of this filter is the size $\boldsymbol{N}$ of the averaging window and can be analytically

written as:

$$\begin{aligned} h_d(k) &= 1 \quad \text{for} & -N \leq k < 0 \\ h_d(k) &= 0 \quad \text{for} & k = 0 \\ h_d(k) &= -1 \quad \text{for} & 0 < k \leq N \end{aligned} \tag{11.9}$$

First Derivative of a Gaussian (FDOG): This filter is equivalent to the execution of a Gaussian smoothing prior to the derivative. The filter is parametrised by the $\boldsymbol{\sigma}$ of the Gaussian:

$$h_d(k) = -k\ e^{\frac{k^2}{2\sigma^2}} \tag{11.10}$$

Deriche: This algorithm, described in [133], is characterized by the following impulse response, parametrised by the exponential decay length $\boldsymbol{\alpha}$:

$$h_d(k) = -k\ e^{-\alpha|k|} \tag{11.11}$$

Shen: Similar to the previous one, this algorithm, described in [134], is equivalent to an exponential smoothing and presents a discontinuity in the derivative at $k = 0$:

$$\begin{aligned} h_d(k) &= e^{\alpha k} \quad \text{for} & -N \leq k < 0 \\ h_d(k) &= 0 \quad \text{for} & k = 0 \\ h_d(k) &= -e^{-\alpha k} \quad \text{for} & 0 < k \leq N \end{aligned} \tag{11.12}$$

Excluding the first, all the filters are unlimited in the domain, therefore we use a cut-off parameter beyond which the filter response is 0 by definition. For the FDOG filter the cut-off is defined as a multiple of σ, for the Shen and Deriche filter as a multiple of $1/\alpha$. The DIR of the analysed filters for different values of their characteristic parameter is shown in fig. 11.1.

11.3.1 Single response window size

The first parameter we will evaluate is the multiple response estimator which is calculated as the average distance between the features detected by applying the algorithm on a constant, noisy function. This quantity is plotted for all filters analysed in fig. 11.2. This quantity is particularly relevant when there are multiple features next to each other as it allows to estimate the maximum size of the filter to use to detect them independently.

One noteworthy feature is that the FDOG and Deriche filter grow linearly with the size while DOB and Shen filter, which are those that have a discontinuity in the origin, tend asymptotically to a finite value. This fact was derived analytically in [132] where the authors demonstrate that in all filters with a discontinuity at the origin $\boldsymbol{C_{d3} < 6}$.

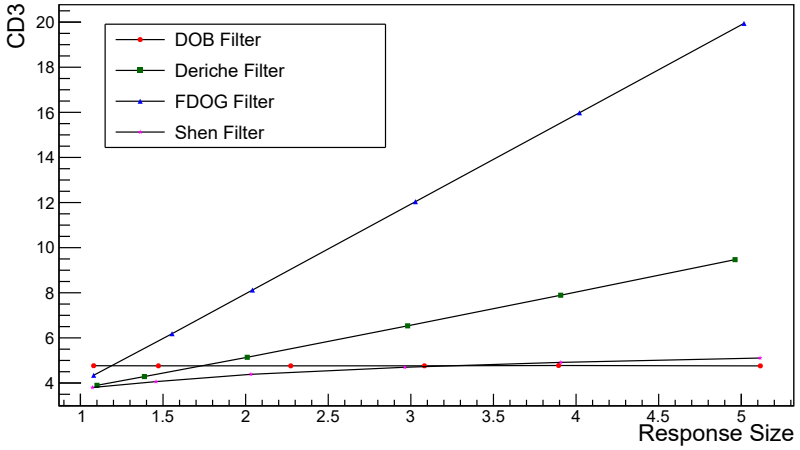

Figure 11.2: Comparison of the multiple response criteria C_{d3} for different filters of different sizes. Note that the Shen and DOB filter are not increasing beyond the value 6.

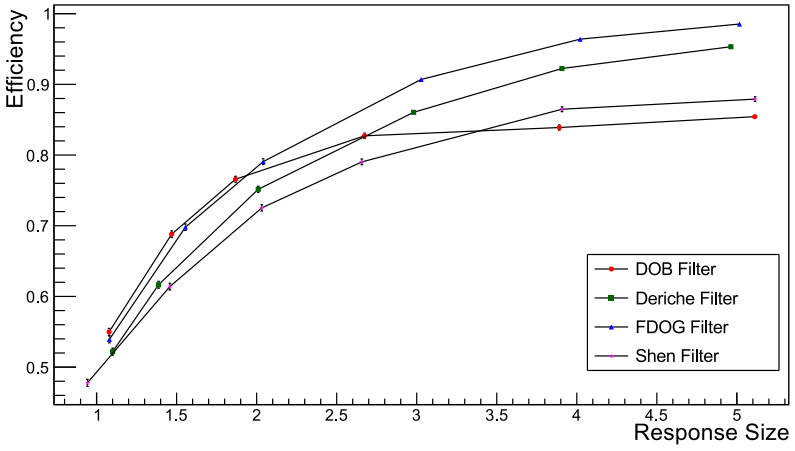

Figure 11.3: Comparison of the edge detection efficiency of several filters of different size when the algorithm is applied on an ideal step function with a superimposed white noise with the same amplitude as the step (SNR = 1)

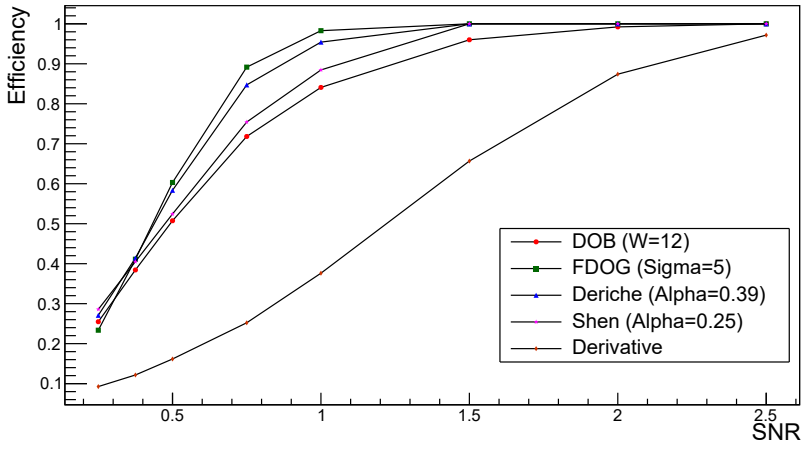

Figure 11.4: The efficiency of the four analysed filters, compared to that of the traditional derivative are plotted against the Signal-to-Noise-Ratio. A random peak choice would result in an efficiency of about 5%. The size of the filter is about 5.

11.3.2 Detection efficiency

The second parameter we evaluated is the algorithm efficiency for different filters and different filter sizes. To evaluate this parameter, for each signal function, after the superposition of white noise with fixed RMS, we calculate the probability that the detected feature with the maximum response is also the one one closest to the *true* step position.

This probability was calculated by executing the detection algorithm on a sample step-like function a fixed number of times. The position of the *true* feature is randomly chosen in each experiment and the noise is generated independently in each evaluation. As we are not interested in the absolute position of the detected edges, we are not using any peak interpolation algorithm. The test algorithm allows to vary freely the sample function, the noise amplitude as well as the filter parameters.

The result of this evaluation for all the filters, using an ideal step model function with $\mathbf{A/N = 1}$, is shown in fig. 11.3. A noteworthy feature in this plot is the monotonic increase of the efficiency with the filter size.

Finally we can compare different filters of similar size (5 in the example shown in fig. 11.4) varying the Signal-to-Noise ratio of the sample function. In general we can notice that the most efficient of the analysed filters is the FDOG, but that all of them achieve perfect efficiency when $S/N \gtrsim 2.5$. It also noticeable that all of them are much more efficient than the normal derivative, confirming the increased robustness of the algorithm to the noise.

11.3.3 Localization resolution

Finally we can proceed to evaluate the localization performance of the algorithm. This parameter is calculated by evaluating the average distance of the detected edge from its *true* position in a toy Monte Carlo experiment. The mean value of this quantity represents the systematic bias ($\hat{\boldsymbol{L}}$) for the type of edge under consideration, while the standard deviation is the localization error ($\boldsymbol{\sigma_L}$), which we can associate to the systematic error in the edge

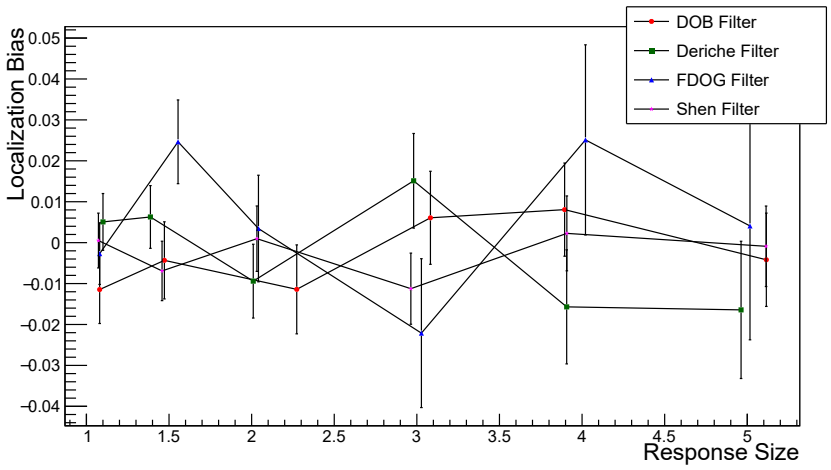

Figure 11.5: The localization bias of all the filter under evaluation is plotted against the filter size. The value is generally compatible with 0 at all sizes. The parameter is calculated for an ideal filter with $S/N = 0.5$

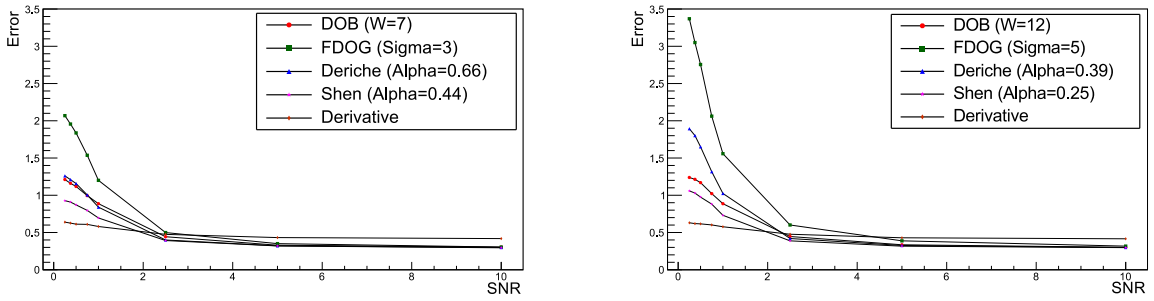

(a) (b)

Figure 11.6: The localization error of filters of similar size is plotted against the SNR of the sample ideal step. In the left panel all the filters have a characteristic size of about 3, on the right panel the size is about 5. In both cases the localization improves asymptotically. The limiting value is slightly lower with smaller size, as can be seen comparing the left and right panel.

position determination. We can also calculate the intrinsic statistical error on the bias determination as $\boldsymbol{\sigma_{\hat{L}}} = \frac{\sigma}{\sqrt{n}}$, where $\boldsymbol{n}$ is the number of measurement used to calculate the average.

In general this quantities depend not only on the filter choice or their scale parameters but also on the edge shape and the peak-interpolation algorithm used (§ 11.2.1). For a symmetric edge shape though, the bias of our algorithm is always extremely low and compatible with 0, as shown in fig. 11.5, for any filter at all sizes. Considering that both the sample and the kernel functions are symmetric this is an expected results and a benchmark to verify the correctness of the developed numerical algorithm. On the other hand, the localization error depends on all the test parameters, namely the filter size, the peak interpolation algorithm, the sample function shape and its Signal-to-Noise Ratio.

To decouple as much as possible the different effects we will start looking at the algorithm response to an ideal step. This type of function is a generic representation of a very sharp feature in a spectrum and its characterizing parameter is the Signal-to-Noise

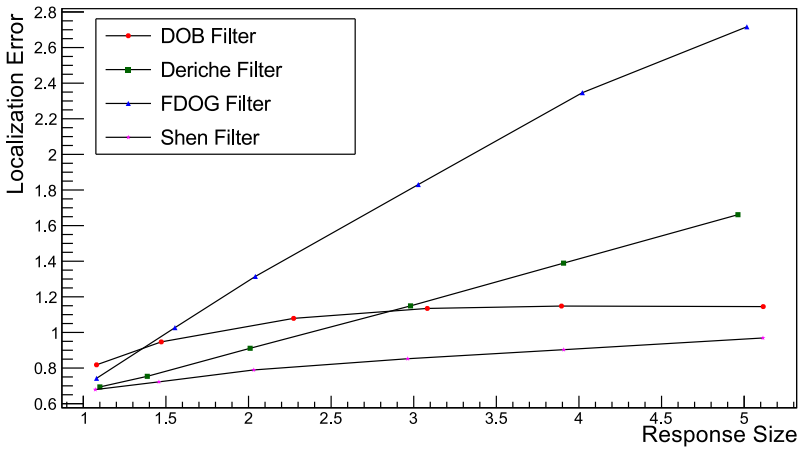

Figure 11.7: The localization error is compared for all the evaluated filters at a fixed $SNR = 1$. The quadratic peak interpolation is used in all cases. In those conditions the Shen filter performs better than the other and its performance shows a smaller dependence on the filter size.

ratio (SNR). Varying that we can obtain plots like those in fig. 11.6 for any set of filters.

For small values of SNR we can notice relevant differences between the filters and that the localization rankings are typically the inverse of the efficiency rankings we observed before with the FDOG filter typically providing the worst localization power. We can also observe that in this case, just as it was for the efficiency, all the filters are roughly equivalent when the SNR is greater than about 2.5.

At high SNR the performance is mostly influenced by the choice of the peak interpolation algorithm that we compare in fig. 11.8. It is evident there that all the algorithms provide a major improvement over the simple identification of the local extrema. The barycentric method provides a measurable improvement but this depends substantially on the filter size which is undesirable. The quadratic and Gaussian interpolation provide similar performances, in all cases better than the barycentric approximation. The latter is marginally better but computationally more expensive and implying the additional assumption of a Gaussian shape response which is theoretically valid only for that of the FDOG filter to an ideal step. For this reasons we generally prefer the quadratic peak interpolation and use it as a typical algorithm for all the benchmarks, unless otherwise noted.

In the case of an extended edge, we need to introduce an additional variable, that is the width of the step (**W**), already defined in § 11.2.2. Fixing this parameter while changing the amplitude, hence the SNR, as in fig. 11.9, we can observe a trend similar to that of the ideal function: the localization error decreases with the relative noise amplitude and reaches similar asymptotic values for all filters when the noise is negligible. Moreover we can here clearly observe a major improvement in the localization property of the algorithm when compared to the normal numerical derivative.

If we now fix the SNR value and change the width we observe the other important characteristic of this algorithm: the localization reaches an optimal value before increasing again (fig. 11.10).

The position and the relevance of this feature depends on both the filter size and type. By comparing the localization curves of all the analysed filters we can observe that:

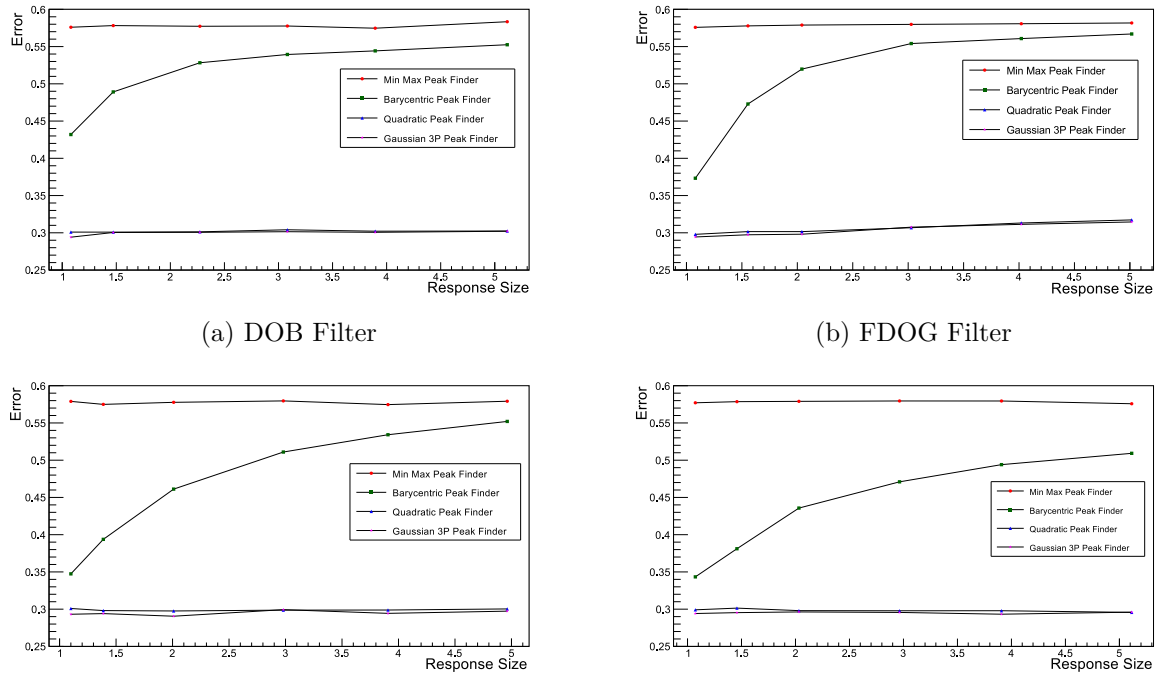

(a) DOB Filter

(b) FDOG Filter

(c) Deriche Filter

(d) Shen Filter

Figure 11.8: Comparison of the localization performance of the different peak interpolation algorithms for all filters. An ideal step with a SNR of 10 is used as a sample function. This plot also shows that for high SNR the performance of the quadratic and Gaussian algorithms is independent from the filter size.

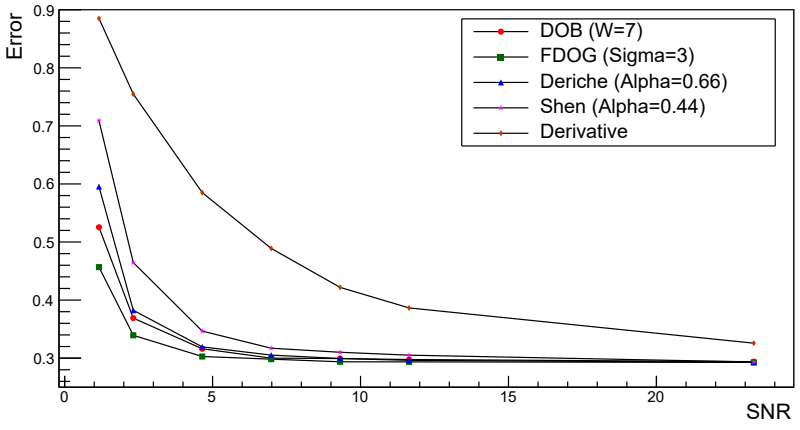

Figure 11.9: The localization error of different filters of similar size (≈ 3) is calculated on a smooth step of fixed size ($W = 10$) but different amplitude, equivalent to different S/N, which is calculated as the ratio between the derivative of the ideal function in the flex point and the uniform noise overlay.

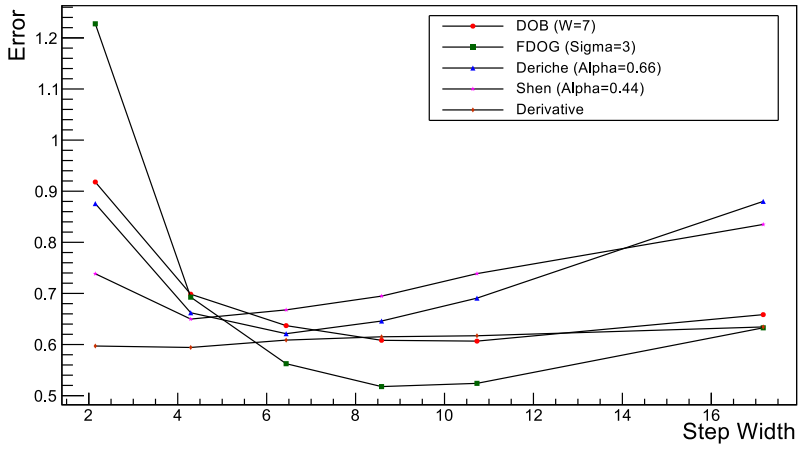

Figure 11.10: The localization error of the edge finder algorithm, applied to a smooth step function with fixed $S/N = 0.5$, is plotted in this figure for a variable step width. At low S/N the presence of an optimal filter size is particularly evident but this characteristic is generally present for any value of S/N

- For small feature size the Shen filter is typically the most accurate while the FDOG filter shows the worst performances
- When the step width is larger than about 4 units the most accurate filter is the FDOG filter.
- For both the FDOG and the Deriche filter the localization in the optimal configuration tends to improve with the filter size.

The optimality of the FDOG filter for the detection of edge features when those are relatively wide can be considered a confirmation of the validity of the algorithm as it reproduces the analytical results derived in [131] and described in 11.1. In fact, for large enough filter size, the effect of the sampling discretization on the algorithm result should become negligible.

11.3.4 Algorithm optimization procedures

To use the algorithm we developed to measure the edge position in a binned distribution we defined an optimization procedure that allows us to obtain the most accurate results. This can be performed using the same tools we presented in the rest of this section.

To define this procedure we should distinguish the identification of a feature from the measurement of its position as the two steps can be performed independently. When the **S/N** value is large all filters have perfect identification power so we can optimize the measurement by minimizing the localization error. If **S/N** is small we can use high efficiency filters like a large size FDOG to perform this step and optimize the localization error in a second step in a restricted volume.

The best way to optimize the filter to minimize the measurement error is to execute the same type of toy Monte Carlo experiment we used to characterize the algorithm to identify the optimal parametrization.

When the binning can be chosen arbitrarily we can use also this parameter to optimize our measurement. In fact we noticed that, when **S/N** is large enough (above 10 in the

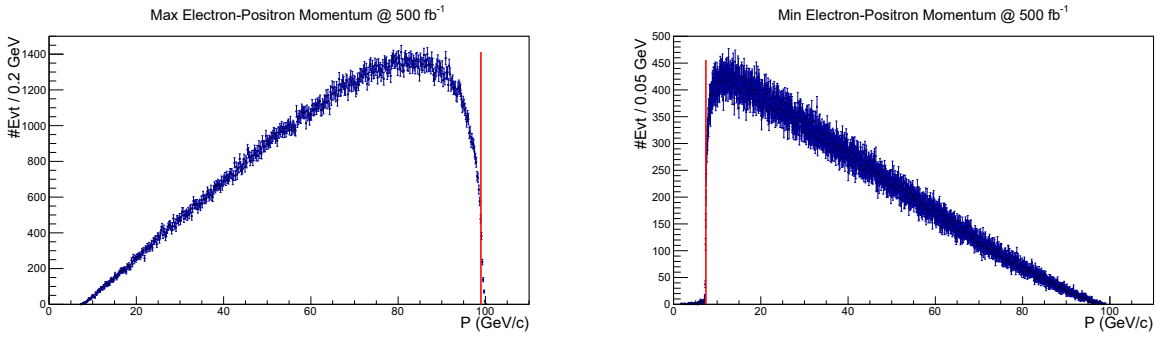

(a) Maximum momenta.

(b) Minimum momenta.

Figure 11.11: Momentum distribution of the decay products of the $\tilde{e}$ production as extracted from the generator without degradation due to the detector reconstruction. a shows the momentum spectrum of the electron or positron, among the pair produced in the decay, with the highest momentum. b shows the same distribution for the electron or positron with the lowest momentum. The red line marks the edge position detected by the optimized algorithm. The histogram binning was chosen to optimize the position measurement. In both cases we assume an integrated luminosity of 500 fb^{-1} at 500 GeV nominal centre-of-mass energy, 80% right-polarized electrons and 30% left-polarized positrons.

metric we used in the above treating), an FDOG filter as large as possible is the optimal choice. Hence, in this case, we can start from an arbitrary binning, preferably coarse enough to guarantee a good identification and iteratively increase the resolution while increasing the filter size proportionally to identify the best combination.

Finally, until now we only evaluated the performance of the algorithm on edges which are symmetric. In real application this is not usually true and the bias in the edge localization can be introduced in the measurement which can be estimated if the feature to measure can be compared to its true value. In this case such a bias can be calibrated away, as long as the error on the bias is negligible when compared to the localization error.

11.4 Edge finder benchmark on the signal data

The tools and procedures described earlier were developed to measure the position of the kinematic edges that would be found in the momentum spectrum of the decay products of heavy particles, in particular the $\tilde{e}$. Before applying the algorithm to a complete ILC simulation, we will test it on the signal samples generated as described in § 12.1. No degradation due to detector effects, reconstruction and selection will be considered in this best-case-scenario analysis. This will allows to determine the best performances achievable by the algorithm and later evaluate the effect of the selection and the detector reconstruction on the measurement.

Because the upper and lower edge of the momentum distribution of the $\tilde{e}$ decay products have different width we are going to analyse them independently applying our procedure to the histogram shown in fig. 11.11.

Contrary to the ideal test cases, the realistic distribution we are going to analyse is

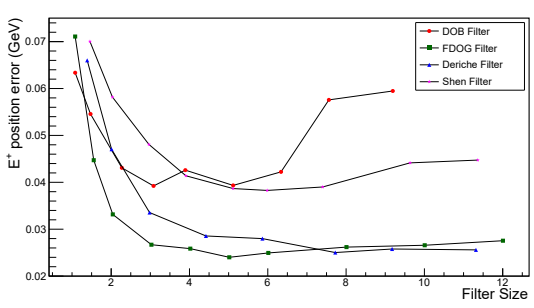

(a) Error

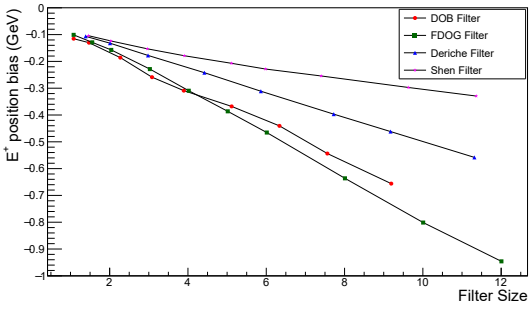

(b) Bias

Figure 11.12: Summary of the optimization procedure applied to the high-momentum edge shown in fig. 11.11a. a shows the localization error measured for all filters of different sizes for the optimal binning of 200 MeV per bin. The lowest error is obtained using an FDOG filter of size 5. b plots the offset between the measured edge position and the position of the theoretical kinematic end-point calculated from the input parameters of the simulation. For the optimal algorithm parametrization the bias is -388 MeV

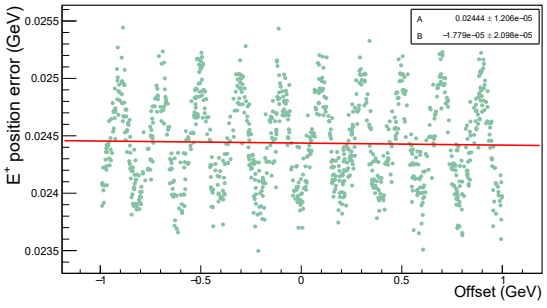

(a) Error

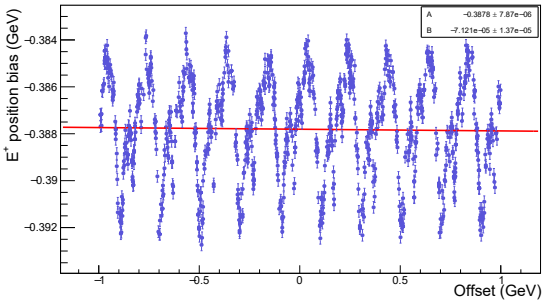

(b) Bias

Figure 11.13: Summary of the calibration procedure for the high-momentum edge. a shows the localization error and b the localization bias. Both quantities show a modulation with the same period as the chosen binning size. The RMS of this modulation is 0.3 MeV for the error and 2 MeV for the bias. There is no detectable linear dependency of either quantity from the offset.

not symmetrical around the flex point. Moreover the quantity that we want to measure, that is the position of the kinematic end-points, does not correspond to the position of the maximum of the derivative of the distribution because of the physical processes we mentioned in § 10.2.2. For those reasons the measured edge position is expected to be displaced with respect to the *true* kinematic edges calculated from the input parameters of the simulation. This offset will be reflected in the bias of the localization measurement which can then be subtracted to the measured position to obtain a calibrated measurement which can be used to calculate the masses of the $\tilde{e}$ and the $\tilde{\chi}_1^0$.

In addition to the intrinsic statistic error on the bias measurement $\sigma_{\hat{\mathbf{L}}}$, we can also evaluate a calibration curve, that is the dependency of the localization parameters on the *true* edge position. This was done through an additional Monte Carlo procedure: once the optimal parametrization for the localization algorithm is defined, we perform several measurement of the edge position adding an offset to the momentum of the input particles. The value of the offset is chosen randomly for each of the measurement within a range multiple of the bin size. Finally, applying a linear fit to the results we obtain the dependency of the bias on the offset value and we can define the calibration to apply as the value of the fit function when the offset is equal 0.

The results of our optimization procedure, when applied to the measurement of the high-momentum edge is summarized by the plots in fig. 11.12. Similar results are obtained with both the FDOG and Deriche filter. Because a larger filter is computationally more expensive, the FDOG is preferable to the Deriche filter. Hence the optimal localization error, obtained with an FDOG filter of size 5, is 24 MeV. For the same filter parameters the localization bias is estimated to be 388 MeV. The optimal results are obtained with a resolution of 200 MeV per bin.

The calibration procedure, summarized by the plots in fig. 11.13, shows a modulation of the localization parameters with the same period of the bin size but no linear dependency on the offset itself. The amplitude of the bias modulation is one order of magnitude smaller than the localization error, with a standard deviation of 2 MeV.

The same optimization procedure, applied to the low-momentum edge is summarized in fig. 11.14. The optimal results in this case are obtained with an FDOG filter of size 4 and a binning of 50 MeV per bin. In the optimal configuration the localization error is estimated at 8 MeV and the bias from the *true* edge position is 119 MeV.

Applying the calibration procedure we obtain the results summarized in fig. 11.15. Once again we see a modulation with the same period as the histogram binning but with an amplitude an order magnitude smaller than the relevant errors. Through this procedure we estimate the error on the localization bias to 0.7 MeV with no appreciable linear dependency between that measurement and the edge offset.

The measurement of the kinematic edges presented in the rest of this thesis is finalized to the determination of the $\tilde{e}_R$ and $\tilde{\chi}_1^0$ masses. In our simulation the absolute values of those masses is defined by the generator and our goal is to evaluate the best accuracy achievable applying our algorithm to the realistic data distribution that can be obtained with the ILD at the ILC. The relationship between the edge positions and those masses was derived in § 10.2.1 and expressed by eq. 10.16 and eq. 10.17.

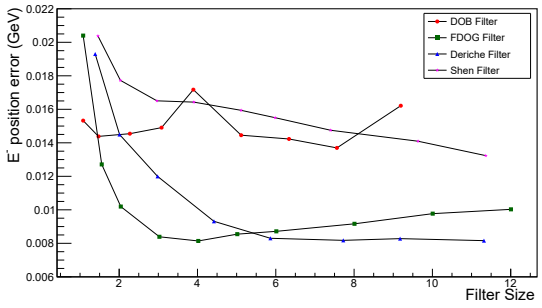

(a) Error

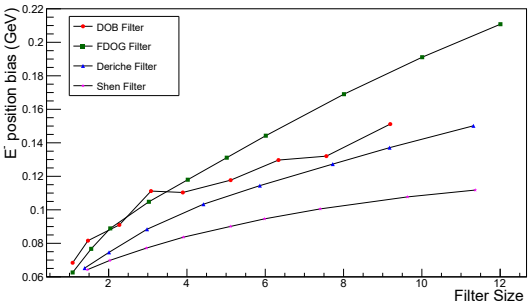

(b) Bias

Figure 11.14: Summary of the optimization procedure applied to the low-momentum edge shown in fig. 11.11b. The plot in a shows the localization error measured for all filters of different sizes for the optimal binning of 50 MeV per bin. The best performance is obtained with the FDOG filter of size 4. In b we summarize the localization bias between the measured and the *true* edge positions. For the optimal algorithm parametrization the bias is 119 MeV

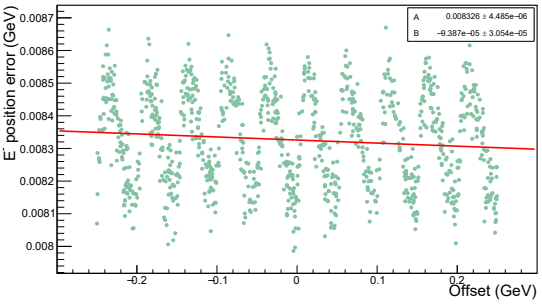

(a) Error

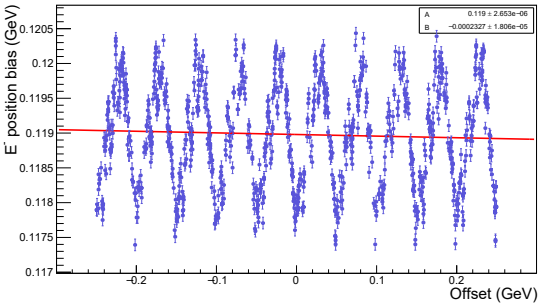

(b) Bias

Figure 11.15: Summary of the calibration procedure for the low-momentum edge shown in fig. 11.11b. a shows the localization error and b the localization bias. Both quantities show a modulation with the same period as the chosen binning size. The RMS of this modulation is 0.14 MeV for the error and 0.7 MeV for the bias. There is no detectable linear dependency of either quantity from the offset.

To estimate the uncertainties of those measurements we differentiate those equations to obtain a function of the edge position uncertainties. Labelling as $\delta(x)$ the error estimated for the variable x, we can calculate the uncertainty in the determination of the $\tilde{e}$ mass with the following equation:

$$\boldsymbol{\delta(M_{\tilde{e}})^2} = \left(\frac{1}{\gamma}\ \delta(E_{\mathrm{CM}})\right)^2 + \left(\frac{-E_{\mathrm{CM}}\ \gamma\ W_e\ E^+}{(2C_e)^3}\ \delta(E^-)\right)^2 + \left(\frac{E_{\mathrm{CM}}\ \gamma\ W_e\ E^-}{(2C_e)^3}\ \delta(E^+)\right)^2 \tag{11.13}$$

In a similar way the χ^0 mass uncertainty is estimated with the following formula:

$$\begin{aligned}\boldsymbol{\delta(M_{\chi^0})^2} = &\left[\left(\frac{E_{\mathrm{CM}}}{2\gamma^2} - C_e - \frac{W_e^2}{4C_e}\right)\frac{\delta(E_{\mathrm{CM}})}{2M_{\chi^0}}\right]^2 + \\ &+ \left[\frac{E^+\ E_{\mathrm{CM}}\,[(E_{\mathrm{CM}}+2E^+)E^- - E^+\ E_{\mathrm{CM}} + 2(E^+)^2]}{(2C_e)^3}\frac{\delta(E^-)}{2M_{\chi^0}}\right]^2 + \\ &+ \left[\frac{E^-\ E_{\mathrm{CM}}\,[(E_{\mathrm{CM}}+2E^-)E^+ - E^-\ E_{\mathrm{CM}} + 2(E^-)^2]}{(2C_e)^3}\frac{\delta(E^+)}{2M_{\chi^0}}\right]^2\end{aligned} \tag{11.14}$$

As the error on the bias determination was estimated to be more than an order of magnitude smaller than the edge position error we can safely neglect the first and, using the corrected edge positions, we obtain the following estimation for the best mass resolution we can achieve using this new method on the given data-set:

$$\boldsymbol{\delta(M_{\tilde{e}})} \approxeq 61\,\mathrm{MeV} \tag{11.15}$$

$$\boldsymbol{\delta(M_{\chi^0})} \approxeq 24\,\mathrm{MeV} \tag{11.16}$$

Chapter 12

Measuring the $\tilde{e}$ and $\tilde{\chi}_1^0$ masses at the ILC

The most stringent experimental limits for the $\tilde{\chi}_1^0$ and the $\tilde{e}_R$ masses, listed in the latest *PDG*[1] Review of Particle Physics [4] are still dominated by the final results from the LEP experiments. In particular, for the lightest Neutralino, the final combined searches of the DELPHI experiment sets a lower mass limit of $M_{\tilde{\chi}_1^0} > 46\,\mathrm{GeV/c^2}$ under very general assumptions [29]. For the right-handed s-electrons, the most stringent limits were obtained by the OPAL experiment which set a lower mass limit to $M_{\tilde{e}_R} > 97.5\,\mathrm{GeV/c^2}$ [28]. The only relevant constraint of that analysis is that it applies to mass differences between the $\tilde{e}_R$ and the LSP larger than 10 GeV. Similar results were obtained by the other LEP experiments [29, 27, 30].

The characteristic signature of the process $\boldsymbol{e^-e^+ \rightarrow \tilde{e}_R\bar{\tilde{e}}_R \rightarrow e^{\pm}e^{\mp}\tilde{\chi}_1^0\tilde{\chi}_1^0}$ is the presence of an isolated electron and an isolated positron not correlated to each other and a relevant amount of missing energy and momentum, carried away by the undetectable Neutralinos. Due to the inability to reconstruct the complete kinematics of each decay in each event, we need to calculate the masses of the $\tilde{e}_R$ and of the $\tilde{\chi}_1^0$ from the measurement of the kinematic edges in the momentum spectra of the visible decay products, as we described in details in §§ 10.1 and 10.2.

To perform those measurements, we developed a new algorithm which allows the identification of edge-like features in a 1-dimensional distribution and an accurate measurement of their position. Moreover we developed an optimization and calibration procedure to determine in a reliable way the experimental errors related to such a measurement. The detailed description of the algorithm and its optimization procedure was presented in chapter 11.

Assuming the current mass limits, we can evaluate the range of the possible positions of those kinematic edges at a 500 GeV lepton collider like the ILC, calculated according to the formulae described in § 10.2.1. By randomly choosing the two masses according to those constraints we can obtain the plot in fig. 12.1 and from that we can determine that the maximum expected value for the high-momentum kinetic edge that is about 205 GeV/c

[1] *Particle Data Group*

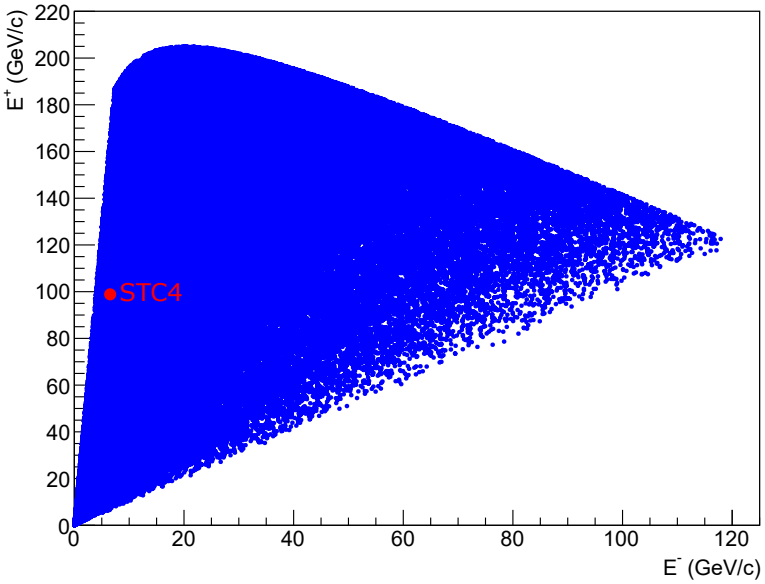

Figure 12.1: Spectrum of the possible positions of the kinematic edges from the $\tilde{e}_R$ decay at a 500 GeV ILC, consistent from the current limits on the masses of $\tilde{e}_R$ and $\tilde{\chi}_1^0$. In analogy with the definition of § 10.2.1 E^- labels the position of the low-momentum edge and E^+ that of the high-momentum edge.

and for the low-momentum kinematic edge is 120 GeV/c.

On the other end, the minimum values of the kinematic edges positions tend to 0 as the mass difference between the $\tilde{e}_R$ and of the $\tilde{\chi}_1^0$ decreases (see eq. 10.11). Increasing the centre-of-mass energy and, therefore, the boost of the parent s-electron can mitigate this effect, in particular for the high-momentum kinematic edge.

The STC4 benchmark scenario, which we described in § 10.3.1, is well-suited to study the potential of the ILD detector to discover and measure accurately the property of possible supersymmetric particles, in particular the s-electrons. The two kinematic edges of the $e^-e^+ \to \tilde{e}_R\bar{\tilde{e}}_R$ at $\sqrt{s} = 500$ GeV, highlighted in fig. 12.1, sit in two very different areas of the momentum spectrum. The low-momentum edge at $\boldsymbol{E^-} = 7.298$ GeV/c is dominated by strong backgrounds which we will need to reduce to produce an accurate measurements. The high-momentum edge, at $\boldsymbol{E^+} = 99.362$ GeV/c, sits in a more favourable area of the parameter space, where the backgrounds are easier to identify but, due to the higher momentum of the final-state particles which increases the effect of radiative losses, the edge is less sharp and the major challenge will be the accurate measurement of its position.

To perform an accurate measurement we will first need to accurately select those events most likely to be compatible with our signal process. This selection will proceed through a sequence of cuts on a set of relevant parameters which will be described in § 12.3. Due to the different characteristics of the background and signal events in the high-momentum and low-momentum regions we prepared two sets of cuts to be applied separately to highlight the two edges.

Once the backgrounds are properly reduced, our edge detection algorithm can be optimized and calibrated to obtain the position of the two edges and, more importantly determine the accuracy which can be expected in that measurement in a realistic experiment.

Those measurements will be finally use to calculate the masses of the two supersymmetric particles.

12.1 Data generation and particle reconstruction

The data used for the analysis we are going to present were generated using the tools provided and approved by the ILD collaboration detector concept group. In particular the primary events for both the standard model and the SUSY processes were generated with `Whizard`[2] `1.95` [135] assuming a nominal centre-of-mass energy $E_{\mathrm{CM}} = 500\,\mathrm{GeV}$. The generator also takes in account the effects of the initial state radiation and includes a realistic beam energy spectrum. Since `Whizard 1.95` only generates hard interactions, `PYTHIA 6.4` [136] is internally used for the fragmentation and hadronization of the primary particles.

The steering parameters for the generation of the SUSY samples, defining the STC4 benchmark point, were provided by the authors of [123] and are the same as those used for the other analyses on the same benchmark model for the ILD collaboration described in that article. The cross section for all the processes with visible decay products, accessible to the ILC experiments at 500 GeV, are listed in tab. 12.1 as they are calculated by the generator.

To simulate the beam effects we applied the same conditions described in [45]. In particular the beamsstrahlung effects are taken into consideration. For the Standard Model background we used the same samples generated for the ILD detector benchmarking presented in [46] with additional samples produced for the $\gamma\gamma$ processes where the available statistics was insufficient.

To simulate the detector effects we used the fast simulation program SGV [137] interfaced with the detector description used for the aforementioned ILD benchmarking. The tracking simulation is based on the evolution of the full covariance matrix of the charged track helix through the tracker layers from the outside in to finally obtain helix parameters and their covariance matrix at the point of closest approach to the event vertex.

During the tracking the software also simulates bremsstrahlung and pair-production. In the first case though an independent photon is only created in the simulation if the ratio between the electrons transverse momenta after $\boldsymbol{P'_T}$ and before $\boldsymbol{P^0_T}$ the interaction is above a custom threshold. In all samples we use for this analysis, a separate photon is created only if $\frac{\boldsymbol{P'_T}}{\boldsymbol{P^0_T}} < \mathbf{0.9}$.

The calorimeter response is obtained using both charged and neutral particle which are extrapolated to the intersection with each of the detector where, if above a detectability threshold, can trigger a parametrized shower or be treated as a minimum-ionizing particle.

The most relevant feature of the calorimeter simulation is the treatment of neighbouring showers to simulate the particle flow algorithms like the Pandora software used for the ILD detector event reconstruction [138]. The goal of those algorithms is to measure the energy

[2] https://whizard.hepforge.org/

Process	$\sigma(\mathcal{P}_L^L)$	$\sigma(\mathcal{P}_R^L)$	$\sigma(\mathcal{P}_L^R)$	$\sigma(\mathcal{P}_R^R)$	$\sigma(\mathcal{P}_{L30}^{R80})$	$\sigma(\mathcal{P}_{R30}^{L80})$
$e^-e^+ \to \tilde{e}_L\bar{\tilde{e}}_L$	0	84	8	0	7.62	49.42
$e^-e^+ \to \tilde{e}_L\tilde{e}_R$	336	0	0	0	21.84	105.8
$e^-e^+ \to \tilde{e}_R\tilde{e}_L$	0	0	0	335	105.5	21.78
$e^-e^+ \to \tilde{e}_R\bar{\tilde{e}}_R$	0	52	1313	0	769.9	76.38
$e^-e^+ \to \tilde{\mu}_L\bar{\tilde{\mu}}_L$	0	39	8	0	6.045	23.10
$e^-e^+ \to \tilde{\mu}_R\bar{\tilde{\mu}}_R$	0	52	222	0	131.7	38.19
$e^-e^+ \to \tilde{\tau}_1\bar{\tilde{\tau}}_1$	0	77	244	0	145.4	53.59
$e^-e^+ \to \tilde{\tau}_1\bar{\tilde{\tau}}_2$	0	3	2	0	1.275	1.825
$e^-e^+ \to \tilde{\tau}_2\bar{\tilde{\tau}}_1$	0	3	2	0	1.275	1.825
$e^-e^+ \to \tilde{\tau}_2\bar{\tilde{\tau}}_2$	0	26	7	0	5.005	15.46
$e^-e^+ \to \tilde{\chi}_1^\pm\tilde{\chi}_1^\mp$	0	259	0	0	9.065	151.5
$e^-e^+ \to \tilde{\chi}_1^0\tilde{\chi}_2^0$	0	206	11	0	13.65	120.9
$e^-e^+ \to \tilde{\chi}_2^0\tilde{\chi}_2^0$	0	115	0.03	0	4.043	67.28
$e^-e^+ \to \tilde{\nu}_\tau\tilde{\nu}_\tau$	0	22	16	0	10.13	13.43

Table 12.1: The table lists the cross-section of the production processes with visible decay products of the STC4 scenario accessible to the ILC experiments at a centre-of-mass of 500 GeV and different beam polarizations. All the listed cross-section are in fb and calculated by the `Whizard 1.95` event generator. The first four column list the production cross-section of the relevant processes for ideal beam polarizations while the last two list the values calculated assuming the design polarizations of the ILC beams. For each column the superscript and subscript represent the electron and positron polarization, respectively. R and L represent, respectively, a right-handed or left-handed polarized beam and the following number the degree of that polarization. It is possible to easily notice the cross-section enhancements for those processes where the t-channel production is available, e.g. the $\tilde{e}$ pair production.

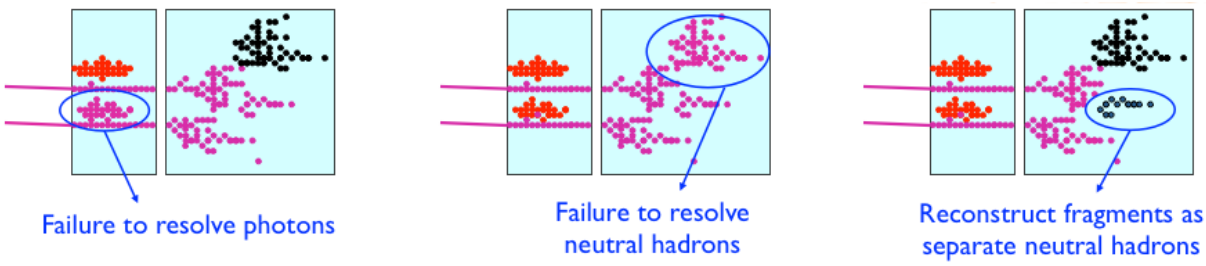

Figure 12.2: Possible sources of confusion errors in the particle flow reconstruction in a fine granularity calorimeter (from [138])

of the charged particles using the tracking information and rely on the calorimeters only for the measurement of the neutral particles, either photons or hadrons. Intrinsic to this approach is the possibility of a wrong assignment of the calorimeter clusters to the relevant particles giving rise to the so-called confusion errors. There are two possible sources of confusion, schematically represented in fig. 12.2. On one hand we can fail to resolve a neutral particle and associate all or part of its calorimeter clusters to a neighbouring charged particle in which case some energy will be effectively lost. On the other hand we could fail to assign part or all the clusters generated by a charged particle shower to the parent thus double counting the energy contained in those clusters. SGV is able to simulate both effects using an analytic parametrization to determine the probability of splitting or merging clusters.

For each process the samples were generated for all combination of beam polarization assuming the ideal case in which each beam can be polarized up to 100%. The different polarization samples were re-weighted in the first steps of the analysis to obtain the required realistic polarization which, unless otherwise specified, is that of an 80% right-polarized electron beam and 30% left-polarized positron beam.

To simulate a data set of the required integrated luminosity, we scaled the weight of each process taking in account the calculated cross-section and the number of available event that were generated. Unless noted otherwise, all the errors in the presented plots were calculated assuming a Poisson statistics.

12.2 Electron reconstruction algorithm

The typical signature of the signal events is the presence of an electron and a positron not correlated to any other primary particle. To identify those particles and appropriately reconstruct their initial momenta we developed a special reconstruction algorithm. In the following description, unless otherwise specified, the term *electron* will refer to both the electron proper and the positron.

The procedure was developed to be used on the data after an initial preselection, that is in the assumption that all or most of the events with a relevant hadronic or muonic activity were already filtered out. Alternatively an algorithm similar to that which we developed can be applied after the removal of the reconstructed hadrons and muons from the signal candidates. Under this assumption all the remaining charged particle are considered electrons candidates.

In a hermetic, omni-purpose experiment like ILD, an electron is identified by a signal in the tracker matching a cluster in the electromagnetic calorimeter of similar energy, within the measurement errors. In an ideal case the electron would be completely absorbed by that first calorimeter but, depending on the particle's energy and the radiation thickness of the detector, part of the electromagnetic shower can *leak* in the hadronic calorimeter which immediately follows. In the SGV simulation we used, though, there is no energy leakage between the electromagnetic and hadronic calorimeter and an electron is always completely absorbed in the former. This feature is not considered harmful to our ana-

lysis nor we believe makes the following statements unrealistic mainly because the calorimetric information is actually irrelevant to the correct assignment of a charged particle momentum, usually obtained through the higher precision information of the tracking system. Moreover, the large thickness of the electromagnetic calorimeter (§ 3.2.3) drastically reduces the chances of such a leakage to occur and anyway, due to the high granularity of the hadronic calorimeter, it would be possible to match the leaked energy to the electromagnetic shower.

The most important effect which influences the electrons momentum measurement is the energy loss as the particle passes through the tracker. Those are usually divided in continuous and discrete interactions. To reduce the magnitude of both the material budget of the tracker should be minimized. In the ILD case the material budget of the barrel is kept below 10% of a radiation length (see § 3.2).

The continuous part, due to the multiple scattering within the tracking materials, continuously reduces the curvature of the particle track. This is usually taken in account by the advanced tracking algorithms used for the reconstruction, such as the Kalman filter [139, 140] or the general broken lines method [141]. The SGV simulation and reconstruction software we use for this analysis does not perform a full tracking but includes the inaccuracies due to those losses in the full correlation matrix describing the momentum measurement errors.

Additionally an electron can lose a relevant fraction of its energy emitting a single real photon. The practical effect is the presence of a kink in the particle trajectory where the emission took place. The emitted photon, which is undetectable in the tracker will then create an energetic shower in the calorimeter pointing back to the kink. In the SGV simulation and reconstruction the two parts of the tracks are kept separated and the neutral cluster can be associated to either one of them or shared between both.

Thus, the main challenge of our electron reconstruction algorithm is the identification of the different signals generated by a radiative event, merging them together to form a single object of the appropriate momentum.

To do this we start from the consideration that, among the particle involved in a radiative event, we are interested in the reconstruction of the kinematic properties of the primary, that is the one with the highest momentum. Thus we iteratively search for the charged particle with the highest momentum among all those reconstructed and select all the objects, neutral or charged, within two cones of custom size, one for each of the two categories, centred along the seed particle track, removing them from the candidate list of the iterative search. The cone size is chosen independently for charged and neutral particles.

If the sum of the charges of the remaining charged particles in the relevant cone is 0, we assume that they are the product of the conversion of a photon in an electron-positron pair. Therefore we sum the four-momenta of the positive and negative particle with the highest momentum among them and we use this value to create a new neutral, composite object. All the other charged particles in the cone are discarded. All the neutral objects that were not included in any cone around any charged particle are treated as isolated photons. The final result of this algorithm is to sort all the reconstructed particles of the

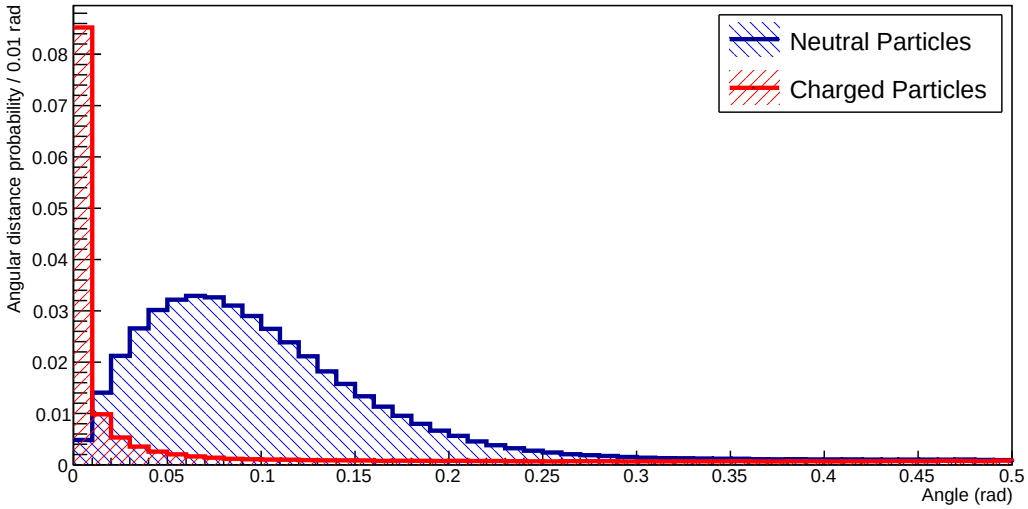

Figure 12.3: Angular distance between the seed charged particle and any other reconstructed object in a $e^+e^- \to \tilde{e}_R\bar{\tilde{e}}_R$. This process is characterized by a an uncorrelated electron-positron pair and provides a clean sample of isolated leptons to use for the isolation test. The distance is plotted separately for charged and neutral particles and limited to a maximum of 0.5 rad from the seed particle for visualization purposes.

original event in isolated charged or neutral objects.

One possible issue may come from a radiative event happening before or in the very first layers of the tracking system. In the first case the primary particle would have a diminished momentum compared to the initial state but that information could be recovered identifying the photon emitted in the process and summing it's four-vector to the one of the seed particle. Unfortunately the energy resolution of the electromagnetic calorimeter which is to be used to measure that momentum is much worse than that of the tracker and that would reflect on the accuracy of the measurement of the primary particle's momentum.

In the second case, a very short track in the tracker would result in a reduced momentum resolution. In that case we could either apply the same algorithm we described for the previous case or we can ignore those tracks where the momentum error exceeds a predefined threshold. In the following we will always use the first solution.

The most appropriate cone size was defined empirically by analysing the distribution of the angular distances between the seed particles and all the other in the event. First we observe that distribution in the signal sample, as shown in fig. 12.3, where the final state is characterized by the presence of two isolated and uncorrelated charged particles. In this sample it is clear that the charged and neutral particles closest to the seed are part of the same shower. This allows us to choose the cone size for the charged particles to be 0.075 rad and that for the neutral ones to be 0.3 rad. We should note again that this algorithm is going to be applied only after an initial preselection which would eliminate events with non-negligible hadronic activity which would create high density jets.

To test the algorithm we used the signal samples and we produce the momentum distributions of the two electrons or positrons candidates with the highest momentum

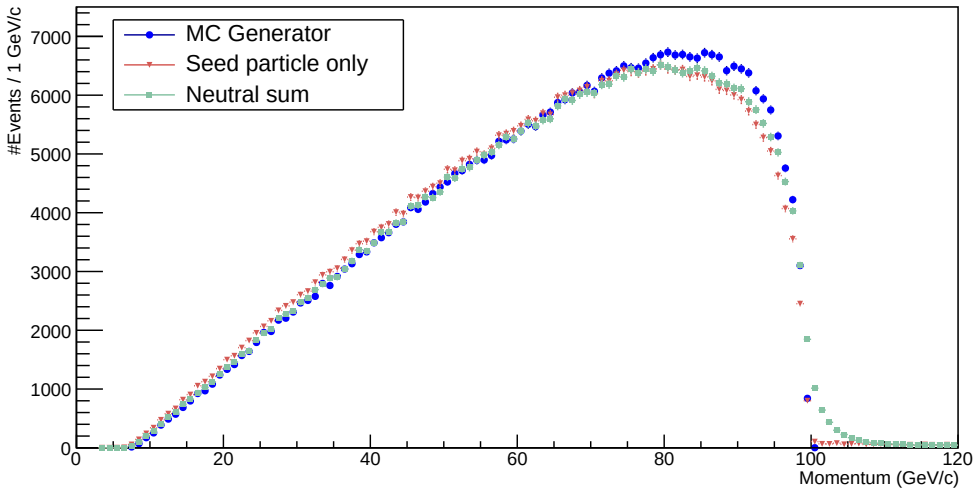

Figure 12.4: Comparison of the momentum distributions of the most energetic electron or positron in the signal sample, measured using different algorithms. In the first distribution the momentum is obtained directly from the Monte Carlo generator. In the red distribution we applied the electron reconstruction algorithm described in this chapter without ignoring all additional particles in the cone around the candidate. Finally the green distribution is obtained using the same algorithm but summing the four-momentum of the neutral particles in a cone of fixed size around the candidate. The distributions are obtained using preselected data with an integrated luminosity of $500\,\mathrm{fb}^{-1}$.

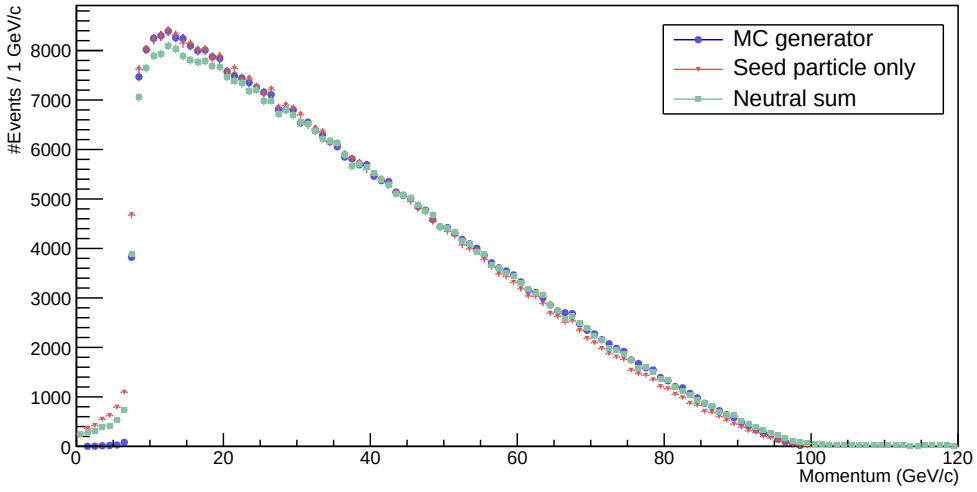

Figure 12.5: Comparison of the momentum distributions of the second most energetic electron or positron in the signal sample, measured using different algorithms. In the first distribution the momentum is obtained directly from the Monte Carlo generator. In the red distribution we applied the electron reconstruction algorithm described in this chapter without ignoring all additional particles in the cone around the candidate. Finally the green distribution is obtained using the same algorithm but summing the four-momentum of the neutral particles in a cone of fixed size around the candidate. The distributions are obtained using preselected data with an integrated luminosity of $500\,\mathrm{fb}^{-1}$.

		MC generator	Seed particle	Neutral sum
Low edge	**Filter**	FDOG ($\sigma = 4$)	FDOG ($\sigma = 4$)	FDOG ($\sigma = 5$)
	Bin resolution (MeV/c)	50	50	50
	Edge error (MeV/c)	8.3	10.6	11.0
	Position bias (MeV/c)	119	113	138
High edge	**Filter**	FDOG ($\sigma = 5$)	FDOG ($\sigma = 6$)	FDOG ($\sigma = 10$)
	Bin resolution (MeV/c)	200	200	200
	Edge error (MeV/c)	24	32	45
	Position bias (MeV/c)	-388	-330	-591
	$\tilde{e}_R$ mass error (MeV/c^2)	62	80	85

Table 12.2: Comparison of the optimal response of the edge detection algorithm applied on the momentum distributions obtained with different electron reconstruction algorithms. The input distributions are those shown in fig. 12.4 and 12.5 with matching labels. For each of the two edges that were tested, the first row describes the optimal filter selected for the measurement, the second row is the size of each bin, the third represents the statistical error on the determination of the edge position and the third the difference between the measured and true edge positions $E^+ = 99.362\,\mathrm{GeV/c}$ and $E^- = 7.298\,\mathrm{GeV/c}$. Finally the last row represents the error on the $\tilde{e}_R$ due to those errors. All results were obtained assuming an integrated luminosity of $500\,\mathrm{fb}^{-1}$, 80% polarized electrons and 30% polarized positrons.

using three different algorithms:

- The benchmark distribution for the test is obtained directly from the primary Monte Carlo generated particles by extracting the momenta of the initial decay products of the $\tilde{e}_R$. Therefore this can be considered the optimal achievable distribution;
- The electron reconstruction algorithm described above is applied to the complete set of particles as reconstructed by the SGV algorithms using a cone size of 0.075 rad for the charged particles and 0.3 rad for the neutral ones choosing only the seed particle to determine the momentum of the reconstructed object. All the other particles in those cones are eliminated from any further consideration;
- We applied the same algorithm as before but we also sum to the four-momentum of the seed particle those of all the neutral objects within its neutral search cone.

The distributions obtained using those algorithms are shown in fig. 12.4 and 12.5. In both plots, but in the first one in particular, is evident that the momenta of the particles reconstructed by the electron reconstruction algorithm are slightly biased towards lower values and that this bias is larger at greater momenta, as could be expected considering that there is a relevant chance that part of the electron energy may be lost in radiative events.

The application of the neutral sum feature of our electron reconstruction algorithm can partially compensate those losses but at the cost of introducing a visible and relevant tail beyond the high-momentum edge of the distribution. The general smearing of the

distribution caused by the inclusion of the calorimetric measurement is also expectable due to the much lower resolution of that measurement as compared to that obtained by the tracker alone.

As the goal of our analysis is to determine precisely the position of the edges visible in those distributions we used them to compare the results of our edge finding algorithm in the different cases. The results of those measurements are summarized in tab. 12.2. The best results are indeed obtained on our Monte Carlo benchmark distributions but the errors measured using the reconstructed particles are within a factor of 2 of the optimal value. Additionally we can notice that the optimal binning and filter size are very similar. Nonetheless we also observe that, especially for the high-momentum edge, the smearing due to the addition of the calorimetric energies reduces the measurement resolution noticeably. Therefore, in the following selection and analysis, we are going always to use the electron reconstruction algorithm without the *neutral sum* option.

12.3 Selection

Even though the cross-section of the $e^-e^+ \rightarrow \tilde{e}_R\bar{\tilde{e}}_R$ process we are going to analyse is relatively high if compared to the other SUSY cross-sections, it is still several order of magnitude smaller than the cross-section of the Standard Model processes, as listed in tab. 12.3. As the accuracy of our localization algorithm depends on the signal-to-noise ratio in the neighbourhood of the edge position, we developed a specific selection to improve that quantity. An additional requirement of our selection is to minimize the distortions in the signal sample in the edge neighbourhood, and to avoid the introduction of additional edge-like features in the background in the same region. As the quality and relevance of the background at the two edge positions is potentially different we developed an independent selection for each of the two measurements.

The selections are based on a set of sequential cuts and is based on the identification of events with a single non-collinear electron-positron pair. A summary of the used cuts and the values of their parameters is presented in tab. 12.4. The cut strategy was devised to avoid any model assumption beyond those derived from the current limits on the s-electron mass which were described in the introduction to this chapter and to tune each cut using the data obtained in the previous steps.

Compared to the previous analysis performed on the same benchmark model, described in [123], we can identify several important differences, the most important of those being the different algorithm used for the electron identification. In that analysis the DELPHI τ finder algorithm [29] was used to identify all the leptons and was used on the complete data set, that is in the very first selection step. That was necessary because the same algorithm was used to select the data relevant to all the s-leptons analysis.

In our case, on the other hand, we developed a analysis dedicated only to the s-electron measurements and we developed an initial preselection based exclusively on global event features so that the electron identification algorithm was only used on a much smaller and cleaner sample and especially tuned to identify electrons only. For this reason, rather than

Process	$\sigma_{\mathcal{P}_{L30}^{R80}}$ (fb)	Generated	Expected @ 500 fb^{-1}	Preselection Acceptance
$\tilde{e}_R$				
$e^-e^+ \to \tilde{e}_R\bar{\tilde{e}}_R$	769.925	683025	384963	0.99
other $\tilde{e}$				
$e^-e^+ \to \tilde{e}_L\bar{\tilde{e}}_L$	7.62	46039	3810	0.90
$e^-e^+ \to \tilde{e}_{R\|L}\bar{\tilde{e}}_{L\|R}$	134.985	381890	63682.5	0.94
other SUSY				
$e^-e^+ \to \tilde{\mu}\tilde{\mu}$	137.735	160930	68867.5	$1.5 \cdot 10^{-6}$
$e^-e^+ \to \tilde{\tau}\tilde{\tau}$	152.99	183872	76495	0.043
$e^-e^+ \to \chi\chi$	36.8825	316535	18441.3	0.042
SM e^-e^+				
$e^-e^+ \to 2f$	17623.5	$2.75 \cdot 10^7$	$8.81 \cdot 10^6$	0.044
$e^-e^+ \to 4f$	11167.3	$2.67 \cdot 10^7$	$5.58 \cdot 10^6$	0.063
$e^-e^+ \to 6f$	473.665	395001	236832	$5.2 \cdot 10^{-5}$
$\gamma\gamma$				
$\gamma\gamma \to 2f$	$2.677 \cdot 10^6$	$1.67 \cdot 10^8$	$8.03 \cdot 10^8$	0.0062
$\gamma\gamma \to 4f$	184.402	21053	74588.7	0.056
$\gamma e^\pm$				
$\gamma e^\pm \to nf$	256602	$2.62 \cdot 10^7$	$9.9 \cdot 10^7$	0.022

Table 12.3: Summary of the generated data and preselection acceptance for the different process categories. In boldface we highlighted the names used in all the plots to differentiate between different datasets. For each one of them we provide further differentiation between the different processes which are included in the category. The columns list, respectively, the process type, its cross-section at a 500 GeV ILC when using an 80% right polarized electron beam and 30% left polarized positron beam, the number of events generated by the Monte Carlo simulation, the expected number of events after accumulating 500 fb^{-1} worth of data and the efficiency of the preselection cut when applied to that process.

Cut name	**Cut variable**	E^+ **selection variable range**	E^- **selection variable range**
Preselection	Number of charged particles	$[2, 8]$	
	HCal energy	0	
	Maximum charged particle momentum	$[0, 205]$ GeV/c	
	ECal total energy	$[0, 420]$ GeV	
ECal ratio	ECal energy ratio	> 0.4	
Charged energy ratio	Charged energy ratio	> 0.6	
ECal energy	ECal total energy (GeV)	$[5, 240]$	$[12, 180]$
Missing mass	Missing mass	$> 300\,\mathrm{GeV/c^2}$	
J_H **selection**	$\theta_{J_H^-}$(rad)	$[0.1, 2.0]$	$[0.64, 2.0]$
	$\theta_{J_H^+}$(rad)	$[1.14, 3.04]$	$[1.14, 2.5]$
	$\lvert\vec{P}\rvert_{J_H}$(GeV/c)	> 0.0	$[0.0, 100.0]$
J_L **selection**	$\theta_{J_L^-}$(rad)	not applied	$[1.0, 3.04]$
	$\theta_{J_L^+}$(rad)		$[0.1, 2.14]$
Acollinearity	Acollinearity (rad)	$[0.7, 3.08]$	< 3.0
Missing P_T	Missing transverse momentum	not applied	$> 10\,\mathrm{GeV/c}$
Acoplanarity	Acoplanarity	not applied	$< 2.5\,\mathrm{rad}$

Table 12.4: Summary of the data selection parameters. For each cut we listed the variables used and their range. The variables are further described in the text. We listed separately the cut range used for the high- and low-momentum edge analysis.

converting that Fortran-based DELPHI code to C++ or finding a way to use it on the existing SGV data samples, we developed a simpler algorithm with a more limited scope which is the one described in the previous section. Another fundamental difference between the two selection algorithms is that, in the cited analysis, a single parameter set was used to select the data to be used for the high- and low-edge position measurement while we decided to tune the selection differently before the measurement of the two edge positions.

12.3.1 Naming, conventions and definitions

In the following discussion we will adopt a naming convention to concisely identify the electron or positron with the highest and the second highest momentum among those identified by the electron identification algorithm in each event, labelling them, respectively $\boldsymbol{J_H}$ and $\boldsymbol{J_L}$. When it is important to distinguish between the electron or the positron we can additionally add the charge superscript to the label, e.g. $\boldsymbol{J_H^+}$ representing the identified positron with the highest momentum in an event. This naming will be applied to both the single particles in an event and to their distribution in the analysed sample. The actual meaning would be clear from the context.

To identify the position of the kinematic edges we aim to measure we will use the same convention we used in the previous chapters and name the position of the falling edge at the higher momentum $\boldsymbol{E^+}$ and that of the rising edge at the lower momentum $\boldsymbol{E^-}$. In some cases we will use the same label also to identify the edge itself, when that meaning is not ambiguous in the context.

To measure the effects of the implemented selection we will often use the following terms, hereby defined:

Cut acceptance: The ratio between the number of events which is accepted by a cut and the number of events before the cut;

Cut background rejection: If we define one of our categories as our signal, in this case the $\boldsymbol{\tilde{e}_R}$, and all the other as background, we define the background rejection as the fraction of background events which are not accepted by a cut;

Signal purity: For a given dataset we define this quantity as the ratio between the events in our signal sample and the total number of events in the dataset.

We will also hereby note that the final edge position measurement will be performed on the J_H and J_L distributions for, respectively, the E^+ and E^- edge. To simplify the comparisons, when we will show those distributions at different stage of the selection, we will use the same binning that will be found to be optimal for the edge finding algorithm at the end of the processing, that is, respectively, 0.2 GeV/c per bin and 0.05 GeV/c per bin. For the same reason, in those plots and in the those showing the selection acceptance as a function of the J_H or J_L variables we will always use the same ranges, that are between 0 GeV/c and, respectively, 120 GeV/c and 80 GeV/c. In the acceptance plots, to provide an easy visual distinction, we will use the light green for the J_H variable and blue for the J_L variable.

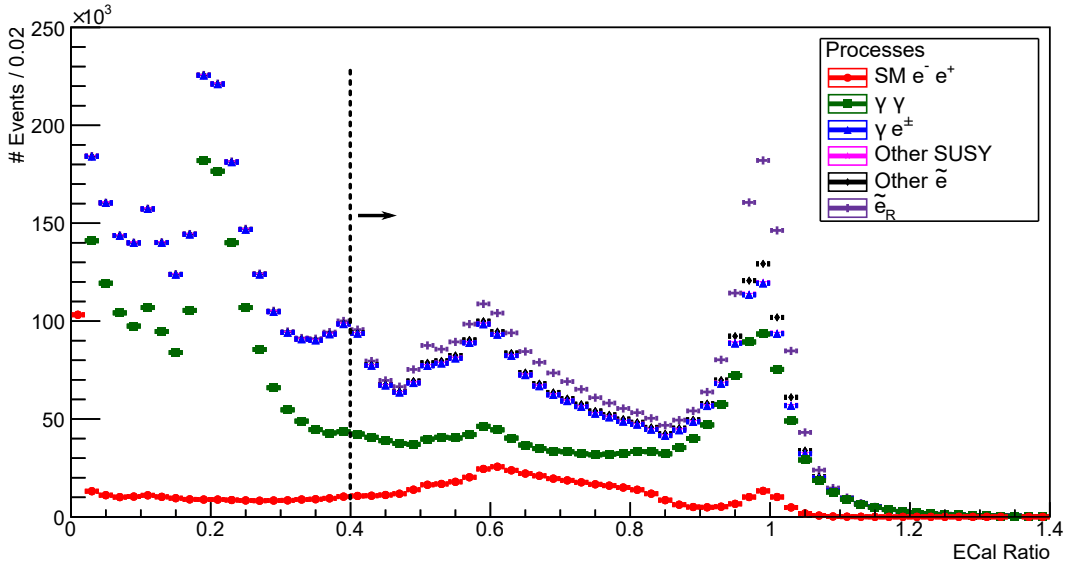

Figure 12.6: The distribution of the *ECal ratio* variable values for all the process categories after the preselection. The histograms are stacked on top of each other. The dashed black line represents the threshold of the cut applied to this variable.

12.3.2 Preselection

The first step of our selection is what we called a *preselection*, that is a broad and simple cut aimed to reduce the total amount of data to process in the further steps with negligible effect on the signal sample. This cut is based only on global event observables and does not make use of any electron identification algorithm.

The cut parameters are chosen assuming only the current experimental limits which, at a 500 GeV electron-positron collider imply the edge position limits described by fig. 12.1. From those assumption we derived the maximum momentum of any charged particle, 205 GeV/c, and the maximum energy recorded in the calorimeter which we will expect in an event, 420 GeV, equivalent to twice the maximum momentum with additional tolerance to take in account the worse energy resolution of the calorimeters as compared to the tracker. The other major requirement is the absence of any activity in the hadronic calorimeter which almost completely removes the hadronic, semi-leptonic and muonic processes from those contributing to the background.

The results of the preselection are collected in tab. 12.3 for the different categories in which we separated the simulated data. The preselection leaves the signal category almost untouched and removes mostly the hadronic and muonic final states. Notice that the labels used in that table will also be used in all the following plots and tables.

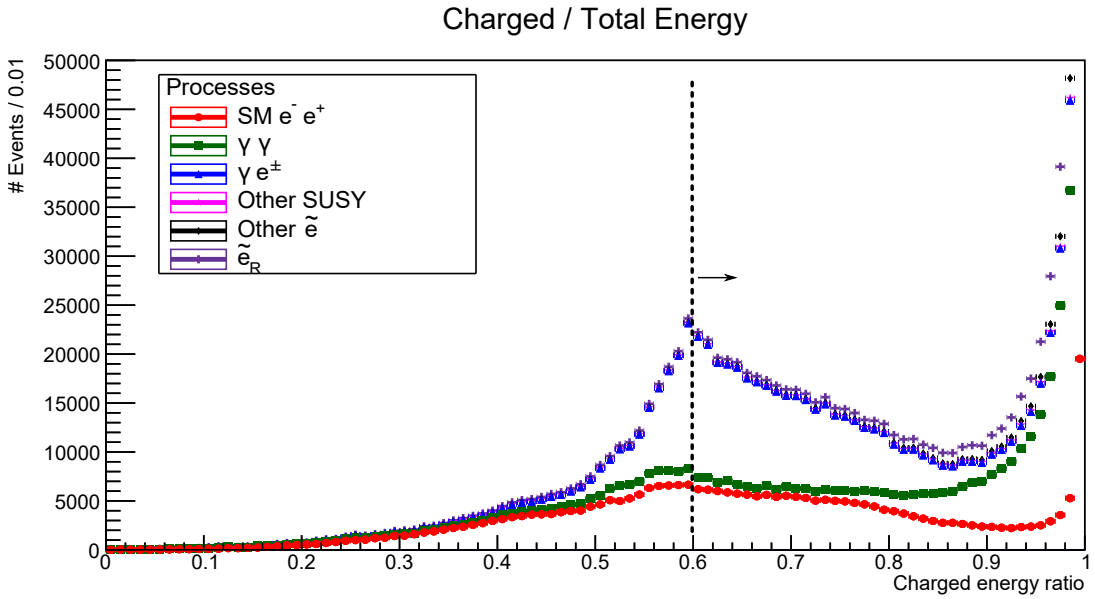

Figure 12.7: The distribution of the *Charged energy ratio* variable values for all the process categories after the application of the *ECal ratio* cut. The histograms are stacked on top of each other. The dashed black line represents the threshold of the cut applied to this variable.

12.3.3 Common selection

The first variable we use for the selection is named *ECal ratio* and is defined as the ratio between the energy measured in the electromagnetic calorimeters and the total visible energy. As the preselection filtered out all events with hadronic activity this variable allows to remove all events with a relatively large amount of energy deposited in the forward calorimeters § 3.2.3.

This variable is a powerful discriminator to reduce the SM t-channel backgrounds, in particular those from the $\gamma\gamma$ and $\gamma e\pm$ interactions. Additionally, the energy resolution of the forward system is relatively poor and the momentum of particles going in such a forward direction cannot be measured as the tracker is not able to cover such small angles, thus the kinematic variables would not be useful for our analysis.

This is a global event variable that can be calculated without any jet or electron reconstruction algorithm. Because this variable depends on general detector characteristics, a cut on this variable can be applied regardless of the actual edges position, that is without any additional assumption on the specific SUSY parameters under study.

The distributions of this variable for all the process categories are shown in fig. 12.6. A noticeable feature is the extension of all the distributions beyond the value of 1. As we discussed in the previous sections of this chapters, this is due to the possible double counting of the energy of the charged particles when their electromagnetic clusters are not associated correctly with the tracker signal.

The second variable we define for the selection is named *Charged energy ratio*, requires the application of our electron identification algorithm and is defined as the ratio between

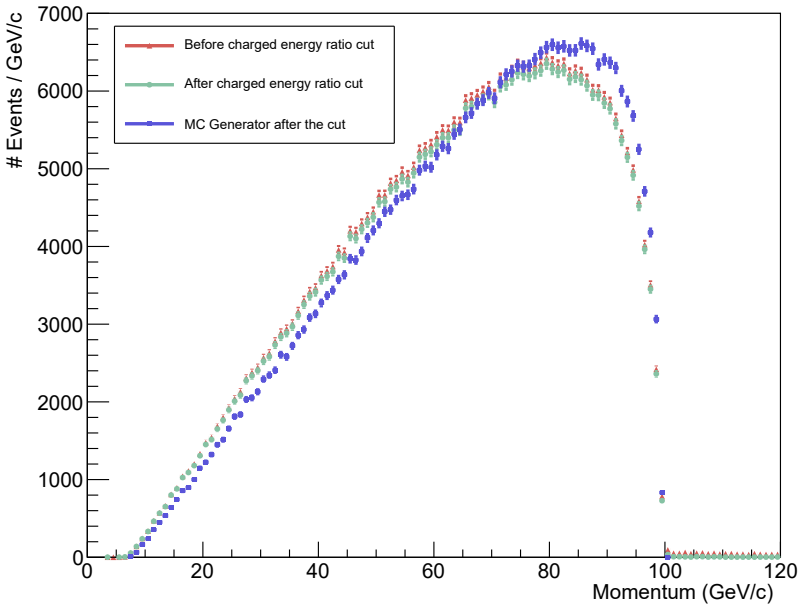

Figure 12.8: Comparison of the distributions of the J_H momenta before and after the *Charged energy ratio* cut and with the distribution of the particle with the highest momentum generated by the decay of a s-electron. All the distributions are obtained from the signal sample only. The plotted variable is the same used for the measurement of the high-momentum edge.

the energy in the charged objects and the total visible energy in all identified objects in the event. The distribution of the values of this variable for the different process categories is shown in fig. 12.7. In our selection we remove all events where this variable has a value lower than 0.6.

When applied to our preselected sample which does not contain hadronic final states, this variable helps in the identification and removal of all those events with a large contribution from the initial- or final-state radiation. The events of the first category, in particular, lowering the centre-of-mass energy of the SUSY process tend to lower the position of the E^+ edge, as we discussed in § 10.2.2, so their removal can improve the accuracy of the measurement of the edge position.

When we observe the effect of that cut on the signal process, comparing the J_H distribution before and after this cut and with the distribution of the electron or positron with the highest momentum whose parent is a s-electron, as obtained directly from the Monte Carlo generator, we observe that the general shape of the distribution is not changed (see fig. 12.8) but all the events beyond the kinematic threshold are strongly suppressed, which is more evident in fig. 12.9a where we plot the acceptance of the cut for the signal sample as a function of the J_H momentum.

This is due to the fact that, in those events, such a high momentum electron or positron cannot come from the $e^-e^+ \to \tilde{e}_R\bar{\tilde{e}}_R$ but, most likely, from the conversion or misidentification of the initial state radiation photon. What is important to note is that this efficiency drop is not correlated to the position of the kinematic edge but to its mere existence. As we would expect from that argument, in fig. 12.9b we don't see any drop corresponding to the E^- edge.

As it listed in tab.12.4, the first two cuts after the preselection are performed with the

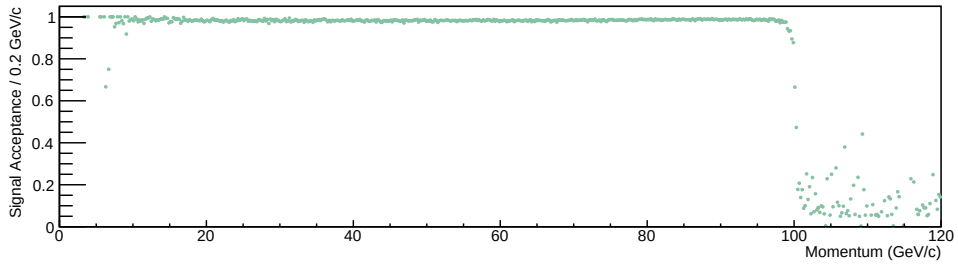

(a) *Charged energy ratio* acceptance as a function of J_H momentum

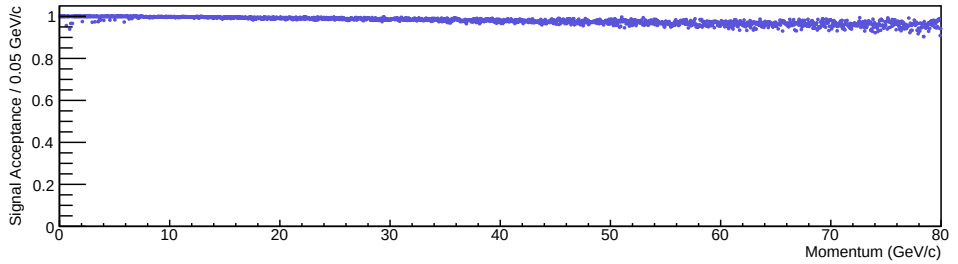

(b) *Charged energy ratio* acceptance as a function of J_L momentum

Figure 12.9: The signal acceptance of the *charged energy ratio* cut plotted as a function of the J_H and J_L momentum in the signal sample. A large drop between 80% and 90% is visible in a after the E^+ position whose true value is $E^+_{\text{true}} = 99.362\,\text{GeV/c}$. No such effect is visible at a position corresponding to the E^- edge in b, whose true value is $E^-_{\text{true}} = 7.298\,\text{GeV/c}$.

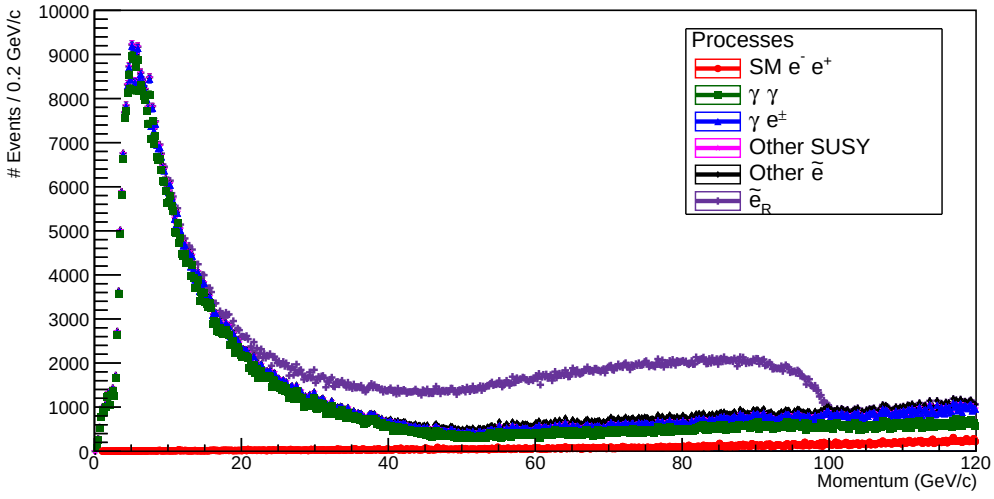

Figure 12.10: The J_H distribution on the complete data set after the *Charged energy ratio* cut. The E^+ edge is clearly visible over the background. Applying our edge detection algorithm to this distribution we measure the position of that edge as $E^+ = 98.66 \pm 0.09\,\text{GeV/c}$.

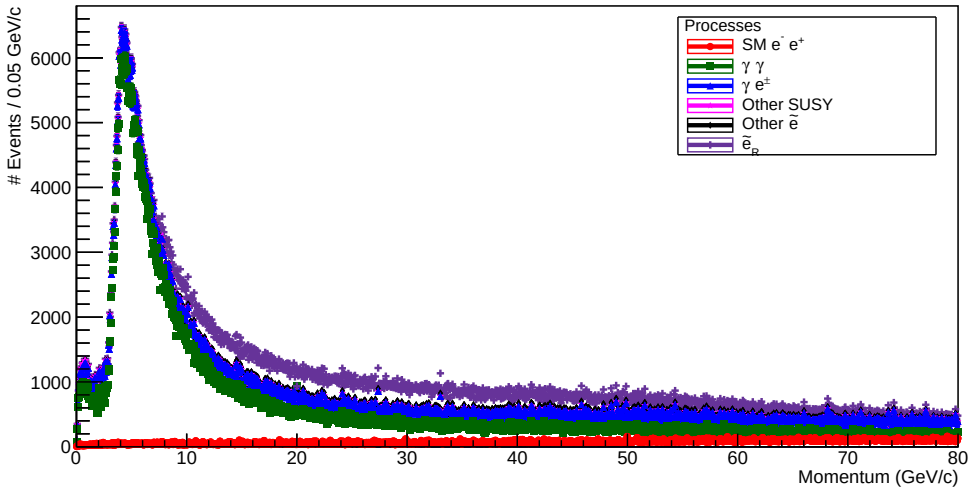

Figure 12.11: The J_L distribution on the complete data set after the *Charged energy ratio* cut. Contrary to the case of the J_H distribution, the low momentum edge, whose true value is $E^-_{\text{true}} = 7.298\,\text{GeV/c}$, cannot be seen in this plot as the massive $\gamma\gamma$ background at lower momenta dominates the sample.

same parameters for both the high- and low-momentum edge selection as both of them depend only on the detector and event features and not to the physical parameters of the process we are studying. After those cuts we can plot the J_H distribution, shown in fig. 12.10, and note that the E^+ edge is already clearly visible.

The application of our edge detection algorithm to that distribution results in a position measurement of $\boldsymbol{E^+ = 98.66 \pm 0.09\,\text{GeV/c}}$, which can be compared to the *true position* of $\boldsymbol{E^+_{\text{true}} = 99.362\,\text{GeV/c}}$. The result is obtained with an FDOG filter of size 6 and a binning of 0.2 GeV/c per bin.

It is relevant to notice that, given the relative uniformity of the background down to a momentum of about 40 GeV/c, a measurement with similar accuracy could be obtained for edge position at least as low at that threshold. If, on the other hand, the high-momentum edge position is lower than that, the spectrum would be so compressed that its relevance above the background would be clearly evident anyway.

On the other hand the analogue E^- edge, which in our benchmark case is located at a position of $E^-_{\text{true}} = 7.298\,\text{GeV/c}$, cannot be seen in the J_L distribution plotted in fig. 12.11, completely overwhelmed by the $\gamma\gamma$ background.

Due to those different background conditions we developed two different selections to enhance the high- and low-momentum edges independently. The position of the former will be performed first and that measurement will be used to tune more accurately the selection to enhance the latter. Note that, even though we will be showing the distribution of the cut variables for the analysed sample which corresponds to a specific benchmark point, the choice of the cut thresholds is always driven by the initial assumptions, those we clearly listed in the introduction to this chapter, and from the information we were able to obtain from the previous steps of the selection.

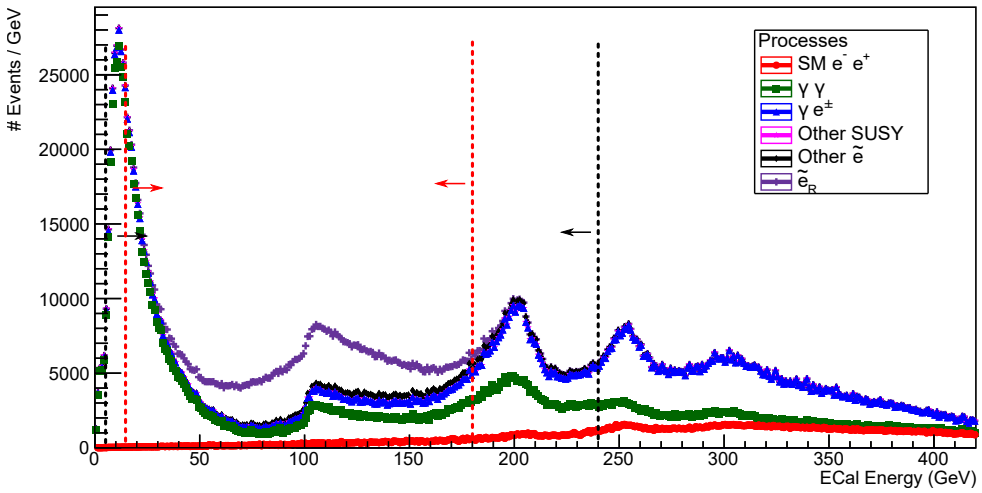

Figure 12.12: The distribution of the *ECal energy* variable values for all the process categories after the application of the *Charged energy ratio* cut. The histograms are stacked on top of each other. The dashed black lines represent the thresholds of the cut applied to this variable for the high-momentum selection. The red dashed lines show the equivalent thresholds for the low-momentum selection.

12.3.4 High-momentum edge selection

After the last cut of the common selection we were able to determine the position of the high-momentum edge with a precision lower than 100 MeV. Knowing that value we can further constrain the total energy we expect to see in the electromagnetic calorimeters to twice that value plus an additional 20% tolerance to take in account the ECal energy resolution, that is 240 GeV. Additionally, from fig. 12.1, we know that, with $E^{+} \approx 100\,\mathrm{GeV/c}$, $E^{-} \gtrsim 5\,\mathrm{GeV/c}$ so we can use that value as the minimum energy we expect in the electromagnetic calorimeter. Both thresholds are represented in fig. 12.12.

Knowing the value of the maximum momentum of an electron in our signal we can also calculate the minimum value for the missing mass parameter which is about $300\,\mathrm{GeV/c^2}$, so we can also apply a cut on that variable as represented by fig. 12.13.

At this point we will finally take advantage of the specific features of the physical process we are analysing. First of all we will require that the two objects with the highest momentum identified by the electron identification algorithm described in the previous section have opposite charge. We can then apply angular and momentum constraints separately on those two objects, labelled J_H and J_L.

Because the process we want to isolate proceeds through a t-channel exchange, there is a strong correlation between the direction of the beam and that of the scattered particle. Moreover, because the $\tilde{e}$ are unstable and the momentum in the laboratory frame of the final-state electron is higher when it is emitted collinearly with the direction of the parent, we expect that the leptons with the highest momentum will have the same type of correlation with the beam with the same charge. Finally, as the $\tilde{\chi}^0$ is a massive particle, we

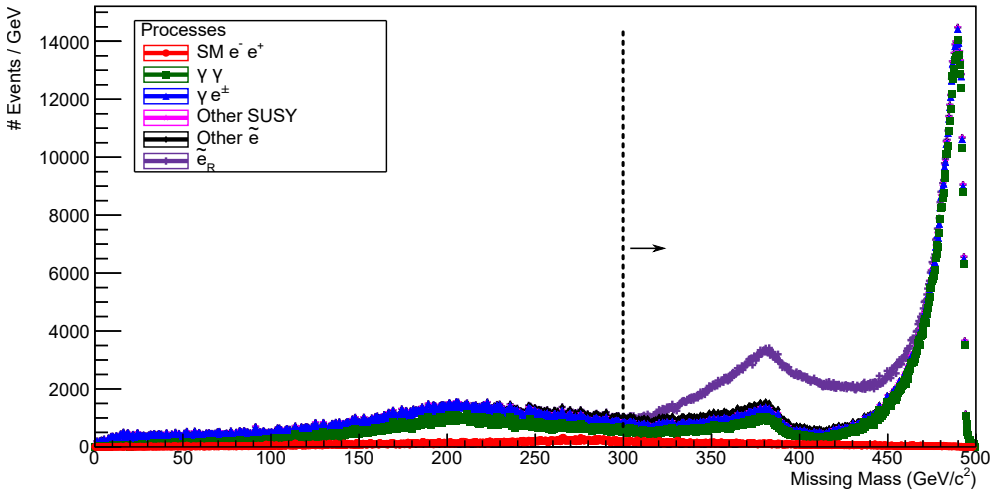

Figure 12.13: The distribution of the *Missing mass* variable values for all the process categories after the application of the *ECal energy* cut. The histograms are stacked on top of each other. The dashed black line represents the threshold of the cut applied to this variable.

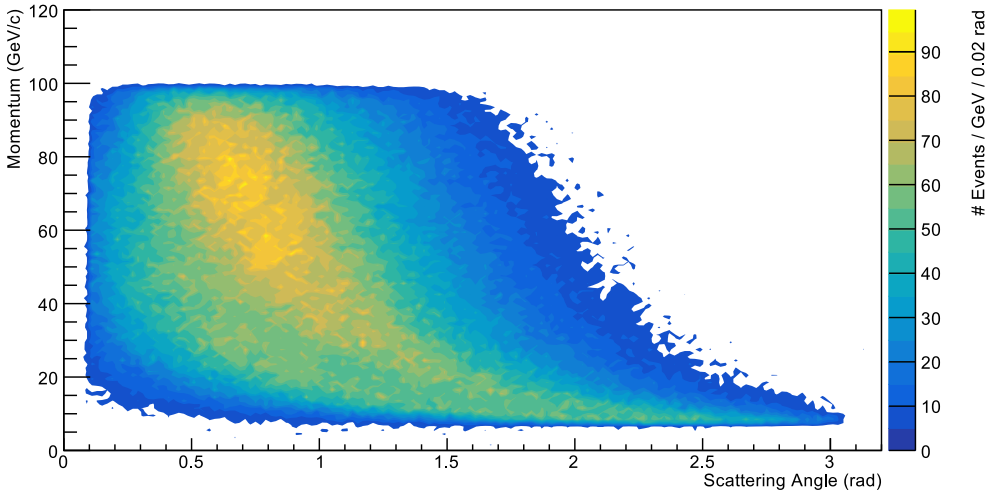

Figure 12.14: Correlation between the scattering angle and the momentum of J^- in the signal sample before the application of the J_H selection cut. The e^- beam direction is at $\theta = 0.07\,\text{rad}$. The correlation between the beam and the scattering directions described in the text is clearly observable.

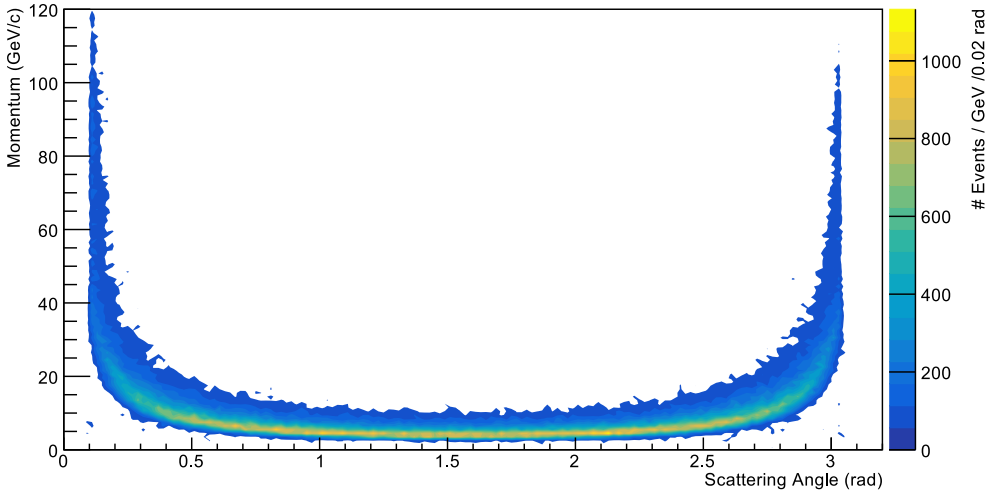

Figure 12.15: Correlation between the scattering angle and the momentum of J^- in the signal sample before the application of the J_H selection cut. The e^- beam direction is at $\theta = 0.07\,\text{rad}$.

know that there is a minimum momentum, equal to the mediator mass, that is going to be transferred in the process from which we can calculate the minimum scattering angle of the produced $\tilde{e}_R$ using the following formula:

$$\min(\cos\theta_{\tilde{e}}) = \frac{2E_0 - M_{\tilde{e}}^2 - 4M_{\tilde{\chi}_1^0}^2}{2E_0\sqrt{E_0^2 - M_{\tilde{e}}^2}} \approxeq 0.676 \tag{12.1}$$

where E_0 is the energy of the incoming electron, that is half of the centre-of-mass energy, and the other symbols are those already introduced in § 10.2.1. Also in this case we neglected the electron mass in the calculation. Because of the isotropic decay of the $\tilde{e}_R$ this would not be visible as an hard limit in the final state but will nonetheless reduce the probability to observe the final state leptons in a very forward direction.

All the features we just described are clearly visible in fig. 12.14, where we plotted the momentum and scattering angles of the J^- particles. A perfectly mirrored distribution is obtained if we look at the J^+ particles instead. As a comparison, we can observe the distribution of the same variable for the $\gamma\gamma$ sample, dominated by the $\gamma\gamma \to e^-e^+$ process. This is also a t-channel exchange process but involves the exchange of an electron, that is a charged and almost massless particle. Additionally the two photons involved do not typically have the same energy so the centre-of-mass frame is not the laboratory frame in this case. The effect, shown in fig. 12.15, is that the angular distribution is almost symmetrical between the forward and backward direction and the highest momentum particles are typically produced in such a forward direction that they are only detected in the forward calorimeters or not at all.

With those considerations in mind we can now apply a filter to the scattering angle of the J_H electrons and positrons choosing only those events where they are emitted in

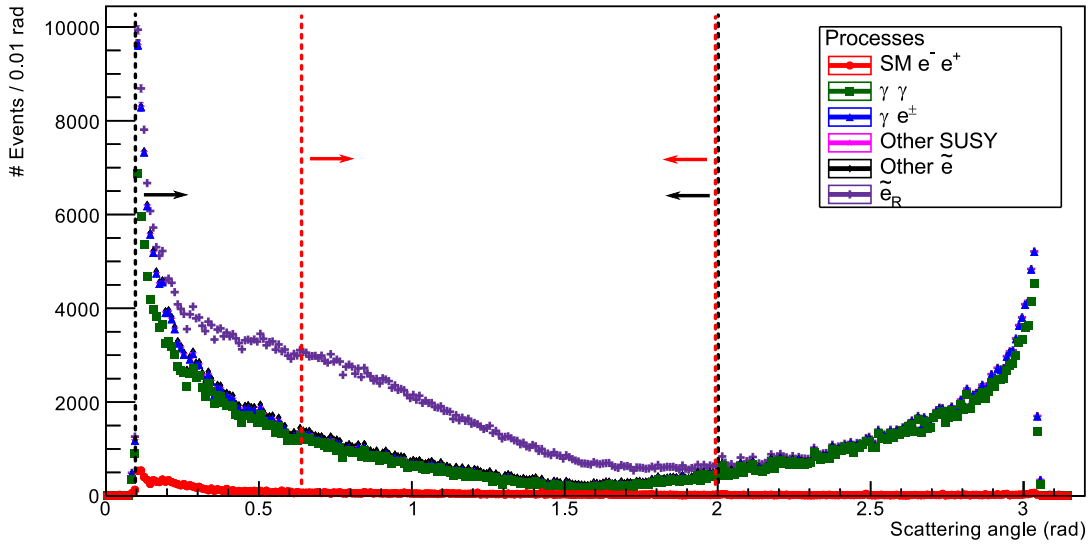

Figure 12.16: The distribution of the J_H^- variable values for all the process categories after the application of the *Missing mass* cut. The histograms are stacked on top of each other. The dashed black line represents the threshold of the cut applied to this variable. The red dashed lines show the equivalent thresholds for the low-momentum selection. Note that the electron beam travels at $\theta = 0.007\,\text{rad}$ and that a symmetric plot is obtained by observing the J_H^+ variable and that the cut threshold are symmetric as well.

the same half-detector of the direction of the beam with the same charge. In fact we used a slightly wider cut window to maximize the number of signal events selected as the background we want to reduce is mostly that in the very backward direction as compared to the beam of the same charge. The distribution of the scattering angle of the J_H^- particle with the applied cut thresholds is shown in fig. 12.16.

One additional deduction we can make from the previous discussion is that, if the direction of both final state particles is correlated with that of the beam with the same charge and that the correlation increases with increasing momentum, considering that the two beams are anti-parallel, then the electron-positron pair in our sample should also tend to be anti-parallel and this tendency should increase with the increase of the J_H momentum. This tendency can be quantified through the angle between the electron and the positron in the pair and this angle is what we call *acollinearity*. This quantity is plotted in fig. 12.17 for our signal sample as a function of the momentum of the J_H particle where we can observe the expected correlation.

Therefore, to selectively choose the events with the highest J_H, we can cut away all the events where the acollinearity between the J_H and J_L particle is below the value of 0.7 rad. Besides that we also cut away the events where the value of that variable exceeds 3.08 rad. This second thresholds gets rid of those events where the two final-state particles are in a back-to-back configuration. In the signal sample this is unlikely as the final-state particles come from the isotropic decay of the $\tilde{e}_R$, even though those are emitted in a back-to-back

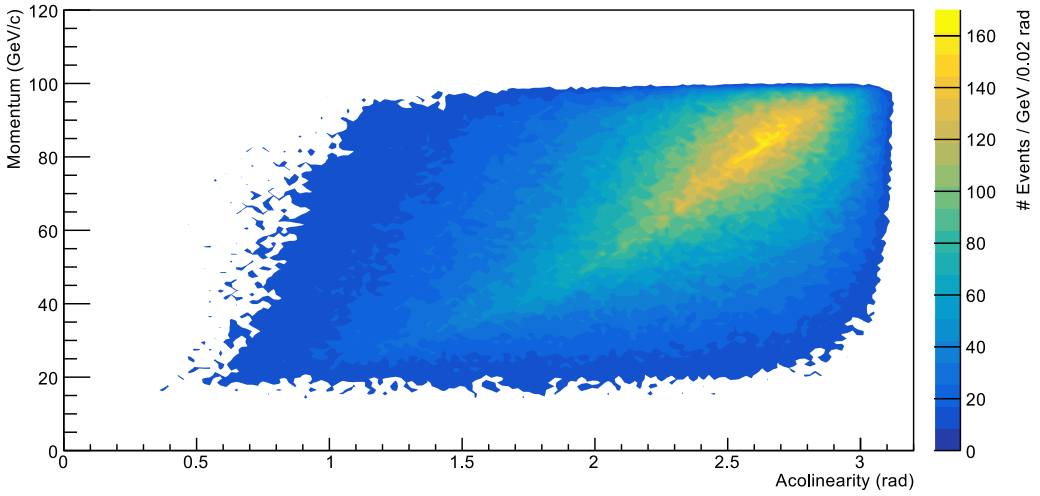

Figure 12.17: Correlation between the acollinearity and the J_H momentum in the signal sample before the application of the *acollinearity* cut.

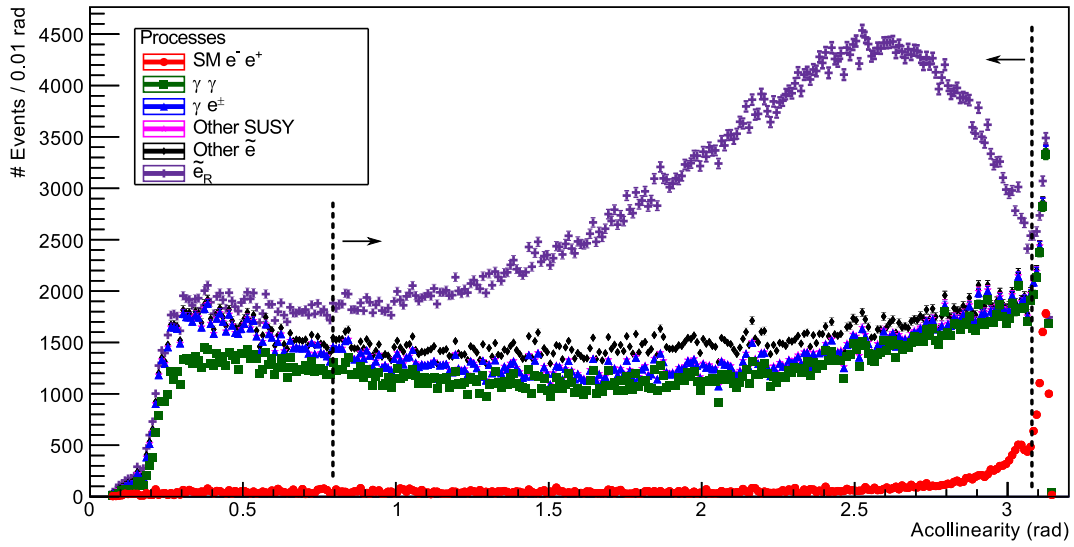

Figure 12.18: The distribution of the *Acollinearity* variable values for all the process categories after the application of the J_H selection cut. The histograms are stacked on top of each other. The dashed black line represents the threshold of the cut applied to this variable.

configuration. The effect of this cut on all process categories is shown in fig. 12.18.

At this point we can evaluate the results of the selection on our benchmark data set. To this end, in tab. C.2, we listed the acceptance and the background rejection of each applied cut, as we defined it earlier in § 12.3.1 and in tab. C.1 we listed the effective numbers of events surviving each of the cuts and the signal purity at each step of the process. After the final step the selection is thus able to produce a dataset with a 97% background rejection and a signal purity of 56.5%.

Even more important than the total numbers is the selection acceptance as a function of the J_H momentum. We already discussed, earlier in this section, the fact that the *charged energy ratio* cut introduces a drop in the signal acceptance immediately after the edge position but that is not harmful as those events are few in absolute numbers and they are mostly due to identified electrons or positrons which are not direct siblings of the primary $\tilde{e}_R$. None of the other cuts shows any similar feature and, as one can see in the plots of fig. 12.19, all the distributions are very smooth in the edge position neighbourhood. Therefore, the final acceptance distribution, shown in fig. 12.20 for the signal and in fig. 12.21 for all the backgrounds is very efficient in highlighting the signal without distorting the edge shape and we can observe in fig. 12.22 the distribution of the J_H momentum on which we will later apply our edge detection algorithm to measure the position of the kinematic edge.

12.3.5 Low-momentum edge selection

The spectrum of the J_L momentum after the common selection was already shown in fig. 12.11. That spectrum is clearly dominated by the $\gamma\gamma$ processes with effective rate, after the initial selection phase, peaking between 4 and 5 GeV/c, completely hiding the lower kinematic edge which, in the benchmark scenario we are analysing is situated at approximately 7 GeV/c. This particular feature makes that benchmark point particularly challenging to study and we can arguably say that it can be considered a worst-case scenario situation.

To tune the low-momentum edge selection we can start from the calculated position of the high-momentum edge at the end of the common selection of $E^+ = 98.66 \pm 0.09$ GeV/c. Using that number, from fig. 12.1 we can estimated the possible range of the low-momentum edge which can range between approximately 5 GeV/c and 90 GeV/c.

Using that estimation we can set the cut range for the *ECal energy variable*, already shown in fig. 12.12, to values between 12 GeV and 180 GeV. The second step of the selection is unchanged and we select only events where the missing mass of the reconstructed e^+e^- pair is larger than 300 GeV/c^2.

The next step of the algorithm is the selection of those events where the J_H and J_L particle have opposite charge and in this stage we also apply additional constraints to the scattering angles and momenta of those particles. In tab. 12.4 this step has been split in two parts, detailing the cuts on the two particles separately.

Compared to the analogous cut we performed in the high-momentum edge selection, the constraints on the J_H kinematic variables are stricter. As we already know that the

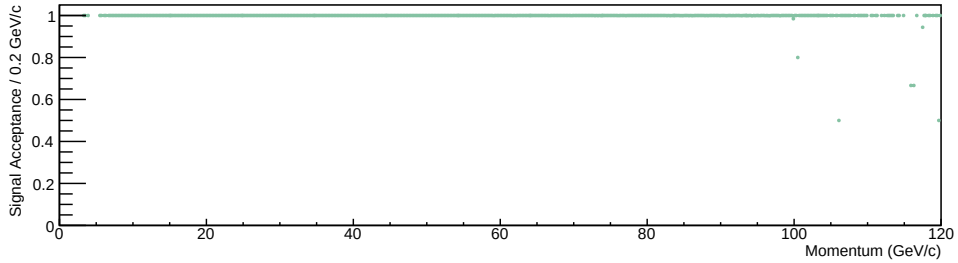

(a) ECal energy cut acceptance

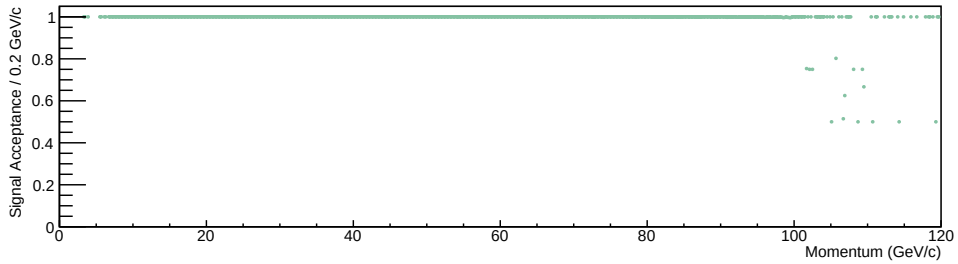

(b) Missing mass cut acceptance

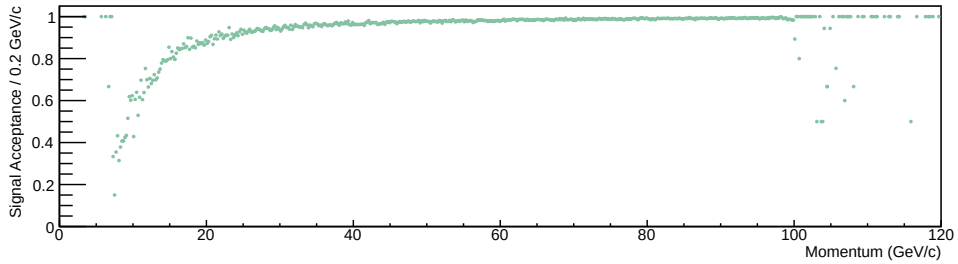

(c) J_H selection cut acceptance

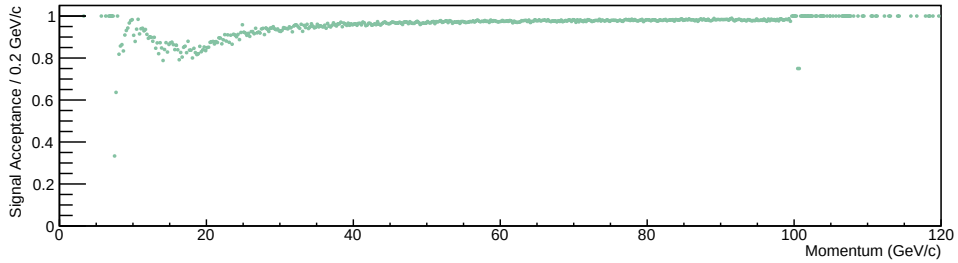

(d) Acollinearity cut acceptance

Figure 12.19: Acceptance of all the cuts of the high-momentum edge selection on the signal sample as a function of the J_H momentum. In all of them the acceptance is a very smooth function, especially in the proximity of the kinematic edge.

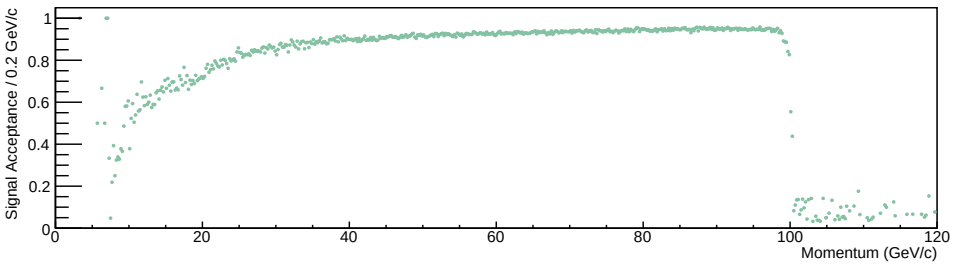

Figure 12.20: Acceptance of the complete high-momentum edge selection plotted as a function of the J_H momentum for the signal sample. The acceptance drop at a momentum of about 100 GeV/c is due to the *charged energy ratio cut* and its cause and the harmlessness of that feature is discussed further in the text.

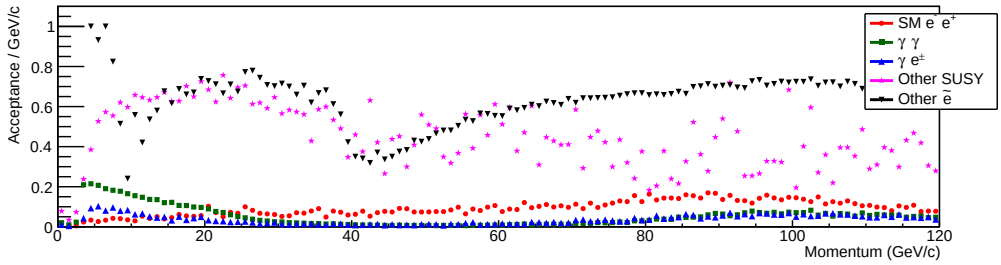

Figure 12.21: Acceptance of the complete high-momentum edge selection plotted as a function of the J_H momentum for all backgrounds. All distributions are superimposed All the distributions are very smooth in proximity of the E^+ edge which is situated at $\approx 99\,\mathrm{GeV/c}$. Note that the binning in this plot has been changed to $1\,\mathrm{GeV/c}$.

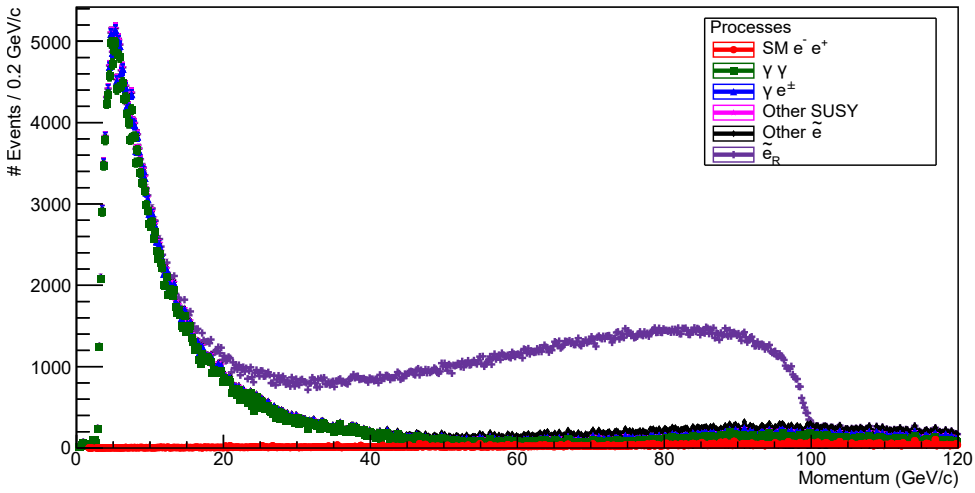

Figure 12.22: J_H momentum distribution at the end of the high-momentum edge selection. That distribution will be used as a template to calculate the position of the high-momentum edge and the error correlated to that measurement.

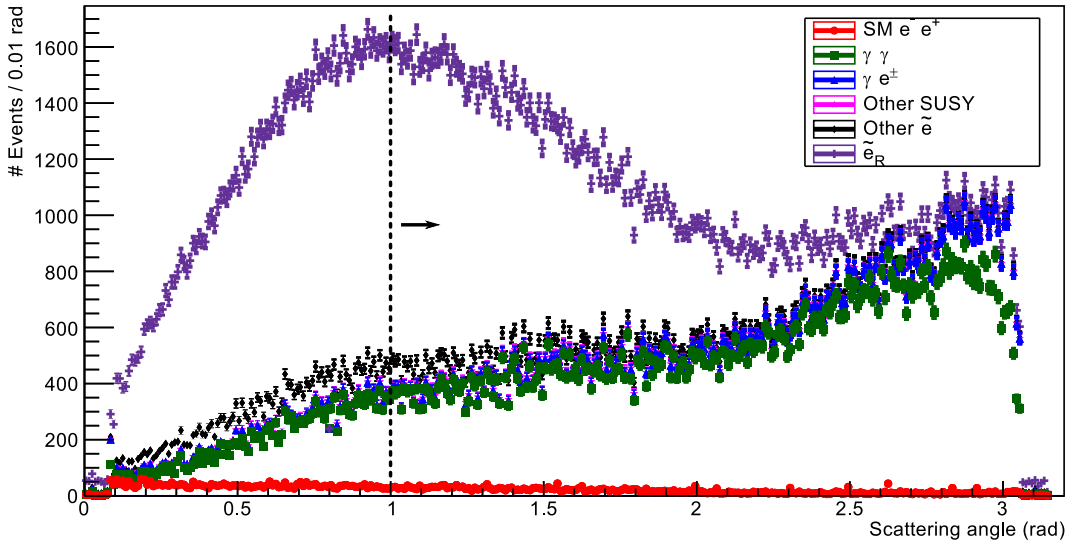

Figure 12.23: The distribution of the J_L^- scattering angle for all the process categories after the application of the J_H selection cut. The histograms are stacked on top of each other. The dashed black line represents the threshold of the cut applied to this variable.

high-momentum edge is at roughly at 100 GeV/c, we can also choose to select only events where the momentum of the J_H particle is lower than that value. Additionally we reduce the acceptance range of the scattering angle of that variable as shown in fig. 12.16. This cut has a limited impact on the signal sample but is able to reduce the backgrounds, and the $\gamma\gamma$ background in particular, by roughly 50% (see tab. C.4 and tab. C.3 for a detailed summary).

The second set of constraints is applied to the J_L particles and the range of the cut on the scattering angle of the negative ones is shown in fig. 12.23. Looking at that plot the usage of this cut seems counterproductive but we should consider the correlation between the scattered particles momenta and their scattering angle which we discussed in the previous section and was represented in fig. 12.14. As we are interested in selecting the event where the J_L particle is closer to the lower kinematic edge, removing those events where those particles are scattered at small angles in comparison to the beam with the same charge is an effective selection criteria.

This can be observed in fig. 12.24, where we compare the acceptance of the J_H and J_L cut, plotted against the momentum of the J_L particle. In the second one, in particular, we can observed that the selection acceptance, even though is on average lower, gets closer to 100% in proximity of the searched edge and then smoothly drops again for low momenta of the J_L particle. Once again we would like to highlight that the visible acceptance drop is not due to any specific choice of the cut parameters but by the mere existence of the kinematic edge. In fact, if the J_L particle has a momentum lower than the kinematic edge it is not a direct daughter of the $\tilde{e}_R$ but either the product of an uncorrelated background

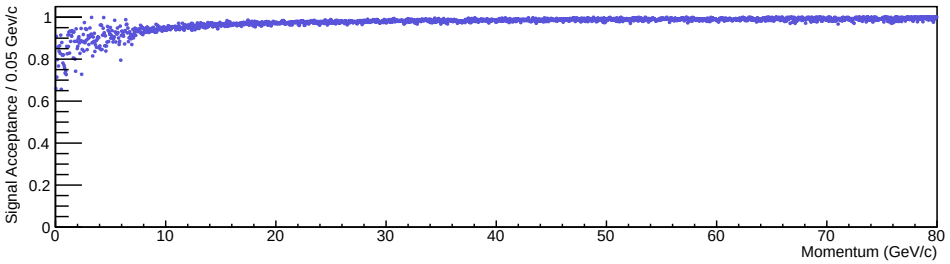

(a) J_H selection acceptance as a function of J_L momentum.

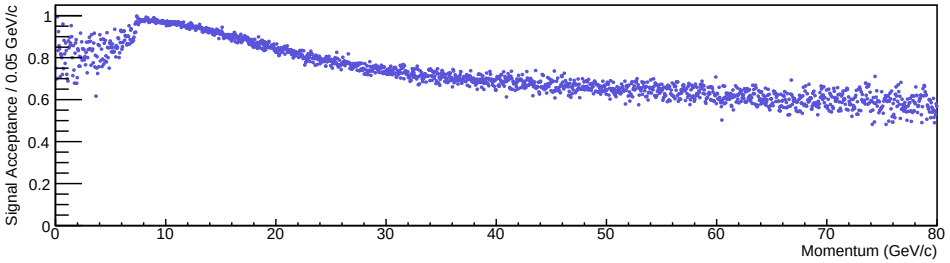

(b) J_L angular selection acceptance as a function of J_L momentum.

Figure 12.24: The signal acceptance of the J_H and J_L angular selections plotted as a function of the J_L momentum in the signal sample.

process, like the conversion of a bremsstrahlung or ISR photon, or it has lost a relevant amount of energy before reaching the tracker. In both cases the correlation between the scattering angle and momentum will be weakened or erased and a selection that relies on that correlation will naturally remove events with misidentified or incorrectly reconstructed J_L particles.

The next variable we are going to use in the selection is the acollinearity of the selected electron-positron pair, that is the angle between the directions of the two particles. The relevance of this cut was already introduced in the last section but its discriminating relevance is much smaller when trying to use it to select events with a small J_L momentum. This can be observed in fig. 12.25 where we plot the correlation between those two variables. Therefore this cut is only applied to remove the events where the two particles are almost back-to-back (fig. 12.26), which filters out much of the remaining SM e^-e^+ background category.

At this stage the selection is not powerful enough to sufficiently reduce the backgrounds, in particular those due to the $\gamma\gamma$ category. To complete the selection we will finally look at the kinematic in the transverse plane, that is the plane perpendicular to the beams direction. The main reason why the above-mentioned background survives most of the cuts we already applied, and in particular the angular and acollinearity cuts, is that the initial-state photons have an energy spectrum very different and much broader than that of the two beams as they are radiated from the beam particles. This implies that the two photons can have very different initial energy and that the centre-of-mass will be boosted along the beams direction. Hence, even if a process, like the $\gamma\gamma \to e^-e^+$ has a back-to-

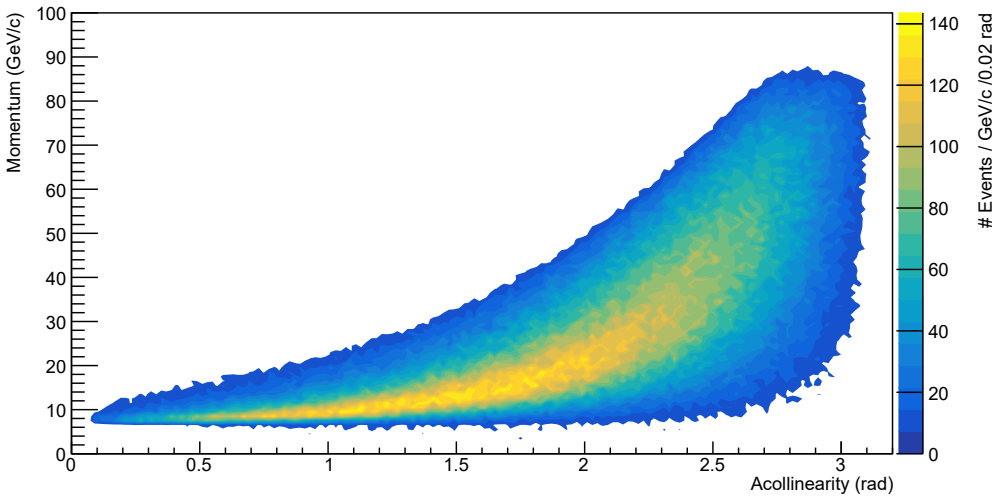

Figure 12.25: Correlation between the acollinearity and the J_L momentum in the signal sample before the application of the *acollinearity* cut in the low-momentum edge selection.

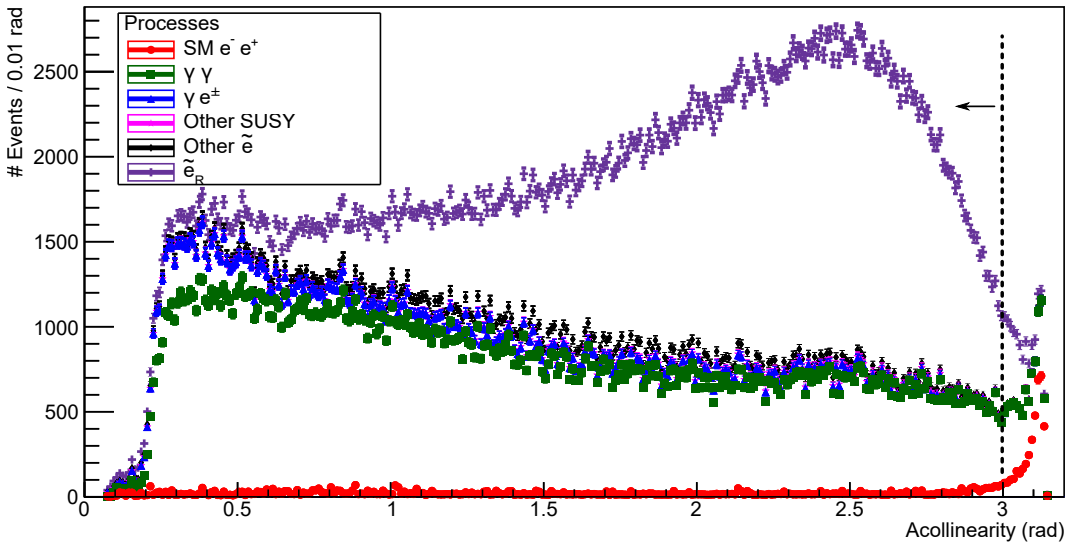

Figure 12.26: The distribution of the *Acollinearity* variable values for all the process categories after the application of the J_L selection cut. The histograms are stacked on top of each other. The dashed black line represents the threshold of the cut applied to this variable.

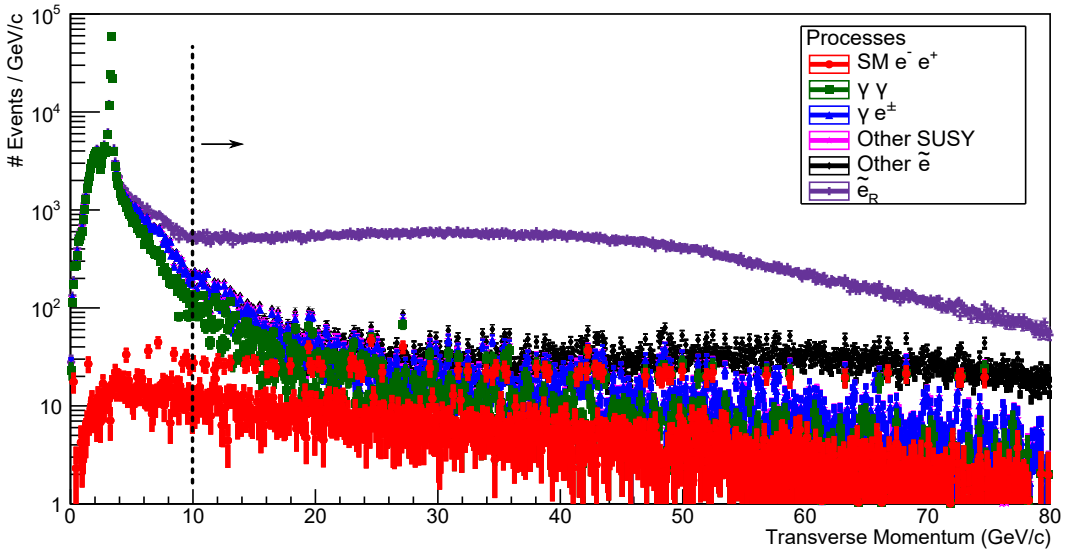

Figure 12.27: The distribution of the *Missing* P_T variable values for all the process categories after the application of the *acollinearity* cut in the low-momentum edge selection. The histograms are stacked on top of each other. The dashed black line represents the threshold of the cut applied to this variable. Note the logarithmic scale on the ordinate axis.

back kinematics in the centre-of-mass frame, when boosted in the laboratory frame the angle between the particles in the final-state pair can be very different than π. On the other hand we can still assume that the two initial-state photons have a small transverse momentum so that centre-of-mass frame will also have a small transverse momentum and, in first approximation, the kinematics of the process in the transverse plane would still be back-to-back.

To measure this imbalance we can use the missing transverse momentum in the identified electron-positron pair, that is the transverse component of the vectorial sum of the momenta of the two particles. Because the two beams are interacting with a small crossing angle of 14 mrad, we subtract the expected centre-of-mass momentum from that vector sum. As expected from the previous argument and visible in fig. 12.27, the value of this variable for the $\gamma\gamma$ process category is very low if compared to the signal sample. Therefore we can remove all the events with a missing transverse momentum lower than 10 GeV/c.

Finally we will define an additional variable, called *acoplanarity*, that is the transverse plane angle between the electron and the positron in the identified pair. The distribution of this variable after the application of last cut is shown in fig. 12.28 where we also show the range of the applied cut. Even though a relevant amount of the signal sample was cut, we can observe in fig. 12.29 that the applied cut preserves most of the samples with a low-momentum J_L, that is the set of particles forming the edge we are going to analyse. In fact we can observe in fig. 12.30c that the cut acceptance on the signal sample smoothly increases as the J_L momentum gets lower and reaches a maximum roughly at the edge

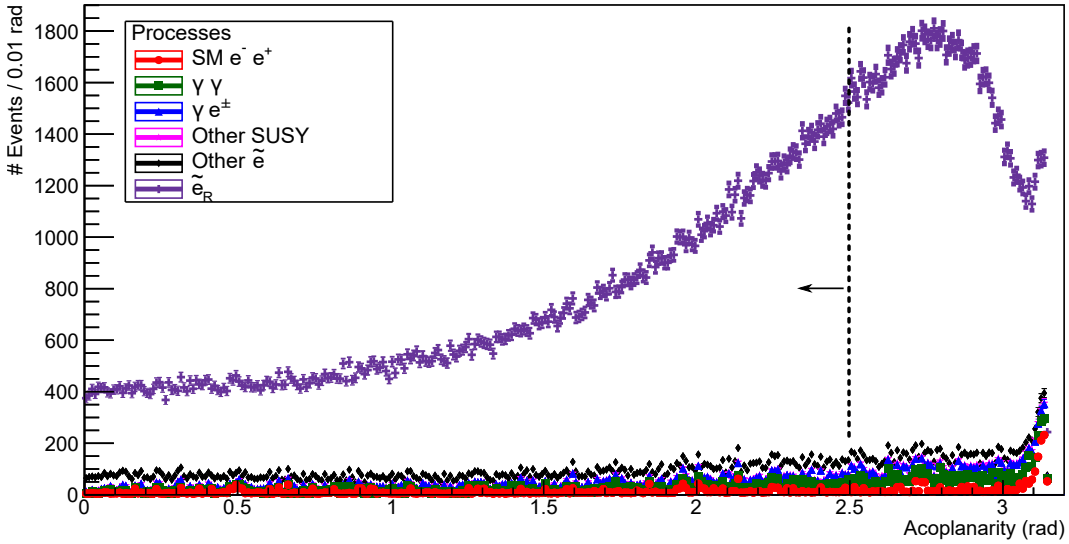

Figure 12.28: The distribution of the *Acoplanarity* variable values for all the process categories after the application of the *Missing* P_T cut. The histograms are stacked on top of each other. The dashed black line represents the threshold of the cut applied to this variable.

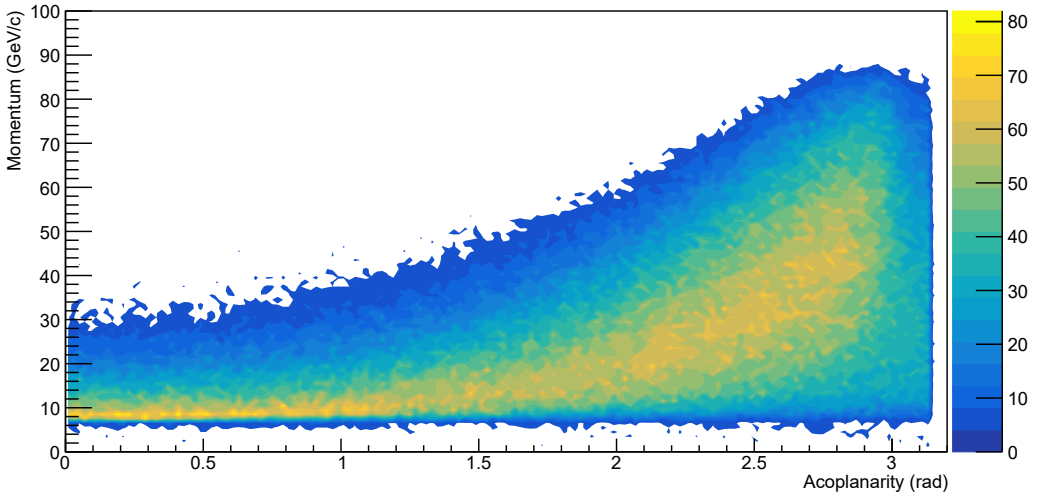

Figure 12.29: Correlation between the acoplanarity and the J_L momentum in the signal sample before the application of the *acoplanarity* cut in the low-momentum edge selection.

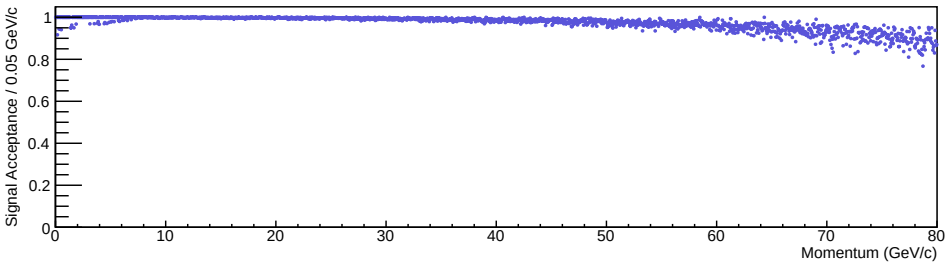

(a) Acollinearity cut acceptance

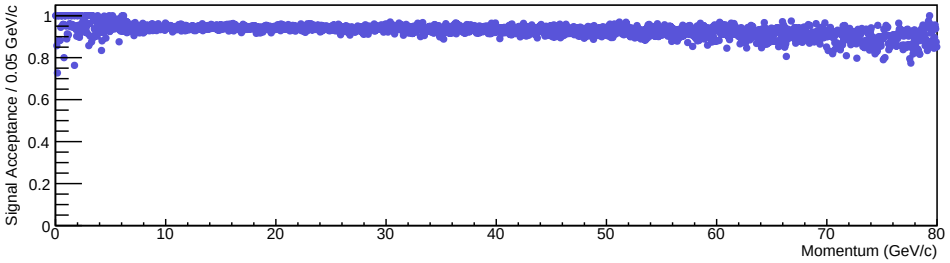

(b) Missing transverse momentum cut acceptance

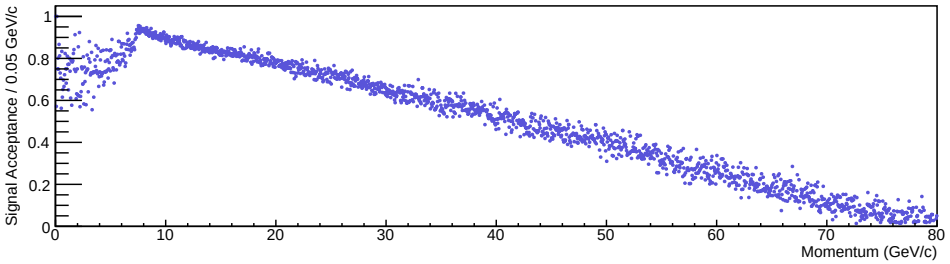

(c) Acoplanarity cut acceptance

Figure 12.30: Acceptance of the three final cuts of the low-momentum edge selection on the signal sample as a function of the J_L momentum.

position. Any particle in the signal sample with a momentum lower than the kinematic edge value cannot be a direct daughter of the decaying $\tilde{e}_R$ and, just as we discussed previously in this and in the previous section, they are more sensitive to cuts which relies on specific angular correlations.

After this last step we obtain the J_L momenta distribution represented in fig. 12.31 which will be used as a template for the determination of the low-momentum edge position which is now very clearly visible above a small and uniform background.

If we observe the signal acceptance of the entire selection as a function of the J_L momentum in fig. 12.32, the most noticeable feature is the smooth acceptance increase as the J_L momentum decreases towards the edge position and a sharp drop after that. As we discussed earlier in this section the presence of this acceptance drop is not due to any specific choice of the cut parameters but by the fact that, in those events in the signal where the J_L particle has a momentum lower than the kinematic edge of the $\tilde{e}_R$ decay,

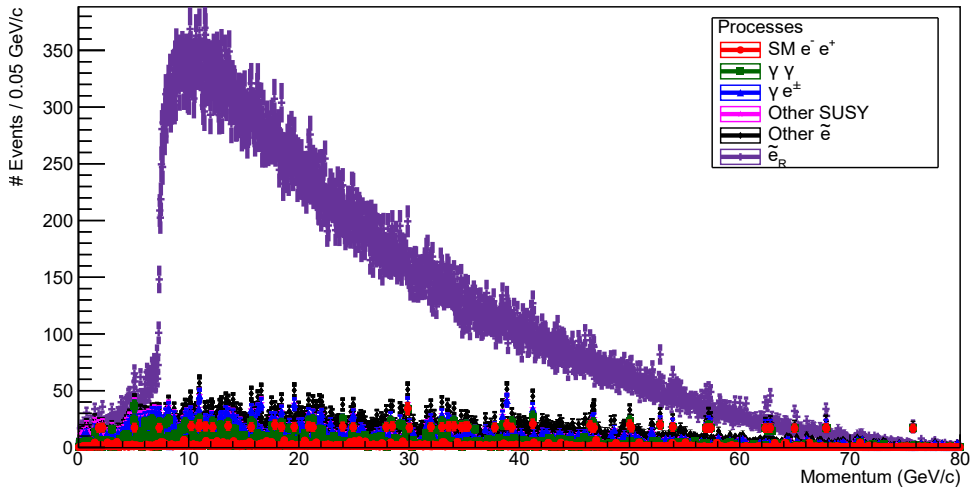

Figure 12.31: Distribution of the J_L momentum after the application of the low-momentum edge selection described in the text. This distribution will be used as a template to calculate the position of the low-momentum edge and the error correlated to that measurement

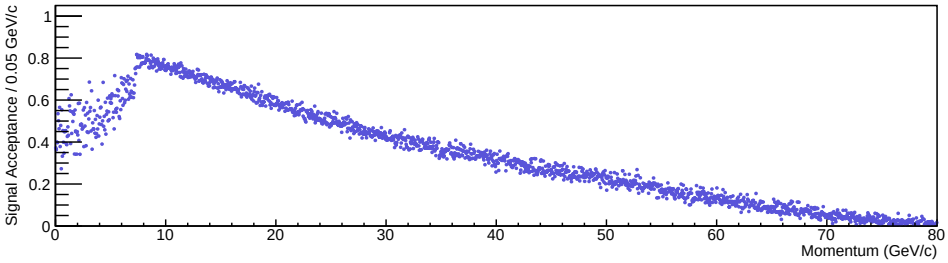

Figure 12.32: Signal acceptance of the complete low-momentum edge selection plotted as a function of the J_L momentum. The selection acceptance increases steadily up to the location of the low-momentum kinematic edge. It should be noticed that the acceptance drop after that point is not due to any specific fine tuning of the selection for our benchmark point but on the kinematic properties of those particles which were incorrectly identified as the J_L.

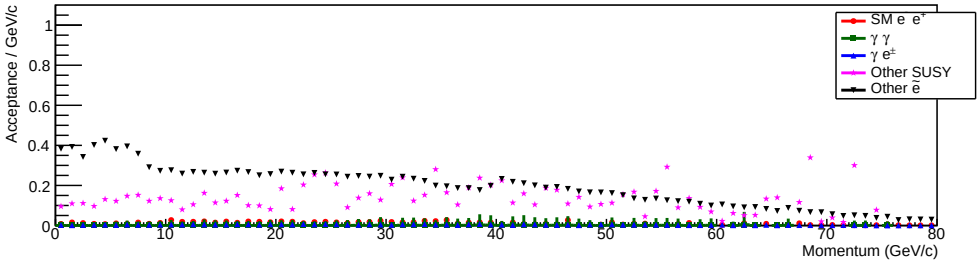

Figure 12.33: Background acceptance of the low-momentum edge selection as a function of the J_L momentum.

that particle is not the daughter of one of the s-electrons or where it has lost a relevant amount of energy before entering the tracker. As a cross-check we can also observe the acceptance plot for all the backgrounds as a function of the J_L momentum which is shown in fig. 12.33 and where a similar feature is only visible for the *Other* $\tilde{e}_R$ process category around 40 GeV/c where it is produced by a similar kinematic edge in the decay of the $\tilde{e}_L$.

12.4 Edge position measurements

As we mentioned before starting the discussion of the selections, to improve the quality of the edge position determination we need to increase the signal-to-noise ratio in its proximity and we need to make sure the underlying backgrounds are smooth in the edge neighbourhood. With the selection algorithm we developed and describe we finally obtain two datasets where the high- and low-momentum kinematic edges from from the decay of a $\tilde{e}_R\bar{\tilde{e}}_R$ pair can be clearly observed on top of a small and uniform background, respectively in fig. 12.22 and fig. 12.31.

Using those two histograms as a template we can now apply the procedure we described thoroughly in chapter 11, that is: for each filter we want to test we use the template to randomly generate a custom number of new histograms in which each bin is obtained by randomly sampling a Poisson distribution whose expectation value is the value of the bin content of the template; then we apply the edge finder algorithm independently to each of the generated histogram to measure the position of the kinematic edge; finally we calculate the mean and the standard deviation of all the measurements to obtain the expected values of the edge position and of its error in a realistic experiment.

We used this procedure to test all the filters described in the previous chapter and for each of them we varied the characteristic size parameter to choose the optimal one, that is the filter which minimizes the error on the measurement of the edge position. The binning of the template histograms, respectively 200 and 50 MeV per bin, were also chosen through our optimization procedure and match the optimal value we calculated for the benchmark measurement on the Monte Carlo sample we described in § 11.4.

As a result of the filter optimization we chose, for both edges, the FDOG filter described in § 11.3, with size of 6 and 5 bins, equivalent to a Gaussian smoothing with $\sigma = 1.2$ GeV/c and 250 MeV/c, respectively for the high- and the low-momentum edge.

Using those optimized parameters we measured the high-momentum edge position to be $\boldsymbol{E^+ = 98.748 \pm 0.043\,GeV/c}$ and the low-momentum edge position $\boldsymbol{E^- = 7.409 \pm 0.012\,GeV/c}$. Those values can be compared to those we obtained in our benchmark measurement described in § 11.4 that are, respectively, $\boldsymbol{E^+_{MC} = 98.974 \pm 0.024\,GeV/c}$ and $\boldsymbol{E^-_{MC} = 7.417 \pm 0.008\,GeV/c}$.

If we look at the low-momentum edge we can notice that the selection didn't introduce any additional relevant bias in the measurement as the obtained values are within the error bands of one another. This is an additional confirmation of the claim we made in the previous section when we commented the shape of the acceptance distribution in fig. 12.32 saying that the drop in the acceptance for momenta lower than the kinematic edge was

due to the ability of the selection algorithm to eliminate those events in the sample where one of the two candidate, J_L in this case, was misidentified or incorrectly reconstructed.

When comparing the results on the high-momentum edge, the difference in the measured central value is more significant. This was also expectable as the benchmark measurement was performed using the data from the Monte Carlo generator before any detector interaction. Because the radiative losses are more important at higher energies we could expect a relatively larger effect of those for the high-momentum edge which in fact is biased towards lower momenta, as we already noted in § 12.2.

Nonetheless, one of the advantages of the edge measurement method we developed is that the we can reabsorb the effect of the selection on the general measurement bias that we are going to calibrate away, as long as the background is smooth enough in the neighbourhood of the edge position.

12.4.1 Measurement calibration

To be able to correct the measurement we obtained with the procedure we described previously, we need to calculate the error of the bias itself. This is done with the same procedure we described in § 11.4. We will first separate the signal and background samples and, keeping the latter unchanged, we will add a random offset to the momentum of all the J_H and J_L objects. This procedure generates a new histogram where the signal distribution is shifted on top of the background by that random offset. We will then use this new distribution as a template for a new determination of the localization parameters. The whole procedure is then repeated as many times as necessary with different random offsets. The distribution of the calculated bias value is then fit with a linear function and the calibration value is defined as the value of that function for an offset of 0. Additionally we will define the bias error as the standard deviation of those measurements.

The results of the calibration procedure are plotted in fig. 12.34 where the measured bias is displayed as a function of the random offset chosen for that measurements. For the high-momentum edge the calculated bias error is 42 MeV while for the low-momentum edge it is 8 MeV. A first degree polynomial of the type $y = (A + Bx)$ is fit to the data and superimposed to the distribution showing the large scale constancy of the measurement bias.

Looking at the superimposed fit function we can appreciate the large-scale constancy of the bias but we can also observe, in both plots, the presence of wide oscillations of the measurements which are due to the background fluctuations. It can also be observed that the period of said oscillations is roughly constant and corresponds to the value of the CD3 parameter for the filter used in the measurement (see § 11.1.1). That parameter represents the average distance between the response peaks when the algorithm is applied to a noise-only distribution. Because our backgrounds are relatively constant within the edge measurement range, we should expect the oscillation period to be a function of the chosen filter as we actually see. The amplitude of the oscillations, on the other hand, is due to the absolute value of the background as the bin error is determined by the Poisson statistics. Contrary to the benchmark measurement we described in 11.4, in this case the

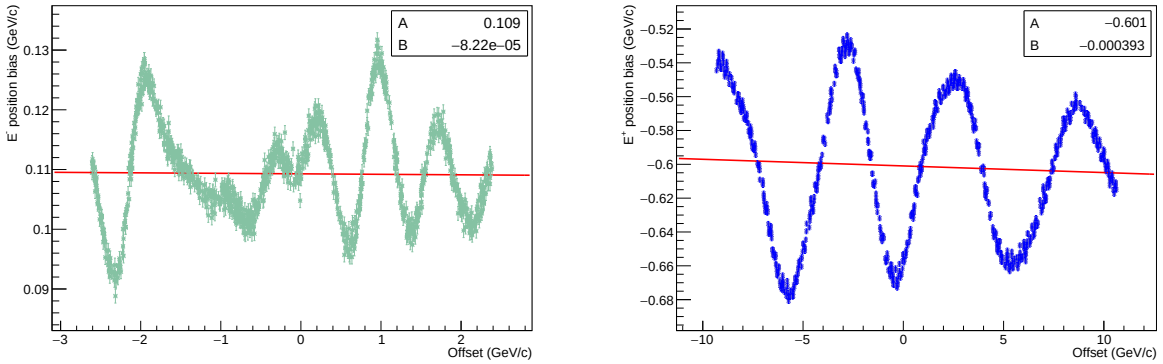

(a) Low-momentum edge calibration

(b) High-momentum edge calibration

Figure 12.34: Calibration graphs of the high-and low-momentum edge measurements. Each data point corresponds to a measurement of the localization parameters on a different distribution template obtaining by applying a random offset to the signal sample. Superimposed to the measurement set we displayed a first degree polynomial fit to the data showing a long range independence of the bias from the offset.

bias error is relevant but, being uncorrelated to the edge position measurement can be quadratically summed.

The value of the fitted function at 0 GeV/c offset is then used to correct the measured edges positions to estimate their true value. Therefore, summarizing the results of the edge analysis, tab. 12.5 shows the value of all the parameters we measured and we can write our final edge measurements results as:

$$\boldsymbol{E}^{+} = 99.349 \pm 0.043(\text{pos}) \oplus 0.042(\text{bias})\ \text{GeV/c} \qquad \boldsymbol{E}^{+}_{\mathbf{true}} = 99.362\ \text{GeV/c} \tag{12.2}$$

$$\boldsymbol{E}^{-} = 7.300 \pm 0.012(\text{pos}) \oplus 0.008(\text{bias})\ \text{GeV/c} \qquad \boldsymbol{E}^{-}_{\mathbf{true}} = 7.298\ \text{GeV/c} \tag{12.3}$$

with the *true* positions calculated using eq. 10.12 and eq. 10.11, assuming a nominal centre-of-mass energy of 500 GeV, $M_{\tilde{e}_R} = 126.235\ \text{GeV/c}^2$ and $M_{\tilde{\chi}_1^0} = 95.586\ \text{GeV/c}^2$, used as input parameters of the Monte Carlo generator, corresponding to the STC4 benchmark scenario parameters listed in tab. 10.1.

12.5 $\tilde{e}_R$ and $\tilde{\chi}_1^0$ mass determination

Having determined the positions of the kinematic edges of the momenta distribution of the products of the $\tilde{e}_R$ decay and the errors we must associate to those measurements, we can finally calculate the masses of the $\tilde{e}_R$ and $\tilde{\chi}_1^0$. The most direct method is to apply the formulae 10.16 and 10.17 using the edge measurements obtained in the previous section and analytically derive the mass errors with the equations 11.13 and 11.14 using the quadratically summed error we calculated.

As the two masses are calculated from the same input parameters, their values will be statistically correlated. The simplest way to calculate this correlation and a valid

	Parameter	Value (GeV/c)
High-momentum edge	Position	**99.349**
	Position error	**0.043**
	Bias	**-0.601**
	Bias error	**0.042**
Low-momentum edge	Position	**7.300**
	Position error	**0.012**
	Bias	**0.109**
	Bias error	**0.008**

Table 12.5: Summary of the measurement of the kinematic edges positions. For each of the two edges we list the measured position and its accuracy, the difference between measured and the *true* value and the error in the determination of that bias.

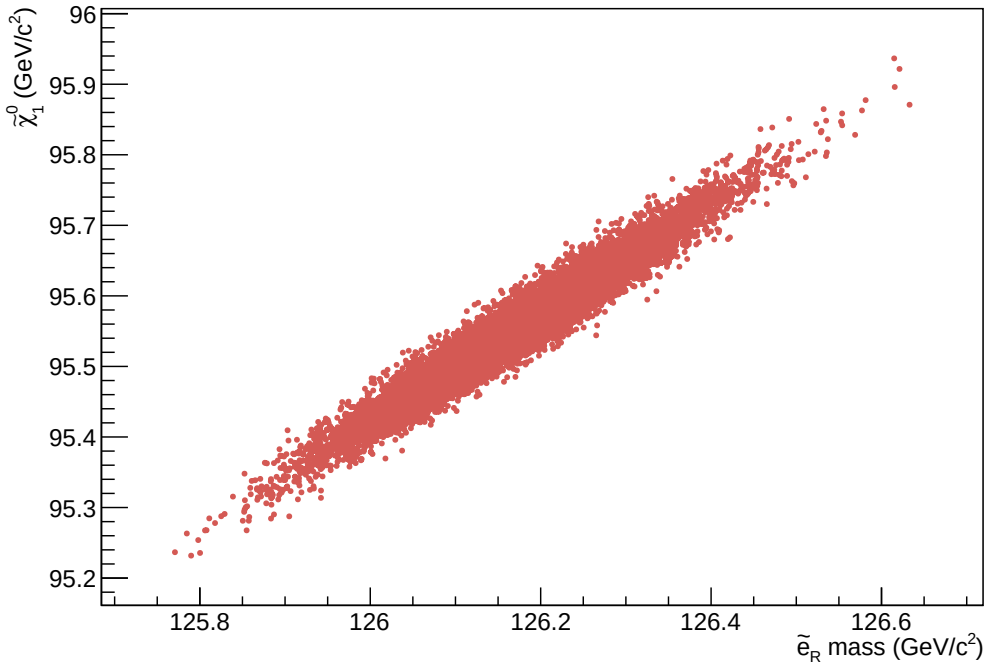

Figure 12.35: Correlation of the $\tilde{e}_R$ and $\tilde{\chi}_1^0$ masses calculated using the measured positions of the kinematic edges of the momenta distribution of the $\tilde{e}_R$ decay products. Each data point is obtained using the procedure described in § 12.5.

cross-check to the analytic calculation is the execution of a Monte Carlo evaluation of the measurements distribution.

To perform that, we used the two distributions in fig. 12.22 and 12.31 as a template to generate a new pair of histograms the content of whose bins is obtained by sampling a Poisson distribution with the same mean value as that of the bin in the template. We then apply the edge finding algorithm to those histograms and we subtract from the measurement we obtain a random offset extracted from a normal distribution, whose mean value is the calculated bias and whose sigma is the bias error, as quoted in tab. 12.5. Then we correct each pair of measurements with the calibration values, that is 0.601 GeV/c and -0.109 GeV/c, respectively for the E^+ and E^- positions and from those corrected measurements we calculate the two masses. This procedure is repeated an arbitrary number of times to generate a large number of data points. From this dataset we can calculate the mean and standard deviation of both masses and their covariance and the correlation coefficient (ρ).

Using that method, whose results are graphically presented in fig. 12.35, we estimate that at the ILC, after collecting 500 fb^{-1} of data with an 80% electron polarization and 30% positron polarization, we will be able to measure the mass of the $\tilde{e}_R$ and of the $\tilde{\chi}_1^0$ with an accuracy of at least:

$$\boldsymbol{M_{\tilde{e}_R}} = 126.20 \pm 0.11\,\mathrm{GeV/c^2} \qquad \boldsymbol{M^{true}_{\tilde{e}_R}} = 126.235\,\mathrm{GeV/c^2} \tag{12.4}$$

$$\boldsymbol{M_{\tilde{\chi}_1^0}} = 95.56 \pm 0.09\,\mathrm{GeV/c^2} \qquad \boldsymbol{M^{true}_{\tilde{\chi}_1^0}} = 95.586\,\mathrm{GeV/c^2} \tag{12.5}$$

$$\mathrm{cov}(M_{\tilde{e}_R}, M_{\tilde{\chi}_1^0}) = 0.0099\,\mathrm{GeV^2/c^4} \qquad \rho = 0.97 \tag{12.6}$$

The fact that the initial generator values for the two s-particle masses comfortably sit within the error range of the measurements is a good indication of the reliability of the measurement algorithm and of the procedure we used to estimate the measurement errors. The same mass error values are also obtained with the analytical calculation.

By comparing the results we obtaining on the signal only distributions in § 11.4 with the final results we finally obtained here we can see that there is still a very limited margin for improvement. As can be deduced by examining eq. 11.13, the error which influences the most the final result is that on the low-momentum edge $\delta(E^-)$, which is also the most difficult to further reduce. As the statistical component of the error is 50% higher than the systematic bias error which is the same as the benchmark best-value obtained in the previous chapter, the results could be improved by increasing the selection efficiency with a multivariate approach.

Compared to previous results, though, the mass resolution achievable with the presented method is already a factor of two better than the best previously published, therefore a more effective approach could be to attempt to use the same method to analyse other processes. Moreover, those results can also be used to decorrelate the measurements of the two masses as obtained here.

Results summary and an outlook for future optimizations

The second part of this thesis is focussed on the description of a new algorithm developed to detect edge-like features in mono-dimensional binned distributions in presence of noise and on its use to precisely determine the position of the kinematic end-points from the decay of s-electrons produced in the $e^-e^+ \to \tilde{e}_R\bar{\tilde{e}}_R$ process at the ILC, using 80% right-polarized electrons and 30% left-polarized positrons and assuming an integrated luminosity of $500\,\mathrm{fb}^{-1}$.

Even though the algorithm presented here was inspired by similar ones commonly used in image processing, the precise determination of the accuracy of the calculated feature position and the calibration of that measurement is not usually taken in consideration in the context of image processing. When applied to a typical physics analysis, the final systematic error is probably the most important result. Therefore a large part of chapter 11 was devoted on the development of a procedure to validate and calibrate the algorithm.

When applied to the ideal distribution of the decay products of the s-electrons from the $\boldsymbol{e^-e^+ \to \tilde{e}_R\bar{\tilde{e}}_R}$, without background and detector effects we were able to determine the position of the high- and low-momentum end-points with an accuracy of 8.3 MeV/c and 24 MeV/c respectively, with a negligible bias (§ 11.4). After the reconstruction of the simulated data, considering all the detector effects and those due to the electron identification algorithm we developed for this analysis but ignoring any background process, we were still able to measure the position of those kinematic edges with an accuracy of 10.6 MeV/c and 32 MeV/c respectively (see tab. 12.2). Finally, when we introduced all the background processes, and after a suitable selection we were able to determine those positions with an accuracy of $(12 \oplus 8)$ MeV/c and $(43 \oplus 42)$ MeV/c respectively, where the first value is the intrinsic localization error and the second is the calibration error (see tab. 12.5).

Using those values we can calculate the masses of the unknown Supersymmetric particles, that are the $\tilde{e}_R$ and the $\tilde{\chi}_1^0$, with an accuracy of $110\,\mathrm{MeV/c^2}$ and $90\,\mathrm{MeV/c^2}$ respectively (see § 12.5). Those accuracies are about a factor of 2 better than the previously published results obtained using the same dataset which measured those same masses with an accuracy of $210\,\mathrm{MeV/c^2}$ and $160\,\mathrm{MeV/c^2}$ respectively [123].

An important feature to note is that the localization error depends only on the algorithm parameters and the data on which the algorithm is applied. On the other hand, to calibrate the results and associate the measurement to a physical parameter, it is necessary to introduce some model assumption. While this is a common situation in any type of analysis, the fact that the calibration procedure is based on a Monte Carlo algorithm, makes it usable even in those cases when the original distribution is not known analytically but can be reliably simulated. This is particularly important in the case of the analysed process, as the detector effects on the final state electrons, which are typically among those that cannot be analytically described, are very relevant and change the distribution to sample.

Even though the current results are already better than the currently published measurements, it may still be possible to further improve the analysis. For example, when comparing the previous results with those presented here we should also notice that not only the edge detection algorithms but also the selection algorithm differs between the two analysis. Therefore it is not possible to precisely estimate how much of the improvement is due to the different selection and how much to the measurement itself.

Moreover this analysis was performed on the data reconstructed through the fast-simulation software SGV and using a specific electron identification algorithm, developed specifically for this thesis. Therefore it could be useful to apply the same selection and the same feature detection algorithm to a dataset obtained through the full reconstruction software of the ILD collaboration. The selection itself can be probably further improved applying more advanced multivariate techniques rather than a sequential cut approach.

Another possible extension of the work that was presented here is the application of the same algorithm to additional physics channels. In the context of the analysis of the Supersymmetry benchmarks of the ILD detector, they could be, for example, the $\tilde{\mu}$ pair production or the $e^-e^+ \to \tilde{e}_{R|L}\bar{\tilde{e}}_{L|R}$. In the first case, the production cross-section would be much smaller but the detector effects almost negligible as the muons won't radiate during their passage through the vertex detector and the TPC. Therefore it would be possible to evaluate the relevance of the detector effects on the algorithm performances. Moreover an analysis on the same channel was already performed on a similar benchmark model [122] and a new comparison between the new algorithm and a more traditional measurement could be obtained. The second case listed previously could be very interesting as it will be necessary to identify a third feature, i.e. one of the kinematic end-points from the decay of the left-handed s-electron.

Finally, different edge detection algorithms based on the same general approach of derivative regularization can be developed and tested and calibrated with the same procedure and algorithms developed for this thesis. One possibility, for example, is to use a Fourier or wavelet base algorithm. Additionally any algorithm should be extensible to multiple dimensions, in particular to bi-dimensional distributions.

This work hopefully was able to demonstrate, once again, why a lepton collider is a necessary complement to the current generation of hadron colliders. Only at a lepton collider like the ILC, with experiment built to deliver with cutting edge technologies, like for example the GEM based TPC described in the first part, it will be possible to measure the parameters of unknown particles, like the s-electrons described here, with a per mill

accuracy or, if nothing is discovered, close most of the theoretical loopholes which hadron collider measurements will leave.

Appendices

Appendix A

Technical drawings

REVISIONS				
SYM.	ZONE	DESCRIPTION	DATE	APP.

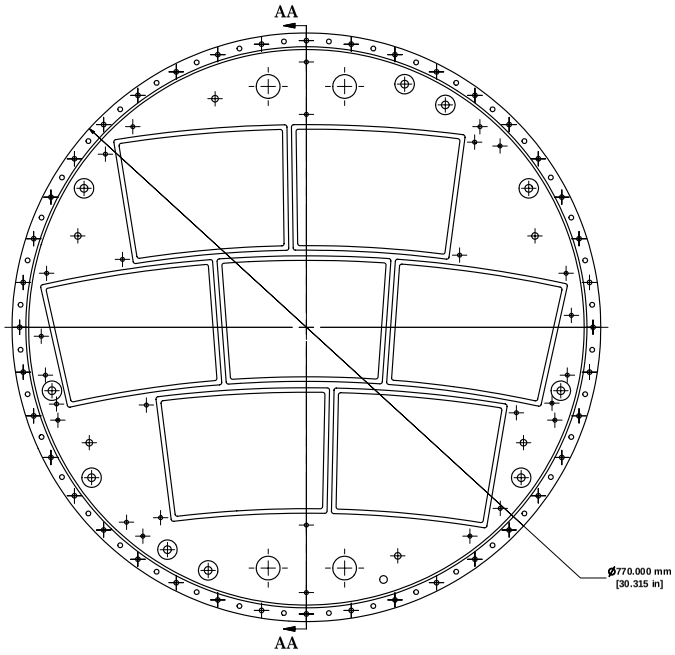

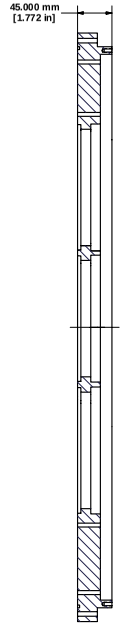

SECTION AA-AA
SCALE 1 / 3

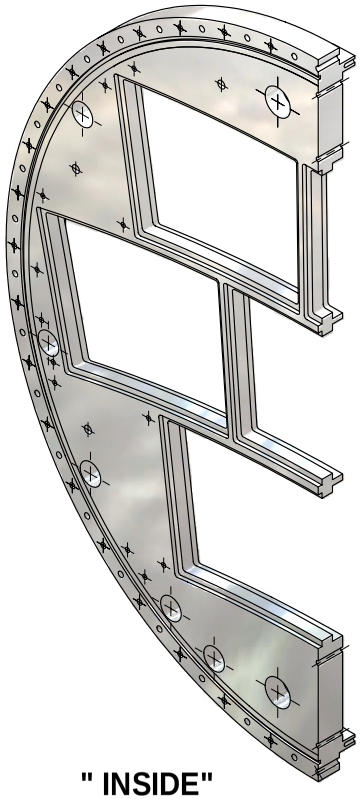

"OUTSIDE"

" INSIDE"

Matl: Alum. 6061 T651 "INSIDE"

Part requires multi-step process.

1) Machine all surfaces and holes (unless noted) leaving 0.030inch extra material.
(At least 0.020inch of material is to be removed from all surfaces.)
2) Deliver part to Cornell for stress relief process (Liquid Nitrogen cold shock).
3) Machine all surfaces and holes (unless noted) leaving 0.010inch extra material.
(At least 0.010inch of material is to be removed from all surfaces.)
4) Deliver part to Cornell for stress relief process (Liquid Nitrogen cold shock).
5) Machine all surfaces and holes to final specifications.

Technical questions,including clarifications and proposals for exceptions,
are to be directed to
Dan Peterson
Senior Physicist, Laboratory for Elementary-Particle Physics, Cornell University
607-255-8784
dpp@lepp.cornell.edu

FOR MACHINING LUBRICANT USE ONLY
ALKALINE DETERGENT LUBRICANT CIMSTAR 40
OR EQUIVALENT APPROVED BY CORNELL LEPP

TECHNICAL RESOURCE APPROVALS REQUIRED BEFORE FABRICATION	OK	DATE	N/A
DRAFTING (O'Connel):			
MACHINE SHOP (Kaminski):			
CHEMISTRY (Conklin):			
ELECTRONICS SHOP (Bartey):			
FURNACE BRAZING (Sherwood):			
BEAM WELDING (Sears):			
WELDING OTHER (Gallagher):			
UTILITIES INTEGRATION (Gallagher):			
STOCKROOMS (Lockwood):			

ITEM	DWG. NO.	DESCRIPTION	QUANTITY G1	G2	G3	REMARKS	REV.

SIZE D | PRINT DISTR. | REV.

PLOT DATE: 6/10/2008
CAD FILE NAME: 6080-102 Endplate.idw

6080-102

UNLESS OTHERWISE SPECIFIED:
DIMENSIONS ARE IN INCHES
TOLERANCES ON:
.00 ± .030
.000 ± .005
FRACTIONS ± 1/64
ANGLES ± 0.5°
ALL SURFACES √

CHECKED BY: Peterson
APPROVED BY: Peterson

CORNELL UNIVERSITY LEPP LABORATORY FOR ELEMENTARY-PARTICLE PHYSICS

CORNELL UNIVERSITY
Floyd R. Newman Laboratory
Ithaca, NY 14853

LCTPC Large Prototype Endplate

DRAWN BY	DRAWN FOR	DATE	SCALE			REV.
MDS	Peterson	5/18/2007	Noted	D	6080-102 SH. NO. 1 OF 16	

REVISIONS				
SYM.	ZONE	DESCRIPTION	DATE	APP.

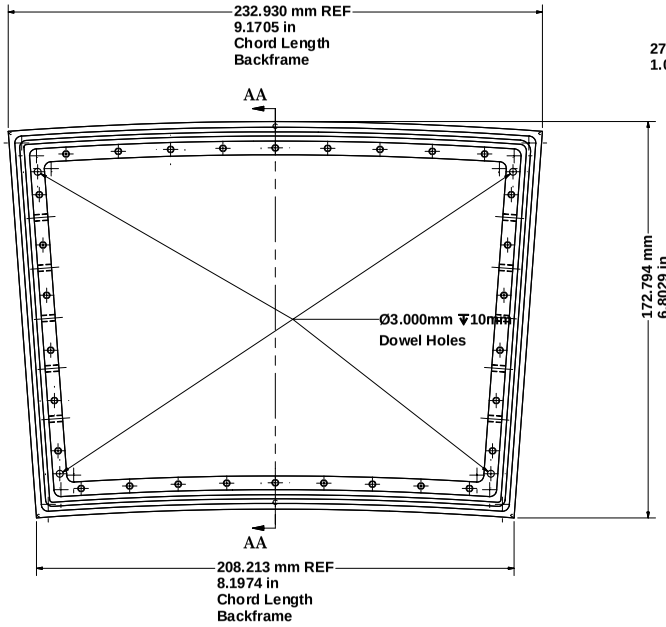

SCALE 1 : 1

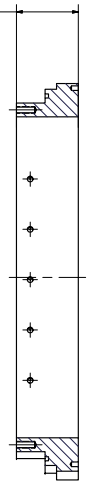

SECTION AA-AA
SCALE 1 : 1

Table		
TYPE	NO.# REQ'd	DIM.
3GEMG	?	27.000 mm
Micromegas	?	41.800 mm
Pixel GEM	?	40.500 mm
3GEM No Gate	?	37.000 mm

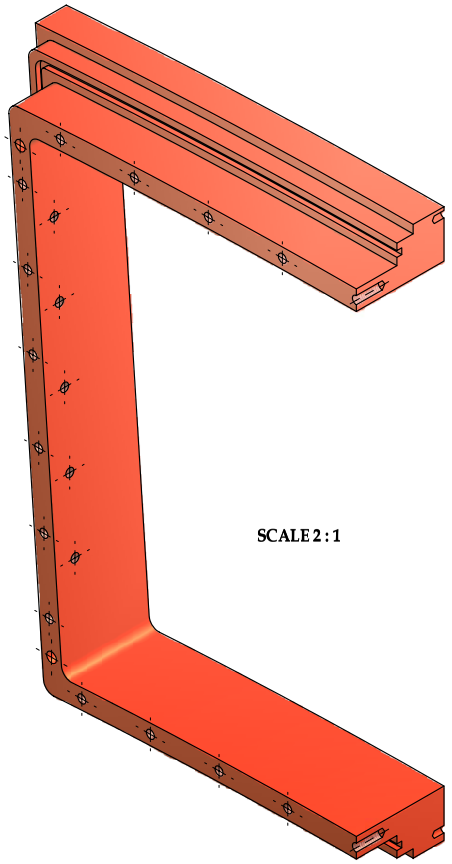

SCALE 2 : 1

Matl: Alum. 6061 T651
Part requires multi-step process.
1) Machine all surfaces and holes (unless noted) leaving 0.030inch extra material.
(At least 0.020inch of material is to be removed from all surfaces.)
2) Deliver part to Cornell for stress relief process (Liquid Nitrogen cold shock).
3) Machine all surfaces and holes (unless noted) leaving 0.010inch extra material.
(At least 0.010inch of material is to be removed from all surfaces.)
4) Deliver part to Cornell for stress relief process (Liquid Nitrogen cold shock).
5) Machine all surfaces and holes to final specifications.

Technical questions,including clarifications and proposals for exceptions,
are to be directed to
Dan Peterson
Senior Physicist, Laboratory for Elementary-Particle Physics, Cornell University
607-255-8784
dpp@lepp.cornell.edu

FOR MACHINING LUBRICANT USE ONLY
ALKALINE DETERGENT LUBRICANT CIMSTAR 40
OR EQUIVALENT APPROVED BY CORNELL LEPP

TECHNICAL RESOURCE APPROVALS REQUIRED BEFORE FABRICATION	OK	DATE	N/A
DRAFTING (O'Connel):			
MACHINE SHOP (Kaminski):			
CHEMISTRY (Conklin):			
ELECTRONICS SHOP (Bartey):			
FURNACE BRAZING (Sherwood):			
BEAM WELDING (Sears):			
WELDING OTHER (Gallagher):			
UTILITIES INTEGRATION (Gallagher):			
STOCKROOMS (Lockwood):			

D | PRINT DISTR. | CR-1 | SHEET 1 of 1 | 6080-104 | REV

ITEM	DWG. NO.	DESCRIPTION	QUANTITY G1	G2	G3	REMARKS	REV.

PLOT DATE: 4/18/2008
CAD FILE NAME: 6080-104 3GEMG backframe.idw

UNLESS OTHERWISE SPECIFIED:
DIMENSIONS ARE IN INCHES
TOLERANCES ON:
.00 ± .030
.000 ± .005
FRACTIONS ± 1/64
ANGLES ± 0.5°
ALL SURFACES √

CORNELL UNIVERSITY LEPP LABORATORY FOR ELEMENTARY-PARTICLE PHYSICS
CORNELL UNIVERSITY
Floyd R. Newman Laboratory
Ithaca, NY 14853

LCTPC Large Prototype Backframe

CHECKED BY: Peterson	DRAWN BY	DRAWN FOR	DATE	SCALE		
APPROVED BY: Peterson	MDS	Peterson	10/19/2007	noted	D	6080-104 SH. NO. 1 OF 12 REV.

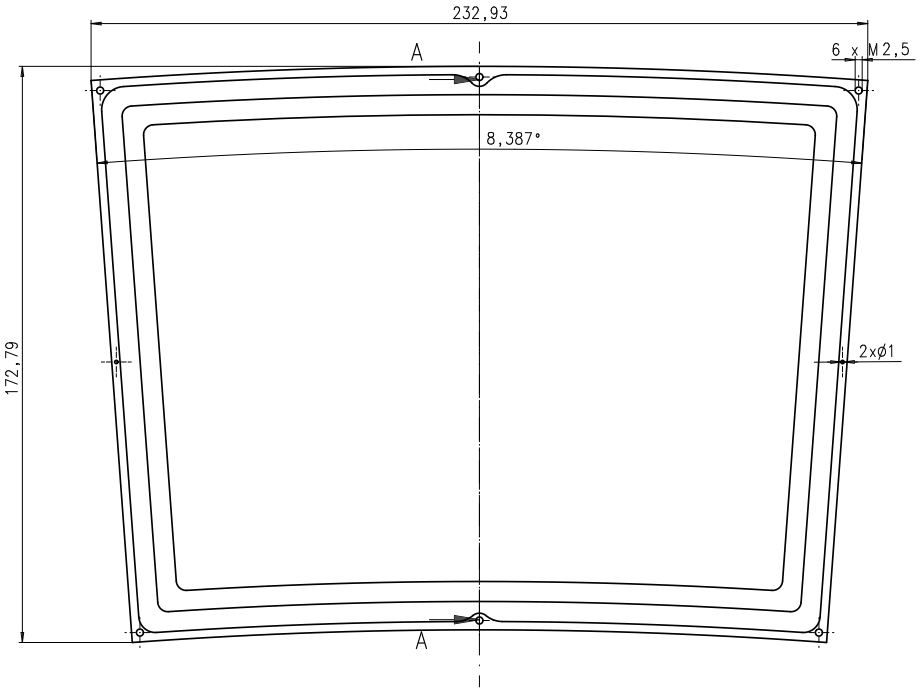

Section A-A

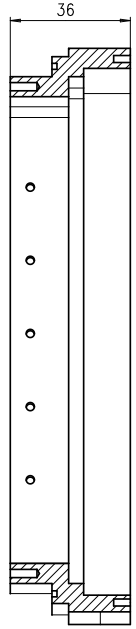

Stückzahl: 2
Material: AlMg4,5Mn

Toleranzgrundsatz: ISO 8015 Oberflächenkennzeichen nach DIN EN ISO 1302, 4287 bzw. 4288			Allg.-Toleranzen nach DIN ISO 2768 Toleranzkl.: mK		AlMg4,5Mn Halbzeug						Gewicht
Eigentum von DESY. Alle Rechte vorbehalten. Vor der Nutzung dieser Unterlagen oder der darin enthaltenen Informationen ist die Zustimmung des DESY-Technologietransfers erforderlich.					Schutzvermerk DIN ISO 16016 (05-2002) beachten Status:			1:1 on DIN A2 Maßstab:		Ort:	Auftrag:
								Material:			
					Datum	Name		backframe_V5_2			
					Gez. 03.02.2011	Volkenborn					
					Gepr.						
					Gen.						
					FLC						
					Teile-Nr.:						Blatt von Blättern Rev.:
Zust.	Änderung		Datum	Name	EDMS-Nr.:			Ers.f.		Ers.d.	Plot

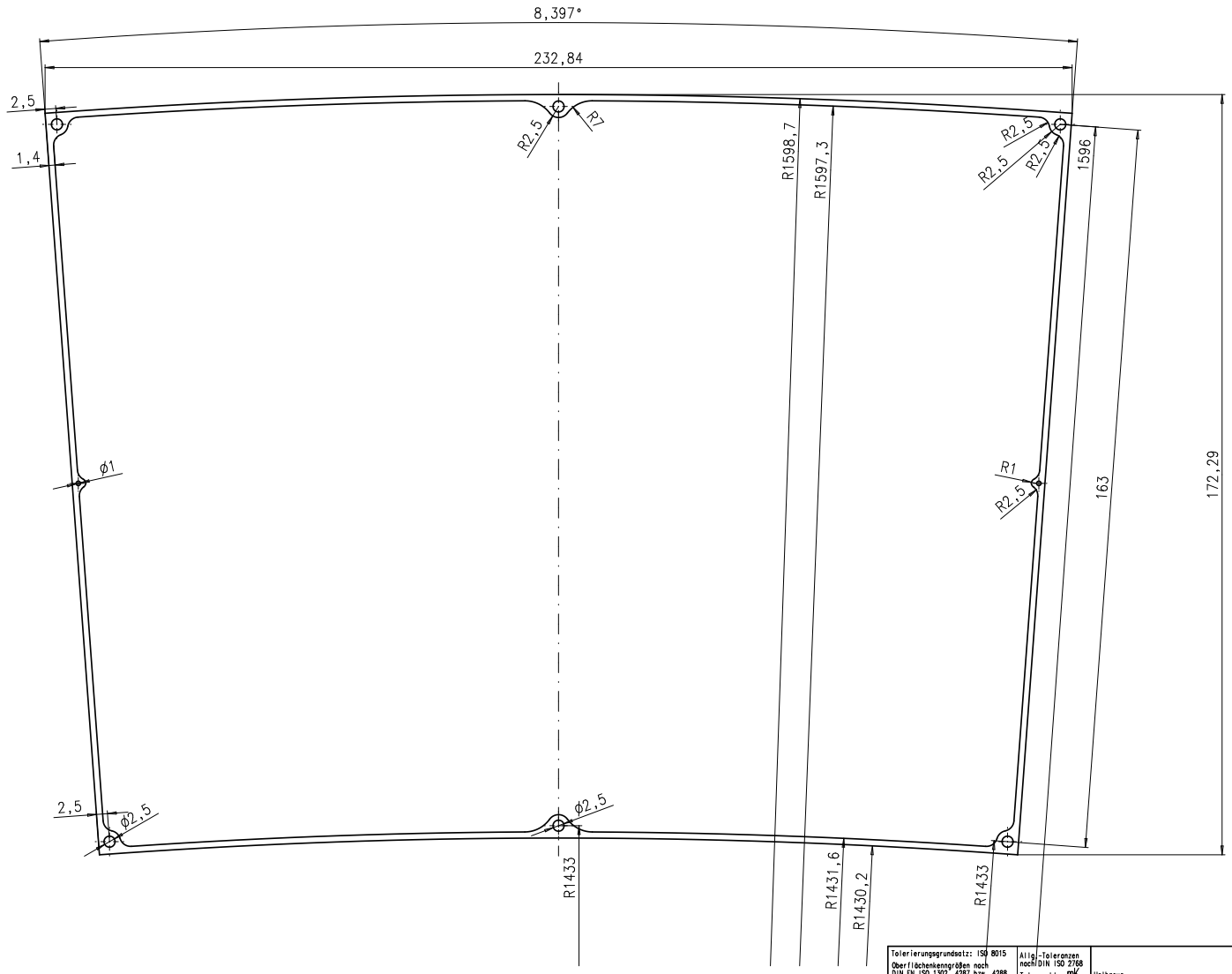

Tolerierungsgrundsatz: ISO 8015
Oberflächenkenngrößen nach
DIN EN ISO 1302, 4287 bzw. 4288

Allg.-Toleranzen
nach DIN ISO 2768
Toleranzkl.: mK

Halbzeug

Gewicht

Eigentum von DESY. Alle Rechte vorbehalten.
Vor der Nutzung dieser Unterlagen oder der darin
enthaltenen Informationen ist die Zustimmung
des DESY-Technologietransfers erforderlich.

Schutzvermerk
DIN ISO 16016
(05-2002)
beachten

Maßstab: 3:2 on DIN A2

Ort:

Auftrag: Auftrag

Status: Working

Material: AnCeram

	Datum	Name
Gez.	25.01.2011	Volkenborn_Robert
Gepr.		
Gen.		

GEMframe_model3.2

DESY FLC

Teile-Nr.: D00000001403632

EDMS-Nr.: D00000000939315

Zust.	Änderung	Datum	Name

Ers.f.

Ers.d.

Rev.: A

Blatt 1
von 1
Blättern

Plot

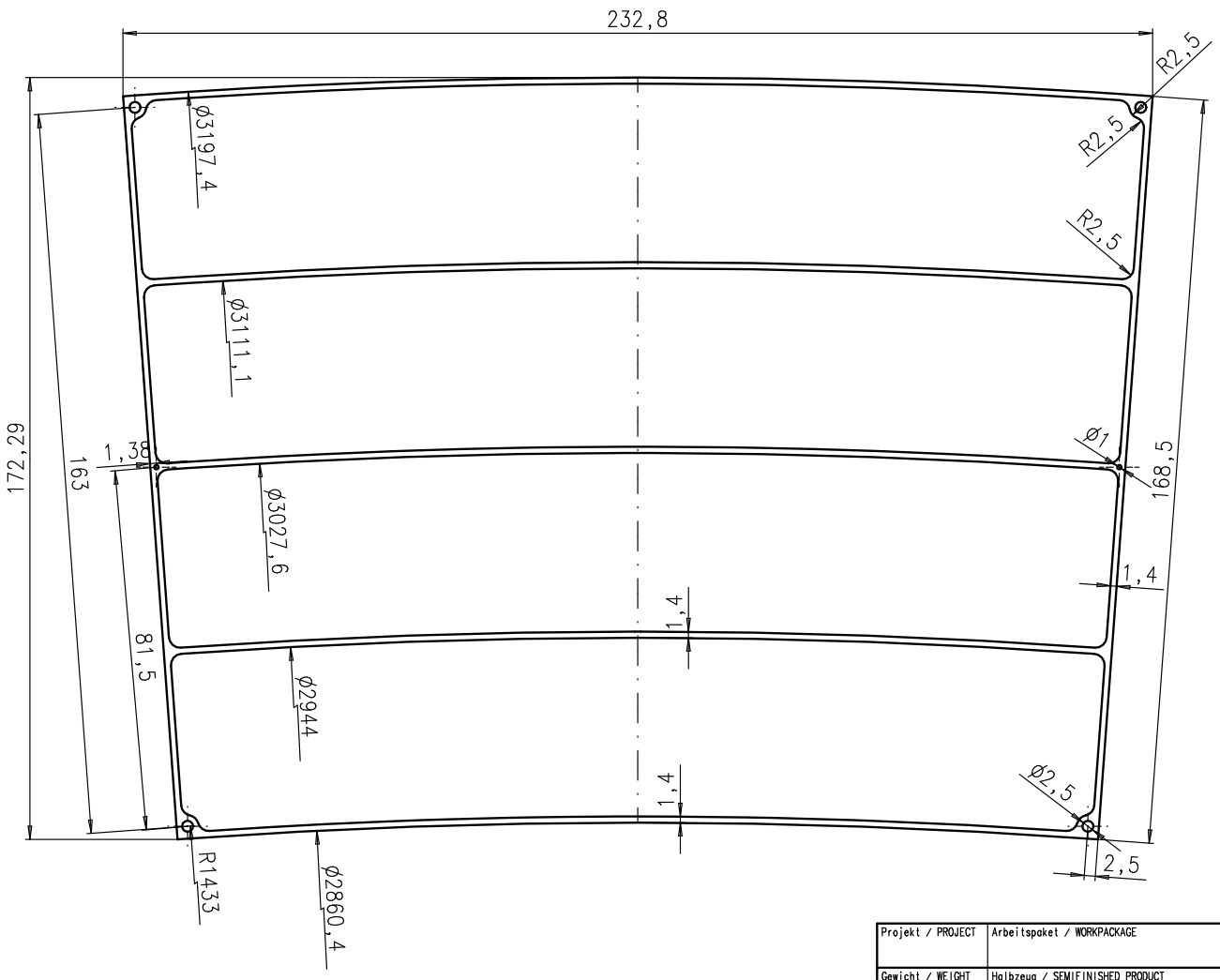

Projekt / PROJECT	Arbeitspaket / WORKPACKAGE		Gruppe / GROUP FLC	Ers.für / REPLACES	Ers.durch / REPLACED BY
Gewicht / WEIGHT	Halbzeug / SEMIFINISHED PRODUCT			Werkstoff / MATERIAL	Format/SIZE
Allg. Toleranzen / GENERAL TOLERANCES ISO 2768 ISO 13920			Maßstab / SCALE 1:1	Titel / TITLE GEMframepattern Version 3h	
Tolerierungsgrundsatz / FUNDAMENTAL TOLERANCING PRINCIPLE ISO 8015		Toleranzklasse / TOLERANCE CLASS mH	Teil-ID PART-ID		
Oberflächenkenngrößen / SURFACE TEXTURE ISO 1302 4287, 4288			Datum/DATE: Name / NAME		
			Gez. CRE.: 18.03.2013 Volkenborn		
© DESY. DESY behält sich alle Rechte vor. Schutzvermerk ISO 16016 beachten. Für Rückfragen bitte an -TT- wenden, Tel. +49-40-8998-3675. © DESY. ALL RIGHTS RESERVED. PREFERRED TO PROTECTION NOTICE ISO 16016. FOR FURTHER ENQUIRIES PLEASE CONTACT -TT- TEL. +49-40-8998-3675.			Gepr. REV.: Frei. REL.: Gen. APR.:	Dokument-Nr. / DOCUMENT NO.	Blatt SHEET von OF
				Zchng.-ID DRAW.-ID	Rev. REV. Ver. VER. Status STATUS

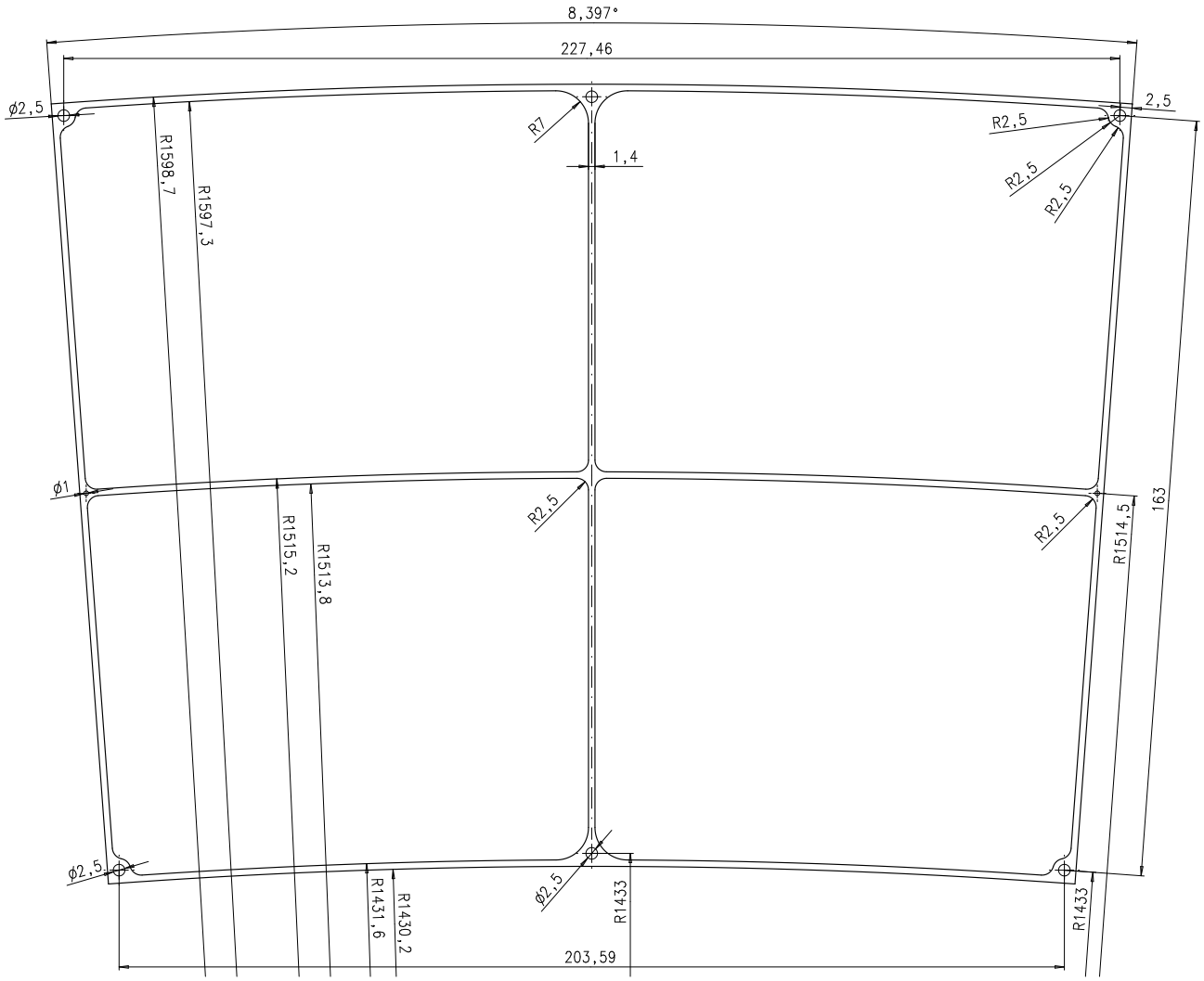

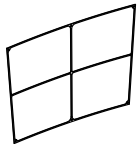

GEMframepattern_32_14
scale 3:2 on DIN A2
DESY, Hamburg, 02.02.2011
Robert Volkenborn

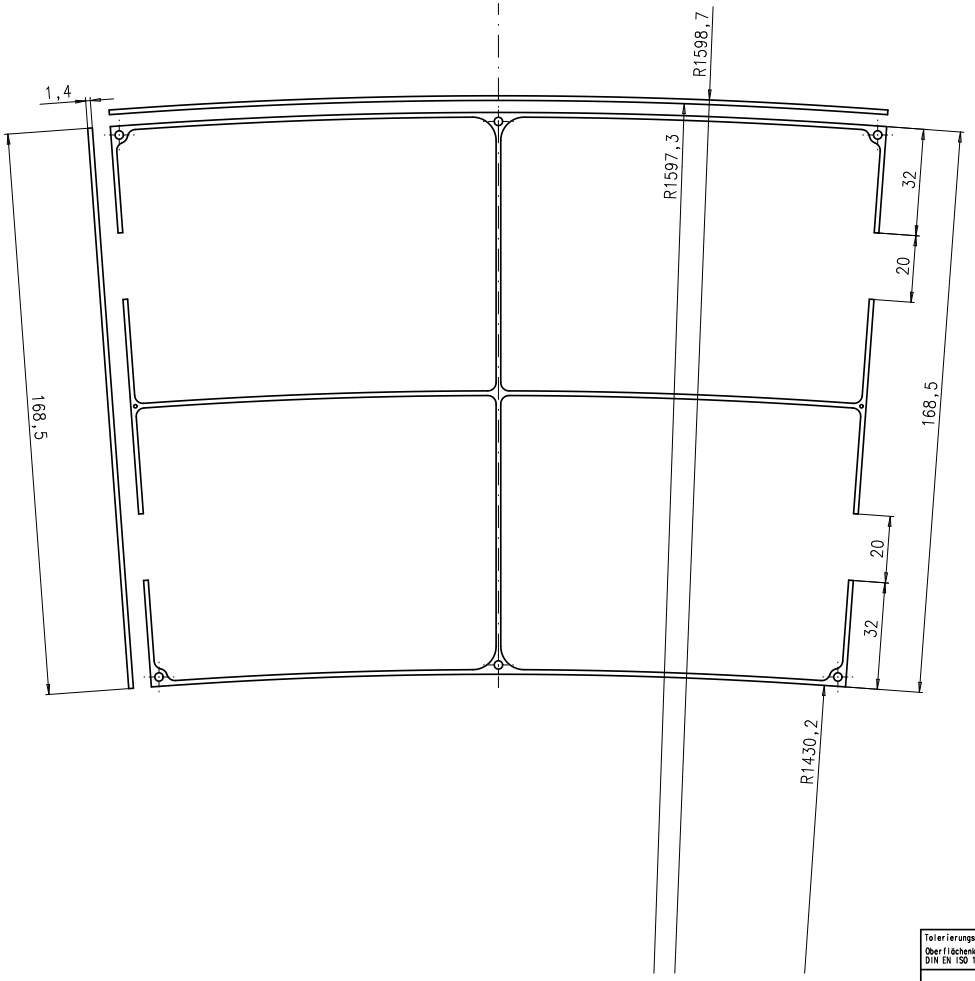

Tolerierungsgrundsatz: ISO 8015 Oberflächenangaben nach DIN EN ISO 1302, 4287 bzw. 4288		Allg.-Toleranzen nach DIN ISO 2768 Toleranzkl.: mK	Halbzeug				Gewicht
Eigentum von DESY. Alle Rechte vorbehalten. Vor der Nutzung dieser Unterlagen oder der darin enthaltenen Informationen ist die Zustimmung des DESY-Technologietransfers erforderlich.			Schutzvermerk DIN ISO 16016 (05-2002) beachten Status:		Maßstab: 1:1 on DIN A2	Ort:	Auftrag:
					Material: AnCeram		
			Datum	Name	GEMgrid_gap mit extra Segment		
			Gez. 04.02.2011	Volkenborn			
			Gepr.				
			Gen.				
			FLC				
			Teile-Nr.:			Rev.:	Blatt 1 von 1 Blättern
Zust.	Änderung	Datum	Name	EDMS-Nr.:	Ers.f.	Ers.d.	Plot tt.mm.jjjj

GEM-layer front side

all drill holes are centered
to their adjacent edges

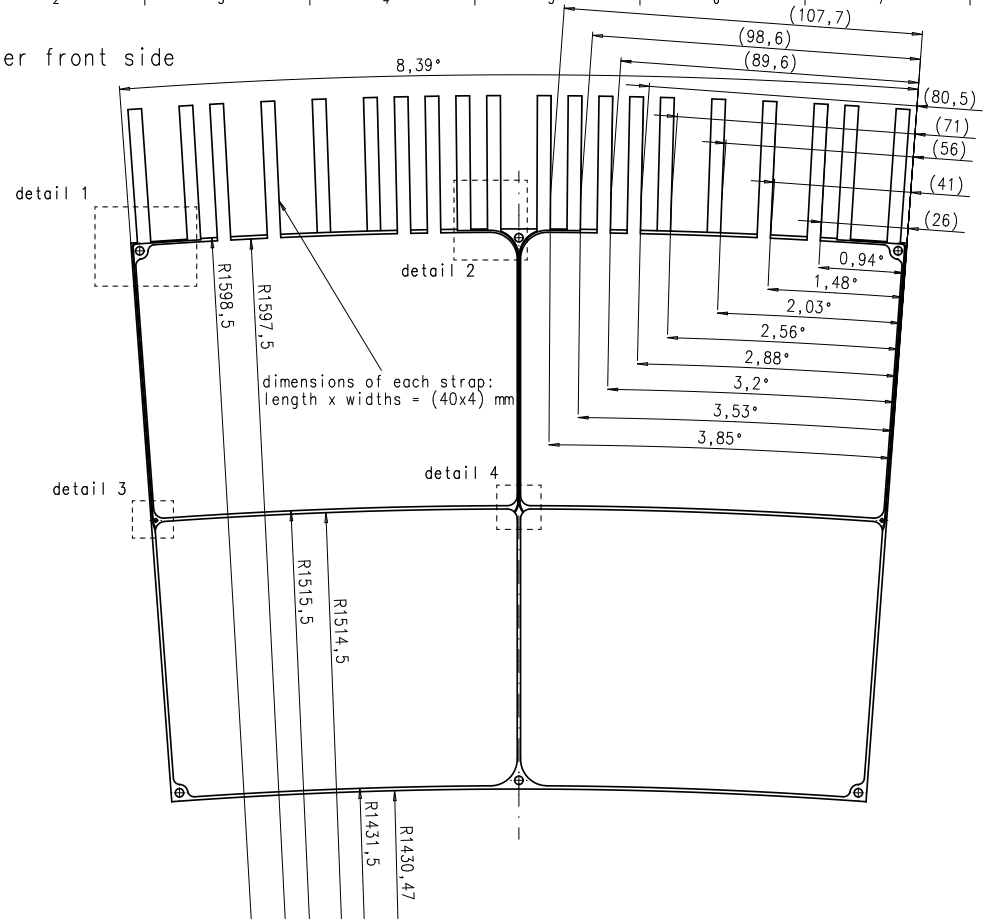

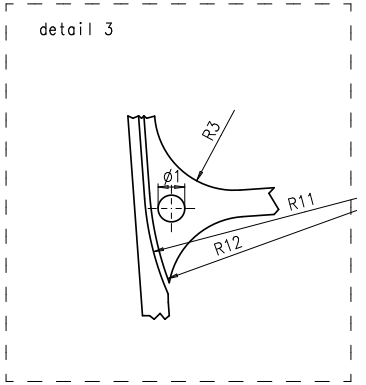

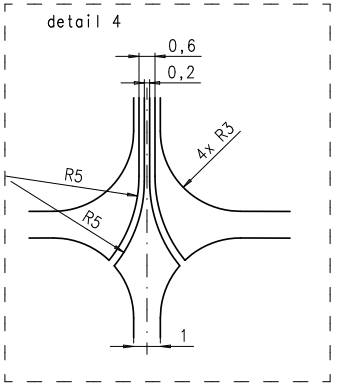

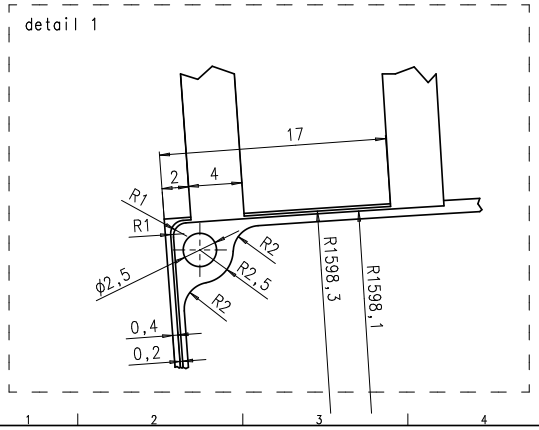

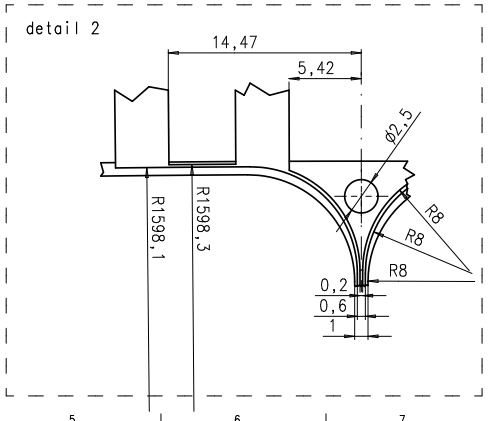

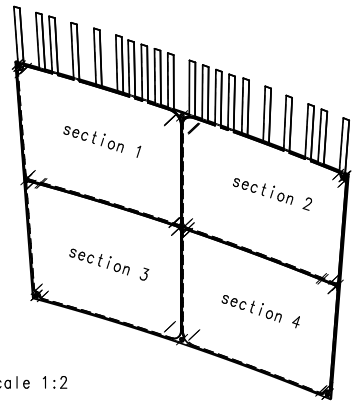

scale 1:2

Toleranzgrundsatz: ISO 8015 Oberflächenkennzeichen nach DIN EN ISO 1302, 4287 bzw. 4288		Allg.-Toleranzen nach DIN ISO 2768 Toleranzkl.: mK		kapton/copper 215mm x 235mm Halbzeug			Gewicht
Eigentum von DESY. Alle Rechte vorbehalten. Vor der Nutzung dieser Unterlagen oder der darin enthaltenen Informationen ist die Zustimmung des DESY-Technologietransfers erforderlich.		Schutzvermerk DIN ISO 16016 (05-2002) beachten		1:1 on DIN A2 Maßstab:	Ort:		Auftrag:
		Status:		Material:			
			Datum	Name	GEMlayer		
		Gez.	30.11.2009	Volkenborn			
		Gepr.					
		Gen.					
		Desy-FLC					
		Teile-Nr.:					Blatt 1 von 1 Blättern
Zust.	Änderung	Datum	Name	EDMS-Nr.:	Ers.f.	Ers.d.	Plot tt.mm.jjjj

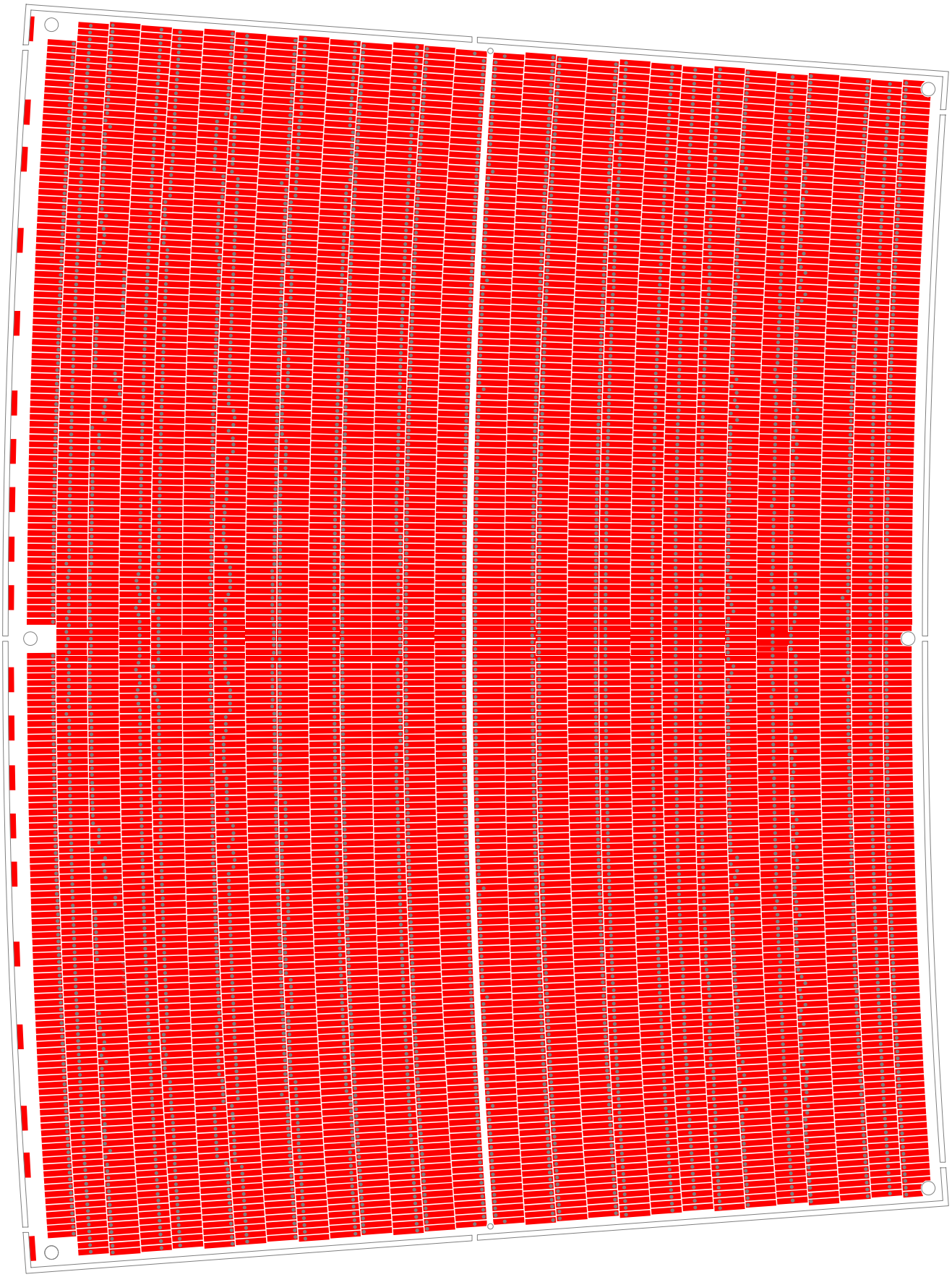

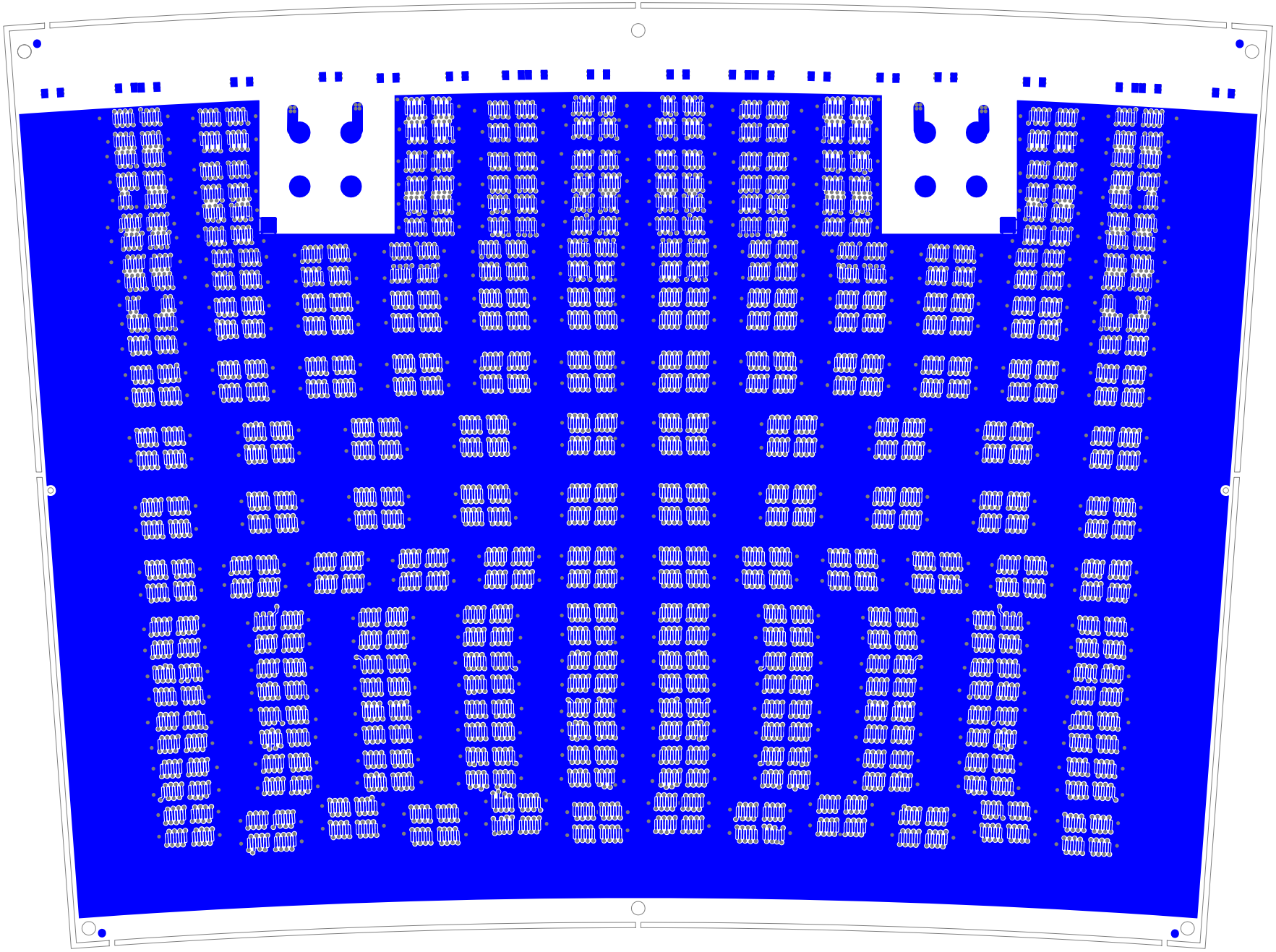

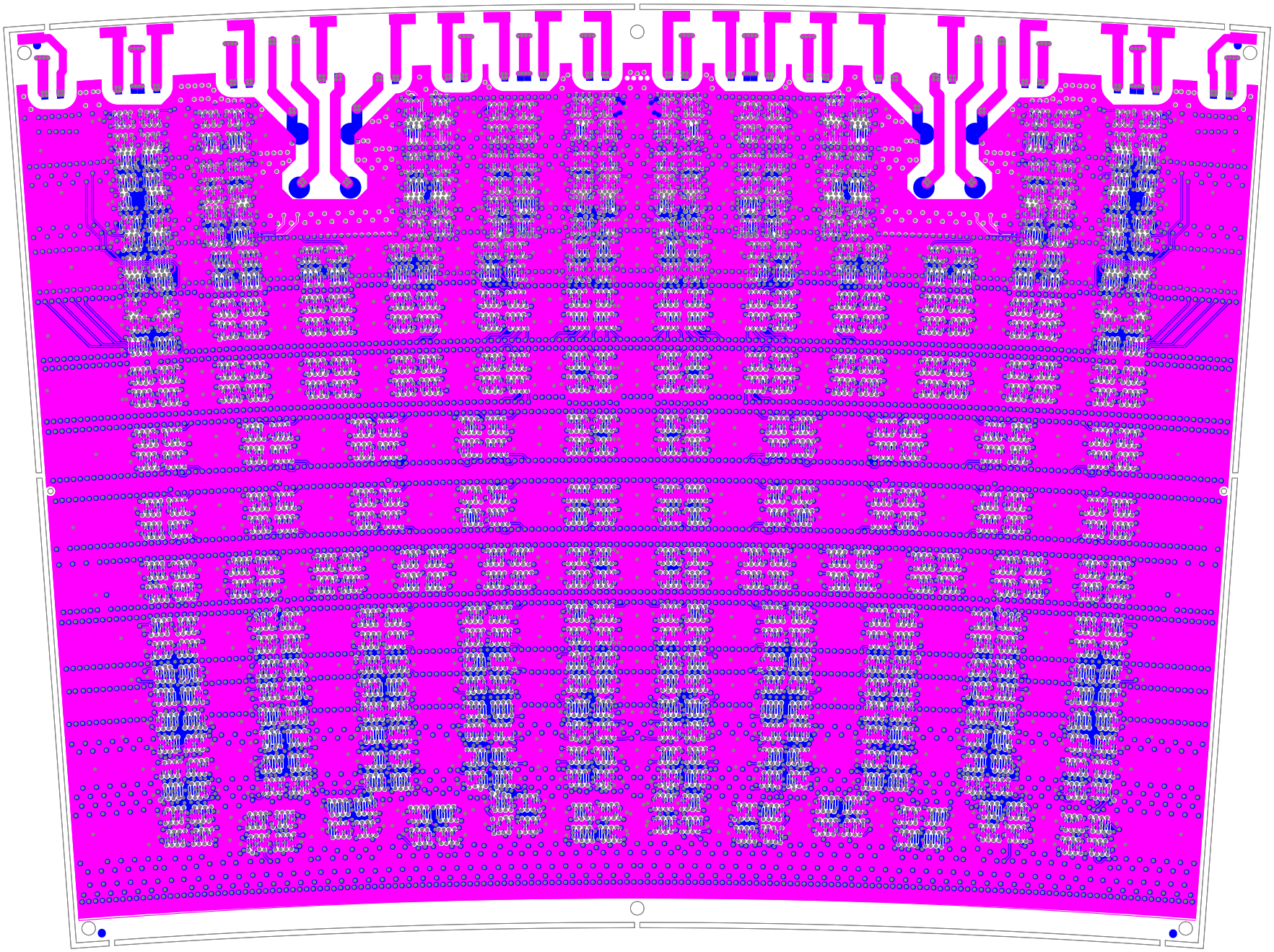

Testbox Assembly:

1) TB_endplate
2) TB_flange (2x)
3) TB_tube
4) TB_bottomlid
5) backframe
6) mounting bracket

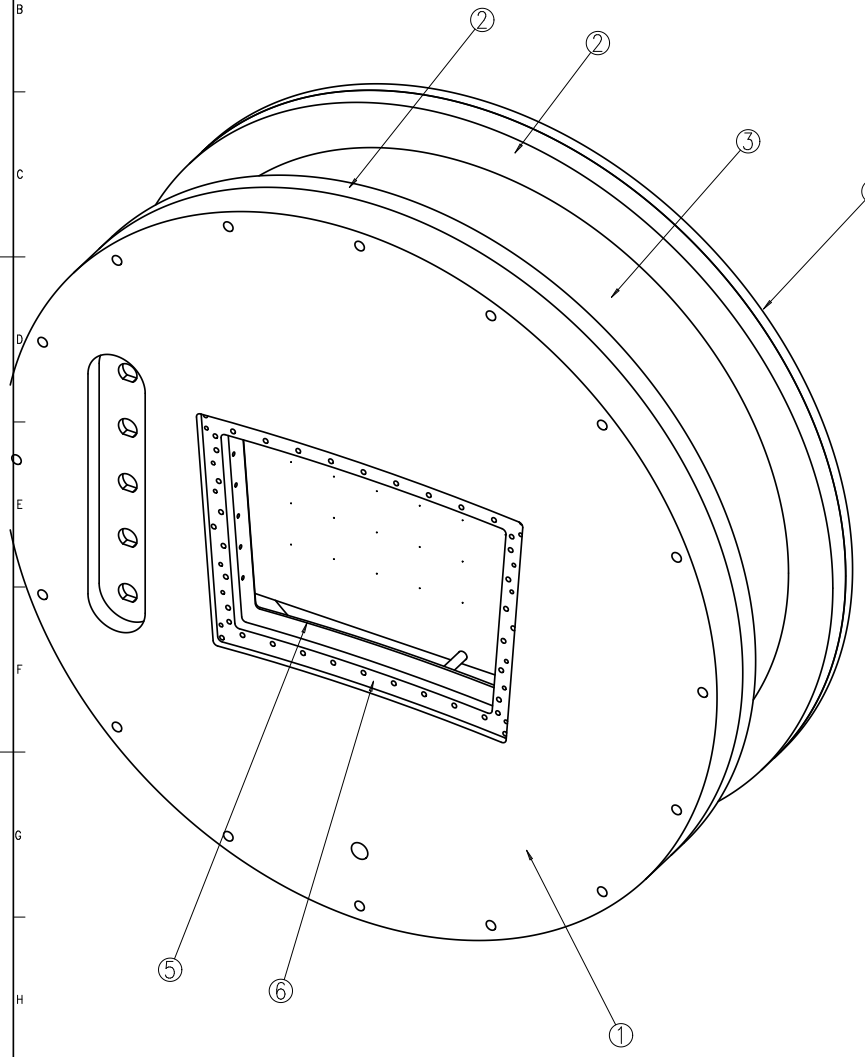

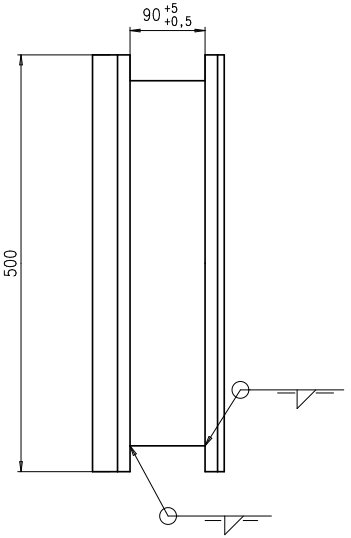

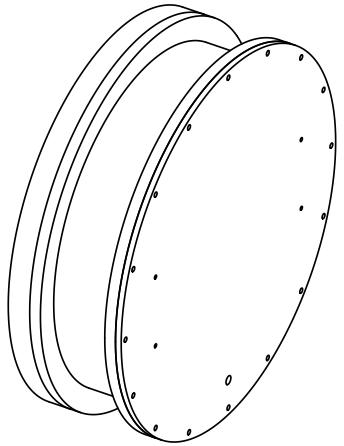

Die Testbox ist ein Gast-Testcontainer für Gasdrücke bis zu 10mbar
Formschlüssige Verbindungen von TB_tube und TB_flange jeweils per rundumlaufender Schweißnaht (gasdicht!)
TB_tube und TB_flange (2x) sollen auf Passung gefertigt werden.

Tolerierungsgrundsatz: ISO 8015 Oberflächenkenngrößen nach DIN EN ISO 1302, 4287 bzw. 4288	Allg.-Toleranzen nach DIN ISO 2768 Toleranzkl.: mK	Halbzeug			Gewicht
Eigentum von DESY. Alle Rechte vorbehalten. Vor der Nutzung dieser Unterlagen oder der darin enthaltenen Informationen ist die Zustimmung des DESY-Technologietransfers erforderlich.		Schutzvermerk DIN ISO 16016 (05-2002) beachten Working Status:	1:4 Maßstab:	Ort:	Auftrag:
			Aluminium / Edelstahl Material:		
	Datum	Name	Testbox assembly		
	Gez. 02.08.2010	Volkenborn_Robert			
	Gepr.				
	Gen.				
FLC				A Rev.:	Blatt 1 von 1 Blättern
Zust. Änderung	Datum	Name	EDMS-Nr.: D000000000916785	Ers.f.	Ers.d.	Plot
			Teile-Nr.: D000000000884133		

Testbox Assembly:

1) TB_endplate
2) TB_flange (2x)
3) TB_tube
4) TB_bottomlid
5) backframe
6) mounting bracket

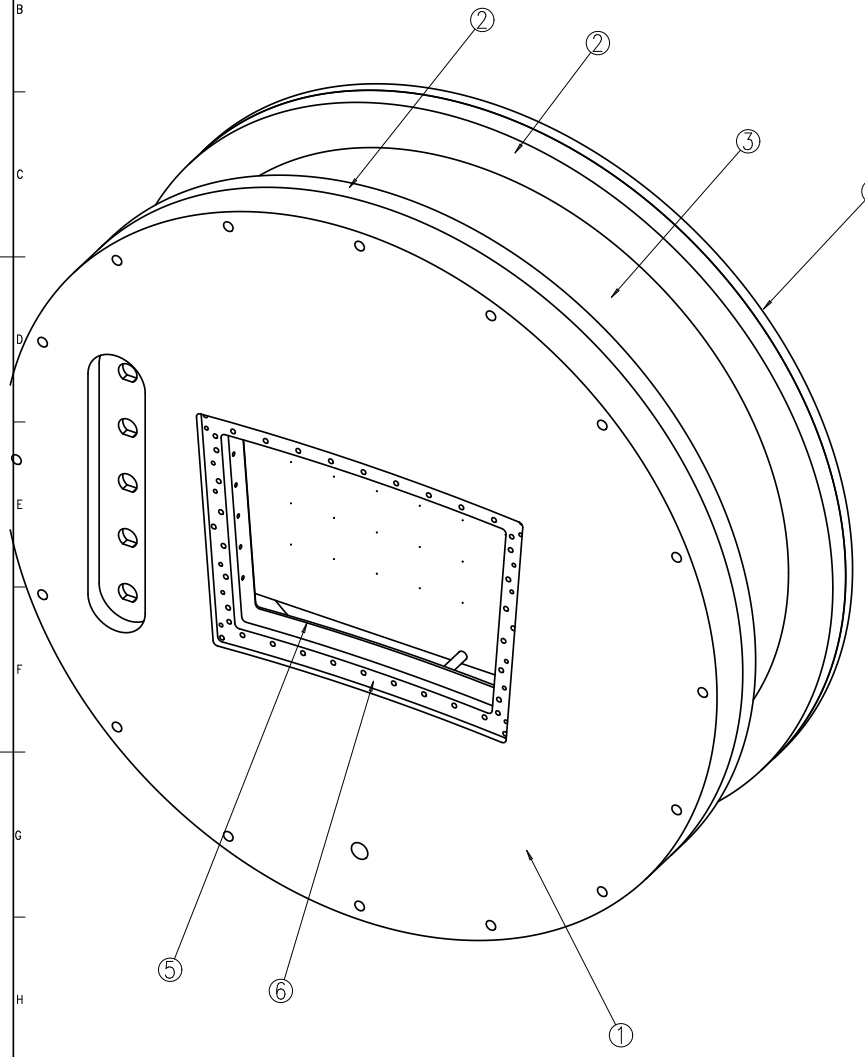

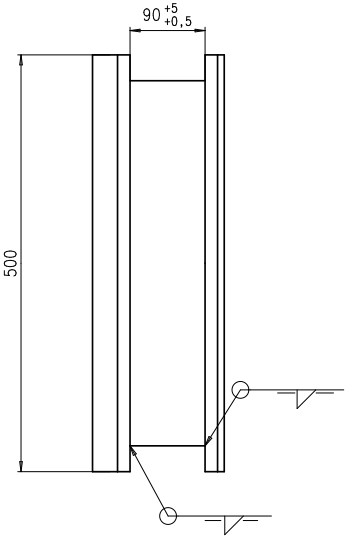

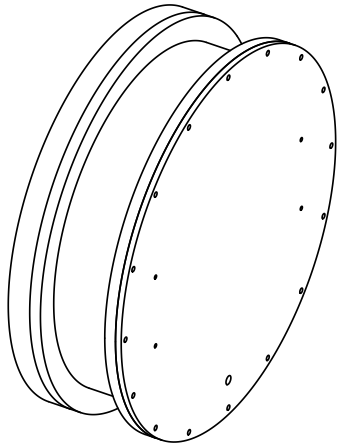

Die Testbox ist ein Gast-Testcontainer für Gasdrücke bis zu 10mbar
Formschlüssige Verbindungen von TB_tube und TB_flange jeweils per rundumlaufender Schweißnaht (gasdicht!)
TB_tube und TB_flange (2x) sollen auf Passung gefertigt werden.

Tolerierungsgrundsatz: ISO 8015 Oberflächenkenngrößen nach DIN EN ISO 1302, 4287 bzw. 4288	Allg.-Toleranzen nach DIN ISO 2768 Toleranzkl.: mK	Halbzeug			Gewicht
Eigentum von DESY. Alle Rechte vorbehalten. Vor der Nutzung dieser Unterlagen oder der darin enthaltenen Informationen ist die Zustimmung des DESY-Technologietransfers erforderlich.		Schutzvermerk DIN ISO 16016 (05-2002) beachten Working Status:	1:4 Maßstab:	Ort:	Auftrag:
			Aluminium / Edelstahl Material:		
	Datum	Name	Testbox assembly		
	Gez. 02.08.2010	Volkenborn_Robert			
	Gepr.				
	Gen.				
FLC				A Rev.:	Blatt 1 von 1 Blättern
Zust. Änderung	Datum	Name	EDMS-Nr.: D000000000916785	Ers.f.	Ers.d.	Plot
			Teile-Nr.: D000000000884133		

Appendix B

Steering files

B.1 GEAR description of the *GridGEM module*

```
<?xml version="1.0"?>
<gear>
  <!-- GEAR xml file describing the endplate of the LP TPC containing
      one GridGEM module in slot 3 -->
  <!-- Global Parameters -->
  <BField z="0.0" y="0.0" x="0.0" type="ConstantBField"/>
  <global detectorName="LPTPC"/>
  <detectors>
  <detector geartype="TPCParameters" name="TPC">
  <!-- Drift length in mm -->
  <maxDriftLength value="569.37"/>
  <coordinateType value="cartesian"/>

  <modules moduleIDStartCount="0">
    <!-- The below description is defined as default module. -->
    <default>
      <readoutFrequency value="20000000"/>
      <!-- There is a pad layout in each module -->
      <PadRowLayout2D type="VersatileDiskRowLayout" rMin="1432.50">
        <!-- row 0 -->
        <row offset="1.503" padHeight="5.25" padWidth="1.05" rowHeight
           ="5.45" padPitch="1.2625" nPad="164"/>
        <!-- row 1 -->
        <row offset="1.924" padHeight="5.65" padWidth="1.05" rowHeight
           ="5.85" padPitch="1.2625" nPad="164"/>
        <!-- row 2 -->
        <row offset="1.721" padHeight="5.65" padWidth="1.05" rowHeight
           ="5.85" padPitch="1.2625" nPad="165"/>
```

```
<!-- row 3 -->
<row offset="1.540" padHeight="5.65" padWidth="1.05" rowHeight
   ="5.85" padPitch="1.2625" nPad="166"/>
<!-- row 4 -->
<row offset="1.962" padHeight="5.65" padWidth="1.05" rowHeight
   ="5.85" padPitch="1.2625" nPad="166"/>
<!-- row 5 -->
<row offset="1.734" padHeight="5.65" padWidth="1.05" rowHeight
   ="5.85" padPitch="1.2625" nPad="167"/>
<!-- row 6 -->
<row offset="1.542" padHeight="5.65" padWidth="1.05" rowHeight
   ="5.85" padPitch="1.2625" nPad="168"/>
<!-- row 7 -->
<row offset="1.962" padHeight="5.65" padWidth="1.05" rowHeight
   ="5.85" padPitch="1.2625" nPad="168"/>
<!-- row 8 -->
<row offset="1.769" padHeight="5.65" padWidth="1.05" rowHeight
   ="5.85" padPitch="1.2625" nPad="169"/>
<!-- row 9 -->
<row offset="1.570" padHeight="5.65" padWidth="1.05" rowHeight
   ="5.85" padPitch="1.2625" nPad="170"/>
<!-- row 10 -->
<row offset="1.996" padHeight="5.65" padWidth="1.05" rowHeight
   ="5.85" padPitch="1.2625" nPad="170"/>
<!-- row 11 -->
<row offset="1.791" padHeight="5.65" padWidth="1.05" rowHeight
   ="5.85" padPitch="1.2625" nPad="171"/>
<!-- row 12 -->
<row offset="1.592" padHeight="5.65" padWidth="1.05" rowHeight
   ="5.85" padPitch="1.2625" nPad="172"/>
<!-- row 13 -->
<row offset="2.008" padHeight="5.65" padWidth="1.05" rowHeight
   ="7.05" padPitch="1.2625" nPad="172"/>
<!-- row 14 -->
<row offset="1.898" padHeight="5.65" padWidth="1.05" rowHeight
   ="5.85" padPitch="1.2625" nPad="173"/>
<!-- row 15 -->
<row offset="1.715" padHeight="5.65" padWidth="1.05" rowHeight
   ="5.85" padPitch="1.2625" nPad="174"/>
<!-- row 16 -->
<row offset="1.510" padHeight="5.65" padWidth="1.05" rowHeight
   ="5.85" padPitch="1.2625" nPad="175"/>
<!-- row 17 -->
<row offset="1.916" padHeight="5.65" padWidth="1.05" rowHeight
   ="5.85" padPitch="1.2625" nPad="175"/>
```

```
      <!-- row 18 -->
      <row offset="1.735" padHeight="5.65" padWidth="1.05" rowHeight
         ="5.85" padPitch="1.2625" nPad="176"/>
      <!-- row 19 -->
      <row offset="1.535" padHeight="5.65" padWidth="1.05" rowHeight
         ="5.85" padPitch="1.2625" nPad="177"/>
      <!-- row 20 -->
      <row offset="1.966" padHeight="5.65" padWidth="1.05" rowHeight
         ="5.85" padPitch="1.2625" nPad="177"/>
      <!-- row 21 -->
      <row offset="1.769" padHeight="5.65" padWidth="1.05" rowHeight
         ="5.85" padPitch="1.2625" nPad="178"/>
      <!-- row 22 -->
      <row offset="1.561" padHeight="5.65" padWidth="1.05" rowHeight
         ="5.85" padPitch="1.2625" nPad="179"/>
      <!-- row 23 -->
      <row offset="1.965" padHeight="5.65" padWidth="1.05" rowHeight
         ="5.85" padPitch="1.2625" nPad="179"/>
      <!-- row 24 -->
      <row offset="1.775" padHeight="5.65" padWidth="1.05" rowHeight
         ="5.85" padPitch="1.2625" nPad="180"/>
      <!-- row 25 -->
      <row offset="1.572" padHeight="5.65" padWidth="1.05" rowHeight
         ="5.85" padPitch="1.2625" nPad="181"/>
      <!-- row 26 -->
      <row offset="1.989" padHeight="5.65" padWidth="1.05" rowHeight
         ="5.85" padPitch="1.2625" nPad="181"/>
      <!-- row 27 -->
      <row offset="1.790" padHeight="5.65" padWidth="1.05" rowHeight
         ="5.85" padPitch="1.2625" nPad="182"/>
    </PadRowLayout2D>
  </default>
  <!-- The position of the modules on the end-plate are set. The
     origin of this coordinate is the center of the end plate. -->

  <!-- Modules in the lower row. They are shifted in x because it is
     assumed that the phi=0 to be the central axis of the end plate
     -->
  <!-- module No.0 -->
  <module>
    <angle value="-0.02083"/>
    <offset y_phi="0" x_r="-172.5"/>
  </module>

  <!-- module No.1 -->
```

```
    <module>
      <angle value="-0.167259"/>
      <offset y_phi="0" x_r="-172.5"/>
    </module>

    <!-- modules in the middle row, no offset -->
    <!-- module No.2 -->
    <module>
      <angle value="0.07516"/>
    </module>

    <!-- module No.3 -->
    <module>
      <angle value=" -0.071268"/>
    </module>

    <!-- module No.4 -->
    <module>
      <angle value="-0.217523"/>
    </module>

    <!-- modules in the upper row -->
    <!-- module No.5 -->
    <module>
      <angle value="0.014076"/>
      <offset y_phi="0" x_r="171.615"/>
    </module>

    <!-- module No.6 -->
    <module>
      <angle value="-0.132353"/>
      <offset y_phi="0" x_r="171.615"/>
    </module>
  </modules>

  </detector>
  </detectors>
</gear>
```

B.2 Typical MarlinTPC Steering file

```
<marlin>
<execute>
  <processor name="MyConditionsProcessor"/>
  <processor name="MyTrackerRawDataToDataConverterProcessor"/>
  <processor name="MyPulseFinder"/>
  <processor name="MyChannelMappingProcessor"/>
  <processor name="MyRowBasedHitFinderProcessor"/>
  <processor name="MyLCIOOutputProcessor"/>
</execute>

<global>
  <parameter name="LCIOInputFiles"> /afs/desy.de/group/flc/pool/tpc/
     share/LPData/June_2011/LCIOrawdata/readout-17694.000.slcio </
     parameter>
  <parameter name="MaxRecordNumber" value="-1" />
  <parameter name="SkipNEvents" value="0" />
  <parameter name="SupressCheck" value="false" />
  <parameter name="GearXMLFile"> /afs/desy.de/group/flc/pool/caiazza/
     LPData/June_2011/gearfile.xml </parameter>
  <parameter name="Verbosity" options="DEBUG0-4,MESSAGE0-4,WARNING0-4,
     ERROR0-4,SILENT"> MESSAGE </parameter>
</global>

<processor name="MyConditionsProcessor" type="ConditionsProcessor">
  <parameter name="DBInit" type="string">lctpcconddb02.desy.
     de:lctpc:lctpcreader:cptr123R </parameter>
  <parameter name="DBCondHandler" type="StringVec">ADCChannelMapping /
     LP1/T24_1/DESY/Grid_GEM_Module_V.2/channelmapping HEAD</parameter
     >
  <parameter name="DBCondHandler" type="StringVec">Pedestals /LP1/
     T24_1/DESY/Grid_GEM_Module_V.2/pedestal_readout HEAD</parameter>
  <parameter name="DBCondHandler" type="StringVec">
     ADCElectronicsParameters /LP1/T24_1/DESY/Grid_GEM_Module_V.2/
     ADCElectronicsParameters HEAD </parameter>
  <parameter name="DBCondHandler" type="StringVec">
     AltroExtElectronicsParameters /LP1/T24_1/DESY/Grid_GEM_Module_V
     .2/AltroExtElectronicsParameters HEAD </parameter>
  <parameter name="Verbosity" options="DEBUG0-4,MESSAGE0-4,WARNING0-4,
     ERROR0-4,SILENT"> WARNING </parameter>
  </processor>

<processor name="MyTrackerRawDataToDataConverterProcessor" type="
    TrackerRawDataToDataConverterProcessor">
```

```
  <parameter name="InputCollectionName" type="string">AltroRawData </
      parameter>
  <parameter name="OutputCollectionName" type="string">TPCData </
      parameter>
  <!--if not 0 the output collection is set transient-->
  <parameter name="SetOutputTransient" type="int"> 0 </parameter>
</processor>

<processor name="MyPulseFinder" type="PulseFinderProcessor">
  <!--PulseFinderProcessor: finds pulses out of the raw data and
      calculate the time and charge (in FADC) information-->
  <!--Name of the conditions collection in which the parameters of the
       read out electronics is stored-->
  <parameter name="ElectronicsParametersCollectionName" type="string">
      ADCElectronicsParameters </parameter>
  <!--Name of the conditions object in which the parameters of the
      read out electronics is stored-->
  <parameter name="ElectronicsParametersObjectName" type="string">
      GenericADCElectronicsParameters </parameter>
  <parameter name="PedestalCollectionName" type="string">Pedestals</
      parameter>
  <!--if true the ADC spectrum will be stored for all pulses-->
  <parameter name="ForceSpectrumSave" type="bool">true </parameter>
  <!--Name of the input TrackerData collection-->
  <parameter name="InputCollectionName" type="string" lcioInType="
      TrackerData">TPCData </parameter>
  <!--Maximum number of the adc spectrum; to determine wether a pulse
      is maxed out. This single value overrides any value, from any
      readout group, which may have been taken from LCCD.-->
  <!-- <parameter name="MaximumADCValueOverride" type="float">1024 </
      parameter> -->
  <!--Declares the minimal height of the maximum entry of a pulse in
      ADC counts.-->
  <parameter name="MinimumPulseHeight" type="float"> 8 </parameter>
  <!--Declares the minimal length of a pulse in time bins above the
      thresholds.-->
  <parameter name="MinimumPulseLength" type="int"> 5 </parameter>
  <!--Name of the output TrackerData collection only the data related
      to a pulse will be stored-->
  <parameter name="OutputTrackerDataCollectionName" type="string"
      lcioOutType="TrackerData">TPCDataInPulses </parameter>
  <!--Name of the output TrackerPulse collection-->
  <parameter name="OutputTrackerPulseCollectionName" type="string"
      lcioOutType="TrackerPulse">TPCPulses </parameter>
```

```
  <!--A pulse ends if the ADC value drops below this value times the
      pedestal width.-->
  <parameter name="PulseEndPedestalWidthFactor" type="float">3 </
      parameter>
  <!--A pulse starts if the ADC value is the given value times the
      pedestal width.-->
  <parameter name="PulseStartPedestalWidthFactor" type="float">5 </
      parameter>
  <parameter name="SaveNBinsAfterEnd" type="int">7 </parameter>
  <!--# bins saved before start threshold (except there is another
      pulse)-->
  <parameter name="SaveNBinsBeforeStart" type="int">3 </parameter>
   <!--SUMQ = 0 (default), FIT_PARABOLA = 1, MAXQ = 2-->
  <parameter name="ChargeCalculationMode" type="int">0 </parameter>
  <!--INFLEXION_POINT = 0 (default), FIT_PARABOLA = 1,
      CENTRE_OF_GRAVITY = 2, FIRST_ABOVE_THRESHOLD = 3, AT_MAXIMUM = 4
      -->
  <parameter name="TimeCalculationMode" type="int">0 </parameter>
  <!--verbosity level of this processor ("DEBUG0-4,MESSAGE0-4,WARNING0
      -4,ERROR0-4,SILENT")-->
  <parameter name="Verbosity" type="string">WARNING </parameter>
  <parameter name="PlateauLengthCutOff" type="int">4</parameter>
  <!--if true the output collection is written-->
  <parameter name="WriteOutputToStorage" type="bool">true </parameter>
</processor>

<processor name="MyChannelMappingProcessor" type="
    ChannelMappingProcessor">
  <!--ChannelMapper changes cellID0 to map from hardware channel
      numbers to sowftware/logical channel numbers.-->
  <!--Name of the input collection-->
  <parameter name="InputCollectionName" type="string" lcioInType="
      TrackerPulse" value="TPCPulses"/>
  <!--Name of the collection with the mapping-->
  <parameter name="ChannelMappingCollectionName" type="string">
      ADCChannelMapping </parameter>
  <parameter name="RemoveChannelsWithoutMapping" value="true" />
  <parameter name="OutputCollectionName" type="string">TPCPulsesMapped
      </parameter>
  <!--if not 0 the output collection is set transient (only if
      OutputCollectionName defined)-->
  <!--parameter name="SetOutputTransient" type="int">0 </parameter-->
  <parameter name="Verbosity" type="string">WARNING </parameter>
</processor>
```

```
<processor name="MyRowBasedHitFinderProcessor" type="
    RowBasedHitFinderProcessor">
  <!--RowBasedHitFinderProcessor calculates TrackerHits from
      TrackerPulses-->
  <!--Optional: The charge conversion factor from ADC values to
      primary electrons-->
  <parameter name="ChargeConversionFactorOverride" type="float">1 </
      parameter>
  <!--Optional: the gear pad indices of dead channels-->
  <!--parameter name="DeadPadsOverride" type="IntVec"> </parameter-->
  <!--Optional: Name of the input collection containing the TPC
      conditions data-->
  <parameter name="InputTPCConditions" type="string"> TPCConditions </
      parameter>
  <!--Name of the input TrackerPulses collection-->
  <parameter name="InputTrackerPulses" type="string" lcioInType="
      TrackerPulse">TPCPulsesMapped </parameter>
  <!--Maximum number of empty consecutive pads in hit (default: 1)-->
  <parameter name="MaxDeadChannelsOverride" type="int">1 </parameter>
  <parameter name="DeadPadsOverride" type="IntVec"> 1</parameter>
  <!--Maximum time between pulses in a hit in ns (default: 200.)-->
  <parameter name="MaxTimeSpreadOverride" type="float">500 </parameter
      >
  <!--Minimum size of hit / Minimum number of Pads (default: 1)-->
  <parameter name="MinHitSizeOverride" type="int"> 2 </parameter>
  <!--Minimum size of the maximum slice value of the maximal pulse (in
       charge) in a hit.-->
  <parameter name="MinMaxPulseSliceHeightOverride" type="float"> 12 </
      parameter>
  <!--Name of the output TrackerHits collection-->
  <parameter name="OutputTrackerHits" type="string" lcioOutType="
      TrackerHit">TPCHits </parameter>
  <!--Optional: If set to true, the output coordinate system is
      changed to be the global coordinates (default is false).-->
  <parameter name="UseGlobalCoordinates" type="bool">true </parameter>
  <!--Optional: Set drift velocity in case there is no conditions data
       in mm/mu s-->
  <parameter name="VDriftOverride" type="float">55.85 </parameter>
  <!--verbosity level of this processor ("DEBUG0-4,MESSAGE0-4,WARNING0
      -4,ERROR0-4,SILENT")-->
  <parameter name="Verbosity" type="string">WARNING </parameter>
  <!--if true, the output hits collection is written to storage (
      default: true)-->
  <parameter name="WriteOutputToStorage" type="bool">true </parameter>
</processor>
```

```
<processor name="MyLCIOOutputProcessor" type="LCIOOutputProcessor">
  <!--Writes the current event to the specified LCIO outputfile. Needs
      to be the last ActiveProcessor.-->
  <!-- name of output file -->
  <parameter name="LCIOOutputFile" type="string"> /afs/desy.de/group/
      flc/pool/caiazza/LPData/June_2011/HitRecoData/HitReco-run17694.
      slcio </parameter>
  <!--write mode for output file:  WRITE_APPEND or WRITE_NEW-->
  <parameter name="LCIOWriteMode" type="string"> WRITE_NEW </parameter
      >
  <!--will split output file if size in kB exceeds given value - does
      not work with APPEND and NEW-->
  <!--parameter name="SplitFileSizekB" type="int">1992294 </parameter
      -->
</processor>

</marlin>
```

B.3 Typical TBA configuration file

```
[database]
#please substitute passwd and the relevant path, e.g. for desy group=
   DESY, module=Grid_GEM_Module_V.2
init_write = lctpcconddb01.desy.de:lctpc:lctpcwriter:passwd
init_read = lctpcconddb02.desy.de:lctpc:lctpcreader:passwd
gen_electronics = /LP1/T24_1/group/module/ADCElectronicsParameters
ext_electronics = /LP1/T24_1/group/module/
   AltroExtElectronicsParameters
pedestal_readout = /LP1/T24_1/group/module/pedestal_readout
pedestal_gear = /LP1/T24_1/group/module/pedestal_gear
channelmapping = /LP1/T24_1/group/module/channelmapping

[files]
gearfile = gearfile.xml
channelmapping = ChannelMapping.slcio

[lcio]
rawdataColName = AltroRawData
detName = LPTPC
runDesciption = Test_beam_run

##########################################################################

#switch reconstruction on and off
[reco]
convert = on
#Coices are "off" or "simple" for a first iteration, and "full" for
   reconstruction with time shift and pulse filter
hitreco = simple
#Coices are off or "pathfinder" or "clupatra" to switch between two
   different tracking options
trackreco = off

#parameters for the reconstruction
[parameters]
# maximum number of events to be processed: -1 or commented out means
   all events are reconstructed
maxEvents=-1
# for pulse and hit reco
MinimumPulseHeight = 8
MinimumPulseLength = 5
PulseStartThreshold = 5
PulseEndThreshold = 3
```

```
PlateauLengthCutOff = 4
#SUMQ = 0 (default), FIT_PARABOLA = 1, MAXQ = 2
ChargeCalculationMode = 0
#INFLEXION_POINT = 0 (default), FIT_PARABOLA = 1, CENTRE_OF_GRAVITY =
    2, FIRST_ABOVE_THRESHOLD = 3, AT_MAXIMUM = 4
TimeCalculationMode = 0
vdrift = 55.85
MinMaxPulseSliceHeightOverride = 12
# for track reco
bfield = on
# Limit the number of hits allowed in event for track reco to run if
   pathfinder is choosen.
maxHitsPerEvent = 100
#List of equipped modules = 0,1,2,3,4,5,6 or subset
modules = 0,3,5
rows = 28
#list of bad rows to be ignored in track finding with cuts
#pair of integers, separated by a colon identifying the module and row
    to select.
#A negative number indicates any row and/or any module. For example -1
    -1 signals to remove all rows from all modules
#badrows = -1:0,-1:1,-1:10,-1:13,-1:14,-1:24,-1:25,-1:27

#switch plotting on and off
[plots]
rawdata = on
autorange_raw=2
dumpFullSpectrum = on
pedestal = on
autorange_pulse=2
pulse = on
pulsecol = TPCPulsesMapped
hit = on
track = on
trackcol = FoundTracksNocut

# List of lcio collection names of a type (Hit, Pulse, Raw or Track)
   to be written to tree
[ROOToutput]
output = on
RawData = AltroRawData
Pulses = TPCPulsesMapped
Hits = TPCHits
Tracks = FoundTracksNocut
```

Appendix C

$\tilde{e}$ selection efficiency tables

Cut	**SM e^-e^+**	**$\gamma e^\pm$**	**$\gamma\gamma$**	**Other $\tilde{e}_R$**	**Other SUSY**	**$\tilde{e}_R$**	**Signal purity**
Preselection	738652	2155210	4977600	63430.2	4032.17	**380927**	0.046
ECal ratio	453579	853158	1057320	62660.7	3812.64	**375060**	0.134
Charged energy ratio	324133	764682	1032230	61938	3282.57	**367934**	0.144
ECal energy	94115.7	308161	900625	59510.7	2945.1	**367362**	0.212
Missing Mass	34932.5	86375.6	669952	44340.4	2923.61	**367236**	0.305
J_H selection	28077	45998.8	351253	38138.5	2150.07	**358251**	0.435
Acollinearity	14369.1	23477.2	173630	27527.9	1970.78	**312431**	0.565

Table C.1: Summary of the effective number of events accepted by the high-momentum edge selection. For each applied cut we list the number of events accepted, divided between the different processes among which we split the dataset. In the last column we list the signal purity after that cut, defined as the ratio between the signal and the total number of events.

Cut	**SM e^-e^+**	**$\gamma e^\pm$**	**$\gamma\gamma$**	**Other $\tilde{e}_R$**	**Other SUSY**	**$\tilde{e}_R$**	**BG Rejection**
ECal ratio	0.61	0.40	0.21	0.988	0.95	**0.985**	0.69
Charged energy ratio	0.71	0.90	0.976	0.988	0.86	**0.980**	0.10
ECal energy	0.29	0.40	0.87	0.96	0.897	**0.999**	0.38
Missing mass	0.37	0.28	0.74	0.75	0.993	**0.9997**	0.39
J_H selection	0.80	0.53	0.52	0.86	0.74	**0.976**	0.44
Acollinearity	0.51	0.51	0.49	0.72	0.92	**0.87**	0.48
Summary	0.0195	0.0109	0.0349	0.434	0.489	**0.820**	0.970

Table C.2: Summary of the acceptance of the high-momentum edge selection. For each applied cut this table lists the acceptance for each of the process categories among which we split the dataset. The acceptance is defined as the ratio between the number of events after and before the cut. The last column defines the background rejection for each of those cuts, defined as the fraction of background events which are filtered out by that particular cut. In the last row we show a final summary where, for each category and for the background rejection we consider the effect of the entire selection as a whole.

Cut	**SM e^-e^+**	**$\gamma e^\pm$**	**$\gamma\gamma$**	**Other $\tilde{e}_R$**	**Other SUSY**	**$\tilde{e}_R$**	**Signal purity**
Preselection	738652	2155210	4977600	63430.2	4032.17	**380927**	0.046
ECal ratio	453579	853158	1057320	62660.7	3812.64	**375060**	0.134
Charged energy ratio	324133	764682	1032230	61938	3282.57	**367394**	0.144
ECal energy	44014.1	133842	596442	41512.1	2137.39	**359779**	0.305
Missing mass	27882.7	77028.5	525489	40024.3	2124.45	**359718**	0.349
J_H selection	14922.1	30075	248468	23248.8	1528.49	**350772**	0.524
J_L selection	1.159.4	26757.9	233608	17691.5	1367.22	**266114**	0.487
Acollinearity	6084.19	26620.3	228294	14185.3	1303.05	**262060**	0.487
Missing P_T	4754.05	7494.34	5705.87	14022.5	810.31	**244883**	0.882
Acoplanarity	2782.11	4888.96	2669.86	11077.6	460.214	**154593**	0.876

Table C.3: Summary of the effective number of events accepted by the low-momentum edge selection. For each applied cut we list the number of events accepted, divided between the different processes among which we split the dataset. In the last column we list the signal purity after that cut, defined as the ratio between the signal and the total number of events.

Cut	**SM e^-e^+**	**$\gamma e^\pm$**	**$\gamma\gamma$**	**Other $\tilde{e}_R$**	**Other SUSY**	**$\tilde{e}_R$**	**BG Rejection**
ECal ratio	0.61	0.40	0.21	0.988	0.94	**0.985**	0.69
Charged energy ratio	0.71	0.90	0.976	0.988	0.86	**0.980**	0.10
ECal energy	0.14	0.18	0.58	0.67	0.65	**0.979**	0.63
Missing mass	0.63	0.58	0.88	0.96	0.994	**0.999**	0.18
J_H selection	0.54	0.39	0.47	0.58	0.72	**0.975**	0.53
J_L selection	0.68	0.89	0.94	0.76	0.89	**0.76**	0.09
Acollinearity	0.60	0.995	0.977	0.80	0.95	**0.984**	0.05
Missing P_T	0.78	0.28	0.25	0.988	0.62	**0.93**	0.88
Acoplanarity	0.58	0.65	0.47	0.79	0.57	**0.63**	0.33
Summary	0.0033	0.0022	0.0005	0.14	0.10	**0.30**	0.998

Table C.4: For each applied cut this table lists the acceptance for each of the process categories among which we split the dataset. The acceptance is defined as the ratio between the number of events after and before the cut. The last column defines the background rejection for each of those cuts, defined as the fraction of background events which are filtered out by that particular cut. In the last row we show a final summary where, for each category and for the background rejection we consider the effect of the entire selection as a whole.

List of Figures

[1] *Minimal Supersymmetric Standard Model*

List of Tables

Bibliography

[1] C. Burgess and G. Moore, *The Standard Model: A Primer*. Cambridge University Press, 2012.

[2] P.W. Higgs, "Broken symmetries and the masses of gauge bosons," *Phys. Rev. Lett.* **13** (Oct, 1964) 508–509.

[3] P.W. Higgs, "Spontaneous symmetry breakdown without massless bosons," *Phys. Rev.* **145** (1966) 1156–1163.

[4] **Particle Data Group** , C. Patrignani et al., "Review of Particle Physics," *Chin. Phys.* **C40** no. 10, (2016) 100001.

[5] **Particle Data Group** , J. Beringer et al., "Review of particle physics," *Phys.Rev.* **D86** (2012) 1528.

[6] D. Clowe et al., "A direct empirical proof of the existence of dark matter," *Astrophys.J.* **648** (2006) L109–L113, arXiv:astro-ph/0608407 [astro-ph].

[7] H. Hoekstra, H. Yee and M. Gladders, "Current status of weak gravitational lensing," *New Astron.Rev.* **46** (2002) 767–781, arXiv:astro-ph/0205205 [astro-ph].

[8] M. Persic, P. Salucci and F. Stel, "The Universal rotation curve of spiral galaxies: 1. The Dark matter connection," *Mon. Not. Roy. Astron. Soc.* **281** (1996) 27, arXiv:astro-ph/9506004 [astro-ph].

[9] A.H. Peter, "Dark matter: A brief review," arXiv:1201.3942 [astro-ph.CO].

[10] J.P. Miller et al., "Muon (g-2): Experiment and theory," *Ann.Rev.Nucl.Part.Sci.* **62** (2012) 237–264.

[11] **Muon G-2 Collaboration** , G. Bennett et al., "Final report of the muon E821 anomalous magnetic moment measurement at BNL," *Phys.Rev.* **D73** (2006) 072003, arXiv:hep-ex/0602035 [hep-ex].

[12] T. Blum et al., "The muon (g-2) theory value: Present and future," arXiv:1311.2198 [hep-ph].

[13] A. Czarnecki and W.J. Marciano, "The muon anomalous magnetic moment: A harbinger for 'new physics'," *Phys.Rev.* **D64** (2001) 013014, arXiv:hep-ph/0102122 [hep-ph].

[14] J. Wess and B. Zumino, "Supergauge transformations in four-dimensions," *Nucl. Phys.* **B70** (1974) 39–50.

[15] S.P. Martin, "A supersymmetry primer," *Adv.Ser.Direct.High Energy Phys.* **21** (2010) 1–153, arXiv:hep-ph/9709356 [hep-ph].

[16] S. Coleman and J. Mandula, "All possible symmetries of the S matrix," *Phys. Rev.* **159** (Jul, 1967) 1251–1256.

[17] Y. Golfand and E. Likhtman, "Extension of the algebra of poincare group generators and violation of p invariance," *JETP Lett.* **13** (1971) 323–326.

[18] R. Haag, J.T. Lopuszanski and M. Sohnius, "All possible generators of supersymmetries of the S-matrix," *Nuclear Physics B* **88** no. 2, (1975) 257 – 274.

[19] H.E. Haber, "The Status of the minimal supersymmetric standard model and beyond," *Nucl.Phys.Proc.Suppl.* **62** (1998) 469–484, arXiv:hep-ph/9709450 [hep-ph].

[20] J.F. Gunion and H.E. Haber, "Higgs bosons in supersymmetric models. 1.," *Nucl. Phys.* **B272** (1986) 1. [Erratum: Nucl. Phys.B402,567(1993)].

[21] C. Brust et al., "SUSY, the third generation and the LHC," *Journal of High Energy Physics* **2012** no. 3, (Mar, 2012) 103.

[22] **WMAP collaboration** , C.L. Bennett et al., "Nine-year wilkinson microwave anisotropy probe (WMAP) observations: Final maps and results," *Astrophys. J. Suppl.* **208** (2013) 20, arXiv:1212.5225 [astro-ph.CO].

[23] **Planck collaboration** , P.A.R. Ade et al., "Planck 2013 results. XVI. Cosmological parameters," *Astron. Astrophys.* **571** (2014) A16, arXiv:1303.5076 [astro-ph.CO].

[24] G. Jungman, M. Kamionkowski and K. Griest, "Supersymmetric dark matter," *Phys. Rept.* **267** (1996) 195–373, arXiv:hep-ph/9506380 [hep-ph].

[25] H. Baer, A.D. Box and H. Summy, "Neutralino versus axion/axino cold dark matter in the 19 parameter sugra model," *Journal of High Energy Physics* **2010** no. 10, (Oct, 2010) 23.

[26] K. Griest and D. Seckel, "Three exceptions in the calculation of relic abundances," *Phys. Rev. D* **43** (May, 1991) 3191–3203.

[27] **L3 Collaboration** , P. Achard et al., "Search for scalar leptons and scalar quarks at LEP," *Phys.Lett.* **B580** (2004) 37–49, arXiv:hep-ex/0310007 [hep-ex].

[28] **OPAL Collaboration** , G. Abbiendi et al., "Search for anomalous production of dilepton events with missing transverse momentum in e^+e^- collisions at $\sqrt{s} =$ 183 GeV to 209 GeV," *Eur.Phys.J.* **C32** (2004) 453–473, arXiv:hep-ex/0309014 [hep-ex].

[29] **DELPHI Collaboration** , J. Abdallah et al., "Searches for supersymmetric particles in e^+e^- collisions up to 208 GeV and interpretation of the results within the MSSM," *Eur.Phys.J.* **C31** (2003) 421–479, arXiv:hep-ex/0311019 [hep-ex].

[30] **ALEPH Collaboration** , A. Heister et al., "Search for scalar leptons in e^+e^- collisions at center-of-mass energies up to 209 GeV," *Phys.Lett.* **B526** (2002) 206–220, arXiv:hep-ex/0112011 [hep-ex].

[31] **ALEPH Collaboration** , A. Heister et al., "Absolute mass lower limit for the lightest neutralino of the MSSM from e^+e^- data at $\sqrt{s}$ up to 209 GeV," *Phys.Lett.* **B583** (2004) 247–263.

[32] H. Baer and J. List, "Post-LHC8 supersymmetry benchmark points for ILC physics," *Phys. Rev. D* **88** (Sep, 2013) 055004.

[33] **CMS Collaboration** , " Search for supersymmetry in multijet events with missing transverse momentum in proton-proton collisions at 13 TeV,".

[34] **CMS** , A.M. Sirunyan et al., "Search for direct production of supersymmetric partners of the top quark in the all-jets final state in proton-proton collisions at $\sqrt{s} = 13$ TeV," arXiv:1707.03316 [hep-ex].

[35] **ATLAS Collaboration** , "Search for a scalar partner of the top quark in the jets+E_T^{miss} final state at $\sqrt{s} = 13$ TeV with the ATLAS detector,".

[36] **ATLAS Collaboration** , G. Aad et al., "Search for direct production of charginos, neutralinos and sleptons in final states with two leptons and missing transverse momentum in pp collisions at $\sqrt{s} = 8$ TeV with the ATLAS detector," *JHEP* **05** (2014) 071, arXiv:1403.5294 [hep-ex].

[37] **ATLAS Collaboration** , G. Aad et al., "Summary of the ATLAS experiment's sensitivity to supersymmetry after LHC Run 1 interpreted in the phenomenological MSSM," *JHEP* **10** (2015) 134, arXiv:1508.06608 [hep-ex].

[38] **CMS Collaboration** , V. Khachatryan et al., "Searches for electroweak production of charginos, neutralinos, and sleptons decaying to leptons and W, Z, and Higgs bosons in pp collisions at 8 TeV," *Eur.Phys.J.* **C74** no. 9, (2014) 3036, arXiv:1405.7570 [hep-ex].

[39] Y. Gershtein et al., "Working Group Report: New Particles, Forces, and Dimensions," in *Proceedings, Community Summer Study 2013: Snowmass on the Mississippi (CSS2013)*. 2013. arXiv:1311.0299 [hep-ex].

[40] T. Barklow et al., "ILC Operating Scenarios," arXiv:1506.07830 [hep-ex].

[41] **ILC Collaboration** , L. Evans and S. Michizono, "The International Linear Collider machine staging report 2017," arXiv:1711.00568 [physics.acc-ph].

[42] **ILC Collaboration** , T. Behnke et al., "Executive Summary," in *The International Linear Collider Technical Design Report*, vol. 1. 2013. arXiv:1306.6327 [physics.acc-ph].

[43] **ILC Collaboration** , H. Baer et al., "Physics," in *The International Linear Collider Technical Design Report*, vol. 2. 2013. arXiv:1306.6352 [hep-ph].

[44] **ILC Collaboration** , C. Adolphsen et al., "Accelerator in the Technical Design Phase," in *The International Linear Collider Technical Design Report*, vol. 3.1. 2013. arXiv:1306.6353 [physics.acc-ph].

[45] **ILC Collaboration** , C. Adolphsen et al., "Accelerator Baseline Design," in *The International Linear Collider Technical Design Report*, vol. 3.2. 2013. arXiv:1306.6328 [physics.acc-ph].

[46] **ILC Collaboration** , T. Behnke et al., "Detectors," in *The International Linear Collider Technical Design Report*, vol. 4. 2013. arXiv:1306.6329 [physics.ins-det].

[47] J.E. Brau et al., "The physics case for an e^+e^- linear collider," in *Helmholtz Alliance Linear Collider Forum - Proceedings of the Workshops - Hamburg, Munich, Hamburg - 2010-2012*. 2013.

[48] **CMS Collaboration** , S. Chatrchyan et al., "Observation of a new boson with mass near 125 GeV in pp collisions at $\sqrt{s} = 7$ and 8 TeV," *JHEP* **1306** (2013) 081, arXiv:1303.4571 [hep-ex].

[49] **ATLAS Collaboration** , G. Aad et al., "Evidence for the spin-0 nature of the Higgs boson using ATLAS data," *Phys. Lett.* **B726** (2013) 120–144, arXiv:1307.1432 [hep-ex].

[50] K. Fujii et al., "Physics Case for the International Linear Collider," arXiv:1506.05992 [hep-ex].

[51] J.E. Brau et al., "International Linear Collider physics and detectors: 2011 status report,".

[52] R.S. Gupta, H. Rzehak and J.D. Wells, "How well do we need to measure Higgs boson couplings?," *Phys.Rev.* **D86** (2012) 095001, arXiv:1206.3560 [hep-ph].

[53] C. Campagnari and M. Franklin, "The Discovery of the top quark," *Rev. Mod. Phys.* **69** (1997) 137–212, arXiv:hep-ex/9608003 [hep-ex].

[54] A. Arbey et al., "Physics at the e^+e^- linear collider," *Eur. Phys. J.* **C75** no. 8, (2015) 371, arXiv:1504.01726 [hep-ph].

[55] P. Osland, A. Pankov and A. Tsytrinov, "Identification of extra neutral gauge bosons at the International Linear Collider," *Eur.Phys.J.* **C67** (2010) 191–204, arXiv:0912.2806 [hep-ph].

[56] **LHC New Physics Working Group** , D. Alves, "Simplified models for LHC new physics searches," *J. Phys.* **G39** (2012) 105005, arXiv:1105.2838 [hep-ph].

[57] G. Moortgat-Pick et al., "The role of polarized positrons and electrons in revealing fundamental interactions at the linear collider," *Phys.Rept.* **460** (2008) 131–243, arXiv:hep-ph/0507011 [hep-ph].

[58] K. Buesser, "The International Linear Collider," arXiv:1306.3126 [physics.acc-ph].

[59] **ILD Concept Group - Linear Collider Collaboration** , T. Abe et al., "The International Large Detector: Letter of Intent," arXiv:1006.3396 [hep-ex].

[60] M.A. Thomson, "Particle flow calorimetry at the ILC," *AIP Conf. Proc.* **896** (2007) 215–224. [,215(2007)].

[61] V.K. Ermilova et al., "Primary specific ionization of relativistic particles in gases," *Sov. Phys.-JETP* **29** (1969) 861.

[62] H. Fischle, J. Heintze and B. Schmidt, "Experimental determination of ionization cluster size distributions in counting gases," *Nucl. Instrum. Meth.* **A301** (1991) 202–214.

[63] U. Fano, "Penetration of protons, alpha particles, and mesons," *Ann. Rev. Nucl. Part. Sci.* **13** (1963) 1–66.

[64] E. Fermi, "The Ionization Loss of Energy in Gases and in Condensed Materials," *Physical Review* **57** (March, 1940) 485–493.

[65] W.W.M. Allison and J.H. Cobb, "Relativistic Charged Particle Identification by Energy Loss," *Ann. Rev. Nucl. Part. Sci.* **30** (1980) 253–298.

[66] I.B. Smirnov, "Modeling of ionization produced by fast charged particles in gases," *Nucl. Instrum. Meth.* **A554** (2005) 474–493.

[67] M. Ball, *Methods and results for calibration and track separation of a GEM based TPC using an UV-laser*. PhD thesis, Universität Hamburg, 2008.

[68] W. Blum, W. Riegler and L. Rolandi, *Particle Detection with drift Chambers; 2nd ed.* Springer, Berlin, 2008.

[69] S. Ramo, "Currents induced by electron motion," *Proceedings of the IRE* **27** no. 9, (1939) 584–585.

[70] K. Dehmelt, "TPC task: the past and the present," EUDET Memo 19, EUDET, 2010.

[71] H. Raether, *Electron avalanches and breakdown in gases*. Butterworths advanced physics series: Monographs on ionization and electrical discharges in gases. Butterworths, 1964.

[72] M. Capeans, "Aging of gaseous detectors: Assembly materials and procedures," *ICFA Instrum.Bull.* **24** (2002) 85–109.

[73] Y. Giomataris et al., "MICROMEGAS: A High granularity position sensitive gaseous detector for high particle flux environments," *Nucl.Instrum.Meth.* **A376** (1996) 29–35.

[74] F. Sauli, "Gem: A new concept for electron amplification in gas detectors," *Nucl. Instr. and Meth. A* **386** (1997) 531–534.

[75] J.N. Marx and D.R. Nygren, "The time projection chamber," *Phys. Today* **31** no. 10, (1978) 46–53.

[76] **ALICE Collaboration** , K. Aamodt et al., "The ALICE experiment at the CERN LHC," *JINST* **3** (2008) S08002.

[77] **ALEPH Collaboration** , D. Buskulic and . others., "Performance of the ALEPH detector at LEP," *Nucl.Instrum.Meth.* **A360** (1995) 481–506.

[78] R. Diener, "Study of reconstruction methods for a time projection chamber with gem gas amplification system," Master's thesis, University of Hamburg, 2006.

[79] M.E. Janssen, *Performance Studies of a Time Projection Chamber at the ILC and Search for Lepton Flavour Violation at HERA II.* PhD thesis, Universität Hamburg, April, 2008.

[80] M. Titov, "Perspectives of micro-pattern gaseous detector technologies for future physics projects," in *Proceedings, CMS Workshop: Perspectives on Physics and on CMS at Very High Luminosity, HL-LHC: Alushta, Crimea, Ukraine, May 28-31, 2012*, pp. 241–258. 2013. `arXiv:1308.3047 [physics.ins-det]`.

[81] P. Everaerts, *Rate capability and ion feedback in GEM detectors*. PhD thesis, Universiteit Gent, 2006.

[82] S. Bachmann et al., "Charge amplification and transfer processes in the gas electron multiplier," *Nucl. Instr. and Meth. A* **438** (1999) 376–408.

[83] S. Lotze, *Ion Backdrift Minimisation in a GEM-Based TPC Readout*. PhD thesis, Rheinisch-Westfälischen Technischen Hochschule Aachen, 2006.

[84] A. Cardini, "A systematic study on discharge-induced gem-failure phenomena," in *2005 IEEE Nuclear Science Symposium Conference Record*, vol. 2. 2005.

[85] P. Abbon et al., "The compass experiment at cern," *Nucl. Instr. and Meth. A* **577** (2007) 455–518.

[86] C. Altunbas et al., "Construction, test and commissioning of the triple-gem tracking detector for compass," *Nucl. Instr. and Meth. A* **490** (2002) 177–203.

[87] D. Abbaneo et al., "Construction of the first full-size gem-based prototype for the cms high eta muon system," in *2010 IEEE Nuclear Science Symposium Conference Record*. 2010.

[88] L. Hallermann, *Analysis of GEM Properties and Development of a GEM Support Structure for the ILD Time Projection Chamber*. PhD thesis, Universität Hamburg, 2010.

[89] . EUDET, "Infrastructure for detector research and development towards the international linear collider," tech. rep., EUDET, 2012.

[90] P. Schade, *Development and Construction of a Large TPC Prototype for the ILC and Study of τ Polarisation in $\tilde{\tau}$ Decays with the ILD Detector*. PhD thesis, FB Physik, Univ. Hamburg, 2009.

[91] T. Behnke et al., "A lightweight field cage for a large TPC prototype for the ILC," *Journal of Instrumentation* **5** no. 10, (10, 2010) P10011.

[92] K. Dehmelt, "Status of the Large TPC Prototype," EUDET-Report 46, DESY, December, 2008.

[93] I.M. Gregor, "The EUDET research infrastructure for detector R&D," EUDET-Report 4, EUDET, September, 2009.

[94] D. Autiero et al., "Characterization of the T24 electron beam line available at DESY," note, OPERA Collaboration, April, 2004.

[95] T. Behnke et al., "Test beams at DESY," Memo 11, EUDET, June, 2007.

[96] **AIDA Collaboration** , L. Serin et al., "Periodic report," Tech. Rep. 1, AIDA, 2012.

[97] C. Grefe, "Magnetic field map for a large tpc prototype," Master's thesis, Institut für Experimentalphysik Universität Hamburg, June, 2008.

[98] CERN EP/ED, *ALICE TPC Readout Chip User Manual*, 0.2 ed., June, 2002.

[99] L. Musa, "Prototype compact readout system," Memo 31, EUDET, 2009.

[100] L. Jönsson, "Front end electronics for a TPC at future linear colliders," Memo 30, EUDET, Nov, 2010.

[101] L. Musa et al., "The ALICE TPC front end electronics," in *Proc. of the IEEE Nuclear Science Symposium*. Oct, 2003.

[102] M. Vandenbroucke, "Discharge reduction technologies for micromegas detectors in high hadron flux environments," *JINST* **7** (2012) C05014.

[103] S. Bachmann et al., "Performance of gem detectors in high intensity particle beams," *Nucl. Instr. and Meth. A* **470** (2001) 548–561.

[104] D. Linzmaier, "Aufbau eines monitorsystems für gasbasierte detektoren und messung der elektronenanlagerung im kammergas," Master's thesis, Martin-Luther-Universität Halle-Wittenberg, 2008.

[105] M. Villa et al., "Progress on large area gems," *Nucl. Instr. and Meth. A* **628** (2011) 182–186.

[106] K.D. Linsmeier, *Technische Keramik: Werkstoff für höchste Ansprüche*. Die Bibliothek der Technik. Süddeutscher Verlag onpact GmbH, 2 ed., 2010.

[107] Keyence Corporation, *Keyence LK-G Series Users's Manual*.

[108] LANG GmbH, *LSTEP / ECO-STEP Precise Positioning Systems User Manual*.

[109] **T2K ND280 TPC** , N. Abgrall et al., "Time projection chambers for the T2K near detectors," *Nucl. Instrum. Meth.* **A637** (2011) 25–46, `arXiv:1012.0865 [physics.ins-det]`.

[110] I. Heinze, *Development of a Hough Transformation Track Finder for Time Projection Chambers*. PhD thesis, Universität Hamburg, 2013.

[111] J. Alcaraz, "Helicodial Tracks,". L3 Internal Note 1666.

[112] T. Krämer, "Track Parameters in `LCIO`,". LC_DET_2006-004.

[113] F. Gaede et al., "Lcio - a persistency framework for linear collider simulation studies," in *2003 Conference for Computing in High-Energy and Nuclear Physics*. 2003.

[114] J. Abernathy et al., "Latest developments in the MarlinTPC software package," EUDET Report 09, EUDET, December, 2008.

[115] J. Abernathy et al., "MarlinTPC: A Marlin based common TPC software framework for the LC-TPC collaboration," EUDET Report 04, EUDET, 2007.

[116] K. Zenker, "Study of electrostatic distortions and possible corrections for a gem based tpc readout module,". LC-DET-2013-017.

[117] K. Fujii et al., "The potential of the ILC for discovering new particles," `arXiv:1702.05333 [hep-ph]`.

[118] **ATLAS Collaboration** , A. Airapetian et al., "ATLAS: Detector and physics performance technical design report. Volume 2,".

[119] B.C. Allanach et al., "Measuring sparticle masses in nonuniversal string inspired models at the LHC," *JHEP* **09** (2000) 004, `arXiv:hep-ph/0007009 [hep-ph]`.

[120] B. Gjelsten, D. Miller and P. Osland, "Measurement of SUSY masses via cascade decays for SPS 1a," *JHEP* **0412** (2004) 003, `arXiv:hep-ph/0410303 [hep-ph]`.

[121] I. Galon and Y. Shadmi, "Kinematic edges with flavor splitting and mixing," *Phys. Rev.* **D85** (2012) 015010, `arXiv:1108.2220 [hep-ph]`.

[122] N. D'Ascenzo, *Study of the neutralino sector and analysis of the muon response of a highly granular hadron calorimeter at the International Linear Collider*. PhD thesis, Universität Hamburg, 2009.

[123] M. Berggren et al., "Non-Simplified SUSY: $\tilde{\tau}$-Coannihilation at LHC and ILC," `arXiv:1508.04383 [hep-ph]`.

[124] H. Baer et al., "Searching for supersymmetry at e+e- supercolliders," *Int. J. Mod. Phys. A* **04** (1989) 4111–4163.

[125] G. Bonneau and F. Martin, "Hard-photon emission in e^+e^- reactions," *Nuclear Physics B* **27** no. 2, (1971) 381 – 397.

[126] H. Nilles, "Supersymmetry, supergravity and particle physics," *Physics Reports* **110** no. 1 - 2, (1984) 1 – 162.

[127] A. Djouadi, J.L. Kneur and G. Moultaka, "Suspect: A fortran code for the supersymmetric and higgs particle spectrum in the MSSM," *Computer Physics Communications* **176** no. 6, (2007) 426 – 455.

[128] M. Cahill-Rowley et al., "pMSSM Studies at the 7, 8 and 14 TeV LHC," arXiv:1307.8444 [hep-ph].

[129] M. Berggren et al., "Non-Simplified SUSY: $\tilde{\tau}$-Coannihilation at LHC and ILC," arXiv:1307.8076 [hep-ph].

[130] V. Torre and T.A. Poggio, "On edge detection," *IEEE Transactions on Pattern Analysis and Machine Intelligence* **8** no. 2, (1986) 147–163.

[131] J. Canny, "A computational approach to edge detection," *IEEE Transactions on pattern analysis an machine intelligence* **8** (November, 1986) 679–698.

[132] D. Demigny and T. Kamlé, "A discrete expression of canny's criteria for step edge detector performances evaluation," *IEEE Trans. Pattern Anal. Mach. Intell.* **19** no. 11, (Nov., 1997) 1199–1211.

[133] R. Deriche, "Using canny's criteria to derive a recursively implemented optimal edge detector," *International Journal of Computer Vision* **1** no. 2, 167–187.

[134] J. Shen and S. Castan, "An optimal linear operator for step edge detection," *CVGIP: Graph. Models Image Process.* **54** no. 2, (Mar., 1992) 112–133.

[135] W. Kilian, T. Ohl and J. Reuter, "WHIZARD: Simulating multi-particle processes at LHC and ILC," *Eur. Phys. J.* **C71** (2011) 1742, arXiv:0708.4233 [hep-ph].

[136] T. Sjostrand, S. Mrenna and P.Z. Skands, "PYTHIA 6.4 Physics and Manual," *JHEP* **05** (2006) 026, arXiv:hep-ph/0603175 [hep-ph].

[137] M. Berggren, "SGV 3.0 - a fast detector simulation," in *International Workshop on Future Linear Colliders (LCWS11) Granada, Spain, September 26-30, 2011.* 2012. arXiv:1203.0217 [physics.ins-det].

[138] J.S. Marshall and M.A. Thomson, "Pandora Particle Flow Algorithm," in *Proceedings, International Conference on Calorimetry for the High Energy Frontier (CHEF 2013): Paris, France, April 22-25, 2013*, pp. 305–315. 2013. arXiv:1308.4537 [physics.ins-det].

[139] P. Billoir, "Progressive track recognition with a kalman-like fitting procedure," *Computer Physics Communications* **57** no. 1, (1989) 390 – 394.

[140] R. Frühwirth, "Application of kalman filtering to track and vertex fitting," *Nuclear Instruments and Methods in Physics Research Section A: Accelerators, Spectrometers, Detectors and Associated Equipment* **262** no. 2, (1987) 444 – 450.

[141] C. Kleinwort, "General Broken Lines as advanced track fitting method," *Nucl. Instrum. Meth.* **A673** (2012) 107–110, arXiv:1201.4320 [physics.ins-det].